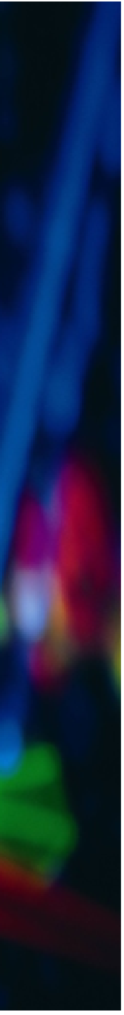

THESIS

in candidacy for the degree of

DOCTOR OF UNIVERSITY PARIS 13

Specialty : **Signals and Images**

defended by

Ba Chien THAI

on December 17, 2018

Tone Mapping Operators for High Dynamic Range Images

Director : **Anissa MOKRAOUI**
Co-supervisor : **Basarab MATEI**

JURY

Amine NAIT-ALI	*Professor, Université Paris-Est Créteil*	**Reviewer**
Maria TROCAN	*Professor, ISEP*	**Reviewer**
Marco CAGNAZZO	*Associate professor, TELECOM ParisTech*	**Examinor**
François-Xavier COUDOUX	*Professor, Université de Valenciennes*	**Examinor**
Anissa MOKRAOUI	*Professor, Université Paris 13*	**Examinor**
Basarab MATEI	*Associate professor, Université Paris 13*	**Examinor**

Contents

List of Tables

List of Figures

List of Algorithms

List of Notations

The notations used in this thesis follow the principles below.

i. The bold capital letters are used to represent a two-dimensional (2D) array, which can be a matrix (LDR luminance $\mathbf{L}_{LDR}$, HDR luminance $\mathbf{L}_{HDR}$, approximations $\mathbf{I}$, $\mathbf{I}'$, low-high details $\mathbf{D}_{lh}$, $\mathbf{D}'_{lh}$, high-low details $\mathbf{D}_{hl}$, $\mathbf{D}'_{hl}$, high-high details $\mathbf{D}_{hh}$, $\mathbf{D}'_{hh}$, horizontal details $\mathbf{D}_{h}$, $\mathbf{D}'_{h}$, vertical details $\mathbf{D}_{v}$, $\mathbf{D}'_{v}$, diagonal details $\mathbf{D}_{d}$, $\mathbf{D}'_{d}$, intermediate matrices $\mathbf{D}$, $\mathbf{D}'$, $\mathbf{U}$, $\mathbf{U}'$, $\mathbf{V}$, $\mathbf{V}'$, $\mathbf{W}$, $\mathbf{W}'$, stenciles $\mathbf{P}u$, $\mathbf{C}u$, $\mathbf{P}v$, $\mathbf{C}v$, $\mathbf{P}w$, $\mathbf{C}w$, $\mathbf{S}$, etc.).

ii. The superscripts j or J a symbol stand for the multiresolution level. For instance, $\mathbf{I}^J$ is HDR logarithm luminance image at multiresolution level J, etc.

iii. The superscript i represents a given bin. For example, $\widetilde{l}^i_{HDR}$ represents pixel of the i-th bin, etc.

iv. The array indexing, which encloses the x-downward, y-rightward directions in parentheses, is used to access an element of the array. E.g. $\mathbf{I}(x_n, y_m)$ is the pixel at n-th row and m-th column of 2D image $\mathbf{I}$, etc.

The list of important notations is described as follows:

$\mathbf{I}$	An image represented as a two-dimensional (2D) array.
$\mathbf{I}(x_n, y_m)$	A pixel in the image $\mathbf{I}(x_n, y_m)$ at n-th row and m-th column.
J	Multiresolution level.
j	A given multiresolution level, $j = 1, 2, ..., J$.
N^j	Height of image at a given level j.
M^j	Width of image at a given level j.
B	Bin number.
i	A given bin number, $i = 1, 2, ..., B$.
$\mathbf{I}^J$	HDR logarithm luminance image at multiresolution level J.
$\tilde{\mathbf{I}}_{HDR}$	HDR logarithm luminance image.
$\tilde{\mathbf{I}}_{LDR}$	Coarse LDR luminance image.
$L_{\min}$	Minimum luminance value.
$L_{\max}$	Maximum luminance value.

L_{ave}	Mean luminance value.
$\sum\sum$	Indicate sum of all elements.
$\otimes$	Product term by term.
$*$	Convolutional product.
$\mathcal{N}(\mu,\sigma^2)$	Gaussian distribution with mean μ and variance σ^2.
$\mathcal{B}(\alpha,\beta)$	Beta distribution.
AME	Absolute Mean Error.
CA	Cell-Average.
CSF	Contrast Sensitivity Function.
DR	Dynamic Range.
DRIM	Dynamic Range Independent Metric.
EDR	Extended Dynamic Range.
FSITM	Feature Similarity Index for Tone-Mapped Images.
HDR	High Dynamic Range.
HVA	Human Visual Adaptation.
HVS	Human Visual System.
JND	Just-Noticeable Difference.
LCD	Liquid Crystal Display.
LDR	Low Dynamic Range.
LED	Light Emitting Diode.
LWMPA	Locally Weighted Mean Phase Angle.
MOS	Mean Opinion Score.
MSE	Mean Squared Error.
MS-SSIM	Multi Scale Structural Similarity Index.
PCG	Binary Phase Congruency Map.
PDF	Probability Density Function.
PLCC	Pearson's Linear Correlation Coefficient.
PSNR	Peak Signal-to-Noise Ratio.
PV	Point-Value.
RGB	Red, Green, Blue.
SDR	Standard Dynamic Range.
SF	Structural Fidelity.
SN	Statistical Naturalness.
SNR	Signal-to-Noise Ratio.
SSIM	Structural Similarity Index.
TMO	Tone Mapping Operator.
TMQI	Tone-Mapped Image Quality Index.
VDP	Visible Difference Predictor.
WCDF	Weighted Cohen-Daubechies-Feauveau Wavelets.
WRB	Weighted Red-Black Wavelets.

CHAPTER 1

Introduction

Chapter content

1 Introduction

Most of natural scenes have a wide range of illumination conditions, ranging from night scenes to outdoor scenes (see Figure 1.1a). The Human Visual System (HVS) processes the scene radiances in a nonlinear manner through different adaptation processes. It forms a percept where all details are visible. Electronic devices capture the scene radiances linearly. An image Tone Mapping Operator (TMO) is necessary to nonlinearly encode the image as well as to map it to the display characteristics so that the displayed image corresponds to our memory of the original scene (see Figure 1.2). Assume that Observer 1 and Observer 2 are looking at the same scene but in two different environments. Observer 2 is viewing the scene on a monitor after it has been captured, stored, and tone mapped. Observer 1, on the other hand, is watching the scene in the real world. The final goal is that the tone mapped scene should match the perception of the real-world scene and thus Observers 1 and 2 will feel that they perceive the same scene.

Luminance is the physical measure of scene radiances, given in candela per square

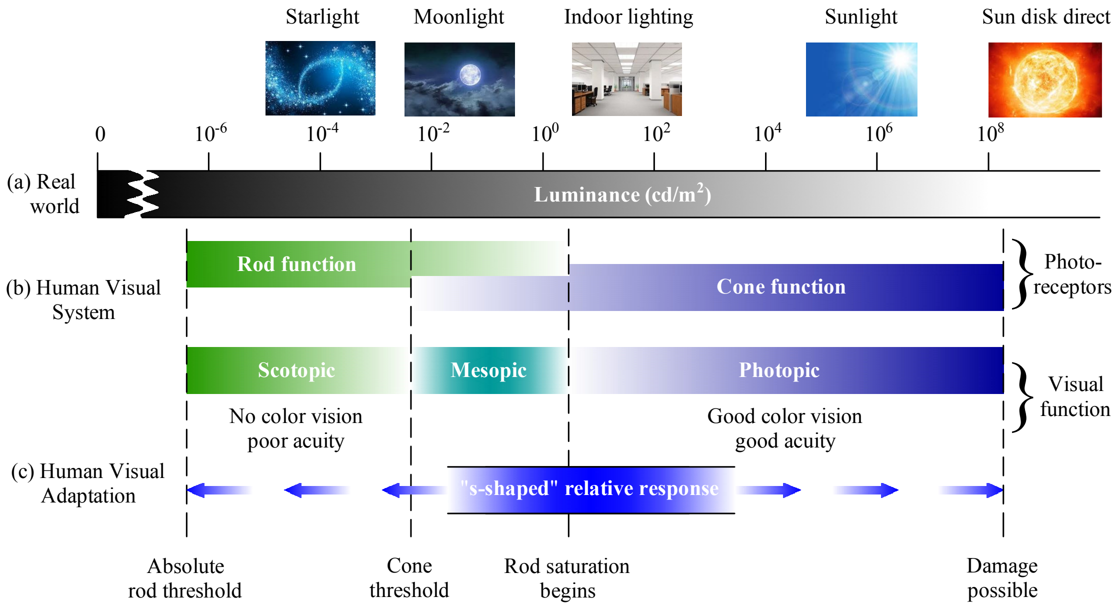

Figure 1.1: *Functional luminance range of the HVS.*

meter (cd/m^2). The dynamic range (or contrast ratio) is the luminance ratio between the brightest and the darkest object in a scene. An unit of contrast ratio in form of logarithm with base 2 is *f-stops*, sometimes, using logarithm with base 10 is then called *orders of magnitude*.

An High Dynamic Range (HDR) image with different levels of (under-exposed or over-exposed) exposure of the scene is the representation of a real-world scene (i.e. HDR scenes where its very dark and bright areas are rendered at the same time) whose dynamic range exceeds by far that of the output displays. With HDR scenes, it is likely that some parts of their representation are clipped by the capturing process. Typical examples of HDR scenes are sunny outdoor scenes or a view of an indoor room with objects visible outside the window. The dynamic ranges of several natural scenes were measured and $1:160$ was found to be an average contrast ratio. Outdoor scenes usually have a larger dynamic range, which can reach a contrast ratio of three orders of magnitude ($1:1000$) or more. Scenes with fog tend to have a small contrast ratio.

Currently used display technologies are Cathode Ray Tube (CRT) or Liquid Crystal Displays (LCD). We will call these standard displays and define their dynamic range as being standard as opposed to HDR displays which have a much larger dynamic range. The contrast ratio of standard displays is generally $1:100$ but new LCD monitors can reach $1:400$. Prints have a contrast ratio of $1:50 - 1:500$, depending on the printing technology. Newly developed HDR displays have a contrast ratio reaching $1:25000$, depending on the viewing conditions. Indeed, most of the display devices available nowadays are not able to natively display HDR content. Entry level monitors/displays have a low contrast ratio of only around $1:200$. Although high-end LCD televisions have

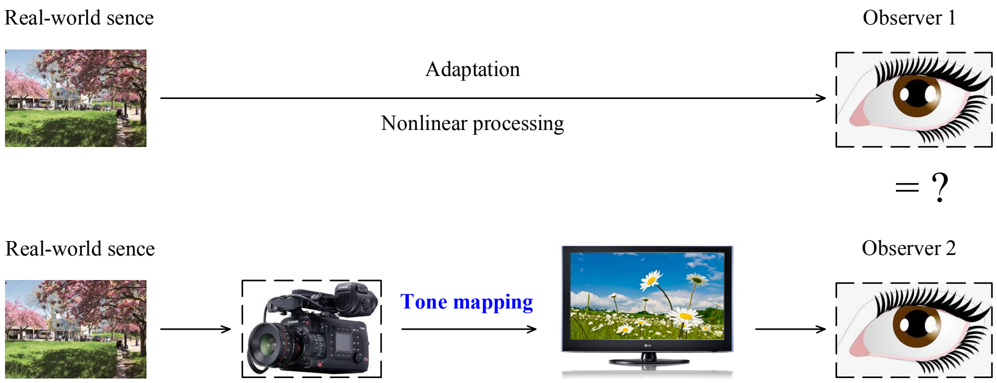

Figure 1.2: *The relationship between the tone mapped image and the real-world scene.*

a much high contrast ratio, on average around 1 : 10000, they are typically discretized at 8-bits and rarely at 10-bits per color channel. This means that colors shades are limited to 255. Moreover HDR display devices currently remain too expensive.

An example is provided in Figure 1.3. The left image, known as "Memorial" HDR test image with 18.38 f-stops in HDR Matlab Toolbox [1], is the image captured by the HDR camera and displayed on LDR device. The right image corresponds to the tone mapped image. The image captured by the HDR camera looks too dark although the image perceived by our visual system has more contrast in the shadows.

The HVS is able to perceive real-word scenes with a wide range of luminance levels and intensities in Figure 1.1b. The different cells in the retina are the main factor how the HVS adapts to different luminance levels. The rod cells are used in high luminance levels (higher than 0.01 cd/m^2) and cone cells in low luminance levels (lower than 10 cd/m^2). The HVS state when only the rod cells are used, is called scotopic vision, and when only cone cells are used, is called photopic vision. The state when both cells are active, is called mesopic vision. Only when cone cells are active the HVS can see color. Therefore at the scotopic vision state, the HVS is color blind (see [2]).

For the most part, the rod and cone cells are the reason for the range of the Human Visual Adaptation (HVA) as shown in Figure 1.1c. The rod and cone cells are also called the photoreceptors. The latter convert absorbed light into neural responses in a nonlinear manner. The relative responses of a dark-adapted rod and cone cells are illustrated in Figure 1.4. It has been proven that the shapes of the response curves at any background are independent of the background. The visual system always maintains its log-linear property for about 3 log units of intensity range around any background when given enough time to adapt. In the psychophysical studies, the HVA is evaluated by measuring the minimum amount of incremental light by which an observer distinguishes

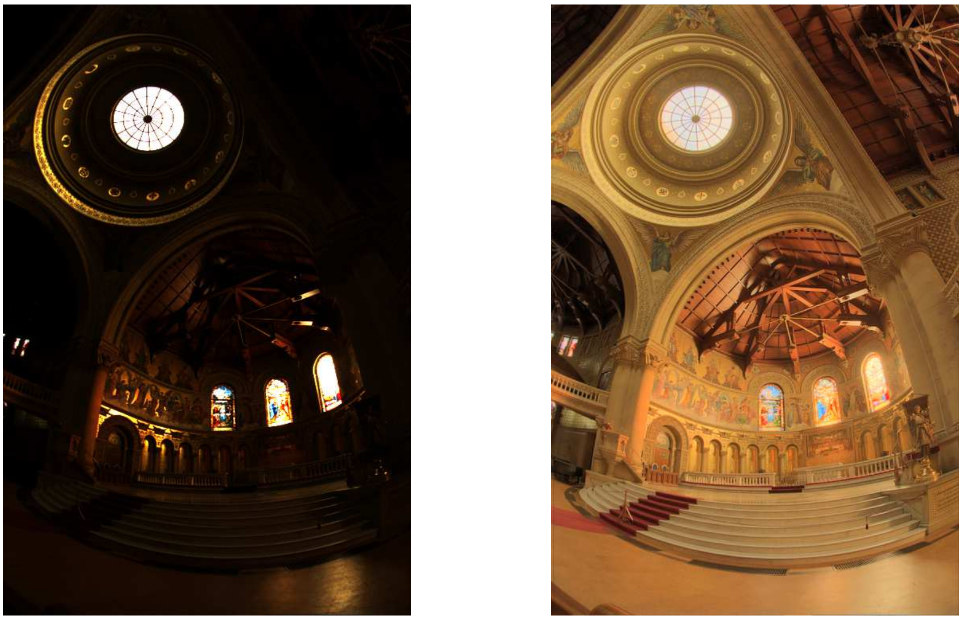

(a) "Memorial" HDR test image **(b)** Our tone mapped image

Figure 1.3: *HDR image and LDR image versus traditional displays: Left image is captured by the HDR camera and displayed on traditional displays; Right image is perceived by our visual system and displayed on traditional displays.*

a test object from the background light. This minimum increment is called a *visual threshold* or *Just-Noticeable Difference* (JND). The perception of luminance obeys the Weber's law, which can be expressed as:

$$\frac{\Delta I_b}{I_b} = K, \tag{1.1}$$

where I_b is the background luminance, ΔI_b is the just noticeable incremental luminance over the background by the HVS, and K is a constant called the Weber fraction. Weber's law is maintained over a wide range of background luminances and breaks only at very low or hight light conditions. This phenomenon is often called light adaptation or luminance masking in the literature of image quality assessment.

Many image TMOs have been proposed. Their main concerns are to reduce the dynamic range (contrast, color gamut, details...) of HDR images to the dynamic range of LDR display device while preserving, as much as possible, the appearance of the captured scene in terms of contrast and the overall impression of brightness and colors.

2 Scope of the thesis

This thesis focuses on the conversion of HDR images into LDR images. Such images are problematic when they are shown on standard LDR monitors since their dynamic range

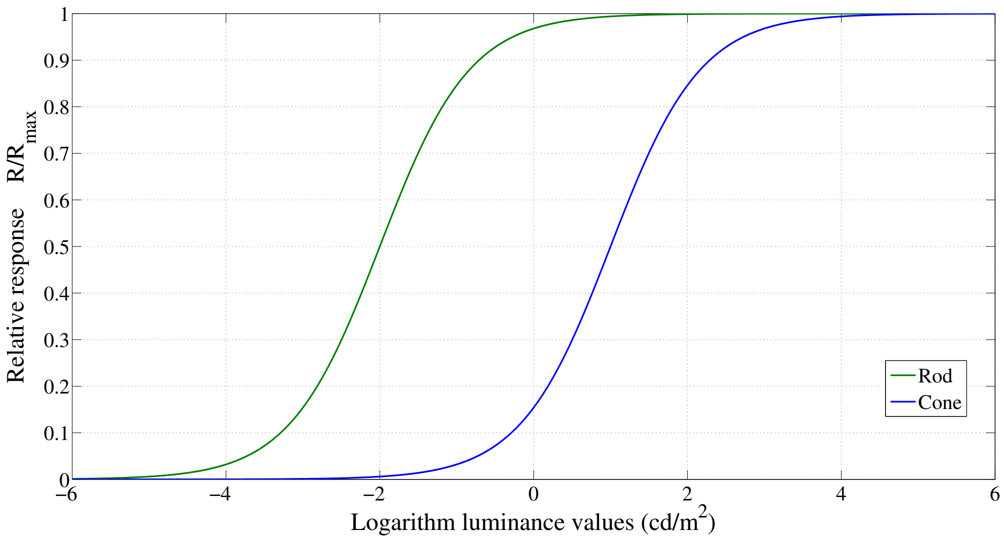

Figure 1.4: *Relative response of dark-adapted rod and cone cells.*

exceeds by far that of the display. To solve this problem, four image tone mapping operators have been proposed. Moreover, investigations have been made to access the image quality of the HDR tone mapped images using an objective quality metric.

3 Organization and contributions of the thesis

This thesis proposes new image tone mapping operators and objective image quality metric. The thesis's organization is provided by Figure 1.5 and summarized below:

Chapter 2 gives a state of art on image tone mapping operators (global, local, frequency, segmentation,...) and reviews some important metric quality evaluations of tone mapped images (HDR image tone mapping metrics). At the end of this chapter, a decision is taken on the metric that will be used to assess the tone mapped images.

Chapter 3 proposes an image tone mapping operator for enhancing the contrast using piecewise linear mapping that models the "s-shaped" curve simulating them, the well-adapted perception of the Human Visual System.

Chapter 4 proposes image tone mapping operators for detail preservations based on Essential Non-Oscillatory (ENO) multiresolution families such as separable approaches (Point-Value, Cell-Average) and non-separable approach (Cell-Average) processed by its multiresolution representation (approximation and details domains).

Chapter 5 proposes an image tone mapping operator with the aim of the contrast enhancement and detail preservation using: (i) the near optimal separable adaptive lifting scheme as the first stage, and (ii) the piecewise linear mapping on the coarse reconstruction as the second stage.

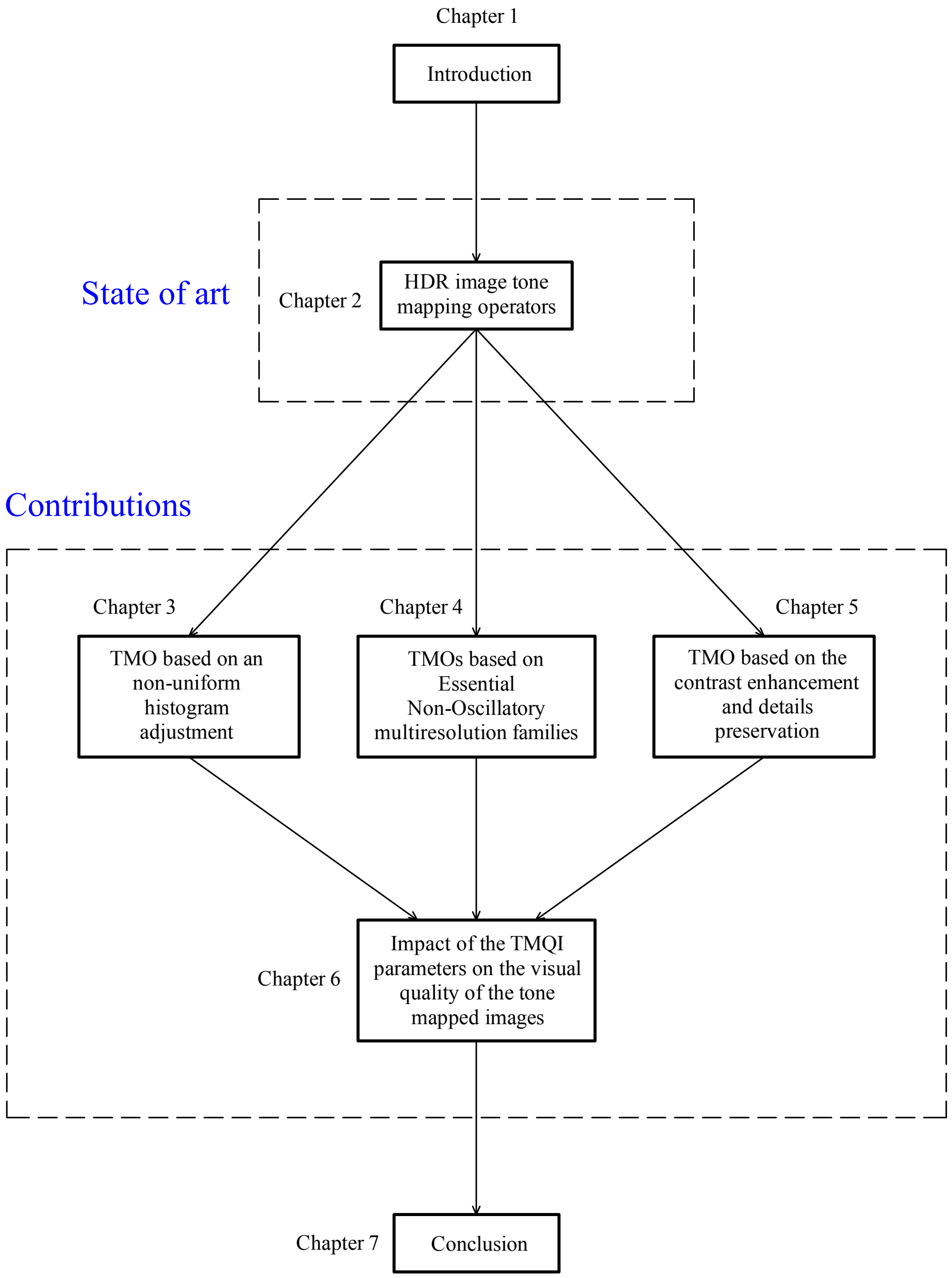

Figure 1.5: *Thesis outline.*

Chapter 6 studies the HDR image tone mapping assessment where the improvement of the tone mapped quality index (TMQI) according to our training dataset is discussed.

Chapter 7 concludes this thesis by summarizing the contributions. It reviews the algorithms that have been proposed and their important roles in the contrast enhancement and preservation of details. Finally it discusses future works.

Appendix A shows the computation of separable multiresolution ENO (Point-Value, Cell-Average) coefficients. Appendix B describes the computation of non-separable multiresolution ENO (Cell-Average) coefficients. Appendix C explains how to compute near optimal filter coefficients. In oder to support the HDR image tone mapping assessment, Matlab user interface has been made (see in Appendix D).

4 List of publications

[1] **B. C. Thai**, A. Mokraoui, and B. Matei. “Contrast Enhancement and Details Preservation of Tone Mapped High Dynamic Range Images”. Journal of Visual Communication and Image Representation (JVCI), Elsevier, 2018.

[2] **B. C. Thai**, A. Mokraoui, and B. Matei. “Piecewise Linear Perceptual Quantizer as a Non-Uniform Histogram Equalization Adjustment for Contrast Enhancement of Tone Mapped HDR Images”. 9th IEEE International Symposium on Signal, Image, Video and Communications (ISIVC), November 2018.

[3] **B. C. Thai**, A. Mokraoui, and B. Matei. “HDR Image Tone Mapping Approach based on Near Optimal Separable Adaptive Lifting Scheme”. 22nd IEEE Signal Processing: Algorithms, Architectures, Arrangements, and Applications (SPA), September 2018.

[4] **B. C. Thai**, A. Mokraoui, B. Matei, and T. Mahdia. “Image Tone Mapping Approach Using Essentially Non-Oscillatory Bi-quadratic Interpolations Combined with a Weighting Coefficients Strategy”. 17th IEEE International Symposium on Signal Processing and Information Technology (ISSPIT), December 2017.

[5] **B. C. Thai**, A. Mokraoui, and B. Matei. “Performance Evaluation of High Dynamic Range Image Tone Mapping Operators Based on Separable Nonlinear Multiresolution Families”. 24th IEEE European Signal Processing Conference (EUSIPCO), August 2016.

CHAPTER 2

State of art on HDR image tone mapping operators

Chapter content

This chapter concerns the state of art on HDR image tone mapping operators. It reviews and classifies the most important methods of tone mapping operators developed in the literature. The end of this chapter discusses the main objective metrics for evaluating the HDR tone mapped images and a decision is taken on the metric that will be used on this thesis to assess the tone mapped images.

1 Introduction

Image tone mapping is the operation that adapts the dynamic range of the HDR content to suit the low dynamic range of a given standard display. Tone mapping operator (TMO) is performed using an operator f which is defined as:

$$f(\mathbf{I}) : \mathbb{R}_{\mathrm{i}}^{N\times M\times ch} \longrightarrow \mathbb{D}_{\mathrm{o}}^{N\times M\times ch}, \tag{2.1}$$

where $\mathbf{I}$ is the HDR image of size $N \times M$; ch is the number of color bands (typically $ch = 3$) with $\mathbb{R}_{\mathrm{i}} \subseteq \mathbb{R}$, $\mathbb{D}_{\mathrm{o}} \subset \mathbb{R}_{\mathrm{i}}$; and the set $\mathbb{D}_{\mathrm{o}} = [0,\ 255]$ is related to the standard LDR monitors.

The human eyes have abilities to be better awareness of details in luminance than in color channels. Therefore, this thesis focuses on changes in luminance. Only luminance is usually tone mapped by a TMO (denote f_{L}), while colors are unprocessed. Therefore, the equation (2.1) becomes:

$$f(\mathbf{I}) : \begin{cases} \mathbf{L}_{LDR} = f_{\mathrm{L}}(\mathbf{L}_{HDR}) : \mathbb{R}_i^{N\times M} \longrightarrow [0,\ 255], \\ \begin{bmatrix} \mathbf{R}_{LDR} \\ \mathbf{G}_{LDR} \\ \mathbf{B}_{LDR} \end{bmatrix} = \mathbf{L}_{LDR} \left(\dfrac{1}{\mathbf{L}_{HDR}} \begin{bmatrix} \mathbf{R}_{HDR} \\ \mathbf{G}_{HDR} \\ \mathbf{B}_{HDR} \end{bmatrix} \right)^{s}, \end{cases} \tag{2.2}$$

where $\mathbf{L}_{LDR}$ and $\mathbf{L}_{HDR}$ are respectively LDR and HDR luminance values, $s \in (0,1]$ is a color saturation factor that decreases the saturation effect.

After the application of f_{L}, each color channel is clamped in the range $[0,\ 255]$. Note that the original gamut is greatly modified in this process, and the tone mapped color appearance can result in great differences from that in the original image. Research addressing this issue will be presented. TMOs can be classified in different groups based on the property of f and the processing techniques that are adopted as summarized in Table 2.1.

2 Image tone mapping operators for high dynamic range images

The four main groups of the classification are:

i. **Global operators:** The operator uses the entire HDR image. The mapping is applied to all pixels with the same operator f_{L}. For more details, one can see the references [3], [4], [5], [6], [7], [8], [9], [10], [25], [26], [27], [28], [29] and [30].

Table 2.1: *Classification of TMOs: Global (G), Local (L), Frequency (F), Segmentation (Seg), Perceptual (Per), Empirical (Em) and Temporal (T).*

	Tone Mapping Operators	**G**	**L**	**F**	**Seg**	**Per**	**Em**	**T**
1	Linear Mapping [3]	✓					✓	
2	Exponential Logarithmic Mapping [3]	✓					✓	
3	Quantization Technique [3]	✓					✓	
4	Perceptual Brightness Reproduction [4]	✓				✓		✓
5	Contrast Based Scale Factor [5]	✓				✓		
6	Visual Adaptation Model [6]	✓				✓		
7	Histogram Adjustment [7] [8]	✓				✓		
8	Time Dependent Visual Adaptation [9]	✓				✓		
9	Adaptive Logarithmic [10]	✓				✓		✓
10	Spatially Variant Tone Reproduction [11]		✓				✓	
11	Photographic Tone Reproduction [12]		✓				✓	
12	Multi-Scale [13]		✓			✓		✓
13	Tone Mapping Operator for High Contrast Images [14]		✓			✓		
14	Local Model of Eye Adaptation [15]		✓			✓		
15	Low Curvature Image Simplifiers [15]			✓			✓	
16	Bilateral Filtering [16]			✓			✓	
17	Gradient Domain Compression [17]			✓			✓	
18	Trilateral Filtering [18]			✓		✓		
19	Image Color Appearance Model [19]			✓		✓		
20	Retinex Methods [20]			✓		✓		
21	Interactive Manipulation [21]				✓		✓	
22	Exposure Fusion [22]				✓		✓	
23	Segmentation Approach [23]				✓	✓		
24	Lightness Perception [24]				✓	✓		
25	Wavelets Domain Compression [25] [26]	✓		✓				
26	Compression Integration [27] [28] [29]	✓						✓
27	Adaptive Histogram Equalization [30]	✓						

ii. **Local operators:** The operator computes a local adaptation for each pixel as well as a neighborhood of pixels i.e. mapping a pixel depends on its neighbors. As a result, local operators are frequently more expensive/costly to compute than global ones. For more details, one can see the references [11], [12], [13] and [15].

iii. **Frequency/Gradient operators:** In the frequency domain, the operator reduces the dynamic range of image components selectively based on their spatial frequency where low and high frequencies of the images are separated. While the operator is applied to the low frequencies, high frequencies are usually kept as they preserve fine details. The gradient operators modify the derivative of an image to achieve dynamic range reduction. These are described in [15], [16], [17], [18], [19], [20], [25] and [26].

iv. **Segmentation operators:** The HDR image is segmented in broad regions and a different mapping is applied to each region. For more information, one can read the following references [21], [22], [23] and [24].

Another classification has been proposed:

i. **Perceptual operators:** These operators can be global, local, based on segmentation, or frequency/gradient operators. The main focus is that the function f models some aspects of the HVS. For more details, one can see the references [4], [5], [6], [7], [8], [9], [10], [13], [14], [15], [18], [19], [20], [23] and [24].

ii. **Empirical operators:** These operators can be global, local, based on segmentation, or frequency/gradient operators. In this case, f_{L} does not try to mimic the HVS, but it tries to create aesthetically-pleasing images inspired by other fields, such as photography. The proposed works are available in [3], [11], [12], [15], [16], [17], [21] and [22].

iii. **Temporal operators:** These operators are designed to be also suitable for HDR video content and animations. The proposed methods are given by the following references [4], [10], [13], [27], [28] and [29].

Following the classifications in local, global, segmentation and frequency operators, let us present below some of them.

2.1 Global tone mapping operators

Among the large set of TMOs, we describe below only the main popular tone mapping operators.

2.1.1 Logarithmic and exponential mapping

Among the nonlinear mappings, the logarithmic and exponential mappings are the most straightforward mapping. The main usages are in providing a baseline result against which all other operators may be compared. After all, any other operator is likely to be more complex and expect other operators to provide improved visual performance compared with logarithm and exponential mappings.

For logarithmic mapping, the luminance is given by:

$$\mathbf{L}_{LDR}(x_n,y_m) = \frac{\log_{10}(1+\mathbf{L}_{HDR}(x_n,y_m))}{\log_{10}(1+L_{HDRmax})}, \tag{2.3}$$

while the luminance of exponential mapping is:

$$\mathbf{L}_{LDR}(x_n,y_m) = 1-\exp\Big(-\frac{\mathbf{L}_{HDR}(x_n,y_m)}{L_{HDRave}}\Big), \tag{2.4}$$

where

$$L_{HDRave} = \exp\Big(\frac{1}{N\times M}\sum_{n=1}^{N}\sum_{m=1}^{M}\log(\mathbf{L}_{HDR}(x_n,y_m)+\epsilon)\Big), \tag{2.5}$$

with ϵ in small parameter to avoid the logarithmic singularities.

2.1.2 Brightness reproduction

In [31], Tumblin and Rushmeier based the work on psychophysical data, realizing that the human visual system is already solving the dynamic range reduction problem. It aims at preserving the sensation of brightness of the HDR image before and after the dynamic range reduction. They proposed the following transform:

$$\mathbf{L}_{LDR}(x_n,y_m) = m(L_{HDRave})\times L_{LDRa}\times\Big(\frac{\mathbf{L}_{HDR}(x_n,y_m)}{L_{HDRave}}\Big)^{\frac{\gamma(L_{HDRave})}{\gamma(L_{LDRa})}}, \tag{2.6}$$

where

$$m(L_{HDRave}) = (\sqrt{C_{\max}})^{\gamma_{\text{wd}}-1}, \qquad \gamma_{\text{wd}} = \frac{\gamma(L_{HDRave})}{1.855+0.4\log_{10}(L_{LDRa})}, \tag{2.7}$$

L_{LDRa} is the display adaptation luminance, typically between 30 and 100 cd/m^2 for LDR displays, $C_{\max}$ is the maximum displayable contrast, and $\gamma(x)$ is given by the following expression:

$$\gamma(x) = \begin{cases} 1.855+0.4\log_{10}(x+2.3\cdot 10^{-5}) & \text{for } x\le 100\ \ cd/m^2 \\ 2.655 & \text{otherwise} \end{cases}. \tag{2.8}$$

2.1.3 Contrast-based scale factor

In [5], Ward focused less on brightness perception and attempt to preserve contrasts instead. The model matches the Just Noticeable Differences (JNDs):

$$\mathbf{L}_{LDR}(x_n,y_m) = m\times\mathbf{L}_{HDR}(x_n,y_m), \tag{2.9}$$

$$\text{with}\quad m = \frac{1}{L_{LDRmax}}\left(\frac{1.219+(\frac{L_{LDRmax}}{2})^{0.4}}{1.219+(L_{HDRave})^{0.4}}\right)^{2.5}, \tag{2.10}$$

with L_{HDRave} given by equation (2.5). The maximum display luminance L_{LDRmax} should be specified by the user, and typically in the range of 30 to 100 cd/m^2. Thus, the differences are preserved without spending the limited number of display steps on differences undetectable by the HVS.

2.1.4 Visual adaptation model

The concept of matching Just Noticeable Differences, as explored by Ward in [5], was also used by Ferwerda et al. in their operator [6]. They based their operator on different psychophysical data, with a somewhat different functional shape as a result. Whereas Ward's contrast-based scale factor incorporates only photopic lighting conditions, Ferwerda et al. in [6] added a scotopic component. They also modeled the loss of visual acuity under scotopic lighting, as well as the process of light and dark adaptation which takes place over time. In Ferwerda's operator, display intensities are computed from world intensities by multiplying the latter with a scale factor and adding an offset which allows contrast and overall brightness to be controlled separately.

2.1.5 Adaptive logarithmic

In [10], Drago applied a logarithmic compression to the input luminance, but the base of the logarithm is adjusted according to each pixel's value. The base is varied between 2 and 10 allowing contrast and detail preservation in dark and medium luminance regions while still compressing light regions by larger amounts using the following relationship:

$$\mathbf{L}_{LDR}(x_n,y_m) = \frac{L_{LDRmax}}{100\log_{10}(1+L_{HDRmax})} \cdot \frac{\log_{10}(1+\mathbf{L}_{HDR}(x_n,y_m))}{\log_{10}\left(2+8\left(\frac{\mathbf{L}_{HDR}(x_n,y_m)}{L_{HDRmax}}\right)^{\alpha}\right)}, \tag{2.11}$$

$$\text{with} \quad \alpha = \frac{\log(b)}{\log(0.5)}, \qquad b \in [0,1].$$

2.1.6 Quantization

In [3], Schlick proposed the following rational function:

$$\mathbf{L}_{LDR}(x_n,y_m) = \frac{p\mathbf{L}_{HDR}(x_n,y_m)}{(p-1)\mathbf{L}_{HDR}(x_n,y_m)+L_{LDRmax}} \quad \text{for} \quad p \in [1,\infty), \tag{2.12}$$

where

$$p = \frac{\Delta L}{2^N} \cdot \frac{L_{HDRmax}}{L_{HDRmin}} \quad \text{for uniform quantization,} \tag{2.13}$$

and

$$p = \frac{\Delta L}{2^N} \cdot \frac{L_{HDRmax}}{L_{HDRmin}} \left(1-k+k\frac{\mathbf{L}_{HDR}(x_n,y_m)}{\sqrt{L_{HDRmax} \cdot L_{HDRmin}}}\right) \quad \text{for non-uniform quantization,} \tag{2.14}$$

where ΔL is the Just Noticeable Difference or quantized display luminance step and $N = 8$, $k \in [0,1]$.

2.1.7 Histogram adjustment

In [8], Duan used the following function to compress the luminance of the high dynamic range image $\mathbf{L}_{HDR}(x_n, y_m)$ to display luminance D:

$$\mathbf{D}(x_n, y_m) = (D_{max} - D_{min}) \times \\ \frac{\log(\mathbf{L}_{HDR}(x_n, y_m) + \tau) - \log(L_{HDRmin} + \tau)}{\log(L_{HDRmax} + \tau) - \log(L_{HDRmin} + \tau)} + D_{min}, \tag{2.15}$$

where D_{max} and D_{min} are the minimum and maximum luminance of the visualization devices. The parameter τ controls the overall brightness of the mapped image.

In general, a larger τ makes the mapped image darker and smaller τ makes the mapped LDR image brighter. The parameter τ can be computed in two ways: (i) the manual choice of τ as a trial-and-error process, $\tau = \alpha(L_{HDRmax} - L_{HDRmin})$, with $\alpha \geq 0$; or (ii) automatically based on the global luminance intensities.

This global tone mapping operator is named Histogram Adjustment based Linear Equalization Quantizer (HALEQ). The straight solution is to find the cutting points, denoted c^0, c^1,..., c^{255} in the range of the HDR image D, which satisfy the following function:

$$c^i = c_u^i + \beta(c_{nu}^i - c_u^i) = (1-\beta)c_u^i + \beta c_{nu}^i, \tag{2.16}$$

where $0 \leq \beta \leq 1$ is a controlling parameter which is a constant for all the process; c_u^i, c_{nu}^i are cutting points of the uniform mapping, of the histogram equalization methods, respectively.

The algorithm first divides the range of D into two segments according to equation (2.16). Then these two segments are each independently divided into 2 sub-segments according to equation (2.16). The process is then applied recursively onto each resultant sub-segment to divide it into 2 sub-segments based on equation (2.16) until the predefined number of sub-segments 256 are created (see Figure 2.1). It then remaps to the display grey-level [0, 255] correspondingly .

Latter, Anas [30] modified the constant β by an adaptive parameter β_i in each bin so that the cutting points c^i are deduced as the average of the logarithm luminance values on each sub-interval $[c_u^i,\ c_{nu}^i]$.

2.2 Local tone mapping operators

Local operators improve the quality of the tone mapped image over global operators by attempting to reproduce both the local and the global contrast. This is achieved by having a function f, the mapping operator, which takes into account the intensity values from the neighboring pixels of the pixel being tone mapped. However, neighbors have to be chosen carefully; otherwise, halos around edges can appear. Let us present at the following some methods developed in the literature.

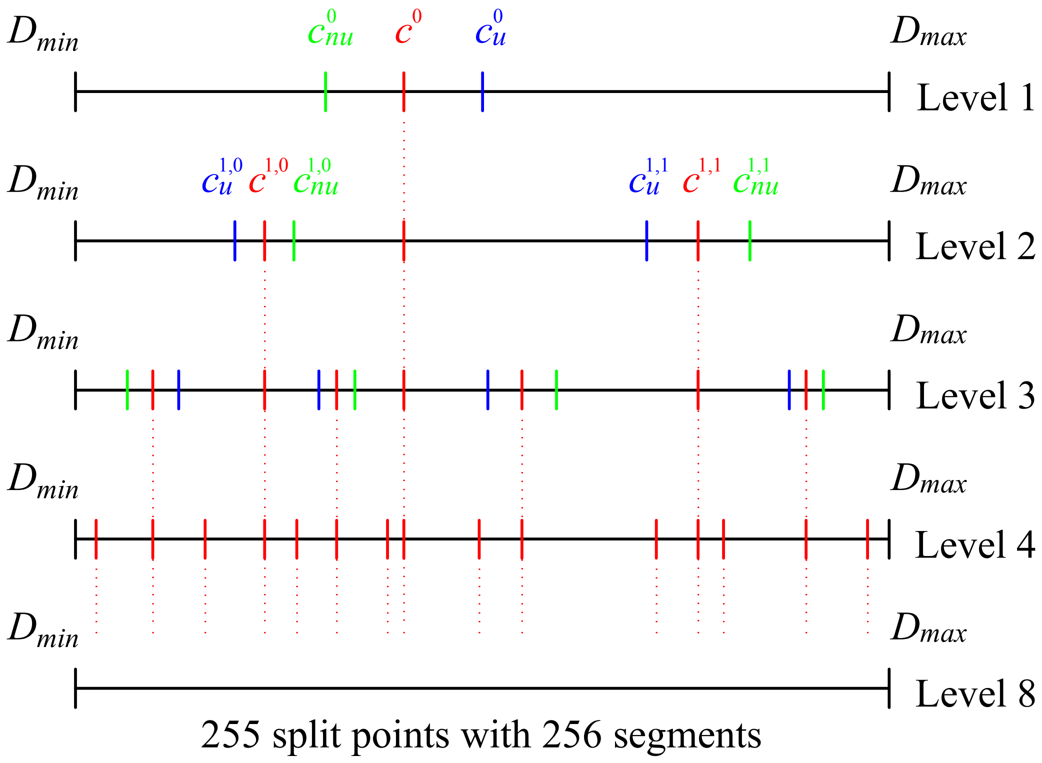

Figure 2.1: *Recursive binary cut approach implementation of HALEQ.*

2.2.1 Spatially variant

In [11], Chiu et al. noted that artists frequently make use of spatially varying techniques to fool the eye into thinking that a much larger dynamic range is present in artwork than actually exists. In particular, the areas around bright features may be dimmed somewhat to accentuate them. The basic formulation of their operator multiplies each pixel's luminance by a scaling factor $s(x,y)$ which depends on the pixel itself and its neighbors. For $s(x,y)$ to represent a local average, it may be produced a low-pass filtered version of the input image. Chiu et al. note that most low-pass filters produce similar results.

2.2.2 Retinex

In [20] and [32], Rahman applied the retinex theory for tone reproduction. It applies on the image by a Gaussian-blurred version with a wide filter kernel. Their operator comes in two different forms: single-scale and multiscale.

For single-scale version, the tone mapped HDR luminance is given by:

$$\mathbf{L}_{LDR}(x_n, y_m) = \exp\Big(\log(\mathbf{L}_{HDR}(x_n, y_m)) - k\log\Big(\mathbf{G}_{\sigma}(x_n, y_m) * \mathbf{L}_{HDR}(x_n, y_m)\Big)\Big). \tag{2.17}$$

For multiscale version, the HDR tone mapped image is provided by:

$$\begin{aligned}\mathbf{L}_{LDR}(x_n, y_m) = \exp\Big[\sum_{n=0}^{N} w_{\mathrm{n}}\Big(\log(\mathbf{L}_{HDR}(x_n, y_m)) -\\ k\log\Big(\mathbf{G}_{\sigma,\,n}(x_n, y_m) * \mathbf{L}_{HDR}(x_n, y_m)\Big)\Big)\Big],\end{aligned} \tag{2.18}$$

where $*$ is the convolutional product; and $\mathbf{G}_{\sigma}(x_n, y_m)$ is a Gaussian filter given by $\mathbf{G}_{\sigma}(x_n, y_m) = \frac{1}{2\pi\sigma^2} e^{-\frac{x^2+y^2}{2\sigma^2}}$ where σ is the standard deviation of the Gaussian distribution. The value of k specifies the relative weight of the blurred image. Larger values of k will cause the compression to be more dramatic but also create bigger halos. N is the number of scales, and w_{n} the weight of n-th scale is given by the relationship $w_{\mathrm{n}} = \frac{(N-n-1)^f}{\sum_{m=1}^{N}(N-m-1)^f}$. The parameter f, controlling the relative weight of each of the scales, determines which of the Gaussian-blurred images carries the most importance.

2.2.3 Image color appearance model

In [12], Fairchild incorporated the spatial processing models in the human visual system for contrast enhancement, photoreceptor light adaptation functions that enhance local details in highlights and shadows, and functions that predict a wide range of color appearance phenomena.

2.2.4 Tone mapping operator for high contrast images

In [14], Ashikhmin proposed three steps. First step: estimating local adaptation luminance at each point in the image. Second step: applying a simple function to these values to compress them into the required display range. Since important image details can be lost during this process; the third step reintroduces details in the final pass over the image.

2.2.5 Photographic tone reproduction

In [12], Reinhard strategy is based on photographic principles. Indeed, this method simulates the burning and dodge effect that photographers applied using the following relation:

$$\mathbf{L}_{LDR}(x_n, y_m) = \frac{L_{\mathrm{m}}(x_n, y_m)\Big(1 + \frac{L_{\mathrm{m}}(x_n, y_m)}{L^2_{\mathrm{white}}}\Big)}{1 + L_{\mathrm{m}}(x_n, y_m)}, \tag{2.19}$$

where $L_{\mathrm{m}}(x_n, y_m) = \frac{a}{L_{HDRa}}$ is the initial scaling of the photographic tone-reproduction; a is the chosen exposure for developing the film in the photographic analogy.

Reinhard views the log average luminance L_{HDRa} as a useful approximation of a scene's key. This equation introduces a new user parameter, L_{white}, which denotes the smallest luminance value that will be mapped to white. By default, this parameter is set to the maximum world luminance (after the initial scaling).

2.2.6 Time dependent visual adaptation

In [9], Pattanaik offered a new operator to include these appearance changes in animations or interactive real-time simulations, and to match a user's visual responses to those the user would experience in a real-world scene.

Large, abrupt changes in scene intensities can cause dramatic compression of visual responses followed by a gradual recovery of normal vision. Asymmetric mechanisms govern these time dependent adjustments, and offer adaptation to increased light that is much more rapid than adjustment to darkness. The operator accepts a stream of scene intensity frames and creates a stream of color display images.

2.3 Frequency tone mapping operators

Frequency-based operators have the same goal of preserving edges and local contrast as local operators. In the case of frequency operators, as the name implies, this is achieved by computing in the frequency domain instead of the spatial domain. The main observation for such methods is that edges and local contrast are preserved if and only if a complete separation between large features and details is achieved. Some methods are briefly described bellow.

2.3.1 Bilateral filtering

In [16], Durand has separated the HDR image into a high-frequency component that contains only LDR information and a low-frequency component with an HDR is explicitly exploited by attenuating low frequencies. Separation of an image into separate components whereby only one of the components needs to be compressed may also be achieved by applying an edge-preserving smoothing operator.

2.3.2 Gradient

In [17], Fattal found that any drastic change in the luminance across a high dynamic range image must give rise to large magnitude luminance gradients at some scales. Fine details, such as texture, on the other hand, correspond to gradients of much smaller magnitude. This idea is then used to identify large gradients at various scales, and attenuate their magnitudes while keeping their direction unaltered. The attenuation must be progressive, penalizing larger gradients more heavily than smaller ones, thus compressing drastic luminance changes, while preserving fine details. A reduced high dynamic range image is then reconstructed from the attenuated gradient field.

2.3.3 Edge-avoiding wavelets

In [25], Fattal used the second generation wavelets, or wavelets based on lifting scheme developed by Swelden. The lifting scheme is an efficient implementation of the fast wavelet transform and more importantly, it provides a methodology for constructing biorthogonal wavelets through space, without the aid of Fourier transform. This makes it a well-suited framework for constructing second-generation wavelets that adapts to the spatial particularities of the data. In this construction one starts with some given simple and often translation-invariant biorthogonal basis and performs a sequence of modifications that adapts and improves the wavelets. The lifting scheme divides this scheme into three main steps: split, predict, and update. Fattal used the edge-avoiding function,

$$w_k^j(l) = \frac{1}{|v^j(k) - v^j(l)|^\alpha + \varepsilon}, \tag{2.20}$$

where indexes k, and l are in neighboring positions of the vector v (all represent for the image); α is between 0.8 and 1.2, and $\varepsilon = 10^{-5}$ for images with pixels ranging from zero and one. It is used to derive two different 2D wavelet constructions: Weighted Cohen-Daubechies-Feauveau Wavelets (WCDF) as (2,2)-CDF wavelets, and Weighted Red-Black Wavelets (WRB) as red-black quincunx lattice approach. The approximation v^{j-1} and details d^{j-1} are scaled the different components before reconstruction such as $\alpha_a \times v^0$ and $\alpha_d \times \{d^0, d^1, ..., d^{j-1}, ..., d^{J-1}\}$.

Both TMO operators are costly in terms of computations and requiring the storage of weight coefficients for the reconstruction step.

2.3.4 Subband compression with wavelets

In [26], Li used a symmetrical analysis-synthesis filter bank typically Haar pyramid and applied local gain control to the subbands. Although so, in computation, Li added the post-processing methods in visual results such as cutting off the brightest and darkest parts as well as adding 15% of a histogram equalized layer to the results, however without post processing it's black. Therefore, the mapped images look like unnatural.

2.4 Segmentation tone mapping operators

Recently, a new approach to the tone mapping problem has emerged in the form of segmentation operators. Strong edges and most of local contrast perception is located along the border of large uniform regions. Segmentation operators divide the image into uniform segments, apply a global operator at each segment, and finally merge them. One additional advantage of such a method is that gamut modifications are minimized because a linear operator for each segment sometimes is, in many cases, sufficient. Some works are described at the following.

2.4.1 Segmentation and adaptive assimilation for detail preservation

The first segmentation-based TMO was introduced by Yee and Pattanaik [23]. Their operator divides the HDR image into regions and calculates an adaptation luminance for each region. This adaptation luminance can be used as an input to a global operator. The first step of the segmentation is to divide the image into regions, called categories, using a histogram in the logarithmic domain. Contiguous pixels of the same category are grouped together using a flood-fill approach. Finally, small groups are assimilated into a bigger one, obtaining a layer.

2.4.2 Interactive manipulation

In [21], Lischinski presented a new interactive tool for making local adjustments of tonal values and other visual parameters in an image. Rather than carefully selecting regions or hand-painting layer masks, the user quickly indicates regions of interest by drawing a few simple brush strokes and then uses sliders to adjust the brightness, contrast, and other parameters in these regions. The effects of the user's sparse set of constraints are interpolated to the entire image using an edge-preserving energy minimization method designed to prevent the propagation of tonal adjustments to regions of significantly different luminance. The resulting system is suitable for adjusting ordinary and high dynamic range images, and provides the user with much more creative control than existing tone mapping algorithms.

3 HDR image quality assessment

The visual quality can be most reliably measured in subjective way where a group of observers assign quality scores to the presented images. This way of assessing, however, is both tedious and expensive and often result in high variance between observers. In many areas, it is much more practical to use instead objective quality metrics to estimate the perceived image quality without subjective judgments. This section gives a short classification of the available metrics to assess tone mapped HDR images and describes in more detail a metric designed for comparing high dynamic range images.

3.1 Objective quality metric classification

Although numerous image comparison algorithms are classified as quality metrics, it does not mean that they compute the same quality measure. Some metrics are better suited for estimating quality of low-bandwidth video transmission, where large distortions are common and acceptable, and other for compression of medical images, where visual distortions must be avoided. Therefore, it is important to distinguish between all kinds of visual metrics, and choose the one that is appropriate for a particular application.

A high-level classification of the metrics is shown in Table 2.2. Depending whether a

Table 2.2: *Classification of HDR image quality assessment - objective quality metrics: Full-reference, Limited-reference and No-reference.*

	HDR Image Quality Assessment - Objective Quality Metrics	**Full-reference**		**Limited-reference**	**No-reference**
		Perceptual -weighted	Structural similarity		Statistical naturalness
1	DRIM [33]	✓			
2	TMQI1 [34]		✓		✓
3	TMQI2 [35]		✓		✓
4	FSITM [36]		✓		

metric requires a non-distorted reference image, some limited statistics of such an image or no image at all, it can be respectively classified as a full-reference, limited-reference and no-reference. Although there are extensive studies on the limited-reference and no-reference metrics, majority of quality metrics require a reference image. No-reference metrics are usually limited to a single type of distortion, such as JPEG blocky artifacts or blurring, and cannot match in accuracy the full-reference metrics.

The metrics can be further divided into those that produce a single quality measure (e.g., a numerical value) for an image or a video sequence and those that produce a distortion map, which estimates the local magnitude of distortion or probability of detection (usually for each pixel). The performance of a metric that computes a single quality measure is usually evaluated in comparison with the subjective data, for example from the LIVE image quality assessment database [37].

The following sections do not cover the area of quality metrics in general, but focus on particular metrics designed especially to assess tone mapped HDR images.

3.2 Current possibilities in objective quality assessment of tone-mapped images

In case of using objective metrics for evaluating tone-mapped images, the situation is similar to the enhanced images. The assessment is restricted either to no reference criteria, which were mostly trained and tested in different context, or the specially adjusted full reference metrics. All of the full reference image quality metrics assume that the dynamic range of the original and processed image are the same. However, in the case of tone-mapped HDR images, the dynamic range between the two versions differ (i.e. $\mathbf{I}_{HDR}$ is an HDR image while $\mathbf{I}_{LDR}$ is LDR). That is why the development of metrics is not easy. The following sections describe the metrics that have been designed in order to overcome this issue.

3.2.1 Dynamic range independent metric

The first metric enabling the comparison of images regardless their dynamic ranges was Dynamic Range Independent Metric (DRIM) [33]. It uses the detection model from HDR-VDP [38], calibrated on the data from ModelFest dataset [39], to indicate which regions contain visible contrast in HDR image and its tone-mapped version. The metric then creates three distortion maps showing the regions where the contrast is either lost (i.e. contrast change is perceivable in HDR but imperceivable in LDR image), amplified (the opposite case), or reversed (the polarity is changed - mostly caused by halo artifacts) by tone-mapping process. The framework of the metric is visualized in Figure 2.2. DRIM inherits high computational requirements and the necessity to specify viewing conditions and display parameters. The metric is designed for visualization of perceived distortions regarding the image contrast. Therefore it does not allow for calculating a single quality value. User graphic interface is available at the web-page site [1] (see Figure 2.3 and Figure 2.4).

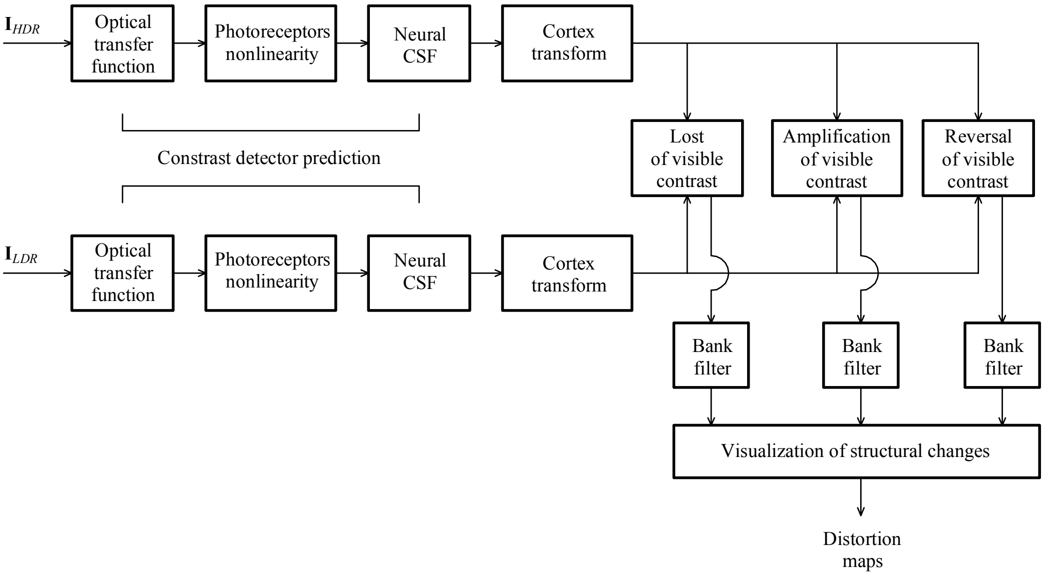

Figure 2.2: *The framework of DRIM.*

3.2.2 Tone-mapped image quality index 1

Another approach has been introduced by Yeganeh and Wang known as Tone-Mapped image Quality Index (called TMQI1) [34]. This quality metric is composed of two parts: the Structural Fidelity 1 ($SF1$) part and Statistical Naturalness 1 ($SN1$) part.

---

[1] `http://driiqm.mpi-inf.mpg.de`

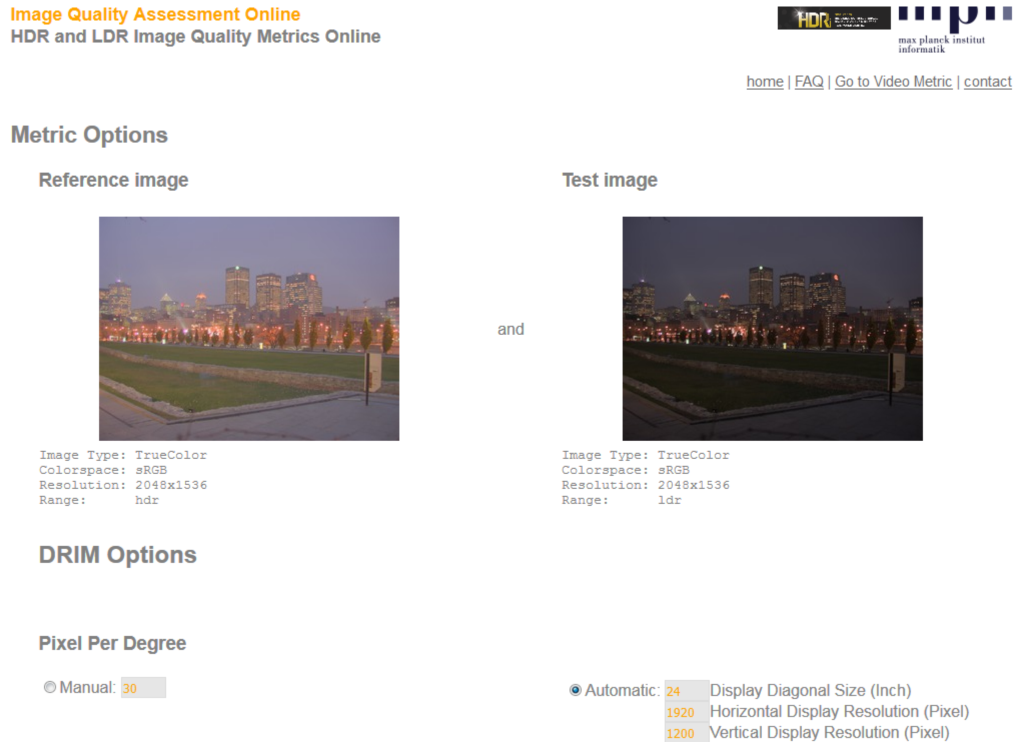

Image Quality Assessment Online
HDR and LDR Image Quality Metrics Online

Metric Options

Reference image

```
Image Type: TrueColor
Colorspace: sRGB
Resolution: 2048x1536
Range:      hdr
```

Test image

```
Image Type: TrueColor
Colorspace: sRGB
Resolution: 2048x1536
Range:      ldr
```

DRIM Options

Pixel Per Degree

○ Manual: 30

● Automatic: 24 Display Diagonal Size (Inch)
1920 Horizontal Display Resolution (Pixel)
1200 Vertical Display Resolution (Pixel)

Figure 2.3: *HDR and LDR image quality metrics online (at the web-page site `http://driiqm.mpi-inf.mpg.de`).*

$SF1$ is a modification of the Multi Scale Structural Similarity Index (MS-SSIM) [40] to be adapted to HDR and LDR images. This modification does not penalize the difference in signal strength if they are both under or over the visibility threshold. This is determined by a nonlinear mapping of the signals' standard deviations according to Contrast Sensitivity Function (CSF). $SF1$ for a patch u is computed as:

$$SF1(\mathbf{I}_{HDR}(u),\mathbf{I}_{LDR}(u)) = \frac{2\sigma'(\mathbf{I}_{HDR}(u))\cdot\sigma'(\mathbf{I}_{LDR}(u))+C_1}{\sigma'^2(\mathbf{I}_{HDR}(u))+\sigma'^2(\mathbf{I}_{LDR}(u))+C_2}\times \frac{\sigma(\mathbf{I}_{HDR}(u),\mathbf{I}_{LDR}(u))+C_2}{\sigma(\mathbf{I}_{HDR}(u))\cdot\sigma(\mathbf{I}_{LDR}(u))+C_2}, \tag{2.21}$$

where $\sigma'(.)$ is the standard deviation of the patch after the nonlinear mapping; $\sigma(\mathbf{I}_{HDR}(u))$, $\sigma(\mathbf{I}_{LDR}(u))$ and $\sigma(\mathbf{I}_{HDR}(u),\mathbf{I}_{LDR}(u))$ are the local standard deviations and cross correlation between the two corresponding patches in HDR and LDR images, respectively; and C_1, C_1 are positive constants that make sure the equation not divided by zero.

Note that the luminance component is missing, compared the SSIM definition, but the structural element (i.e. the second fraction in equation (2.21)) remains the same.

The mapping is defined as follows:

$$\sigma'(\sigma) = \frac{1}{\sqrt{2\pi}\theta_\sigma}\int_{-\infty}^{\sigma}\exp[-\frac{(x-\tau_\sigma)^2}{2\theta_\sigma^2}], \tag{2.22}$$

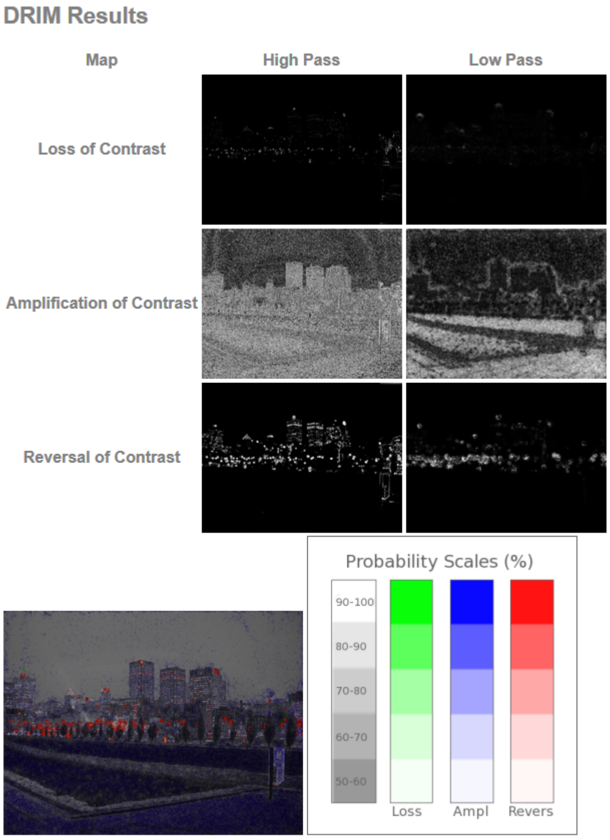

Figure 2.4: *DRIM online result (at the web-page site http://driiqm.mpi-inf.mpg.de).*

where

$$\theta_\sigma(f) = \frac{\tau_\sigma(f)}{k}, \tag{2.23}$$

with f being a spatial frequency and k representing a constant obtained from Crozier's law [41], typically ranging from 2.3 to 4.

The authors proposed to use $k = 3$. The threshold for the signal's standard deviation is given by:

$$\tau_\sigma(f) = \frac{\bar{\mu}}{\sqrt{2} \times \lambda \times CSF(f)}, \tag{2.24}$$

where $\bar{\mu}$ is the mean intensity value (set to 128 by the authors) and λ is a constant used to fit the physiological data. TMQI1 uses the CSF as introduced by Mannos and Sakrison [42] and fits to the data measured by Kelly [43]. The map of $SF1$ is averaged on each scale and the final $SF1$ index is obtained in the same way as in the case of MS-SSIM.

The second measure implemented in TMQI1 – i.e. $SN1$ – does not use reference and is based on the assumption that naturalness of an image can be modeled by the probability distribution of the brightness and contrast (means and standard deviations) in natural gray-scale images. The means and standard deviations, base on the analysis done on 3000 images, follow a Gaussian ($\mathcal{N}$) and a Beta ($\mathcal{B}$) distribution respectively.

The distributions are then given by $\mathcal{N}(115.94,\ 27.99)$ and $\mathcal{B}(4.4,\ 10.1)$.

Assuming that brightness and contrast are mutually independent, the probability that the image is natural is then expressed as:

$$SN1(\mathbf{I}_{LDR}) = \frac{1}{K(\mathbf{I}_{LDR})} \times Pdf_{\mathcal{N}(115.94,\ 27.99)}(\mathbf{I}_{LDR}) \times Pdf_{\mathcal{B}(4.4,\ 10.1)}(\mathbf{I}_{LDR}), \tag{2.25}$$

where K is a factor used for the normalization, thus:

$$K(\mathbf{I}_{LDR}) = \max\{Pdf_{\mathcal{N}(115.94,\ 27.99)}(\mathbf{I}_{LDR}),\ Pdf_{\mathcal{B}(4.4,\ 10.1)}(\mathbf{I}_{LDR})\}. \tag{2.26}$$

The final TMQI1 is a combination of the two measures defined as:

$$TMQI1(\mathbf{I}_{HDR},\mathbf{I}_{LDR}) = a \times SF1^{\alpha}(\mathbf{I}_{HDR},\mathbf{I}_{LDR}) + (1-a) \times SN1^{\beta}(\mathbf{I}_{LDR}). \tag{2.27}$$

The authors used fixed parameters $a = 0.8012$, $\alpha = 0.3046$ and $\beta = 0.7088$.

3.2.3 Tone-mapped image quality index 2

Based on TMQI1, later on, Ma et al. [35] revised both of the terms and proposed a new version of the index Tone Mapped Image Quality Index called TMQI2. It is also composed of two parts: the Structural Fidelity 2 ($SF2$) part and Statistical Naturalness 2 ($SN2$) part. Namely, the contrast visibility model for HDR images has been adapted to the local luminance when calculating $SF2$. The estimate of the contrast in the HDR reference is therefore computed as the standard deviation in a patch divided by the local mean. The $SN2$ term is modified much more severely.

The authors argued that the distribution of the means and standard deviations leading to the natural image depends on the mean and the standard deviation of the original image (obtained from the logarithm of the HDR reference). Therefore, they designed a subjective experiment and let observers adjusting the means and standard deviations of 60 natural images in order to find the lower and upper bounds for naturalness. These bounds were then fitted with a linear model. The transitions from the boundary to the mean are expressed by Gaussian cumulative distribution functions. $SN2$ is then obtained as a product of the probabilities that the image is natural in terms of its mean and its standard deviation. TMQI2 is then given by this relation:

$$TMQI2(\mathbf{I}_{HDR},\mathbf{I}_{LDR}) = \frac{1}{2}SF2(\mathbf{I}_{LDR},\mathbf{I}_{HDR}) + \frac{1}{2}SN2(\mathbf{I}_{LDR}). \tag{2.28}$$

3.2.4 Feature similarity index for tone-mapped images

The last full-reference metric that will be discussed here is a Feature Similarity Index for Tone-Mapped images (FSITM) [36]. It uses the phase congruency features to calculate the difference between original and tone-mapped version of the image. More specifically,

Table 2.3: *Tone Mapped Image Quality Index 1 (TMQI1) (HDR test images are available at the HDR Toolbox [1]; The PLCC with the corresponding MOS is* 0.588*).*

Images \TMOs	DR f-stops	Drago [10]	Reinhard [44]	Ward [7]	Durand [16]	Tumblin [31]	Schlick [3]	Duan [8]	Fattal [25]	Li [26]	Husseis [30]
Lausanne1	7.71	0.824	0.793	0.702	0.837	0.782	0.747	0.914	0.831	0.982	0.916
CraterLake1	8.13	0.842	0.790	0.716	0.792	0.761	0.776	0.946	0.862	0.973	0.954
Shasta2	8.48	0.762	0.727	0.570	0.743	0.707	0.649	0.906	0.794	0.954	0.927
Synagogue	8.57	0.922	0.910	0.827	0.875	0.884	0.913	0.965	0.755	0.949	0.966
Anturium	8.73	0.860	0.794	0.723	0.808	0.768	0.759	0.964	0.889	0.964	0.963
BowRiver	9.53	0.819	0.778	0.726	0.879	0.787	0.783	0.962	0.864	0.960	0.961
Bridges	11.17	0.787	0.757	0.646	0.785	0.720	0.714	0.969	0.860	0.908	0.947
Stairway1	13.37	0.760	0.741	0.554	0.781	0.717	0.792	0.906	0.782	0.887	0.911
ArchRock	13.60	0.798	0.784	0.613	0.800	0.776	0.840	0.976	0.951	0.915	0.961
DollDoll	13.89	0.735	0.722	0.568	0.720	0.721	0.707	0.882	0.733	0.865	0.888
ClockBuilding	14.19	0.755	0.752	0.487	0.757	0.735	0.750	0.951	0.757	0.920	0.965
OxfordChurch	15.43	0.794	0.770	0.459	0.792	0.701	0.836	0.986	0.889	0.877	0.985
BottlesSmall	16.03	0.765	0.770	0.549	0.764	0.691	0.773	0.916	0.928	0.954	0.921
Montreal	16.06	0.617	0.338	0.336	0.668	0.588	0.586	0.862	0.624	0.895	0.945
SmallOffice	16.29	0.735	0.727	0.521	0.736	0.671	0.728	0.955	0.943	0.854	0.966
Light	17.46	0.786	0.778	0.356	0.763	0.551	0.760	0.969	0.971	0.888	0.971
BridgeStudios2	18.13	0.704	0.660	0.461	0.738	0.649	0.767	0.957	0.764	0.890	0.964
Memorial	18.38	0.780	0.768	0.364	0.773	0.535	0.761	0.935	0.927	0.834	0.919
ClaridgeHotel	23.44	0.807	0.772	0.692	0.834	0.751	0.238	0.925	0.856	0.963	0.929
Mistaya1	23.77	0.812	0.787	0.635	0.845	0.784	0.157	0.961	0.861	0.961	0.963
BrookHouse	23.98	0.806	0.768	0.665	0.815	0.756	0.088	0.976	0.982	0.932	0.976
PeaceRocks	24.13	0.841	0.795	0.744	0.819	0.782	0.110	0.918	0.828	0.849	0.912
GGpark2	24.41	0.821	0.776	0.700	0.836	0.766	0.111	0.974	0.842	0.928	0.975
AtriumNight	28.68	0.778	0.741	0.400	0.780	0.622	0.149	0.964	0.965	0.887	0.944

Table 2.4: *Tone Mapped Image Quality Index 2 (TMQI2) (The PLCC with the corresponding MOS is* 0.512*).*

Images \TMOs	DR f-stops	Drago [10]	Reinhard [44]	Ward [7]	Durand [16]	Tumblin [31]	Schlick [3]	Duan [8]	Fattal [25]	Li [26]	Husseis [30]
Lausanne1	7.71	0.790	0.283	0.159	0.372	0.250	0.233	0.795	0.372	0.644	0.760
CraterLake1	8.13	0.921	0.411	0.334	0.420	0.395	0.317	0.401	0.436	0.702	0.355
Shasta2	8.48	0.726	0.261	0.220	0.361	0.256	0.148	0.692	0.327	0.797	0.631
Synagogue	8.57	0.690	0.612	0.377	0.831	0.717	0.523	0.395	0.421	0.565	0.390
Anturium	8.73	0.724	0.337	0.238	0.407	0.306	0.284	0.555	0.396	0.842	0.544
BowRiver	9.53	0.843	0.271	0.140	0.402	0.304	0.397	0.631	0.500	0.768	0.550
Bridges	11.17	0.345	0.303	0.166	0.367	0.226	0.252	0.871	0.394	0.787	0.875
Stairway1	13.37	0.372	0.344	0.139	0.429	0.274	0.367	0.618	0.402	0.826	0.509
ArchRock	13.60	0.412	0.323	0.080	0.454	0.237	0.475	0.656	0.878	0.937	0.519
DollDoll	13.89	0.354	0.330	0.198	0.346	0.270	0.304	0.884	0.336	0.462	0.828
ClockBuilding	14.19	0.348	0.322	0.082	0.411	0.241	0.292	0.849	0.378	0.892	0.717
OxfordChurch	15.43	0.362	0.246	0.055	0.461	0.131	0.559	0.542	0.931	0.597	0.426
BottlesSmall	16.03	0.356	0.352	0.112	0.416	0.190	0.627	0.858	0.853	0.716	0.822
Montreal	16.06	0.262	0.196	0.202	0.367	0.203	0.252	0.533	0.300	0.704	0.243
SmallOffice	16.29	0.305	0.288	0.165	0.336	0.211	0.272	0.882	0.806	0.370	0.878
Light	17.46	0.354	0.327	0.084	0.377	0.074	0.283	0.916	0.873	0.537	0.873
BridgeStudios2	18.13	0.214	0.162	0.059	0.306	0.135	0.422	0.763	0.411	0.570	0.633
Memorial	18.38	0.373	0.320	0.037	0.420	0.048	0.292	0.907	0.908	0.468	0.763
ClaridgeHotel	23.44	0.523	0.355	0.260	0.398	0.335	0.008	0.598	0.352	0.728	0.581
Mistaya1	23.77	0.427	0.361	0.108	0.451	0.300	0.001	0.696	0.529	0.921	0.674
BrookHouse	23.98	0.365	0.303	0.166	0.453	0.269	0.002	0.721	0.896	0.947	0.706
PeaceRocks	24.13	0.520	0.392	0.273	0.448	0.381	0.000	0.526	0.416	0.865	0.508
GGpark2	24.41	0.439	0.335	0.166	0.452	0.286	0.000	0.517	0.397	0.900	0.486
AtriumNight	28.68	0.366	0.256	0.077	0.443	0.118	0.002	0.498	0.692	0.872	0.405

it computes the Locally Weighted Mean Phase Angle (LWMPA) to compute the phase congruency. The main advantage of this feature is its robustness against noise.

Let the $lG^e_{\rho,r}$ and $lG^o_{\rho,r}$ be a quadratic pair of log-Gabor wavelets, i.e. evenly and oddly symmetric, on the scale ρ and orientation r. The responses for a two-dimensional signal (e.g. an image $\mathbf{I}$) are obtained as:

$$[e_{\rho,r}(\mathbf{I}),\ o_{\rho,r}(\mathbf{I})] = [\mathbf{I} * lG^e_{\rho,r} * lG^o_{\rho,r}], \tag{2.29}$$

where the operator $*$ is the convolution operator.

The $LWMPA$ is then computed as:

$$LWMPA(\mathbf{I}) = arctan2\Big[\sum_{\rho,r} e_{\rho,r}(\mathbf{I}),\ \sum_{\rho,r} o_{\rho,r}(\mathbf{I})\Big], \tag{2.30}$$

where $arctan2(.)$ is defined as:

$$arctan2(x,y) = 2arctan\frac{x}{\sqrt{x^2+y^2}+y}. \tag{2.31}$$

The values of $LWMPA(\mathbf{I})$ range from $-\pi/2$ to $\pi/2$. The binary phase congruency map PCG can then be obtained as:

$$PCG(I) = H(LWMPA(\mathbf{I})), \tag{2.32}$$

where $H(.)$ is the Heaviside (unit-step) function defined as:

$$H(t) = \begin{cases} 1 & t > 0 \\ \frac{1}{2} & t = 0 \\ 0 & t < 0. \end{cases} \tag{2.33}$$

The authors proposed to calculate the FSITM for each channel, denoted "ch". The similarity of the congruency maps for a channel "ch" is computed as:

$$SCG^{ch}(\mathbf{I}_{HDR},\mathbf{I}_{LDR}) = \frac{PCG^{ch}(\mathbf{I}^{ch}_{HDR}) \cap PCG^{ch}(\mathbf{I}^{ch}_{LDR})}{N \times M}, \tag{2.34}$$

with N and M being the image width and height, respectively.

The final index can then be obtained from this equation:

$$FSITM^{ch}(\mathbf{I}_{HDR},\mathbf{I}_{LDR}) = \lambda SCG^{ch}(\mathbf{I}_{HDR},\mathbf{I}_{LDR}) + (1-\lambda)SCG^{ch}(ln(\mathbf{I}_{HDR}),\mathbf{I}_{LDR}), \tag{2.35}$$

where the parameter λ is set experimentally between 0 and 1.

Table 2.5: *Feature Similarity Index for Tone-Mapped images (FSITM) with red channel (The PLCC with the corresponding MOS is* 0.018*).*

Images \TMOs	DR f-stops	Drago [10]	Reinhard [44]	Ward [7]	Durand [16]	Tumblin [31]	Schlick [3]	Duan [8]	Fattal [25]	Li [26]	Husseis [30]
Lausanne1	7.71	0.945	0.958	0.958	0.937	0.964	0.932	0.900	0.881	0.896	0.895
CraterLake1	8.13	0.945	0.957	0.962	0.926	0.961	0.943	0.918	0.917	0.901	0.911
Shasta2	8.48	0.953	0.957	0.925	0.929	0.961	0.912	0.903	0.906	0.907	0.885
Synagogue	8.57	0.942	0.950	0.949	0.902	0.955	0.918	0.923	0.855	0.865	0.921
Anturium	8.73	0.928	0.948	0.964	0.908	0.957	0.937	0.882	0.888	0.880	0.877
BowRiver	9.53	0.948	0.967	0.958	0.923	0.965	0.932	0.902	0.904	0.900	0.895
Bridges	11.17	0.896	0.924	0.925	0.872	0.939	0.917	0.837	0.826	0.858	0.777
Stairway1	13.37	0.935	0.940	0.893	0.880	0.942	0.912	0.890	0.892	0.884	0.882
ArchRock	13.60	0.921	0.938	0.930	0.904	0.947	0.884	0.866	0.863	0.858	0.859
DollDoll	13.89	0.794	0.809	0.874	0.775	0.822	0.798	0.719	0.816	0.782	0.717
ClockBuilding	14.19	0.886	0.899	0.844	0.822	0.896	0.902	0.835	0.862	0.816	0.831
OxfordChurch	15.43	0.926	0.939	0.836	0.885	0.935	0.893	0.889	0.874	0.854	0.882
BottlesSmall	16.03	0.835	0.831	0.752	0.794	0.824	0.749	0.790	0.809	0.815	0.780
Montreal	16.06	0.863	0.696	0.660	0.817	0.848	0.851	0.837	0.854	0.817	0.807
SmallOffice	16.29	0.824	0.820	0.698	0.748	0.806	0.796	0.820	0.841	0.824	0.816
Light	17.46	0.868	0.836	0.530	0.835	0.677	0.809	0.830	0.862	0.908	0.830
BridgeStudios2	18.13	0.884	0.884	0.783	0.858	0.895	0.823	0.799	0.845	0.846	0.791
Memorial	18.38	0.915	0.881	0.517	0.895	0.736	0.861	0.879	0.902	0.939	0.852
ClaridgeHotel	23.44	0.929	0.946	0.936	0.864	0.957	0.446	0.845	0.848	0.889	0.844
Mistaya1	23.77	0.929	0.945	0.934	0.889	0.947	0.423	0.885	0.883	0.875	0.885
BrookHouse	23.98	0.908	0.930	0.907	0.892	0.940	0.506	0.852	0.868	0.857	0.852
PeaceRocks	24.13	0.938	0.959	0.959	0.891	0.962	0.517	0.881	0.879	0.879	0.878
GGpark2	24.41	0.940	0.955	0.954	0.905	0.965	0.513	0.881	0.865	0.884	0.875
AtriumNight	28.68	0.843	0.836	0.715	0.809	0.804	0.559	0.815	0.823	0.824	0.809

3.3 Comparison of the reference metrics

Since the DRIM metric does not allow for calculating a single quality value, in order to compare the performance of the metrics, simulations have been conducted under Matlab environnement using the HDR Toolbox ([1]) with 274 HDR test images. The results are obtained with 24 HDR images from 7 f-stops to 29 f-stops, indoor and outdoor scenes, namely, "Lausanne1", "CraterLake1", "Shasta2", "Synagogue", "Anturium", "BowRiver", "Bridges", "Stairway1", "ArchRock", "DollDoll", "ClockBuilding", "OxfordChurch", "BottlesSmall", "Montreal", "SmallOffice", "Light", "BridgeStudios2", "Memorial", "ClaridgeHotel", "Mistaya1", "BrookHouse", "PeaceRocks", "GGpark2" and "AtriumNight". 10 TM methods are used to test such as "Drago" [10], "Reinhard" [44], "Ward" [7], "Durand" [16], "Tumblin" [31], "Schlick" [3], "Duan" [8], "Fattal" WRB [25], "Li" [26] and "Husseis" [30]. The different parameters are chosen so as to give the best results in terms of visual quality in all reference methods. All tone mapped images are rendered in equation (2.2) with color saturation $s = 0.5$. Table 2.3, Table 2.4 and Table 2.5 show tone mapped quality indexes of TMQI1 [34], TMQI2 [35] and FSITM [36] with red channel, respectively.

An observer notes each tone mapped image with a corresponding mark (with no-reference of HDR displays) using the scale ranging from 0 until 5: 5 for *excellent*, 4 *very good*, 3 *good*, 2 *accepted*, 1 *unsatisfactory* and 0 *failed*. The Mean Opinion Score (MOS) table is obtained upon 26 observers. Pearson's Linear Correlation Coefficient (PLCC) is selected to measure the relation between the visual quality of the tone mapped image and the MOS.

In next sections of this thesis, TMQI1 [34] (called TMQI) is selected as a metric to measure the quality of tone mapped images since the PLCC with the corresponding MOS is highest (0.588) compared to TMQI2 [35] (0.512) and FSITM [36] (0.018). This work is investigated in Chapter 6.

4 Conclusion

The state of art shows that the tone mapping problem can be solved by several different approaches. Taking into account different aspects: including global, local contrast reproduction, fine details preservation without introducing halo artifacts, the HVS behavior, etc. Despite the large number of techniques, the dynamic range compression has been mainly tackled on the luminance values of the input HDR image. In spite of the large number of TMOs that have been developed, the tone mapping problem is still an open issue.

Global operators are characterized by a mapping that is identical for all pixels (i.e., a single tone-mapping curve is used throughout the image). This makes them computationally efficient, but there is a limit to the dynamic range of the input image beyond which successful compression becomes difficult. Global operators are of necessity monotonically increasing operators. Otherwise, visually unpleasant artifacts will be introduced. Local operators improve the quality of the tone mapped image over global operators by attempting to reproduce both the local and the global contrast. This is achieved because the mapping operators take into account the intensity values from the neighboring pixels of the pixel being tone mapped. However, neighbors have to be chosen carefully; otherwise, halos around edges can appear. Frequency-dependent operators are interesting from a historical perspective as well as for the observations about image structure they afford. These algorithms may therefore help us better understand the challenges we face when preparing HDR tone mapped images to be displayed on standard LDR display devices. The following also explores gradient domain operators, in that they are algorithmically related to frequency domain operators.

As it has been shown, many techniques have been proposed for HDR image tone mapping. With such a large number of techniques, it is useful to understand the relative merits of each. As a consequence, several methodologies have now been put forward that evaluate and compare the variety of approaches. Evaluation of the techniques provides a better understanding of the relationship between an operator and the image attributes. This can help in the development of operators more suited to a particular application - for example, an improved method for highlighting those parts of an image that are perceptually important to the HVS.

The following chapter proposes the first HDR image tone mapping contribution of this thesis which is based on a non-uniform histogram adjustment.

CHAPTER 3

Proposed TMO based on an non-uniform histogram adjustment

Abstract

This chapter investigates a global tone mapping method. It solves the problems of contrast and is based on piecewise linear perceptual quantizer modeling the "s-shaped" curve of the Human Visual Adaptation. In order to get more optional contrasts, this method can be diverse from changing ℓ-norm space. Our work has been published in the conference IEEE ISIVC 2018 (9th International Symposium on Signal, Image, Video and Communications [1]).

---

[1] [45] B. C. Thai, A. Mokraoui, and B. Matei. “Piecewise Linear Perceptual Quantizer as a Non-Uniform Histogram Equalization Adjustment for Contrast Enhancement of Tone Mapped HDR Images”. In: 9th IEEE International Symposium on Signal, Image, Video and Communications (ISIVC) (Nov. 2018).

Chapter content

1 Introduction

The response curves for both rods and cones in the eye can be fitted with the following equation:

$$\frac{R}{R_{max}} = \frac{I^n}{I^n + \sigma^n}, \tag{3.1}$$

where R is the photoreceptor response $(0 < R < R_{max})$; R_{max} is the maximum response; I is luminance or light intensity; σ is the semi-saturation constant (the intensity that causes the half-maximum response); and n is a sensitivity control exponent that has a value generally between 0.7 and 1.0 (see [46] and [47]). Characteristics of the function are continuous, strictly monotonic increasing according to the positive value of its first derivative (i.e. $n\sigma^n I^{n-1}/(I^n + \sigma^n)^2 > 0,\ \forall I > 0$) and bounded in $[0, 1]$.

This equation, known as the Michaelis-Menten equation (or Naka–Rushton equation), models an "s-shaped" function (on a log-linear plot) that appears repeatedly in both psychophysical experiments and widely diverse direct-neural measurements. The role of σ in equation (3.1) is to control the position of the response curve on the (horizontal) intensity axis. It is thus possible to represent the response curves of rods and cones shown in Figure 3.1 by simply using two different values of σ, called σ_{rod} and σ_{cone}, in equation (3.1).

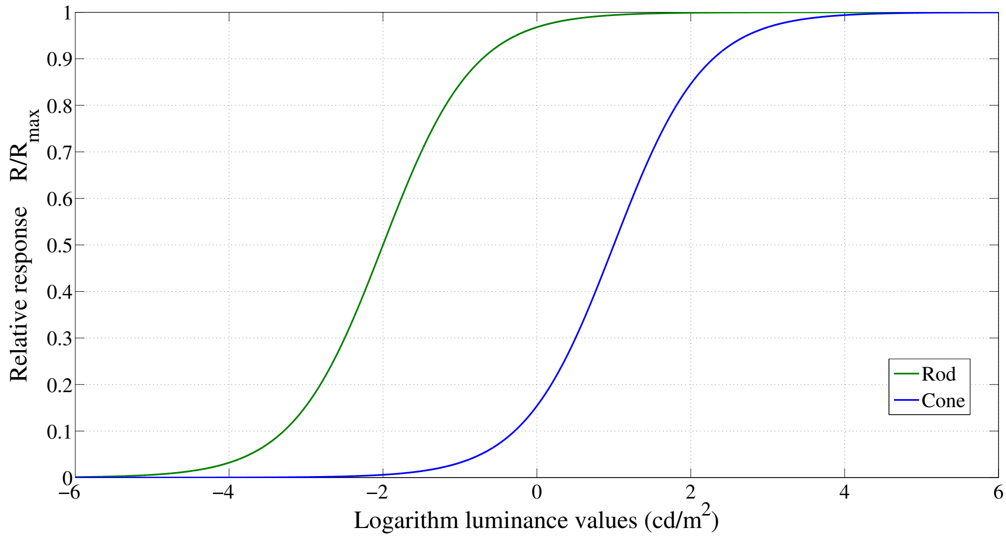

Figure 3.1: *Relative response of dark-adapted rod and cone cells.*

The proposed algorithm adjusts the logarithm luminance distribution of the HDR image according to a perceptual quantizer using a piecewise linear function with respect to modeling an "s-shaped" function of the Human Visual Adaptation (HVA). The proposed algorithm is summarized in Figure 3.2.

2 Non-uniform distribution of the HDR logarithm luminance values

This section proposes to adjust locally the distribution of the HDR image logarithm luminance values according to the HVS to enhance the contrast using a piecewise linear function. This strategy is inspired from [48] which has been developed for compression purpose. However, modifications are made mainly to avoid the problem of empty bins of equal size.

Before describing the proposed HDR image tone mapping approach, introduce some notations. The original HDR image is assumed to be of size $N \times M$. Denote $\mathbf{L}_{HDR}$ the HDR image luminance. In the rest of this chapter, the HDR image luminance is considered in the logarithm domain since it is well adapted to the HVS. It is denoted $\widetilde{\mathbf{I}}_{HDR}$ and defined as follows:

$$\begin{aligned} \widetilde{\mathbf{I}}_{HDR} := \{\widetilde{\mathbf{I}}_{HDR}(x_n, y_m) = \log_{10}(\mathbf{L}_{HDR}(x_n, y_m)) \\ \text{for } 1 \leq n \leq N \text{ and } 1 \leq m \leq M\}, \end{aligned} \tag{3.2}$$

where $\widetilde{\mathbf{I}}_{HDR}(x_n, y_m)$ is the HDR logarithm luminance value of the pixel located at position (x_n, y_m) on the image.

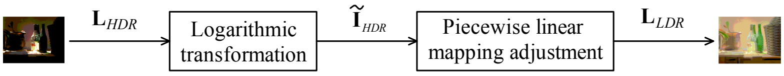

Figure 3.2: *Diagram block of the proposed HDR image TM algorithm based on non-uniform histogram adjustment scheme.*

The $\widetilde{\mathbf{I}}_{HDR}$ values are first sorted and classified into equal B bins defined by cutting points denoted c^{i}_{uHDR} (with $1 \leq i \leq B$). The index i refers to the bin number. A non-uniform histogram equalization is also performed. c^{i}_{nuHDR} (with $1 \leq i \leq B$) cutting points, defining the bounds of the non-uniform consecutive B bins, are deduced. From uniform and non-uniform cutting points, new cutting points locally adapted to the logarithm luminance values are deduced as described below.

The new lower bound (i.e. new cutting point) of each bin, denoted $\widetilde{l}^{i}_{HDR}(1)$, is then adjusted by the introduction of the parameter β_i as follows:

$$\widetilde{l}^{i}_{HDR}(1) = c^{i}_{uHDR} + \beta_i (c^{i}_{nuHDR} - c^{i}_{uHDR}), \tag{3.3}$$

where β_i is a positive parameter smaller than 1 depending on the sub-interval $[c^{i}_{uHDR},\ c^{i}_{nuHDR}]$.

Since the lower cutting point $\widetilde{l}^{i}_{HDR}(1)$ is deduced as the average of the logarithm luminance values on each sub-interval $[c^{i}_{uHDR},\ c^{i}_{nuHDR}]$ as in [30], the parameter β_i is then given by:

$$\beta_i = \frac{\text{mean}(\widetilde{\mathbf{I}}_{HDR}[c^{i}_{uHDR},\ c^{i}_{nuHDR}]) - c^{i}_{uHDR}}{c^{i}_{nuHDR} - c^{i}_{uHDR}}. \tag{3.4}$$

Note that this strategy avoids having empty bins.

Therefore the $\widetilde{\mathbf{I}}^J_{HDR}$ values are classified into non-uniform B bins as follows:

$$\widetilde{\mathbf{I}}^J_{HDR} = \left\{\widetilde{l}_{HDR}(k) \text{ for } k = 1, ..., N^J \times M^J\right\} = \begin{cases} \widetilde{l}^1_{HDR}(1), \ldots, \widetilde{l}^1_{HDR}(K_1) & \text{for bin 1,} \\ \widetilde{l}^2_{HDR}(1), \ldots, \widetilde{l}^2_{HDR}(K_2) & \text{for bin 2,} \\ \vdots & \\ \widetilde{l}^i_{HDR}(1), \ldots, \widetilde{l}^i_{HDR}(K_i) & \text{for bin i,} \\ \vdots & \\ \widetilde{l}^B_{HDR}(1), \ldots, \widetilde{l}^B_{HDR}(K_B) & \text{for bin B,} \end{cases} \tag{3.5}$$

depending on the quantization level set, where K_i is the number of values in the i-th bin (i.e. $1 \leq i \leq B$; $K_i > 0$) and satisfying the following relation:

$$\sum_{i=1}^{B} K_i = N^J \times M^J. \tag{3.6}$$

3 Piecewise linear perceptual quantizer

The "s-shaped" TM perceptual curve, as discussed above, is modeled by a piecewise linear curve on each bin as shown in Figure 3.3. Consider the i-th bin, defined by $[\widetilde{l}^i_{HDR}(1), ..., \widetilde{l}^i_{HDR}(K_i)]$, the HDR values are then modeled as follows:

$$\hat{l}^i_{LDR}(k) = a_i \widetilde{l}^i_{HDR}(k) + b_i \quad \text{with } k \in [1, K_i], \tag{3.7}$$

where a_i (with $a_i \neq 0$) and b_i are two unknown parameters depending on the i-th bin.

To compute these two unknown parameters, we first propose to rewrite equation (3.7) in such a way that it depends only on the parameter a_i. To do so, the parameter a_i is expressed as follows:

$$a_i = \frac{\hat{l}^i_{LDR}(K_i) - \hat{l}^i_{LDR}(1)}{\widetilde{l}^i_{HDR}(K_i) - \widetilde{l}^i_{HDR}(1)}, \tag{3.8}$$

where $\hat{l}^i_{LDR}(K_i)$ and $\hat{l}^i_{LDR}(1)$ are unknown values.

The parameter b_i is then easily deduced as follows:

$$b_i = \hat{l}^i_{LDR}(1) - a_i \widetilde{l}^i_{HDR}(1) = \hat{l}^i_{LDR}(1) - \frac{\hat{l}^i_{LDR}(K_i) - \hat{l}^i_{LDR}(1)}{\widetilde{l}^i_{HDR}(K_i) - \widetilde{l}^i_{HDR}(1)} \widetilde{l}^i_{HDR}(1). \tag{3.9}$$

Replacing this expression in equation (3.7), results in the following equation:

$$\hat{l}^i_{LDR}(k) = a_i \left[\widetilde{l}^i_{HDR}(k) - \widetilde{l}^i_{HDR}(1)\right] + \hat{l}^i_{LDR}(1), \tag{3.10}$$

where $\widetilde{l}^i_{HDR}(k)$ are known values.

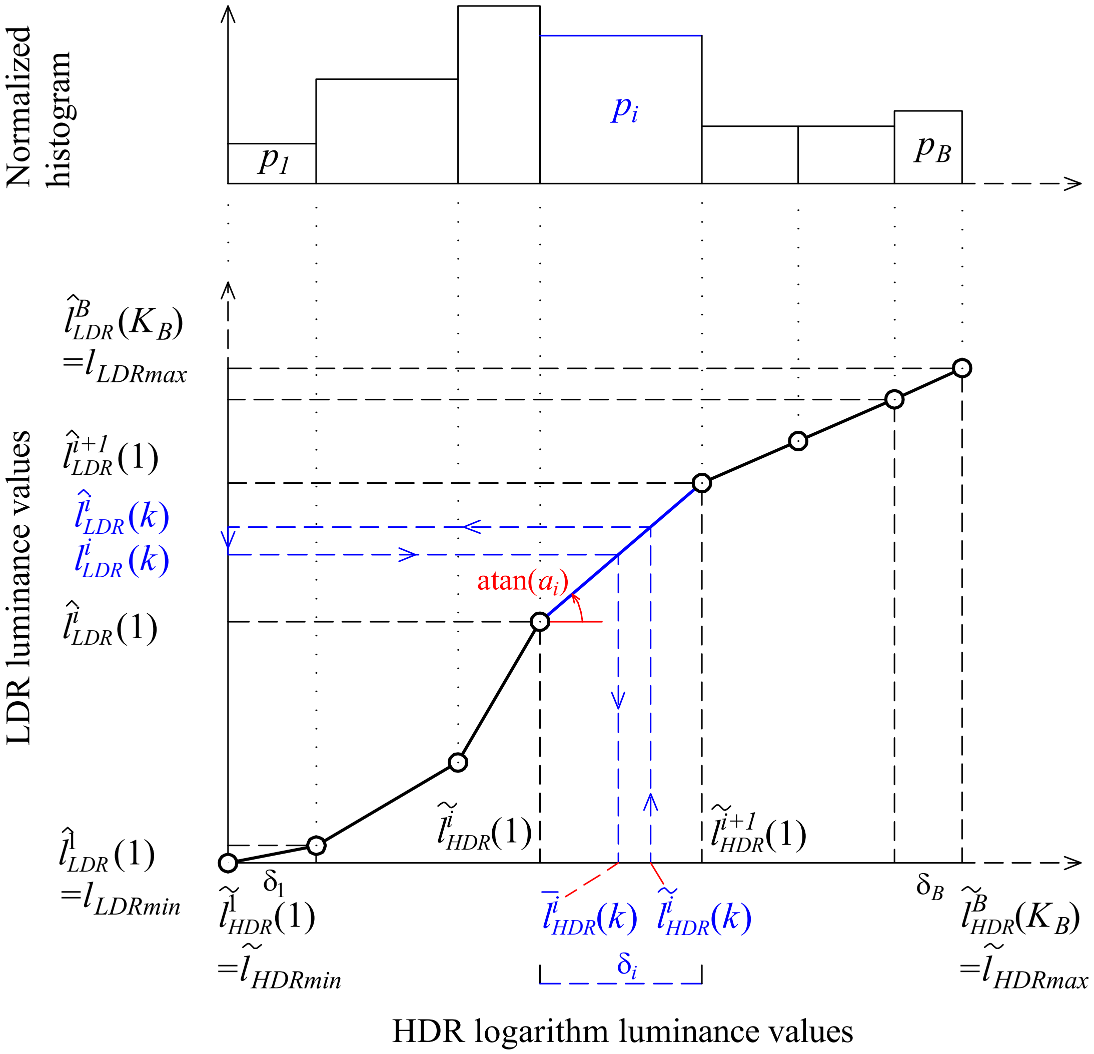

Figure 3.3: *Piecewise linear curve modelization ("s-shaped" curve).*

From equation (3.10), one can deduce the relationship between the $\tilde{l}^i_{HDR}(k)$ and $\hat{l}^i_{LDR}(k)$:

$$\tilde{l}^i_{HDR}(k) = \frac{\hat{l}^i_{LDR}(k) - \hat{l}^i_{LDR}(1)}{a_i} + \tilde{l}^i_{HDR}(1). \tag{3.11}$$

The unknown parameter a_i is then deduced so that the norm-M space error (or Minkowski metric error) between the HDR value and its quantized version, denoted $\bar{l}^i_{HDR}(k)$ (i.e. when $\hat{l}^i_{LDR}(k)$ has been supported a rounding process according to a scalar quantization), is minimized in the i-th bin:

$$\arg\min_{a_i} \|\bar{l}^i_{HDR}(k) - \tilde{l}^i_{HDR}(k)\|^M_M, \quad \text{with } M > 0, \tag{3.12}$$

which is equivalent to:

$$\arg\min_{a_i} \left\| \Big(\frac{\hat{l}^i_{LDR}(k) - \hat{l}^i_{LDR}(1)}{a_i} + \widetilde{l}^i_{HDR}(1) \Big) - \Big(\frac{l^i_{LDR}(k) - \hat{l}^i_{LDR}(1)}{a_i} + \widetilde{l}^i_{HDR}(1) \Big) \right\|^M_M . \tag{3.13}$$

This equation is simplified as follows:

$$\arg\min_{a_i} \sum_{k=1}^{K_i} \left| \frac{l^i_{LDR}(k) - \hat{l}^i_{LDR}(k)}{a_i} \right|^M \cdot p_i, \tag{3.14}$$

where p_i is the probability of the $\widetilde{l}^i_{HDR}(k)$ value in the i-th bin given by:

$$p_i = \frac{K_i}{\sum_{i=1}^{B} K_i}. \tag{3.15}$$

Extending this relation to all bins involves the computation of a global norm-M space error Ψ between the HDR values and its quantized version, denoted $\bar{l}^i_{HDR}(k)$ (i.e. when $\hat{l}^i_{LDR}(k)$ has been supported a rounding process according to a scalar quantization):

$$\Psi = \sum_{i=1}^{B} \sum_{k=1}^{K_i} \left| \frac{l^i_{LDR}(k) - \hat{l}^i_{LDR}(k)}{a_i} \right|^M \cdot p_i. \tag{3.16}$$

If we assume that the expected value $\sum_{k=1}^{K_i} \left| \hat{\hat{l}}^i_{LDR}(k) - \hat{l}^i_{LDR}(k) \right|^M$ in each bin is the same:

$$\sum_{k=1}^{K_i} \left| \hat{\hat{l}}^i_{LDR}(k) - \hat{l}^i_{LDR}(k) \right|^M = \xi = const,\ \forall i = 1 ... B, \tag{3.17}$$

equation (3.16) is simplified and becomes:

$$\Psi = \sum_{i=1}^{B} \frac{p_i}{(a_i)^M} \cdot \xi, \quad \text{with } a_i > 0. \tag{3.18}$$

Denote l_{LDRmax} (respectively l_{LDRmin}) the maximum (respectively minimum) LDR luminance value. Introduce δ_i as the difference between HDR logarithm luminance in two consecutive bins:

$$\delta_i = \widetilde{l}^{i+1}_{HDR}(1) - \widetilde{l}^i_{HDR}(1). \tag{3.19}$$

However a constraint related to the limit sum of the projected heights equal to the entire LDR range:

$$\sum_{i=1}^{B} a_i \cdot \delta_i = l_{LDRmax} - l_{LDRmin}. \tag{3.20}$$

Note that (see Figure 3.3):

$$\sum_{i=1}^{B} \delta_i = \widetilde{l}^B_{HDR}(K_B) - \widetilde{l}^1_{HDR}(1). \tag{3.21}$$

Therefore, the optimization problem can now be written by the slope a_i:

$$\arg\min_{a_i} \sum_{i=1}^{B} \frac{p_i}{(a_i)^M} \cdot \xi, \quad \text{s.t} \quad \sum_{i=1}^{B} a_i \cdot \delta_i = l_{LDRmax} - l_{LDRmin}. \tag{3.22}$$

This problem can be solved analytically using the Lagrangian function:

$$\mathcal{L}(a_i, \lambda) = \sum_{i=1}^{B} \frac{p_i}{(a_i)^M} \cdot \xi + \lambda \Big(\sum_{i=1}^{B} a_i \cdot \delta_i - l_{LDRmax} + l_{LDRmin} \Big), \tag{3.23}$$

where λ is the Lagrangian multiplier.

The partial derivatives of the Lagrangian $\mathcal{L}(a_i, \lambda)$ with respect to the parameter a_i and λ must be equal to zero:

$$\begin{cases} \frac{\partial \mathcal{L}(a_i,\lambda)}{\partial a_i} = 0 \\ \frac{\partial \mathcal{L}(a_i,\lambda)}{\partial \lambda} = 0. \end{cases} \tag{3.24}$$

These equations lead to solve the following system:

$$\begin{cases} -M\xi \frac{p_i}{(a_i)^{M+1}} + \lambda \cdot \delta_i = 0, \\ \sum_{i=1}^{B} a_i \cdot \delta_i - l_{LDRmax} + l_{LDRmin} = 0. \end{cases} \tag{3.25}$$

The slopes a_i is deduced from the first equation of the system (3.25):

$$a_i = (\frac{M\xi \cdot p_i}{\lambda \cdot \delta_i})^{1/(M+1)}. \tag{3.26}$$

Replacing this result in the second equation of the system (3.25) provides:

$$\sum_{i=1}^{B} (\frac{M\xi \cdot p_i}{\lambda \cdot \delta_i})^{1/(M+1)} \cdot \delta_i = l_{LDRmax} - l_{LDRmin}, \tag{3.27}$$

where one can deduce that:

$$(\frac{M\xi}{\lambda})^{1/(M+1)} = \frac{l_{LDRmax} - l_{LDRmin}}{\sum_{i=1}^{B} \delta_i \cdot (\frac{p_i}{\delta_i})^{1/(M+1)}}. \tag{3.28}$$

These last equations involve the following result:

$$a_i = \frac{l_{LDRmax} - l_{LDRmin}}{\sum_{i=1}^{B} \delta_i \cdot (\frac{p_i}{\delta_i})^{1/(M+1)}} \cdot (\frac{p_i}{\delta_i})^{1/(M+1)}, \tag{3.29}$$

which is equivalent to:

$$a_i = \frac{l_{LDRmax} - l_{LDRmin}}{\sum_{i=1}^{B} (\delta_i)^{M/(M+1)} \cdot (p_i)^{1/(M+1)}} \cdot (\frac{p_i}{\delta_i})^{1/(M+1)}. \tag{3.30}$$

As it can be seen in equation (3.30) the slope a_i is positive. The slope a_i is proportional to p_i which satisfies the constrained condition given by equation (3.20), the more probability p_i (with the same interval δ_i) the more value a_i, and vice versa.

In the specific cases: (i) if the parameter $M \to \infty$, the limitation of slope a_i is constant:

$$\begin{aligned}
a_i &= \lim_{M\to\infty} \frac{l_{LDRmax} - l_{LDRmin}}{\sum_{i=1}^{B} (\delta_i)^{M/(M+1)} \cdot (p_i)^{1/(M+1)}} \cdot (\frac{p_i}{\delta_i})^{1/(M+1)} \\
&= \frac{l_{LDRmax} - l_{LDRmin}}{\sum_{i=1}^{B} (\delta_i)^{1} \cdot (p_i)^{0}} \cdot (\frac{p_i}{\delta_i})^{0} = \frac{l_{LDRmax} - l_{LDRmin}}{\sum_{i=1}^{B} \delta_i} \\
&= \frac{l_{LDRmax} - l_{LDRmin}}{\widetilde{l}_{HDR}^{B}(K_B) - \widetilde{l}_{HDR}^{1}(1)} = const, \qquad (3.31)
\end{aligned}$$

therefore the "s-shaped" curve is globally linear, (ii) if the parameter $M \to 0$, the limitation of slope a_i is:

$$\begin{aligned}
a_i &= \lim_{M\to 0} \frac{l_{LDRmax} - l_{LDRmin}}{\sum_{i=1}^{B} (\delta_i)^{M/(M+1)} \cdot (p_i)^{1/(M+1)}} \cdot (\frac{p_i}{\delta_i})^{1/(M+1)} \\
&= \frac{l_{LDRmax} - l_{LDRmin}}{\sum_{i=1}^{B} (\delta_i)^{0} \cdot (p_i)^{1}} \cdot (\frac{p_i}{\delta_i})^{1} = \frac{l_{LDRmax} - l_{LDRmin}}{\sum_{i=1}^{B} p_i} \cdot \frac{p_i}{\delta_i} \\
&= \frac{l_{LDRmax} - l_{LDRmin}}{\delta_i} \cdot p_i. \qquad (3.32)
\end{aligned}$$

Hence the unknown parameter b_i is calculated (i.e. $b_i = \hat{l}_{LDR}^{i}(1) - a_i \times \widetilde{l}_{LDR}^{i}(1)$) and LDR mapped values are deduced according to equation (3.7). The global piecewise linear curve is continuous and strictly monotonic increasing according to the positive slopes (i.e. $a_i > 0$, or angles $0° < \mathrm{atan}(a_i) < 90°$).

4 Simulation results

This section discusses the performance of the proposed HDR image tone mapping approach. The tone mapped image quality is measured with the Tone-Mapped image Quality Index 1 (TMQI1) metric [34]. Simulations have been conducted under Matlab environnement using the HDR Toolbox ([1]) with 274 test HDR images. The results are obtained with 24 HDR images from 7 f-stops to 29 f-stops, indoor and outdoor scenes, namely, "Lausanne1", "CraterLake1", "Shasta2", "Synagogue", "Anturium", "BowRiver", "Bridges", "Stairway1", "ArchRock", "DollDoll", "ClockBuilding", "OxfordChurch", "BottlesSmall", "Montreal", "SmallOffice", "Light", "BridgeStudios2", "Memorial", "ClaridgeHotel", "Mistaya1", "BrookHouse", "PeaceRocks", "GGpark2" and "AtriumNight". The different parameters are chosen so as to give the best results in terms of TMQI1 metric in all reference methods. All tone mapped images are rendered in equation (2.2) with color saturation $s = 0.5$.

The proposed TM approaches, namely:

i. "Proposed_NUHA_NM" deployed with $\ell_M = \ell_1, \ell_2, \ell_3, \ell_4, \ell_6, \ell_{10}$,

ii. "Proposed_NUHA_NIn" for ℓ_∞ with a_i given by equation (3.31),

iii. "Proposed_NUHA_NZe" for a_i given by equation (3.32),

are used for $B = 256$, $l_{LDRmax} = 255$ and $l_{LDRmin} = 0$.

Table 3.1 provides the TMQI1 metrics. The results show that our TM approach is competitive to those developed in the literature. Moreover less norm space concerns, more the performance increases. On the other hand, the "Proposed_NUHA_NZe" almost has the higher metric but the visual quality of tone mapped image is less good since artifacts appear, see Figure 3.4c and Figure 3.6c. By comparison, the details around light are clearly visible on Figure 3.4. Indeed Figure 3.5, providing the tone mapping curves with different norm spaces, confirms the performance when the computation is derived in the ℓ_1 norm space since the curve is closest to the "s-shaped" curve. The "s-shaped" curve can be diverse, see Figure 3.7 and of course, the contrast will change, see Figure 3.6.

The normalized histograms of "Light" tone mapped images with different norm spaces are shown in Figure 3.8b, Figure 3.8c, Figure 3.8d, Figure 3.8e, Figure 3.8f, Figure 3.8h, and Figure 3.8g. The normalized histogram of "Proposed_NUHA_NZe" tends to be flat, as a result, it gets more contrast. The derivation in ℓ_1 space (the mean absolute error measure, or "Proposed_NUHA_N1") allows both small and large values to be represented. One can also observe that the visual quality of our tone mapped image given in Figure 3.9a is better than "Duan" tone mapped image provided in Figure 3.9b in particular around the light.

Figure 3.10 compares the visual quality of the "OxfordChurch" tone mapped image using "Duan" method and our approach (in ℓ_1). The stained glass window at the church background presents a better contrast and details with our approach although our TMQI is lower (0.897 compared to 0.986).

Figure 3.11 compares the visual quality of the "WardFlowers" tone mapped image using "Fattal" WRB and our approach (in ℓ_1). Some details, on flowers and rocks, are lost on "Fattal" tone mapped image compared to our approach. Moreover, our tone mapped image is of better contrast.

The performance of proposed approach is confirmed on more than 274 test HDR images where the details and contrast are better represented than other competitive methods.

Table 3.1: *Tone Mapped Image Quality Index 1 (TMQI1).*

Images	DR f-stops	Pro_NUHA_NZe	Pro_NUHA_N1	Pro_NUHA_N2	Pro_NUHA_N3	Pro_NUHA_N4	Pro_NUHA_N6	Pro_NUHA_N10	Pro_NUHA_NIn
Lausanne1	7.71	**0.918**	0.872	0.863	0.859	0.856	0.853	0.850	0.844
CraterLake1	8.13	**0.949**	0.861	0.846	0.839	0.834	0.829	0.825	0.817
Shasta2	8.48	**0.933**	0.826	0.807	0.799	0.794	0.789	0.785	0.778
Synagogue	8.57	**0.965**	0.811	0.790	0.782	0.777	0.772	0.767	0.761
Anturium	8.73	**0.957**	0.929	0.920	0.915	0.912	0.908	0.905	0.898
BowRiver	9.53	**0.958**	0.852	0.830	0.820	0.814	0.808	0.803	0.795
Bridges	11.17	**0.953**	0.942	0.934	0.930	0.926	0.923	0.919	0.905
Stairway1	13.37	**0.909**	0.848	0.839	0.833	0.829	0.824	0.820	0.810
ArchRock	13.60	**0.944**	0.918	0.894	0.882	0.875	0.868	0.861	0.851
DollDoll	13.89	**0.886**	0.842	0.831	0.825	0.821	0.818	0.815	0.809
ClockBuilding	14.19	**0.967**	0.901	0.883	0.873	0.867	0.861	0.855	0.846
OxfordChurch	15.43	**0.974**	0.897	0.876	0.866	0.861	0.855	0.849	0.839
BottlesSmall	16.03	**0.915**	0.850	0.840	0.835	0.832	0.828	0.825	0.820
Montreal	16.06	**0.941**	0.752	0.731	0.721	0.715	0.709	0.703	0.692
SmallOffice	16.29	**0.962**	0.927	0.918	0.912	0.909	0.905	0.901	0.893
Light	17.46	**0.958**	0.916	0.888	0.872	0.863	0.852	0.843	0.827
BridgeStudios2	18.13	**0.964**	0.845	0.826	0.815	0.809	0.802	0.795	0.785
Memorial	18.38	0.907	**0.922**	0.890	0.874	0.865	0.855	0.846	0.832
ClaridgeHotel	23.44	**0.934**	0.766	0.753	0.748	0.744	0.740	0.737	0.732
Mistaya1	23.77	**0.963**	0.823	0.806	0.799	0.795	0.791	0.788	0.782
BrookHouse	23.98	**0.971**	0.851	0.824	0.813	0.808	0.803	0.799	0.792
PeaceRocks	24.13	**0.879**	0.788	0.771	0.766	0.763	0.760	0.757	0.747
GGpark2	24.41	**0.972**	0.794	0.781	0.776	0.774	0.771	0.769	0.764
AtriumNight	28.68	**0.924**	0.842	0.814	0.802	0.795	0.788	0.782	0.765

(a) Proposed_NUHA_N1 (TMQI1=0.916) **(b)** Proposed_NUHA_N2 (TMQI1=0.888)

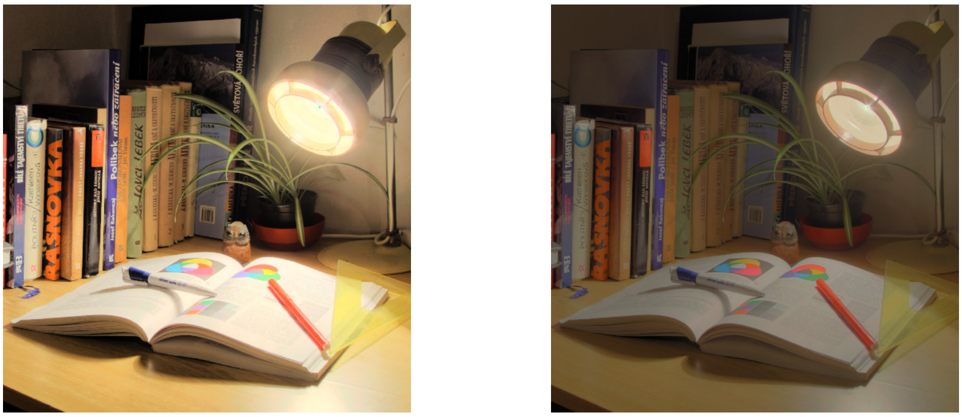

(c) Proposed_NUHA_NZe (TMQI1=0.958) **(d)** Proposed_NUHA_NIn (TMQI1=0.827)

Figure 3.4: *"Light" HDR test image (17.46 f-stops) with several norms.*

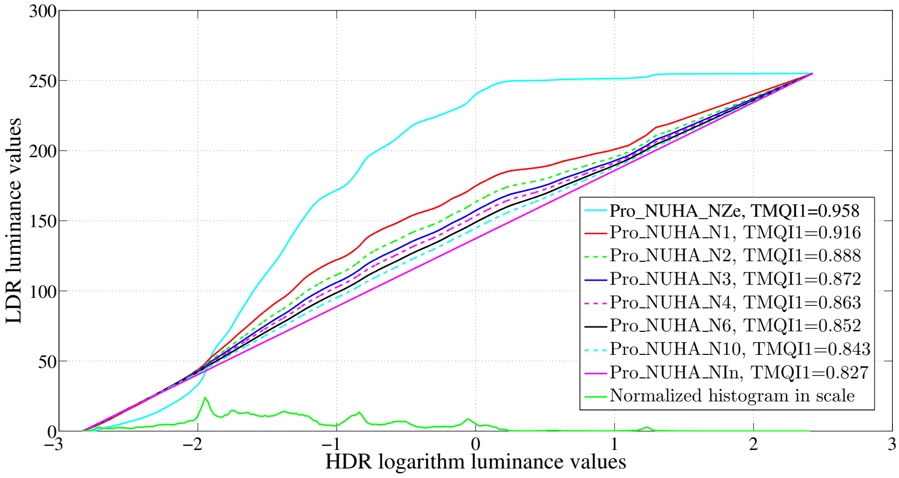

Figure 3.5: *Tone-mapping curves with ℓ_M norm space for "Light" HDR test image.*

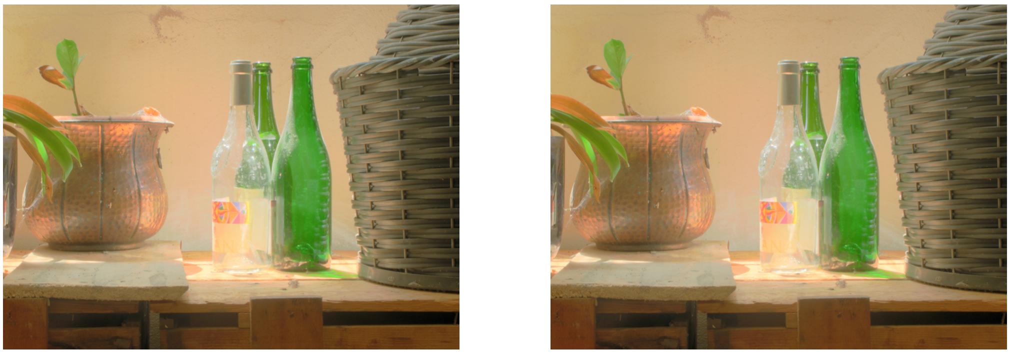

(a) Proposed_NUHA_N1 (TMQI1=0.850) **(b)** Proposed_NUHA_N2 (TMQI1=0.840)

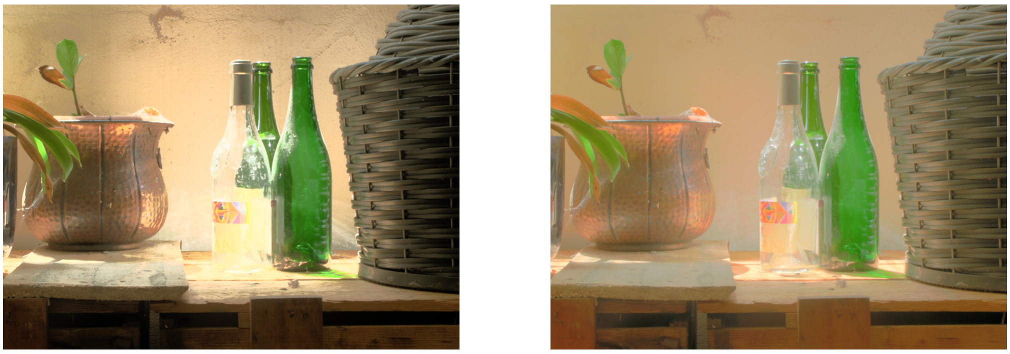

(c) Proposed_NUHA_NZe (TMQI1=0.915) **(d)** Proposed_NUHA_NIn (TMQI1=0.820)

Figure 3.6: *"BottlesSmall" HDR test image (16.03 f-stops) with several norms.*

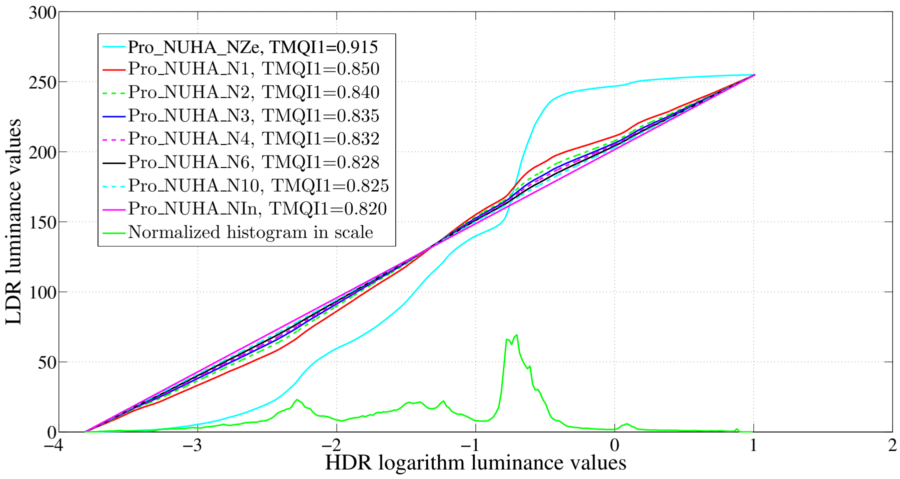

Figure 3.7: *Tone-mapping curves with ℓ_M norm space for "BottlesSmall" HDR test image.*

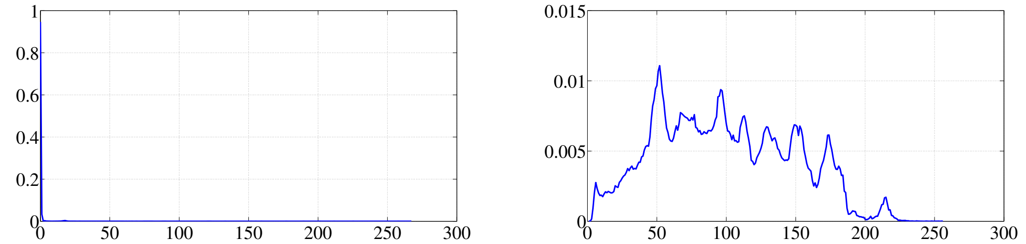

(a) Original HDR luminance **(b)** Proposed_NUHA_N1 (ℓ_1)

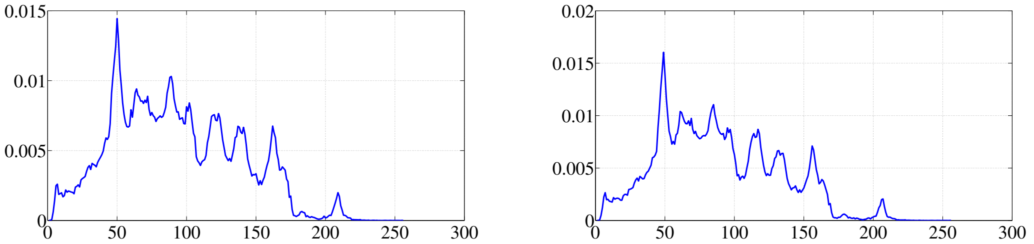

(c) Proposed_NUHA_N2 (ℓ_2) **(d)** Proposed_NUHA_N3 (ℓ_3)

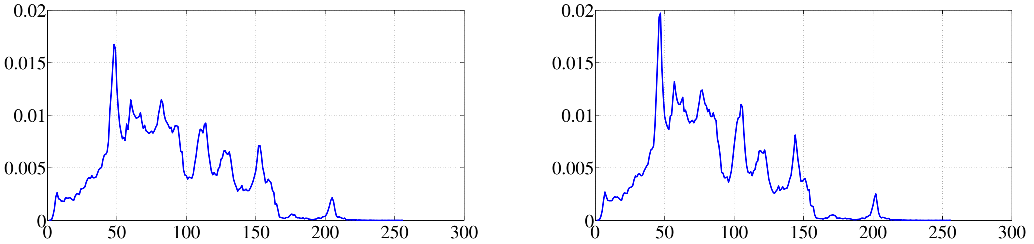

(e) Proposed_NUHA_N4 (ℓ_4) **(f)** Proposed_NUHA_N10 (ℓ_{10})

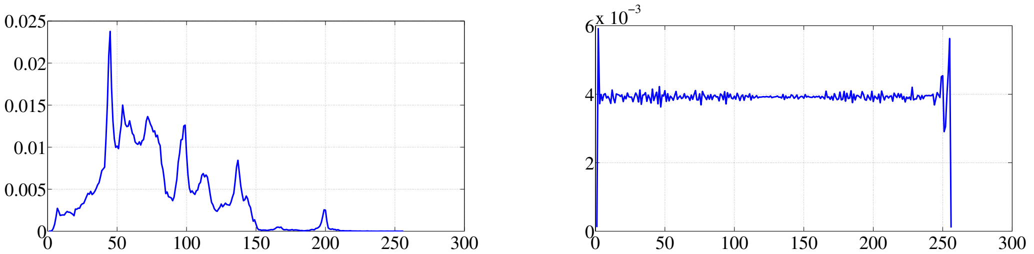

(g) Proposed_NUHA_NIn (ℓ_∞) **(h)** Proposed_NUHA_NZe

Figure 3.8: *Normalized histograms of "Light" tone mapped images (norm spaces $\ell_1, \ell_2, \ell_3, \ell_4, \ell_{10}$, NZe and NIn).*

(a) Proposed_NUHA_N1 (ℓ_1) **(b)** "Duan"

Figure 3.9: *"Light" HDR test image (17.46 f-stops) - Left image: Proposed_NUHA_N1 (TMQI1=0.916); Right image: "Duan" (TMQI1=0.969).*

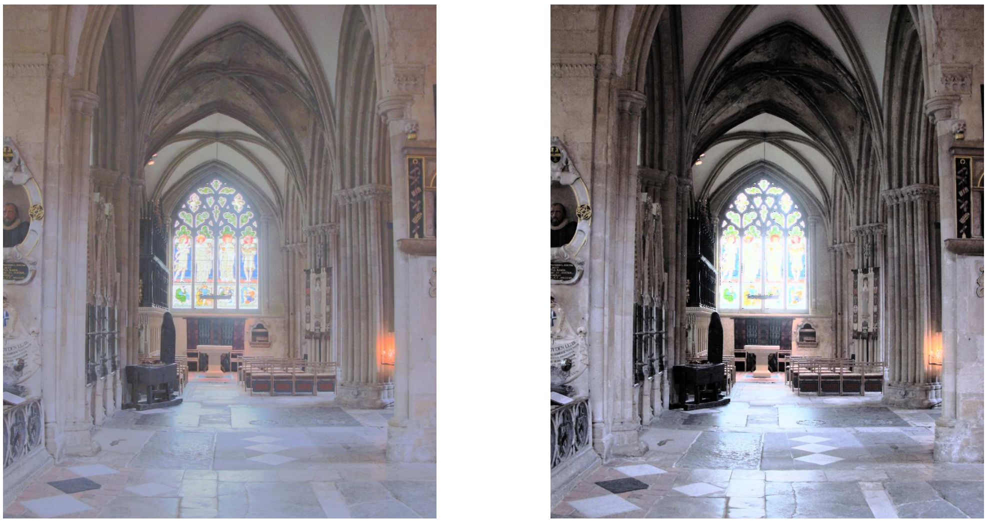

Figure 3.10: *"OxfordChurch" HDR test image (15.43 f-stops) - Left image: Proposed_NUHA_N1 (TMQI1=0.897); Right image: "Duan" (TMQI1=0.986).*

Figure 3.11: *"WardFlowers" HDR test image (14.01 f-stops) - Left image: Proposed_NUHA_N1 (TMQI1=0.930); Right image: "Fattal" WRB (TMQI1=0.875).*

5 Conclusion

The proposed HDR image TM approach is able to enhance the contrast of LDR images. This is due to the adjustment of the HDR logarithm luminance values distribution according to the perceptual piecewise linear function. Simulation results confirm the relevance of the proposed approach both in terms of the TMQI1 metric and the visual quality of the displayed images.

The next chapter proposes tone mapping operators using multiresolution technique to enhance the details visibility.

CHAPTER

4

Proposed TMOs based on Essential Non-Oscillatory multiresolution families

Abstract

This chapter investigates a new kind of local tone mapping operators based on multiresolutions according to separable (Point-Value, Cell-Average) or non-separable (Cell-Average) multiresolution approaches using Essential Non-Oscillatory strategies. These methods improve detail visibility because the purpose of decomposition is to better represent the details of the complex HDR image preserving as much as possible the HDR image quality. Two detailed descriptions of our proposed methods have been published in the conferences EUSIPCO 2016 [1]and ISSPIT 2017 [2].

---

[1] [49] B. C. Thai, A. Mokraoui, and B. Matei. "Performance Evaluation of High Dynamic Range Image Tone Mapping Operators Based on Separable Nonlinear Multiresolution Families". In: 24th IEEE European Signal Processing Conference (EUSIPCO) (Aug. 2016), pp. 1891-1895.

[2] [50] B. C. Thai et al. "Image Tone Mapping Approach Using Essentially Non-Oscillatory Bi-quadratic Interpolations Combined with a Weighting Coefficients Strategy". In: IEEE International Symposium on Signal Processing and Information Technology (ISSPIT) (Dec. 2017), pp. 089-094.

Chapter content

1 Introduction

To adapt the prediction near the singularities of the data, Harten et al. proposed to use Essentially Non-Oscillatory interpolation techniques. In [51], Harten et al. introduced a data-dependent piecewise-polynomial interpolation technique which they refer to as Essentially Non-Oscillatory (ENO) interpolation. The original intention behind ENO interpolation is to avoid the Gibbs-like phenomenon obtained when using centered interpolation techniques in approximating functions with jump discontinuities. An ENO interpolant produces a monotone profile when interpolating across a jump. The basic idea behind an ENO technique is to construct the piecewise polynomial pieces using only information from regions of smoothness of the interpolated function when this is possible.

The proposed Image TMOs rely on separable and non-separable nonlinear multiresolution approaches based on data dependent interpolation. It exploits the ENO interpolation strategy developed by Harten [52], [53], [51] and [54] where Point-Value (PV) mutiresolution family and Cell-Averarage (CA) multiresolution family are considered. These families have the ability to introduce in their mathematical model the isolated singularities such as edge points in the image thus avoiding the Gibbs phenomenon particularly harmful in tone mapped images.

2 Global TMO scheme based on ENO multiresolution families

The proposed approaches are described in the following sections and summarized by the block diagram in Figure 4.1. The original HDR image, considered at the finest resolution level denoted J, is assumed to be of size $N^J \times M^J$. Denote $\mathbf{L}_{HDR}$ and $\mathbf{L}_{LDR}$ respectively the HDR and LDR image luminance. The index j refers to the resolution level (with $j = 1, ..., J$).

In the rest of this chapter, the HDR image luminance is considered in the logarithm domain since it is well adapted to the HVS. It is denoted $\mathbf{I}^J$ and defined as follows:

$$\mathbf{I}^J := \left\{ \mathbf{I}^J(x_n, y_m) = \log_{10}(\mathbf{L}_{HDR}(x_n, y_m)) \text{ for } 1 \leq n \leq N^J \text{ and } 1 \leq m \leq M^J \right\}, \quad (4.1)$$

where $\mathbf{I}^J(x_n, y_m)$ is the HDR logarithm luminance value of the pixel located at position (x_n, y_m).

The proposed TMOs are based on multiresolution approaches:

i. Separable multiresolution ENO Point-Value (PV) and Cell-Average (CA),

ii. Non-separable multiresolution ENO Cell-Average (CA).

They will be described at the following sections.

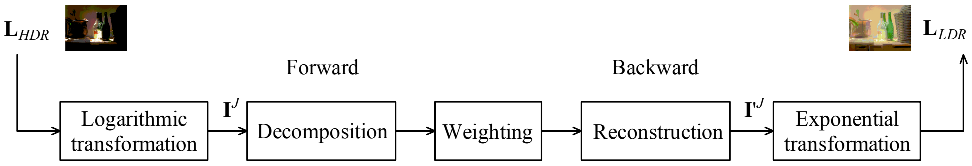

Figure 4.1: *Diagram block of the proposed HDR image TM algorithm based on multiresolution scheme.*

3 TMO based on separable multiresolution ENO point-value scheme

The separable multiresolution ENO Point-Value scheme consists of three main stages: (forward) decomposition, weighting and (backward) reconstruction described as follows.

3.1 Separable forward algorithm

This section concerns the first stage of the HDR image TM algorithm. It decomposes the logarithm luminance of the original HDR image into approximations and details resolution levels. This decomposition is achieved according to the forward process of a separable (i.e. 1D-signal in horizontal and vertical directions) Point-Value lifting scheme. This choice, among the various developed decomposition strategies in the literature, is motivated by the fact that the relevant details are accurately predicted since the coefficients of the filters are adapted locally to the data to be processed.

The decomposition process consists to go from the finest resolution level J to the coarsest resolution level 0. At a given resolution level j (with $1 \leq j \leq J$), the algorithm deals with the approximation coefficients obtained at resolution level j i.e. $\mathbf{I}^j(x_n, y_k)$ (with $1 \leq n \leq N^j$ and $1 \leq k \leq M^j$) as shown in Figure 4.2. The forward process steps of the separable decomposition algorithm are described below.

3.1.1 Split 1D-signal into odd and even indexes (step 1)

At a given resolution level j and a given n belonging to $[1, N^j]$ (i.e. x_n), the algorithm starts with splitting the horizontal 1D-signal, i.e. $\mathbf{I}^j(x_n, y_k)$ for $1 \leq k \leq M^j$, into a set of odd $\mathbf{I}^j(x_n, y_{2k-1})$ and even $\mathbf{I}^j(x_n, y_{2k})$ indexes as down-sampling:

$$\begin{aligned} &\{\mathbf{I}^j(x_n, y_k) \text{ with } 1 \leq k \leq M^j\} \\ := &\{\mathbf{I}^j(x_n, y_{2k-1}),\ \mathbf{I}^j(x_n, y_{2k}) \ \text{ with } \ 1 \leq k \leq M^j/2\ \}. \end{aligned} \tag{4.2}$$

The process is then repeated on each row until $n = N^j$.

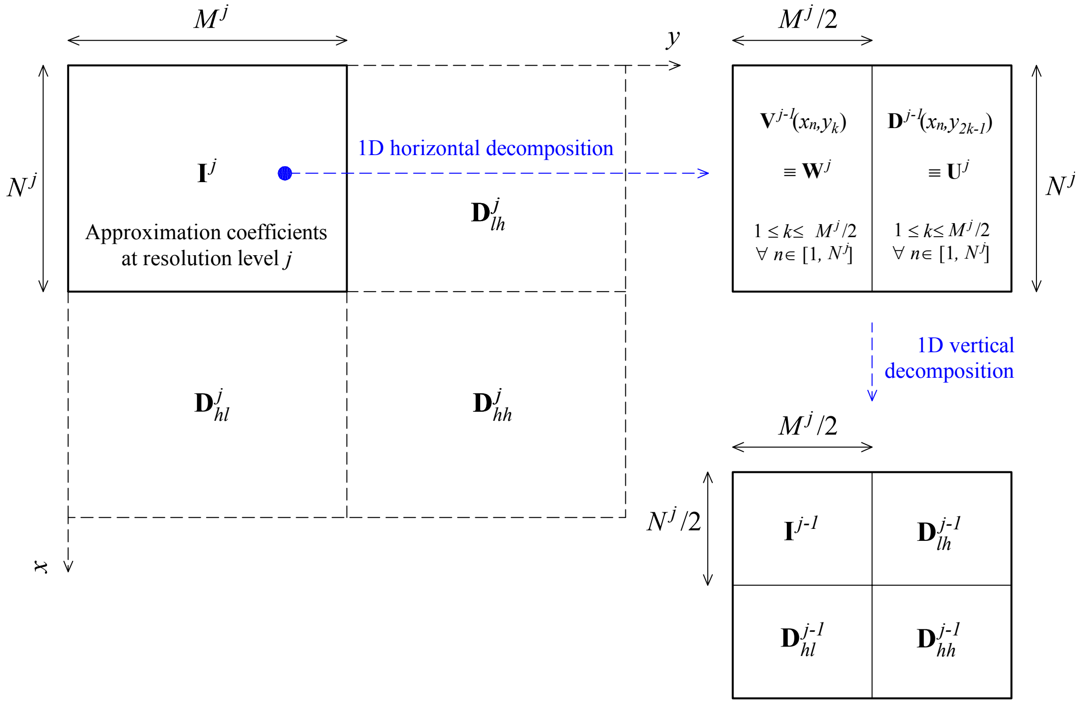

Figure 4.2: *Separable lifting scheme decomposition principle.*

3.1.2 Approximation resolution level in a point-value scheme (step 2)

Based on this split, the approximation coefficient located at position (x_n, y_k), denoted $\mathbf{V}^{j-1}(x_n, y_k)$ for a given n, is computed on a PV scheme as follows:

$$\mathbf{V}^{j-1}(x_n, y_k) = \mathbf{I}^j(x_n, y_{2k}) \quad \text{for } 1 \le k \le M^j/2. \tag{4.3}$$

The process is then repeated until $n = N^j$. The pixel value $\mathbf{V}^{j-1}(x_n, y_k)$ is defined by the Point-Value of the underlying cubic Lagrange function $p(x)$ at the mid point of the cell $[k,\ k+1]$:

$$\mathbf{V}^{j-1}(x_n, y_k) = p(k+1/2). \tag{4.4}$$

3.1.3 Detail resolution level based on 1D point-value ENO prediction (step 3)

The detail coefficient, denoted $\mathbf{D}^{j-1}(x_n, y_{2k-1})$ for a given n, is then computed at odd indexes (x_n, y_{2k-1}) as follows:

$$\mathbf{D}^{j-1}(x_n, y_{2k-1}) = \mathbf{I}^j(x_n, y_{2k-1}) - \hat{\mathbf{I}}^j(x_n, y_{2k-1}) \text{ for } 1 \le k \le M^j/2, \tag{4.5}$$

where $\hat{\mathbf{I}}^j(x_n, y_{2k-1})$ is the predicted logarithm luminance value at odd position (x_n, y_{2k-1}) and resolution level j.

This predicted value is approximated by using those approximation coefficients from the prediction stencil of length equal to four defined as:

$$\mathbf{P}u^{j-1}(x_n, y_k, u) := \{k+u-1,\ k+u,\ k+u+1,\ k+u+2\}, \tag{4.6}$$

where u is an integer in $[-1,0,1]$, corresponding to the position of the stencil with respect to k. There are then three kinds of stencils, left, center and right with $u=-1,0,1$, respectively as follows: for the left stencil:

$$\mathbf{P}u^{j-1}(x_n,y_k,-1) := \{k-2,\ k-1,\ k,\ k+1\}, \tag{4.7}$$

for the center stencil:

$$\mathbf{P}u^{j-1}(x_n,y_k,0) := \{k-1,\ k,\ k+1,\ k+2\}, \tag{4.8}$$

for the right stencil:

$$\mathbf{P}u^{j-1}(x_n,y_k,1) := \{k,\ k+1,\ k+2,\ k+3\}. \tag{4.9}$$

A cubic Lagrange polynomial $p_u(x)$ is defined to interpolate four values of approximation coefficients $\mathbf{V}^{j-1}$ on the stencil $\mathbf{P}u^{j-1}(x_n,y_k,u)$. Therefore there are three polynomials $(p_{-1}(x),\ p_0(x),\ p_1(x))$ attached to the corresponding stencils. The four unknown coefficients are deduced from the four interpolation conditions on the stencil, see in Appendix A.1.

In order to measure the degree of oscillations of such polynomials, the following functions for summation of relevant points on the stencils are used: for the left stencil:

$$\zeta(\mathbf{P}u^{j-1}(x_n,y_k,-1)) = |\mathbf{V}^{j-1}(x_n,y_{k-2}) - \mathbf{V}^{j-1}(x_n,y_{k-1})| + \\ |\mathbf{V}^{j-1}(x_n,y_{k-1}) - \mathbf{V}^{j-1}(x_n,y_k)| + |\mathbf{V}^{j-1}(x_n,y_k) - \mathbf{V}^{j-1}(x_n,y_{k+1})|,$$

for the center stencil:

$$\zeta(\mathbf{P}u^{j-1}(x_n,y_k,0)) = |\mathbf{V}^{j-1}(x_n,y_{k-1}) - \mathbf{V}^{j-1}(x_n,y_k)| + \\ |\mathbf{V}^{j-1}(x_n,y_k) - \mathbf{V}^{j-1}(x_n,y_{k+1})| + |\mathbf{V}^{j-1}(x_n,y_{k+1}) - \mathbf{V}^{j-1}(x_n,y_{k+2})|,$$

for the right stencil:

$$\zeta(\mathbf{P}u^{j-1}(x_n,y_k,1)) = |\mathbf{V}^{j-1}(x_n,y_k) - \mathbf{V}^{j-1}(x_n,y_{k+1})| + \\ |\mathbf{V}^{j-1}(x_n,y_{k+1}) - \mathbf{V}^{j-1}(x_n,y_{k+2})| + |\mathbf{V}^{j-1}(x_n,y_{k+2}) - \mathbf{V}^{j-1}(x_n,y_{k+3})|.$$

The predicted value is deduced so that the optimal value u is the solution of the following minimization problem:

$$u^* = \underset{-1\leq u\leq 1}{\arg\min}\ \zeta(\mathbf{P}u^{j-1}(x_n,y_k,u)). \tag{4.10}$$

This is expressed as the ENO interpolations as choosing the best stencil. The pixel value $\hat{\mathbf{I}}^j(x_n,y_{2k-1})$ is defined on the mid point of cell $[k,\ k+1]$ as follows:

$$\hat{\mathbf{I}}^j(x_n,y_{2k-1}) = p_{u^*}(k+1/2). \tag{4.11}$$

The predicted value $\hat{\mathbf{I}}^j(x_n, y_{2k-1})$ is one of three possibilities as follows:

$$\begin{cases} p_{-1}(k+1/2) & \text{for the left stencil at } u=-1 \\ p_0(k+1/2) & \text{for the center stencil at } u=0 \\ p_1(k+1/2) & \text{for the right stencil at } u=1 \end{cases} \tag{4.12}$$

$$= \begin{cases} +\frac{1}{16}\mathbf{V}^{j-1}(x_n,y_{k-2}) - \frac{5}{16}\mathbf{V}^{j-1}(x_n,y_{k-1}) + \frac{15}{16}\mathbf{V}^{j-1}(x_n,y_k) + \frac{5}{16}\mathbf{V}^{j-1}(x_n,y_{k+1}) \\ -\frac{1}{16}\mathbf{V}^{j-1}(x_n,y_{k-1}) + \frac{9}{16}\mathbf{V}^{j-1}(x_n,y_k) + \frac{9}{16}\mathbf{V}^{j-1}(x_n,y_{k+1}) - \frac{1}{16}\mathbf{V}^{j-1}(x_n,y_{k+2}) \\ +\frac{5}{16}\mathbf{V}^{j-1}(x_n,y_k) + \frac{15}{16}\mathbf{V}^{j-1}(x_n,y_{k+1}) - \frac{5}{16}\mathbf{V}^{j-1}(x_n,y_{k+2}) + \frac{1}{16}\mathbf{V}^{j-1}(x_n,y_{k+3}) \end{cases} \tag{4.13}$$

$$= \begin{cases} \sum\left[+\frac{1}{16} \quad -\frac{5}{16} \quad +\frac{15}{16} \quad +\frac{5}{16}\right] \otimes \left[\mathbf{V}^{j-1}(x_n,y_{k-2}) \quad \mathbf{V}^{j-1}(x_n,y_{k-1}) \quad \mathbf{V}^{j-1}(x_n,y_k) \quad \mathbf{V}^{j-1}(x_n,y_{k+1})\right] \\ \sum\left[-\frac{1}{16} \quad +\frac{9}{16} \quad +\frac{9}{16} \quad -\frac{1}{16}\right] \otimes \left[\mathbf{V}^{j-1}(x_n,y_{k-1}) \quad \mathbf{V}^{j-1}(x_n,y_k) \quad \mathbf{V}^{j-1}(x_n,y_{k+1}) \quad \mathbf{V}^{j-1}(x_n,y_{k+2})\right] \\ \sum\left[+\frac{5}{16} \quad +\frac{15}{16} \quad -\frac{5}{16} \quad +\frac{1}{16}\right] \otimes \left[\mathbf{V}^{j-1}(x_n,y_k) \quad \mathbf{V}^{j-1}(x_n,y_{k+1}) \quad \mathbf{V}^{j-1}(x_n,y_{k+2}) \quad \mathbf{V}^{j-1}(x_n,y_{k+3})\right] \end{cases} \tag{4.14}$$

in compact forms where $\otimes$ is the product term by term. The predict value chooses one of three possibilities depended on optimized stencil where the difference of pixels on coarse is less oscillated.

All the best stencils $\mathbf{P}u^{j-1}(x_n, y_k, u^*)$ are stored to be used in the adaptive lifting scheme backward process to reconstruct the decomposed 1D-signal. The horizontal decomposition steps (i.e. 1, 2 and 3) are summarized in Figure 4.3.

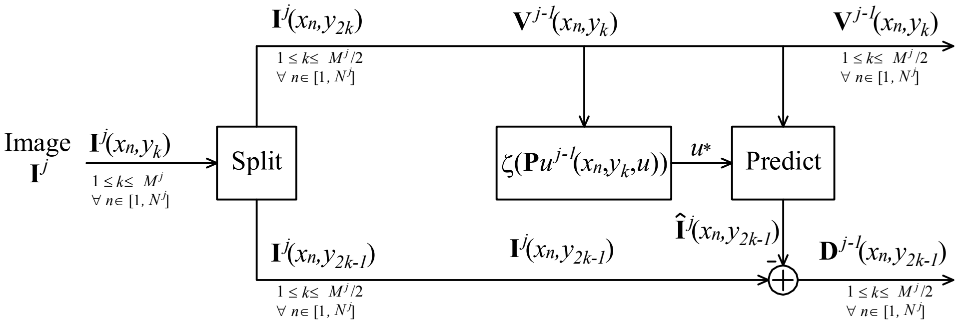

Figure 4.3: *1D-signal decomposition using separable multiresolution ENO PV in a horizontal direction.*

3.1.4 Arrangement of approximation and detail coefficients

To process the 1D-signal in the vertical direction and for sake of convenience, the approximation and details coefficients are organized as shown in Figure 4.3 and renamed as follows:

$$\begin{aligned} &\{\mathbf{V}^{j-1}(x_n, y_k) \text{ for } 1 \le k \le M^j/2 \text{ and } \forall n \in [1, N^j]\} \\ := &\{\mathbf{W}^j(x_k, y_m) \text{ for } 1 \le k \le N^j \text{ and } \forall m \in [1, M^j/2]\}. \end{aligned} \tag{4.15}$$

$$\begin{aligned} &\{\mathbf{D}^{j-1}(x_n, y_{2k-1}) \text{ for } 1 \le k \le M^j/2 \text{ and } \forall n \in [1, N^j]\} \\ := &\{\mathbf{U}^j(x_k, y_m) \text{ for } 1 \le k \le N^j \text{ and } \forall m \in [1, M^j/2]\}. \end{aligned} \tag{4.16}$$

3.1.5 Repeat steps 1, 2 and 3

Steps 1, 2 and 3 are now being applied on $\mathbf{W}^j(x_k, y_m)$ and $\mathbf{U}^j(x_k, y_m)$ for a given $m \in [1, M^j/2]$. Figure 4.4 summarizes the vertical 1D-signal forward decomposition. Note that the approximation step requires the prediction of $\hat{\mathbf{W}}^j(x_{2k-1}, y_m)$ (respectively $\hat{\mathbf{U}}^j(x_{2k-1}, y_m)$) based on a set of best stencils $\mathbf{P}v^{j-1}(x_k, y_m, v^*)$ (respectively $\mathbf{P}w^{j-1}(x_k, y_m, w^*)$. These stencils need to be stored for the backward process lifting scheme to reconstruct the decomposed logarithm luminance image.

Finally, the approximation resolution level $\mathbf{I}^j(x_n, y_m)$ is divided into four blocks: ll, lh, hl and hh. The block ll concerns the approximation resolution denoted $\mathbf{I}^{j-1}$; and the other three blocks lh, hl and hh contain the detail resolutions, named $\mathbf{D}_{lh}^{j-1}, \mathbf{D}_{hl}^{j-1}, \mathbf{D}_{hh}^{j-1}$, respectively (see Figure 4.2). Note that the size of each block is deduced as the half size of $\mathbf{I}^j$ in each direction:

$$\mathcal{M}\ \mathbf{I}^j \quad := \quad \left(\mathbf{I}^{j-1},\ \mathbf{D}_{lh}^{j-1},\ \mathbf{D}_{hl}^{j-1},\ \mathbf{D}_{hh}^{j-1}\right). \tag{4.17}$$

The decomposition process can be iterated on $\mathbf{I}^{j-1}$ until $\mathbf{I}^0$. The finest HDR logarithm luminance $\mathbf{I}^J$ is then represented by $3J+1$ resolution levels as follows:

$$\mathcal{M}\ \mathbf{I}^J \quad := \quad \left(\mathbf{I}^0, \mathbf{D}_{lh}^0, \mathbf{D}_{hl}^0, \mathbf{D}_{hh}^0, ..., \mathbf{D}_{lh}^{j-1}, \mathbf{D}_{hl}^{j-1}, \mathbf{D}_{hh}^{j-1}, ..., \mathbf{D}_{lh}^{J-1}, \mathbf{D}_{hl}^{J-1}, \mathbf{D}_{hh}^{J-1}\right). \tag{4.18}$$

3.2 Weightings

To reduce the dynamic range, we propose to modify differently the coefficients of each resolution level as follows:

$$\begin{aligned} \mathbf{I}'^0 &= \alpha_a \times \mathbf{I}^0, \\ \mathbf{D}'^0_{lh} = \alpha_d \times \mathbf{D}^0_{lh}, \quad \mathbf{D}'^0_{hl} = \alpha_d \times \mathbf{D}^0_{hl}, \quad \mathbf{D}'^0_{hh} &= \alpha_d \times \mathbf{D}^0_{hh}, \\ &\cdots \\ \mathbf{D}'^{j-1}_{lh} = \alpha_d \times \mathbf{D}^{j-1}_{lh}, \quad \mathbf{D}'^{j-1}_{hl} = \alpha_d \times \mathbf{D}^{j-1}_{hl}, \quad \mathbf{D}'^{j-1}_{hh} &= \alpha_d \times \mathbf{D}^{j-1}_{hh}, \\ &\cdots \\ \mathbf{D}'^{J-1}_{lh} = \alpha_d \times \mathbf{D}^{J-1}_{lh}, \quad \mathbf{D}'^{J-1}_{hl} = \alpha_d \times \mathbf{D}^{J-1}_{hl}, \quad \mathbf{D}'^{J-1}_{hh} &= \alpha_d \times \mathbf{D}^{J-1}_{hh}. \end{aligned} \tag{4.19}$$

where $0 < \alpha_a, \alpha_d < 1$. Figure 4.5 summarizes the weighting process.

In order to reduce the dynamic range, these positive constant parameters α_a, α_d are set less than 1 in an empirical way. The important condition $\alpha_a < \alpha_d$ is used to enhance details visibility when reconstructing.

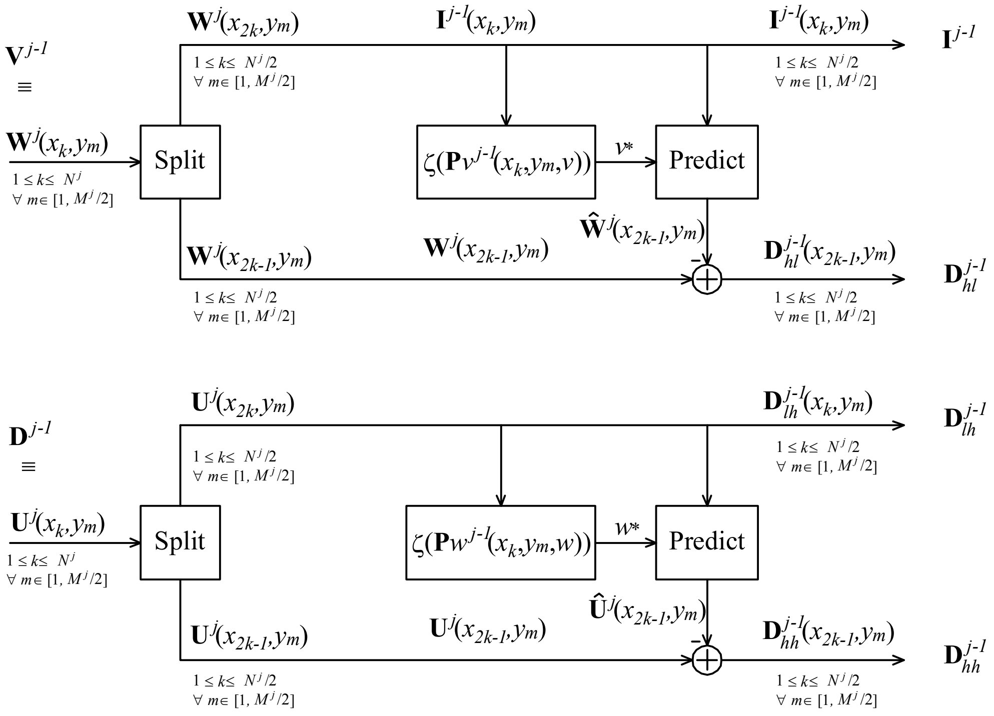

Figure 4.4: *1D-signal decomposition using separable multiresolution ENO PV in a vertical direction.*

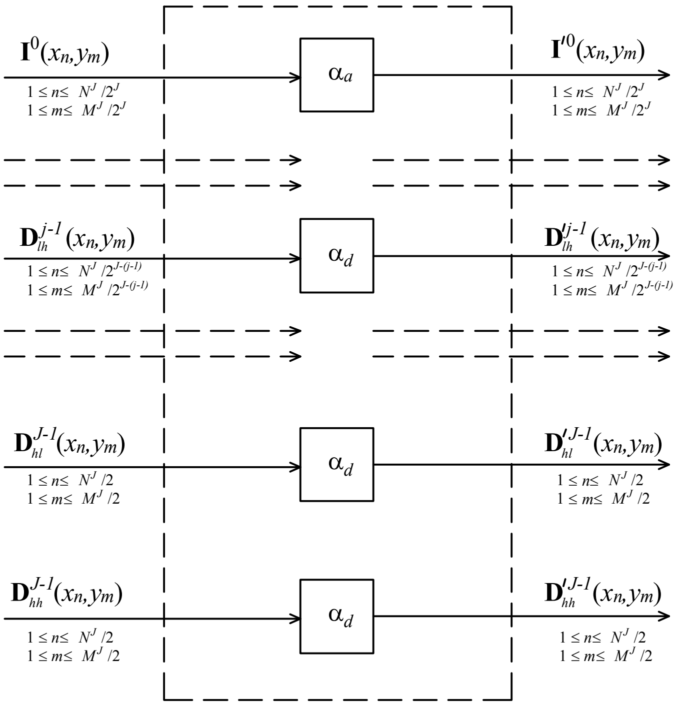

Figure 4.5: *Constant weightings.*

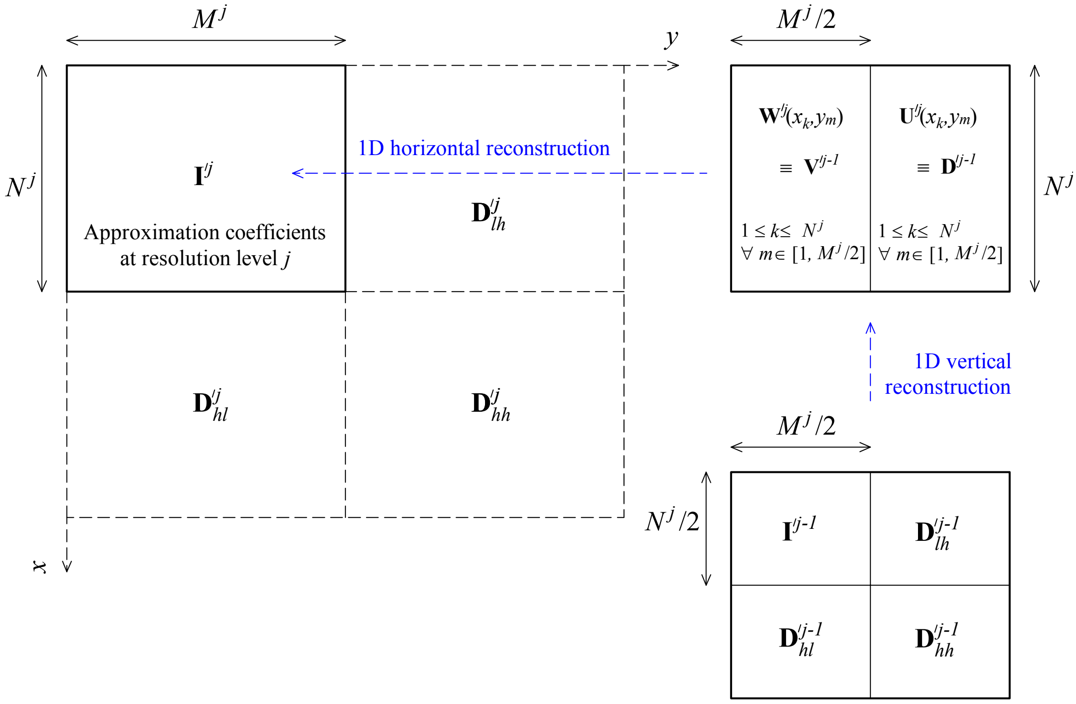

Figure 4.6: *Separable lifting scheme reconstruction principle.*

3.3 Separable backward algorithm

The adaptive lifting scheme backward process starts with the four coarsest resolution levels, i.e ($\mathbf{I}'^0$, $\mathbf{D}'^0_{lh}$, $\mathbf{D}'^0_{hl}$, $\mathbf{D}'^0_{hh}$), to generate the approximation coefficients $\mathbf{I}'^1$. The same process is then iterated until reaching the finest resolution i.e. $j = J$ corresponding to the intermediate HDR image, denoted $\mathbf{I}'^J$, of size $N^J \times M^J$.

Assume first that the algorithm processed all resolution levels until $j-1$. Therefore the next step consists to recover the approximation image $\mathbf{I}'^j$ of size $N^j \times M^j$ using the following blocks: $\mathbf{I}'^{j-1}$, $\mathbf{D}'^{j-1}_{lh}$, $\mathbf{D}'^{j-1}_{hl}$ and $\mathbf{D}'^{j-1}_{hh}$. The reconstruction processes are carried out inversely to the decomposition stage, first in a vertical direction (see Figure 4.7) and then in a horizontal direction (see Figure 4.8). The mathematical equations describing this process are derived in what follows.

First the algorithm deals with the coefficients in a vertical direction using $\mathbf{I}'^{j-1}$ and $\mathbf{D}'^{j-1}_{hl}$. At a given m, the approximation coefficients at odd positions $\mathbf{W}'^j(x_{2k-1}, y_m)$ with $1 \le k \le N^j/2$ are deduced as follows:

$$\mathbf{W}'^j(x_{2k-1}, y_m) = \hat{\mathbf{W}}'^j(x_{2k-1}, y_m) + \mathbf{D}'^{j-1}_{hl}(x_k, y_m) \text{ for } 1 \le k \le N^j/2, \tag{4.20}$$

where $\hat{\mathbf{W}}'^j(x_{2k-1}, y_m)$ is the predicted coefficient, at odd position, deduced from ENO PV scheme of the neighboring approximation coefficients $\mathbf{I}'^{j-1}(x_{2k-1}, y_m)$ as follows:

$$\hat{\mathbf{W}}'^j(x_{2k-1}, y_m) = p_{v^*}(k + 1/2). \tag{4.21}$$

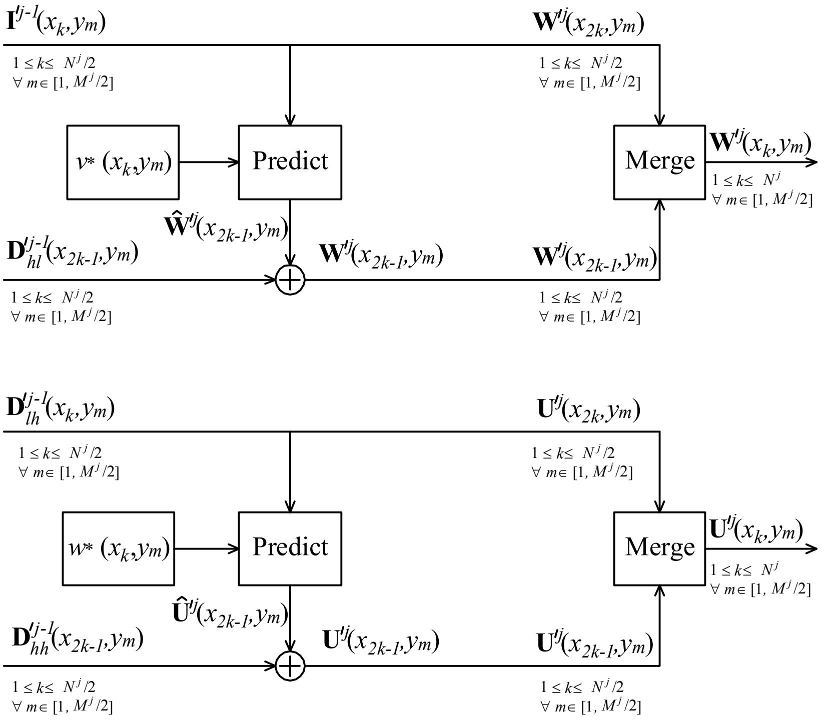

Figure 4.7: *1D-signal reconstruction using separable multiresolution ENO PV in a vertical direction.*

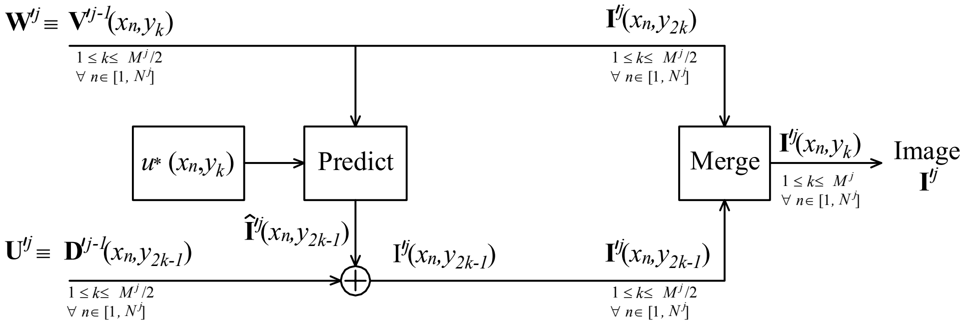

Figure 4.8: *1D-signal reconstruction using separable multiresolution ENO PV in a horizontal direction.*

The predicted value $\hat{\mathbf{W}}'^{j}(x_{2k-1}, y_m)$ is one of three possibilities as follows:

$$\begin{cases} p_{-1}(k+1/2) & \text{for the left stencil at } v=-1 \\ p_0(k+1/2) & \text{for the center stencil at } v=0 \\ p_1(k+1/2) & \text{for the right stencil at } v=1 \end{cases} \tag{4.22}$$

$$= \begin{cases} \sum \left[+\frac{1}{16} \quad -\frac{5}{16} \quad +\frac{15}{16} \quad +\frac{5}{16}\right] \otimes \left[\mathbf{I}'^{j-1}(x_{k-2}, y_m) \quad \mathbf{I}'^{j-1}(x_{k-1}, y_m) \quad \mathbf{I}'^{j-1}(x_k, y_m) \quad \mathbf{I}'^{j-1}(x_{k+1}, y_m)\right] \\ \sum \left[-\frac{1}{16} \quad +\frac{9}{16} \quad +\frac{9}{16} \quad -\frac{1}{16}\right] \otimes \left[\mathbf{I}'^{j-1}(x_{k-1}, y_m) \quad \mathbf{I}'^{j-1}(x_k, y_m) \quad \mathbf{I}'^{j-1}(x_{k+1}, y_m) \quad \mathbf{I}'^{j-1}(x_{k+2}, y_m)\right] \\ \sum \left[+\frac{5}{16} \quad +\frac{15}{16} \quad -\frac{5}{16} \quad +\frac{1}{16}\right] \otimes \left[\mathbf{I}'^{j-1}(x_k, y_m) \quad \mathbf{I}'^{j-1}(x_{k+1}, y_m) \quad \mathbf{I}'^{j-1}(x_{k+2}, y_m) \quad \mathbf{I}'^{j-1}(x_{k+3}, y_m)\right] \end{cases} \tag{4.23}$$

The best stencil $\mathbf{P}v^{j-1}(x_k, y_m, v^*)$ is those computed and stored in the decomposition process. The approximation coefficients $\mathbf{W}'^{j}(x_{2k}, y_m)$, at even positions, are deduced:

$$\mathbf{W}'^{j}(x_{2k}, y_m) = \mathbf{I}'^{j-1}(x_k, y_m) \text{ for } 1 \leq k \leq N^j/2. \tag{4.24}$$

The odd and even approximation coefficients are then merged to constitute the 1D-signal as follows:

$$\begin{aligned} &\{\mathbf{W}'^{j}(x_k, y_m) \text{ for } 1 \leq k \leq N^j\} \\ := &\{\mathbf{W}'^{j-1}(x_{2k-1}, y_m),\ \mathbf{W}'^{j-1}(x_{2k}, y_m) \text{ for } 1 \leq k \leq N^j/2\}. \end{aligned} \tag{4.25}$$

This process is repeated for all m to build $\mathbf{W}'^{j}$ of size $N^j \times M^j/2$.

On the other hand, these same steps are applied to $\mathbf{D}'^{j-1}_{lh}$ and $\mathbf{D}'^{j-1}_{hh}$ to generate the new block $\mathbf{U}'^{j}$ of size $N^j \times M^j/2$ (see Figure 4.7). As in the decomposition strategy, $\mathbf{W}'^{j}$ and $\mathbf{U}'^{j}$ are respectively renamed $\mathbf{V}'^{j-1}$ and $\mathbf{D}'^{j-1}$ and the same steps are performed but according to a horizontal direction (see Figure 4.8). Finally, we get the approximation coefficients $\mathbf{I}'^{j}$ at resolution level j.

$$\mathbf{I}'^{j} \quad := \quad \mathcal{M}^{-1}\left(\mathbf{I}'^{j-1}, \mathbf{D}'^{j-1}_{lh}, \mathbf{D}'^{j-1}_{hl}, \mathbf{D}'^{j-1}_{hh}\right). \tag{4.26}$$

The process is then iterated until $j = J$:

$$\mathbf{I}'^{J} \quad := \quad \mathcal{M}^{-1}\left(\mathbf{I}'^{0}, \mathbf{D}'^{0}_{lh}, \mathbf{D}'^{0}_{hl}, \mathbf{D}'^{0}_{hh}, \ldots, \mathbf{D}'^{j-1}_{lh}, \mathbf{D}'^{j-1}_{hl}, \mathbf{D}'^{j-1}_{hh}, \ldots, \mathbf{D}'^{J-1}_{lh}, \mathbf{D}'^{J-1}_{hl}, \mathbf{D}'^{J-1}_{hh}\right). \tag{4.27}$$

Simulation results will be discussed in section 6.1.

4 TMO based on separable multiresolution ENO cell-average scheme

This TMO algorithm has the same steps as TMO based on separable ENO Point-Value scheme. The difference lies in computations of approximation in section 4.1.2 and predicted values in section 4.1.3.

4.1 Separable forward algorithm

4.1.1 Split 1D-signal into odd and even indexes

The process is the same as in section 3.1.1.

4.1.2 Approximation resolution level in a cell-average scheme

The approximation resolution level is replaced (i.e. the equation (4.3)) by:

$$\mathbf{V}^{j-1}(x_n, y_k) = \frac{1}{2}\Big(\mathbf{I}^j(x_n, y_{2k-1}) + \mathbf{I}^j(x_n, y_{2k})\Big) \text{ for } 1 \leq k \leq M^j/2. \tag{4.28}$$

The pixel value $\mathbf{V}^{j-1}(x_n, y_k)$ is defined by the Cell-Average of the underlying quadratic Lagrange function $p(x)$ as follows:

$$\mathbf{V}^{j-1}(x_n, y_k) = \int\limits_{C_k^{j-1}} p(x)dx = \int_k^{k+1} p(x)dx, \tag{4.29}$$

where the cell C_k^{j-1} is defined as $[k,\ k+1]$.

4.1.3 Detail resolution level based on 1D cell-average ENO prediction

The process is the same as in section 3.1.3. In the detail resolution level, this predicted value is approximated by using those approximation coefficients from a prediction stencil of length equal to three cells defined as:

$$\mathbf{C}u^{j-1}(x_n, y_k, u) := \{[k+u-1, k+u],\ [k+u, k+u+1],\ [k+u+1, k+u+2]\}, \tag{4.30}$$

where u is an integer in $[-1, 0, 1]$, corresponding to the position of the stencil with respect to k. There are then three kinds of stencils, left, center and right with $u = -1, 0, 1$, respectively as follows: for the left stencil:

$$\mathbf{C}u^{j-1}(x_n, y_k, -1) := \{[k-2, k-1],\ [k-1, k],\ [k, k+1]\}, \tag{4.31}$$

for the center stencil:

$$\mathbf{C}u^{j-1}(x_n, y_k, 0) := \{[k-1, k],\ [k, k+1],\ [k+1, k+2]\}, \tag{4.32}$$

for the right stencil:

$$\mathbf{C}u^{j-1}(x_n, y_k, 1) := \{[k, k+1],\ [k+1, k+2],\ [k+2, k+3]\}. \tag{4.33}$$

A quadratic Lagrange polynomial $p_u(x)$ is defined to interpolate three values of approximation coefficients $\mathbf{V}^{j-1}$ on the stencil $\mathbf{C}u^{j-1}(x_n, y_k, u)$. Therefore there are three polynomials ($p_{-1}(x)$, $p_0(x)$, $p_1(x)$) attached to the corresponding stencils. The three unknown coefficients are deduced from the three interpolation conditions on the stencil, see in Appendix A.2.

In order to to measure the degree of oscillations of such polynomials, the following functions for summation of relevant points on the stencils are used: for the left stencil:

$$\begin{aligned}\zeta(\mathbf{C}u^{j-1}(x_n,y_k,-1)) = |\mathbf{V}^{j-1}(x_n,y_{k-2}) - \mathbf{V}^{j-1}(x_n,y_{k-1})| + \\ |\mathbf{V}^{j-1}(x_n,y_{k-1}) - \mathbf{V}^{j-1}(x_n,y_k)|,\end{aligned} \tag{4.34}$$

for the center stencil:

$$\begin{aligned}\zeta(\mathbf{C}u^{j-1}(x_n,y_k,0)) = |\mathbf{V}^{j-1}(x_n,y_{k-1}) - \mathbf{V}^{j-1}(x_n,y_k)| + \\ |\mathbf{V}^{j-1}(x_n,y_k) - \mathbf{V}^{j-1}(x_n,y_{k+1})|,\end{aligned} \tag{4.35}$$

for the right stencil:

$$\begin{aligned}\zeta(\mathbf{C}u^{j-1}(x_n,y_k,1)) = |\mathbf{V}^{j-1}(x_n,y_k) - \mathbf{V}^{j-1}(x_n,y_{k+1})| + \\ |\mathbf{V}^{j-1}(x_n,y_{k+1}) - \mathbf{V}^{j-1}(x_n,y_{k+2})|.\end{aligned} \tag{4.36}$$

The predicted value is deduced so that the optimal value u is the solution of the following minimization problem:

$$u^* = \underset{-1\leq u\leq 1}{\arg\min}\, \zeta(\mathbf{C}u^{j-1}(x_n,y_k,u)). \tag{4.37}$$

The pixel value $\hat{\mathbf{I}}^j(x_n,y_{2k-1})$ is defined on the lower-half cell $[k,\ k+1/2]$ as follows:

$$\hat{\mathbf{I}}^j(x_n,y_{2k-1}) = 2\int_k^{k+1/2} p_{u^*}(x)dx. \tag{4.38}$$

Discussion: The pixel value $\mathbf{V}^{j-1}(x_n,y_k)$ is defined on the cell $[k,\ k+1]$,

$$\mathbf{V}^{j-1}(x_n,y_k) = \int_k^{k+1} p_{u^*}(x)dx, \tag{4.39}$$

while the predicted value $\hat{\mathbf{I}}^j(x_n,y_{2k})$ at the even index is defined on the remained upper-half cell $[k+1/2,\ k+1]$,

$$\hat{\mathbf{I}}^j(x_n,y_{2k}) = 2\int_{k+1/2}^{k+1} p_{u^*}(x)dx. \tag{4.40}$$

Note that due to the consistency condition, the prediction and projection operators satisfy:

$$\hat{\mathbf{I}}^j(x_n,y_{2k-1}) + \hat{\mathbf{I}}^j(x_n,y_{2k}) = 2\mathbf{V}^{j-1}(x_n,y_k). \tag{4.41}$$

The predicted value $\hat{\mathbf{I}}^j(x_n,y_{2k-1})$ is one of three possibilities as follows:

$$\begin{cases} 2\int_k^{k+1/2} p_{-1}(x)dx & \text{for the left stencil at } u=-1 \\ 2\int_k^{k+1/2} p_0(x)dx & \text{for the center stencil at } u=0 \\ 2\int_k^{k+1/2} p_1(x)dx & \text{for the right stencil at } u=1 \end{cases} \tag{4.42}$$

$$= \begin{cases} \sum \left[-\frac{1}{8} \quad +\frac{1}{2} \quad +\frac{5}{8}\right] \otimes \left[\mathbf{V}^{j-1}(x_n,y_{k-2}) \quad \mathbf{V}^{j-1}(x_n,y_{k-1}) \quad \mathbf{V}^{j-1}(x_n,y_k)\right] \\ \sum \left[+\frac{1}{8} \quad +1 \quad -\frac{1}{8}\right] \otimes \left[\mathbf{V}^{j-1}(x_n,y_{k-1}) \quad \mathbf{V}^{j-1}(x_n,y_k) \quad \mathbf{V}^{j-1}(x_n,y_{k+1})\right] \\ \sum \left[+\frac{11}{8} \quad -\frac{1}{2} \quad +\frac{1}{8}\right] \otimes \left[\mathbf{V}^{j-1}(x_n,y_k) \quad \mathbf{V}^{j-1}(x_n,y_{k+1}) \quad \mathbf{V}^{j-1}(x_n,y_{k+2})\right]. \end{cases} \tag{4.43}$$

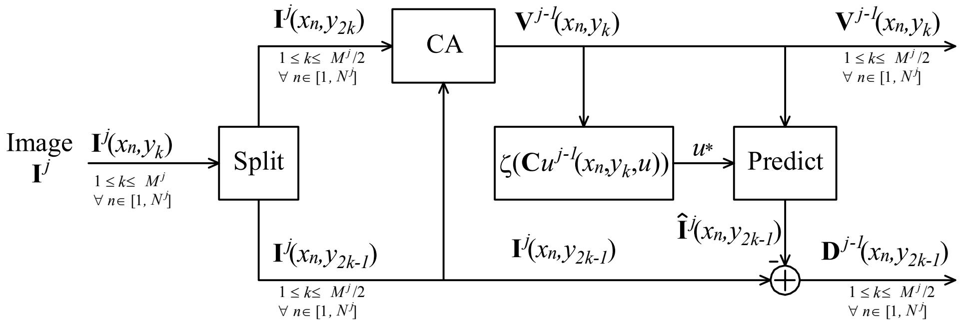

Figure 4.9: *1D-signal decomposition using separable multiresolution ENO CA in a horizontal direction.*

4.1.4 Arrangement of approximation and detail coefficients

The process is the same as in section 3.1.4. The processes are summarized in Figure 4.9 and Figure 4.10.

4.1.5 Repeat steps 1, 2 and 3

The process is the same as in section 3.1.5. The approximation resolution level $\mathbf{I}^j(x_n,y_m)$ is divided into four blocks: ll, lh, hl and hh.

$$\mathcal{M}\,\mathbf{I}^j \quad := \quad \left(\mathbf{I}^{j-1},\ \mathbf{D}^{j-1}_{lh},\ \mathbf{D}^{j-1}_{hl},\ \mathbf{D}^{j-1}_{hh}\right). \tag{4.44}$$

The decomposition process can be iterated on $\mathbf{I}^{j-1}$ until $\mathbf{I}^0$. The finest HDR logarithm luminance $\mathbf{I}^J$ is then represented by $3J+1$ resolution levels (or subbands) as follows:

$$\mathcal{M}\,\mathbf{I}^J \quad := \quad \left(\mathbf{I}^0,\mathbf{D}^0_{lh},\mathbf{D}^0_{hl},\mathbf{D}^0_{hh},...,\mathbf{D}^{j-1}_{lh},\mathbf{D}^{j-1}_{hl},\mathbf{D}^{j-1}_{hh},...,\mathbf{D}^{J-1}_{lh},\mathbf{D}^{J-1}_{hl},\mathbf{D}^{J-1}_{hh}\right). \tag{4.45}$$

4.2 Weightings

The process is the same as in section 3.2.

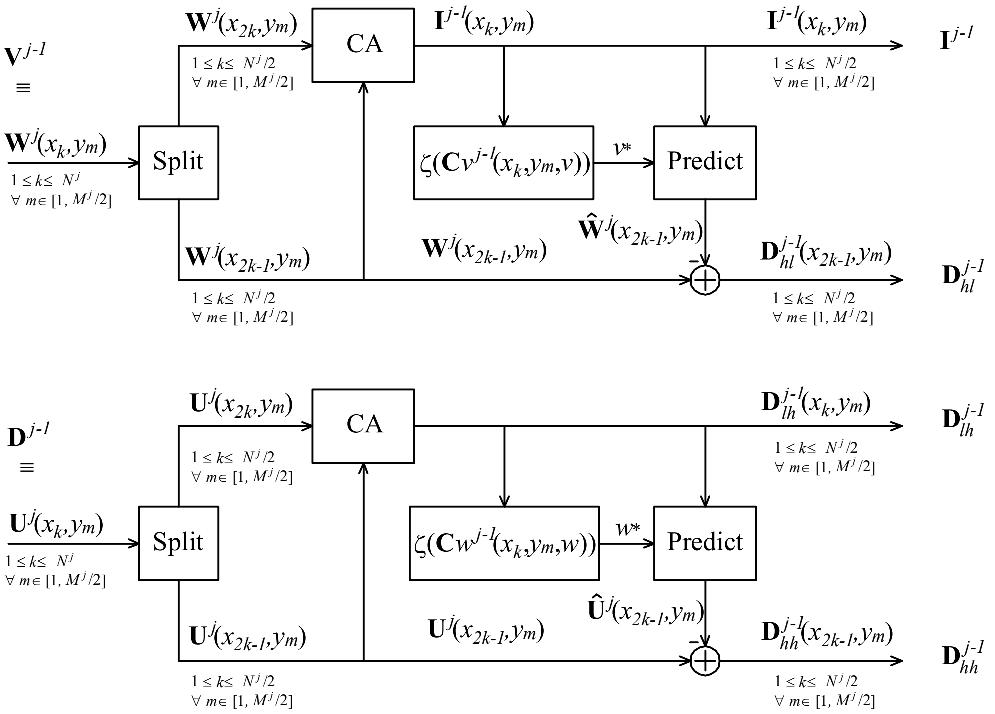

Figure 4.10: *1D-signal decomposition using separable multiresolution ENO CA in a vertical direction.*

4.3 Separable backward algorithm

In separable backward algorithm (see Figure 4.11 and Figure 4.12), the modified approximation coefficients $\mathbf{W}'^{j-1}(x_{2k-1}, y_m)$ are computed as follows:

$$\hat{\mathbf{W}}'^{j}(x_{2k-1}, y_m) = 2\int_k^{k+1/2} p_{v^*}(x)dx. \tag{4.46}$$

The predicted value $\hat{\mathbf{W}}'^{j}(x_{2k-1}, y_m)$ is one of three possibilities as follows:

$$\begin{cases} 2\int_k^{k+1/2} p_{-1}(x)dx & \text{for the left stencil at } v=-1 \\ 2\int_k^{k+1/2} p_{0}(x)dx & \text{for the center stencil at } v=0 \\ 2\int_k^{k+1/2} p_{1}(x)dx & \text{for the right stencil at } v=1 \end{cases} \tag{4.47}$$

$$= \begin{cases} \sum\left[-\frac{1}{8} \quad +\frac{1}{2} \quad +\frac{5}{8}\right] \otimes \left[\mathbf{I}'^{j-1}(x_{k-2}, y_m) \quad \mathbf{I}'^{j-1}(x_{k-1}, y_m) \quad \mathbf{I}'^{j-1}(x_{k}, y_m)\right] \\ \sum\left[+\frac{1}{8} \quad +1 \quad -\frac{1}{8}\right] \otimes \left[\mathbf{I}'^{j-1}(x_{k-1}, y_m) \quad \mathbf{I}'^{j-1}(x_{k}, y_m) \quad \mathbf{I}'^{j-1}(x_{k+1}, y_m)\right] \\ \sum\left[+\frac{11}{8} \quad -\frac{1}{2} \quad +\frac{1}{8}\right] \otimes \left[\mathbf{I}'^{j-1}(x_{k}, y_m) \quad \mathbf{I}'^{j-1}(x_{k+1}, y_m) \quad \mathbf{I}'^{j-1}(x_{k+2}, y_m)\right]. \end{cases} \tag{4.48}$$

Instead of using equation (4.24), the approximation coefficients $\mathbf{W}'^{j}(x_{2k}, y_m)$, at

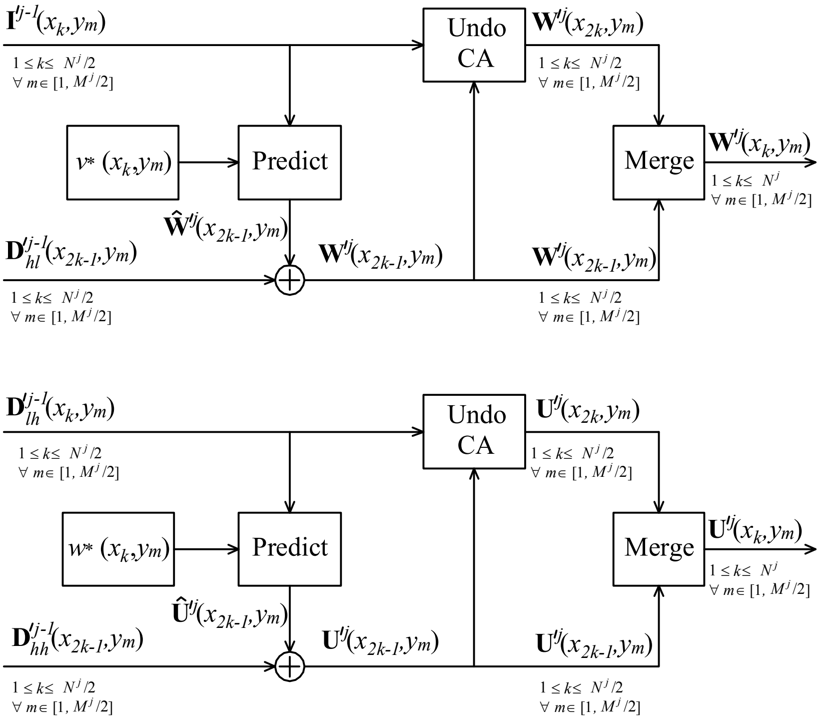

Figure 4.11: *1D-signal reconstruction using separable multiresolution ENO CA in a vertical direction.*

even positions, are deduced:

$$\mathbf{W}'^j(x_{2k}, y_m) = 2\mathbf{I}'^{j-1}(x_k, y_m) - \mathbf{W}'^j(x_{2k-1}, y_m) \text{ for } 1 \leq k \leq N^j/2. \tag{4.49}$$

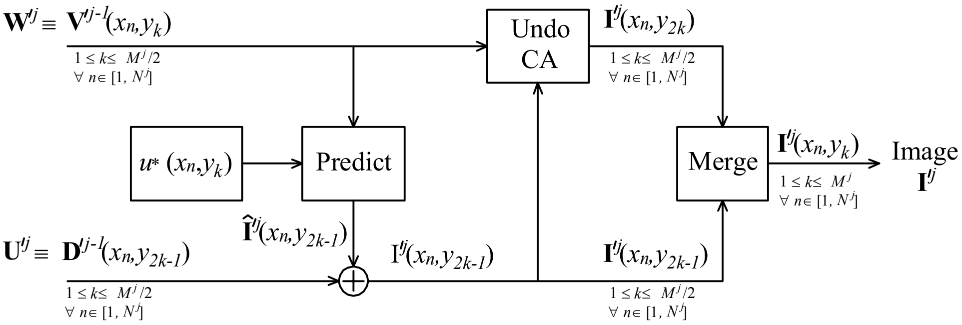

Figure 4.12: *1D-signal reconstruction using separable multiresolution ENO CA in a horizontal direction.*

Finally, we get the approximation coefficients $\mathbf{I}'^j$ at resolution level j.

$$\mathbf{I}'^j \quad := \quad \mathcal{M}^{-1}\left(\mathbf{I}'^{j-1}, \mathbf{D}'^{j-1}_{lh}, \mathbf{D}'^{j-1}_{hl}, \mathbf{D}'^{j-1}_{hh}\right). \tag{4.50}$$

The process is then iterated until $j=J$:

$$\mathbf{I}'^{J} \quad := \quad \mathcal{M}^{-1}\left(\mathbf{I}'^{0},\mathbf{D}'^{0}_{lh},\mathbf{D}'^{0}_{hl},\mathbf{D}'^{0}_{hh},...,\mathbf{D}'^{j-1}_{lh},\mathbf{D}'^{j-1}_{hl},\mathbf{D}'^{j-1}_{hh},...,\mathbf{D}'^{J-1}_{lh},\mathbf{D}'^{J-1}_{hl},\mathbf{D}'^{J-1}_{hh}\right). \tag{4.51}$$

Simulation results will be discussed in section 6.1.

5 TMO based on non-separable multiresolution ENO scheme

Considering the advantages of the prediction (left, right) polynomials, the separable multiresolution ENO scheme can extract details information from a 2D-signal in four directions (i.e. for the horizontal: 0°, 180°, and for the vertical: 90°, 270°). Besides the four directions, the non-separable multiresolution ENO scheme can extract details information from the 2D-signal in four diagonal directions such as 45°, 135°, 225° and 315° due to extension of more predict directions.

The proposed HDR image tone mapping operator is based on the non-separable decomposition developed in [55] and [56]. The prediction operator is related on the smoothness properties of the function $p(x,y)$, considered as a bi-dimensional smooth function and represented by a piecewise polynomial function of degree two, modeling the complex HDR image (i.e. smooth regions separated by edges). To adapt the prediction near the singularities, ENO interpolation techniques are then deployed. There are three main stages: (forward) decomposition, weighting and (backward) reconstruction. Unlike the separable case, the non-separable decomposition and reconstruction don't use intermediate steps (see Figure 4.13), and the weighting stage applies for an adaptive way (without constant). Three stages are described as follows.

5.1 Non-separable forward algorithm

The decomposition process consists to go from the finest resolution level J to the coarsest resolution level 0. The forward process steps of the separable decomposition algorithm are described below (see Figure 4.14).

5.1.1 Split 2D-signal into four indexes

Assume a 2D-signal of size $[N^j \times M^j]$ at a given resolution level j, and the lengths N^j, M^j divided by 2. The algorithm starts with splitting 2D-signal into a set of $\mathbf{I}^j(x_{2n-1},y_{2m-1})$, $\mathbf{I}^j(x_{2n-1},y_{2m})$, $\mathbf{I}^j(x_{2n},y_{2m-1})$ and $\mathbf{I}^j(x_{2n},y_{2m})$ pixel values as follows:

$$\{\mathbf{I}^j(x_n,y_m) \text{ with } 1 \le n \le N^j \text{ and } 1 \le m \le M^j\} \tag{4.52}$$

$$:= \left\{ \begin{bmatrix} \mathbf{I}^j(x_{2n-1},y_{2m-1}) & \mathbf{I}^j(x_{2n-1},y_{2m}) \\ \mathbf{I}^j(x_{2n},y_{2m-1}) & \mathbf{I}^j(x_{2n},y_{2m}) \end{bmatrix} \right\} \tag{4.53}$$

$$:= \{\mathbf{I}^j(x_{2n-1},y_{2m-1}),\ \mathbf{I}^j(x_{2n-1},y_{2m}),\ \mathbf{I}^j(x_{2n},y_{2m-1}),\ \mathbf{I}^j(x_{2n},y_{2m}), \tag{4.54}$$

$$\text{with} \quad 1 \le n \le N^j/2 \quad \text{and} \quad 1 \le m \le M^j/2 \ \}.$$

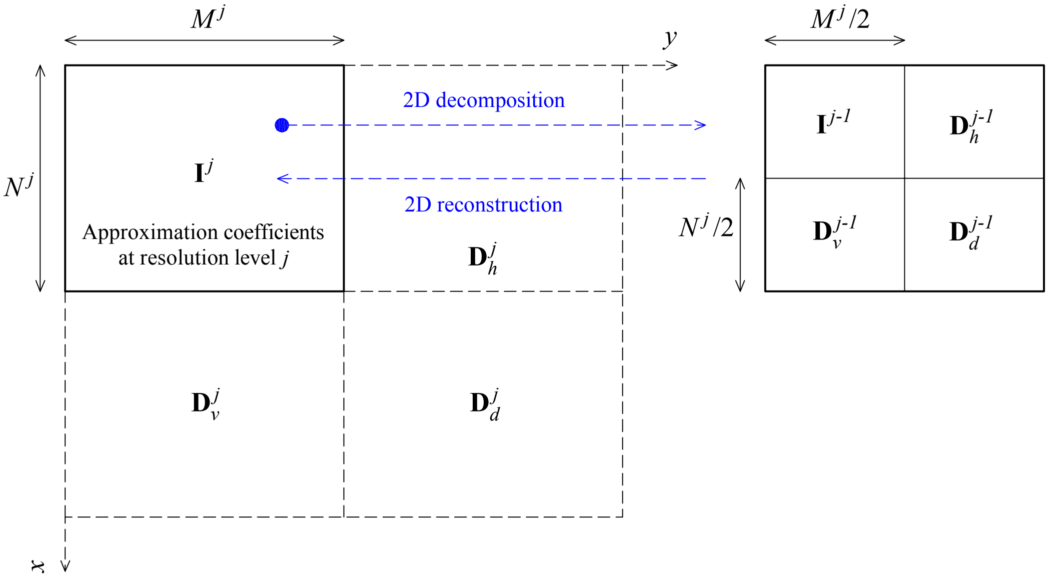

Figure 4.13: *Non-separable lifting scheme decomposition and reconstruction principle.*

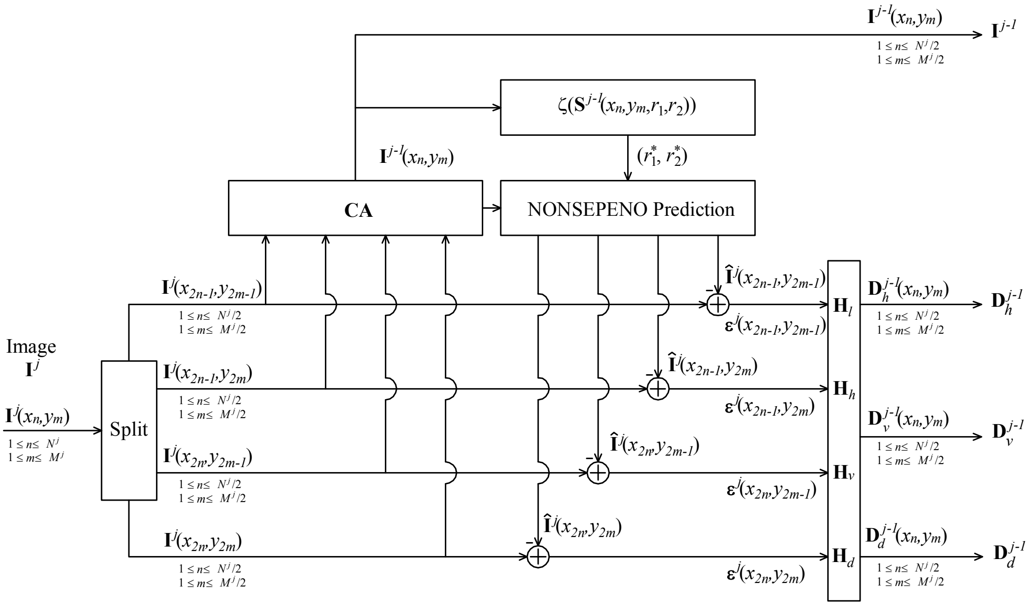

Figure 4.14: *Non-separable multiresolution ENO decomposition.*

5.1.2 Approximation resolution level in a 2D cell-average scheme

Based on this split, the approximation coefficient located at position (x_n, y_m), denoted $\mathbf{I}^{j-1}(x_n, y_m)$ for a given n and m, is computed on a CA scheme as follows:

$$\begin{gathered}\mathbf{I}^{j-1}(x_n, y_m) = \frac{1}{4}\sum\sum\begin{bmatrix}\mathbf{I}^j(x_{2n-1}, y_{2m-1}) & \mathbf{I}^j(x_{2n-1}, y_{2m}) \\ \mathbf{I}^j(x_{2n}, y_{2m-1}) & \mathbf{I}^j(x_{2n}, y_{2m})\end{bmatrix} \\ = \frac{1}{4}\Big(\mathbf{I}^j(x_{2n-1}, y_{2m-1}) + \mathbf{I}^j(x_{2n-1}, y_{2m}) + \mathbf{I}^j(x_{2n}, y_{2m-1}) + \mathbf{I}^j(x_{2n}, y_{2m})\Big), \\ \text{with } \ 1 \le n \le N^j/2 \ \text{ and } \ 1 \le m \le M^j/2,\end{gathered} \tag{4.55}$$

where $\sum\sum$ indicates sum of all elements in matrix.

The pixel value $\mathbf{I}^{j-1}(x_n, y_m)$ is defined by the Cell-Average of the underlying bidimensional function $p(x,y)$ modeling the image, as follows:

$$\mathbf{I}^{j-1}(x_n, y_m) = \int_{\mathbf{C}^{j-1}_{(n,m)}} p(x,y)dxdy = \int_n^{n+1}\int_m^{m+1} p(x,y)dxdy, \tag{4.56}$$

where the 2D cell $\mathbf{C}^{j-1}_{(n,m)}$ is defined as $[n, n+1] \times [m, m+1]$.

5.1.3 Detail resolution level based on 2D cell-average ENO prediction

The error coefficients, denoted $\varepsilon^j(x_{2n-1},\ y_{2m-1})$, $\varepsilon^j(x_{2n-1}, y_{2m})$, $\varepsilon^j(x_{2n}, y_{2m-1})$ and $\varepsilon^j(x_{2n}, y_{2m})$, are then computed as follows:

$$\begin{gathered}\begin{bmatrix}\varepsilon^j(x_{2n-1}, y_{2m-1}) & \varepsilon^j(x_{2n-1}, y_{2m}) \\ \varepsilon^j(x_{2n}, y_{2m-1}) & \varepsilon^j(x_{2n}, y_{2m})\end{bmatrix} = \\ = \begin{bmatrix}\mathbf{I}^j(x_{2n-1}, y_{2m-1}) & \mathbf{I}^j(x_{2n-1}, y_{2m}) \\ \mathbf{I}^j(x_{2n}, y_{2m-1}) & \mathbf{I}^j(x_{2n}, y_{2m})\end{bmatrix} - \begin{bmatrix}\hat{\mathbf{I}}^j(x_{2n-1}, y_{2m-1}) & \hat{\mathbf{I}}^j(x_{2n-1}, y_{2m}) \\ \hat{\mathbf{I}}^j(x_{2n}, y_{2m-1}) & \hat{\mathbf{I}}^j(x_{2n}, y_{2m})\end{bmatrix},\end{gathered} \tag{4.57}$$

or

$$\begin{cases}\varepsilon^j(x_{2n-1}, y_{2m-1}) = \mathbf{I}^j(x_{2n-1}, y_{2m-1}) - \hat{\mathbf{I}}^j(x_{2n-1}, y_{2m-1}) \\ \varepsilon^j(x_{2n-1}, y_{2m}) = \mathbf{I}^j(x_{2n-1}, y_{2m}) - \hat{\mathbf{I}}^j(x_{2n-1}, y_{2m}) \\ \varepsilon^j(x_{2n}, y_{2m-1}) = \mathbf{I}^j(x_{2n}, y_{2m-1}) - \hat{\mathbf{I}}^j(x_{2n}, y_{2m-1}) \\ \varepsilon^j(x_{2n}, y_{2m}) = \mathbf{I}^j(x_{2n}, y_{2m}) - \hat{\mathbf{I}}^j(x_{2n}, y_{2m}).\end{cases} \tag{4.58}$$

These predicted values $\hat{\mathbf{I}}^j(x_{2n-1}, y_{2m-1})$, $\hat{\mathbf{I}}^j(x_{2n-1}, y_{2m})$, $\hat{\mathbf{I}}^j(x_{2n}, y_{2m-1})$ and $\hat{\mathbf{I}}^j(x_{2n}, y_{2m})$ are approximated by using those approximation coefficients from prediction stencil of size (equal to 3×3 cells) defined on cells as:

$$\mathbf{S}^{j-1}(x_n, y_m, r_1, r_2) = \begin{bmatrix}\mathbf{C}^{j-1}_{(n+r_1-1,m+r_2-1)} & \mathbf{C}^{j-1}_{(n+r_1-1,m+r_2)} & \mathbf{C}^{j-1}_{(n+r_1-1,m+r_2+1)} \\ \mathbf{C}^{j-1}_{(n+r_1,m+r_2-1)} & \mathbf{C}^{j-1}_{(n+r_1,m+r_2)} & \mathbf{C}^{j-1}_{(n+r_1,m+r_2+1)} \\ \mathbf{C}^{j-1}_{(n+r_1+1,m+r_2-1)} & \mathbf{C}^{j-1}_{(n+r_1+1,m+r_2)} & \mathbf{C}^{j-1}_{(n+r_1+1,m+r_2+1)}\end{bmatrix}, \tag{4.59}$$

where r_1, r_2 is an integer in $[-1, 0, 1]$, corresponding to the position of the stencil with respect to (n, m). There are then nine kinds of stencil positions: down-left (DL) with $(r_1, r_2) = (-1, -1)$, down-center (DC) with $(r_1, r_2) = (-1, 0)$, down-right (DR) with $(r_1, r_2) = (-1, 1)$, center-left (CL) with $(r_1, r_2) = (0, -1)$, center-center (CC) with $(r_1, r_2) = (0, 0)$, center-right (CR) with $(r_1, r_2) = (0, 1)$, upper-left (UL) with $(r_1, r_2) = (1, -1)$, upper-center (UC) with $(r_1, r_2) = (1, 0)$ and upper-right (UR) with $(r_1, r_2) = (1, 1)$.

A bi-quadratic Lagrange polynomial $p_{(r_1,r_2)}(x, y)$ is defined to interpolate nine values of approximation coefficients $\mathbf{I}^{j-1}$ on the stencil $\mathbf{S}^{j-1}(x_n, y_m, r_1, r_2)$. Therefore there are nine polynomials ($p_{(-1,-1)}(x, y)$, $p_{(-1,0)}(x, y)$, $p_{(-1,1)}(x, y)$, $p_{(0,-1)}(x, y)$, $p_{(0,0)}(x, y)$, $p_{(0,1)}(x, y)$, $p_{(1,-1)}(x, y)$, $p_{(1,0)}(x, y)$ and $p_{(1,1)}(x, y)$) attached to nine corresponding stencils. The nine unknown coefficients are deduced from the nine interpolation conditions on the stencil, see in Appendix B.

In order to measure the degree of oscillations of such polynomials, the following functions are used:

$$\zeta(\mathbf{S}^{j-1}(x_n, y_m, r_1, r_2)) = \sum_{\mathbf{S}^{j-1}(x_n, y_m, r_1, r_2)}\sum |\Delta \mathbf{I}_x^{j-1}| + |\Delta \mathbf{I}_y^{j-1}|, \tag{4.60}$$

where $\Delta \mathbf{I}_x^{j-1}$ and $\Delta \mathbf{I}_y^{j-1}$ indicate differences of pixels on vertical and horizontal directions, respectively.

The predicted value is deduced so that the optimal values (r_1, r_2) are the solution of the following minimization problem:

$$(r_1^*, r_2^*) = \underset{-1 \le r_1, r_2 \le 1}{\arg\min}\ \zeta(\mathbf{S}^{j-1}(x_n, y_m, r_1, r_2)). \tag{4.61}$$

This is expressed as the ENO interpolations as choosing the best stencil. The predicted values are interpolated on the approximation resolution level $\mathbf{I}^{j-1}(x_n, y_m)$, and defined in one-fourths (i.e. $[n, n+1/2] \times [m, m+1/2]$, $[n, n+1/2] \times [m+1/2, m+1]$, $[n+1/2, n+1] \times [m, m+1/2]$ and $[n+1/2, n+1] \times [m+1/2, m+1]$) of the 2D cell as follows:

$$\begin{bmatrix} \hat{\mathbf{I}}^j(x_{2n-1}, y_{2m-1}) & \hat{\mathbf{I}}^j(x_{2n-1}, y_{2m}) \\ \hat{\mathbf{I}}^j(x_{2n}, y_{2m-1}) & \hat{\mathbf{I}}^j(x_{2n}, y_{2m}) \end{bmatrix} =$$

$$4 \begin{bmatrix} \int_n^{n+1/2} \int_m^{m+1/2} p_{(r_1^*, r_2^*)}(x, y)dxdy & \int_n^{n+1/2} \int_{m+1/2}^{m+1} p_{(r_1^*, r_2^*)}(x, y)dxdy \\ \int_{n+1/2}^{n+1} \int_m^{m+1/2} p_{(r_1^*, r_2^*)}(x, y)dxdy & \int_{n+1/2}^{n+1} \int_m^{m+1} p_{(r_1^*, r_2^*)}(x, y)dxdy \end{bmatrix}. \tag{4.62}$$

For example, if the pair of $(r_1^*, r_2^*) = (0, 0)$ as the center-center case, the four predicted values are deduced as follows:

$$\begin{bmatrix} \hat{\mathbf{I}}^j(x_{2n-1}, y_{2m-1}) & \hat{\mathbf{I}}^j(x_{2n-1}, y_{2m}) \\ \hat{\mathbf{I}}^j(x_{2n}, y_{2m-1}) & \hat{\mathbf{I}}^j(x_{2n}, y_{2m}) \end{bmatrix} = \tag{4.63}$$

$$= 4 \begin{bmatrix} \sum\sum \begin{bmatrix} +\frac{1}{256} & +\frac{1}{32} & -\frac{1}{256} \\ +\frac{1}{32} & +\frac{1}{4} & -\frac{1}{32} \\ -\frac{1}{256} & -\frac{1}{32} & +\frac{1}{256} \end{bmatrix} \otimes \mathbf{I}_{CC}^{j-1} & \sum\sum \begin{bmatrix} -\frac{1}{256} & +\frac{1}{32} & +\frac{1}{256} \\ -\frac{1}{32} & +\frac{1}{4} & +\frac{1}{32} \\ +\frac{1}{256} & -\frac{1}{32} & -\frac{1}{256} \end{bmatrix} \otimes \mathbf{I}_{CC}^{j-1} \\ \sum\sum \begin{bmatrix} -\frac{1}{256} & -\frac{1}{32} & +\frac{1}{256} \\ +\frac{1}{32} & +\frac{1}{4} & -\frac{1}{32} \\ +\frac{1}{256} & +\frac{1}{32} & -\frac{1}{256} \end{bmatrix} \otimes \mathbf{I}_{CC}^{j-1} & \sum\sum \begin{bmatrix} +\frac{1}{256} & -\frac{1}{32} & -\frac{1}{256} \\ -\frac{1}{32} & +\frac{1}{4} & +\frac{1}{32} \\ -\frac{1}{256} & +\frac{1}{32} & +\frac{1}{256} \end{bmatrix} \otimes \mathbf{I}_{CC}^{j-1} \end{bmatrix} \tag{4.64}$$

where

$$\mathbf{I}_{CC}^{j-1} = \begin{bmatrix} \mathbf{I}^{j-1}(x_{n-1}, y_{m-1}) & \mathbf{I}^{j-1}(x_{n-1}, y_{m}) & \mathbf{I}^{j-1}(x_{n-1}, y_{m+1}) \\ \mathbf{I}^{j-1}(x_{n}, y_{m-1}) & \mathbf{I}^{j-1}(x_{n}, y_{m}) & \mathbf{I}^{j-1}(x_{n}, y_{m+1}) \\ \mathbf{I}^{j-1}(x_{n+1}, y_{m-1}) & \mathbf{I}^{j-1}(x_{n+1}, y_{m}) & \mathbf{I}^{j-1}(x_{n+1}, y_{m+1}) \end{bmatrix}, \tag{4.65}$$

and $\otimes$ is the product term by term.

Discussion: Due to the consistency condition, the prediction and projection operators satisfy:

$$\sum\sum \begin{bmatrix} \hat{\mathbf{I}}^{j}(x_{2n-1}, y_{2m-1}) & \hat{\mathbf{I}}^{j}(x_{2n-1}, y_{2m}) \\ \hat{\mathbf{I}}^{j}(x_{2n}, y_{2m-1}) & \hat{\mathbf{I}}^{j}(x_{2n}, y_{2m}) \end{bmatrix} = 4\mathbf{I}^{j-1}(x_n, y_m). \tag{4.66}$$

Four predicted values are one of nine possibilities as shown in Appendix B. All the best stencils $\mathbf{S}^{j-1}(x_n, y_m, r_1^*, r_2^*)$ are stored to be used in the lifting scheme backward process to reconstruct the decomposed 2D-signal. These errors can be written in a non-redundant way with a base matrix of change $\mathbf{H}$. The matrix of this change $\mathbf{H}$ has

$$\mathbf{H}_l = \frac{1}{4}\begin{bmatrix} +1 & +1 \\ +1 & +1 \end{bmatrix}, \quad \mathbf{H}_h = \frac{1}{4}\begin{bmatrix} +1 & +1 \\ -1 & -1 \end{bmatrix}, \tag{4.67}$$

$$\mathbf{H}_v = \frac{1}{4}\begin{bmatrix} +1 & -1 \\ +1 & -1 \end{bmatrix}, \quad \mathbf{H}_d = \frac{1}{4}\begin{bmatrix} +1 & -1 \\ -1 & +1 \end{bmatrix}. \tag{4.68}$$

Therefore the detail subbands are deduced from

$$\begin{bmatrix} \varepsilon^{j}(x_{2n-1}, y_{2m-1}) & \varepsilon^{j}(x_{2n-1}, y_{2m}) \\ \varepsilon^{j}(x_{2n}, y_{2m-1}) & \varepsilon^{j}(x_{2n}, y_{2m}) \end{bmatrix} \tag{4.69}$$

as follows: for the horizontal detail subband:

$$\mathbf{D}_h^{j-1}(x_n, y_m) = \sum\sum \mathbf{H}_h \otimes \begin{bmatrix} \varepsilon^{j}(x_{2n-1}, y_{2m-1}) & \varepsilon^{j}(x_{2n-1}, y_{2m}) \\ \varepsilon^{j}(x_{2n}, y_{2m-1}) & \varepsilon^{j}(x_{2n}, y_{2m}) \end{bmatrix} \tag{4.70}$$

$$= \sum\sum \frac{1}{4}\begin{bmatrix} +1 & +1 \\ -1 & -1 \end{bmatrix} \otimes \begin{bmatrix} \varepsilon^{j}(x_{2n-1}, y_{2m-1}) & \varepsilon^{j}(x_{2n-1}, y_{2m}) \\ \varepsilon^{j}(x_{2n}, y_{2m-1}) & \varepsilon^{j}(x_{2n}, y_{2m}) \end{bmatrix} \tag{4.71}$$

for the vertical detail subband:

$$\mathbf{D}_v^{j-1}(x_n,y_m) = \sum\sum \mathbf{H}_v \otimes \begin{bmatrix} \varepsilon^j(x_{2n-1},y_{2m-1}) & \varepsilon^j(x_{2n-1},y_{2m}) \\ \varepsilon^j(x_{2n},y_{2m-1}) & \varepsilon^j(x_{2n},y_{2m}) \end{bmatrix} \tag{4.72}$$

$$= \sum\sum \frac{1}{4}\begin{bmatrix} +1 & -1 \\ +1 & -1 \end{bmatrix} \otimes \begin{bmatrix} \varepsilon^j(x_{2n-1},y_{2m-1}) & \varepsilon^j(x_{2n-1},y_{2m}) \\ \varepsilon^j(x_{2n},y_{2m-1}) & \varepsilon^j(x_{2n},y_{2m}) \end{bmatrix} \tag{4.73}$$

for the diagonal detail subband:

$$\mathbf{D}_d^{j-1}(x_n,y_m) = \sum\sum \mathbf{H}_d \otimes \begin{bmatrix} \varepsilon^j(x_{2n-1},y_{2m-1}) & \varepsilon^j(x_{2n-1},y_{2m}) \\ \varepsilon^j(x_{2n},y_{2m-1}) & \varepsilon^j(x_{2n},y_{2m}) \end{bmatrix} \tag{4.74}$$

$$= \sum\sum \frac{1}{4}\begin{bmatrix} +1 & -1 \\ -1 & +1 \end{bmatrix} \otimes \begin{bmatrix} \varepsilon^j(x_{2n-1},y_{2m-1}) & \varepsilon^j(x_{2n-1},y_{2m}) \\ \varepsilon^j(x_{2n},y_{2m-1}) & \varepsilon^j(x_{2n},y_{2m}) \end{bmatrix}. \tag{4.75}$$

However, due to the consistent condition, we get

$$\sum\sum \mathbf{H}_l \otimes \begin{bmatrix} \varepsilon^j(x_{2n-1},y_{2m-1}) & \varepsilon^j(x_{2n-1},y_{2m}) \\ \varepsilon^j(x_{2n},y_{2m-1}) & \varepsilon^j(x_{2n},y_{2m}) \end{bmatrix} \tag{4.76}$$

$$= \sum\sum \frac{1}{4}\begin{bmatrix} +1 & +1 \\ +1 & +1 \end{bmatrix} \otimes \begin{bmatrix} \varepsilon^j(x_{2n-1},y_{2m-1}) & \varepsilon^j(x_{2n-1},y_{2m}) \\ \varepsilon^j(x_{2n},y_{2m-1}) & \varepsilon^j(x_{2n},y_{2m}) \end{bmatrix} = 0. \tag{4.77}$$

Finally, the approximation resolution level $\mathbf{I}^j(x_n,y_m)$ is divided into four subbands: l, h, v and d. The subband l concerns the approximation resolution denoted $\mathbf{I}^{j-1}$; and the other three subbands h, v and d contain the detail resolutions, named $\mathbf{D}_h^{j-1}, \mathbf{D}_v^{j-1}, \mathbf{D}_d^{j-1}$, respectively (see Figure 4.13). Note that the size of each subband is deduced as the half size of $\mathbf{I}^j$ in each direction:

$$\mathcal{M}\,\mathbf{I}^j \quad := \quad \left(\mathbf{I}^{j-1}, \mathbf{D}_h^{j-1}, \mathbf{D}_v^{j-1}, \mathbf{D}_d^{j-1}\right). \tag{4.78}$$

The decomposition process can be iterated on $\mathbf{I}^{j-1}$ until $\mathbf{I}^0$. The finest HDR logarithm luminance $\mathbf{I}^J$ is then represented by $3J+1$ resolution levels or subbands as follows:

$$\mathcal{M}\,\mathbf{I}^J \quad := \quad \left(\mathbf{I}^0, \mathbf{D}_h^0, \mathbf{D}_v^0, \mathbf{D}_d^0, \ldots, \mathbf{D}_h^{j-1}, \mathbf{D}_v^{j-1}, \mathbf{D}_d^{j-1}, \ldots, \mathbf{D}_h^{J-1}, \mathbf{D}_v^{J-1}, \mathbf{D}_d^{J-1}\right). \tag{4.79}$$

5.2 Adaptive weightings

This section proposes to individually weight each subband's coefficient in order to reduce in an appropriate manner the HDR image dynamic range. For this, the proposed weight is a positive value between 0 and 1 depending on the statistical properties of each subband and the neighborhood. The main operations are described in the following (see Figure 4.15).

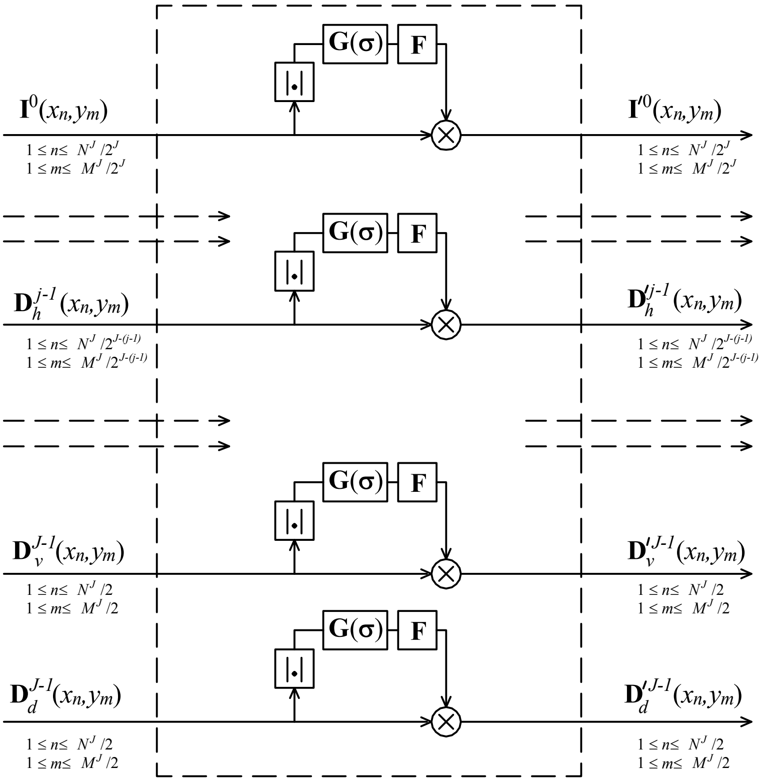

Figure 4.15: *Adaptive weightings.*

First, the absolute value of the subband coefficients is taken: $\mathbf{A}_l^0 = |\mathbf{I}^0|$, $\mathbf{A}_h^{j-1} = |\mathbf{D}_h^{j-1}|$, $\mathbf{A}_v^{j-1} = |\mathbf{D}_v^{j-1}|$, $\mathbf{A}_d^{j-1} = |\mathbf{D}_d^{j-1}|$ for $j = 1,...,J$. Denote $\mathbf{A}_{sb}^{j-1}(x,y)$, with $sb = l,h,v,d$ and $j = 1,...,J$, the positive coefficient at position (x,y) in the subband sb at resolution level $j-1$. We associate to this coefficient its weighted average in the domain corresponding to the subband sb:

$$\mathbf{a}_{sb}^{j-1}(x,y) = \mathbf{A}_{sb}^{j-1}(x,y) * \mathbf{G}(x,y), \tag{4.80}$$

where $*$ is the convolutional product; and $\mathbf{G}(x,y)$ is a Gaussian filter given by:

$$\mathbf{G}(x,y) = \frac{1}{2\pi\sigma_{sb}^2} e^{-\frac{x^2+y^2}{2\sigma_{sb}^2}}, \tag{4.81}$$

where σ_{sb} is the standard deviation of the Gaussian distribution of the subband sb deduced from the median component in [56]:

$$\sigma_{sb} = \frac{\text{median}(\mathbf{A}_{sb}^{j-1})}{0.6745}. \tag{4.82}$$

After this, a monotonic nonlinear decreasing function $\mathbf{F}$ (as in [26]) is applied on the coefficients $\mathbf{a}_{sb}^{j-1}$, resulting in the positive weighting coefficient $\mathbf{q}_{sb}^{j-1}(x,y)$ between 0 and 1, as follows:

$$\mathbf{q}_{sb}^{j-1}(x,y) = \mathbf{F}(\mathbf{a}_{sb}^{j-1}(x,y)) = \frac{1}{(\frac{\mathbf{a}_{sb}^{j-1}(x,y)+\varepsilon}{\delta_{j-1}})^{1-\gamma}}, \tag{4.83}$$

where $\gamma \in [0,1]$ is the compressive factor; $j-1$ the resolution level (i.e. $j = 1,...,J$) associated to the subband sb. ε is used to avoid singularities when the power $1-\gamma$ is a positive value. δ_{j-1} is considered as a gain control stability level depending on the resolution level $j-1$, and the intensity of subband:

$$\delta_{j-1} = [1 - \frac{(j-1)(1-\xi)}{J}] \times \bar{\mathbf{A}}_{sb}^{j-1}, \tag{4.84}$$

where $\bar{\mathbf{A}}_{sb}^{j-1}$ is the average of $\mathbf{A}_{sb}^{j-1}$. The subband coefficients are then weighted as follows:

$$\mathbf{I}'^{0} = \mathbf{q}_l^0 \otimes \mathbf{I}^0 \quad \text{and} \quad \mathbf{D}'^{j-1}_{sb} = \mathbf{q}_{sb}^{j-1} \otimes \mathbf{D}_{sb}^{j-1}, \tag{4.85}$$

with $sb = h,v,d$; $j = 1,...,J$; and $\otimes$ is the product term by term. The modified subbands (or multiresolution levels) can be rewritten as follows:

$$\left(\mathbf{I}'^{0}, \mathbf{D}'^{0}_h, \mathbf{D}'^{0}_v, \mathbf{D}'^{0}_d, ..., \mathbf{D}'^{j-1}_h, \mathbf{D}'^{j-1}_v, \mathbf{D}'^{j-1}_d, ..., \mathbf{D}'^{J-1}_h, \mathbf{D}'^{J-1}_v, \mathbf{D}'^{J-1}_d\right). \tag{4.86}$$

5.3 Non-separable backward algorithm

The non-separable backward algorithm performs the inverse procedures of the non-separable forward steps as described below (see Figure 4.16).

5.3.1 Modified errors in 2D cell-average scheme

In the backward process, the matrix of this change of basis $\tilde{\mathbf{H}}$ has the following forms:

$$\tilde{\mathbf{H}}_l = \begin{bmatrix} +1 & +1 \\ +1 & +1 \end{bmatrix}, \quad \tilde{\mathbf{H}}_h = \begin{bmatrix} +1 & +1 \\ -1 & -1 \end{bmatrix}, \tag{4.87}$$

$$\tilde{\mathbf{H}}_v = \begin{bmatrix} +1 & -1 \\ +1 & -1 \end{bmatrix}, \quad \tilde{\mathbf{H}}_d = \begin{bmatrix} +1 & -1 \\ -1 & +1 \end{bmatrix}. \tag{4.88}$$

Like the separable backward algorithm, the non-separable backward process starts with the four coarsest resolution levels, i.e ($\mathbf{I}'^{0}$, $\mathbf{D}'^{0}_h$, $\mathbf{D}'^{0}_v$, $\mathbf{D}'^{0}_d$), to generate the approximation coefficients $\mathbf{I}'^{1}$. The same process is then iterated until reaching the finest resolution i.e. $j = J$ corresponding to the intermediate HDR image, denoted $\mathbf{I}'^{J}$, of size $N^J \times M^J$.

Assume first that the algorithm processed all resolution levels until $j-1$. Therefore the next step consists to recover the approximation image $\mathbf{I}'^{j}$ of size $N^j \times M^j$ using the following blocks: $\mathbf{I}'^{j-1}$, $\mathbf{D}'^{j-1}_h$, $\mathbf{D}'^{j-1}_v$ and $\mathbf{D}'^{j-1}_d$.

Based on three subbands $\mathbf{D}'^{j-1}_h$, $\mathbf{D}'^{j-1}_v$ and $\mathbf{D}'^{j-1}_d$, the modified errors are organized and computed as follows:

$$\begin{bmatrix} \varepsilon'^{j}(x_{2n-1}, y_{2m-1}) & \varepsilon'^{j}(x_{2n-1}, y_{2m}) \\ \varepsilon'^{j}(x_{2n}, y_{2m-1}) & \varepsilon'^{j}(x_{2n}, y_{2m}) \end{bmatrix}, \tag{4.89}$$

where

$$\varepsilon'^{j}(x_{2n-1},y_{2m-1}) = \sum\sum \tilde{\mathbf{H}}_l \otimes \begin{bmatrix} 0 & \mathbf{D}'^{j-1}_h(x_n,y_m) \\ \mathbf{D}'^{j-1}_v(x_n,y_m) & \mathbf{D}'^{j-1}_d(x_n,y_m) \end{bmatrix} \tag{4.90}$$

$$= \sum\sum \begin{bmatrix} +1 & +1 \\ +1 & +1 \end{bmatrix} \otimes \begin{bmatrix} 0 & \mathbf{D}'^{j-1}_h(x_n,y_m) \\ \mathbf{D}'^{j-1}_v(x_n,y_m) & \mathbf{D}'^{j-1}_d(x_n,y_m) \end{bmatrix} \tag{4.91}$$

$$\varepsilon'^{j}(x_{2n-1},y_{2m}) = \sum\sum \tilde{\mathbf{H}}_h \otimes \begin{bmatrix} 0 & \mathbf{D}'^{j-1}_h(x_n,y_m) \\ \mathbf{D}'^{j-1}_v(x_n,y_m) & \mathbf{D}'^{j-1}_d(x_n,y_m) \end{bmatrix} \tag{4.92}$$

$$= \sum\sum \begin{bmatrix} +1 & +1 \\ -1 & -1 \end{bmatrix} \otimes \begin{bmatrix} 0 & \mathbf{D}'^{j-1}_h(x_n,y_m) \\ \mathbf{D}'^{j-1}_v(x_n,y_m) & \mathbf{D}'^{j-1}_d(x_n,y_m) \end{bmatrix} \tag{4.93}$$

$$\varepsilon'^{j}(x_{2n},y_{2m-1}) = \sum\sum \tilde{\mathbf{H}}_v \otimes \begin{bmatrix} \mathbf{I}'^{j-1}(x_n,y_m) & \mathbf{D}'^{j-1}_h(x_n,y_m) \\ \mathbf{D}'^{j-1}_v(x_n,y_m) & \mathbf{D}'^{j-1}_d(x_n,y_m) \end{bmatrix} \tag{4.94}$$

$$= \sum\sum \begin{bmatrix} +1 & -1 \\ +1 & -1 \end{bmatrix} \otimes \begin{bmatrix} 0 & \mathbf{D}'^{j-1}_h(x_n,y_m) \\ \mathbf{D}'^{j-1}_v(x_n,y_m) & \mathbf{D}'^{j-1}_d(x_n,y_m) \end{bmatrix} \tag{4.95}$$

$$\varepsilon'^{j}(x_{2n},y_{2m}) = \sum\sum \tilde{\mathbf{H}}_d \otimes \begin{bmatrix} 0 & \mathbf{D}'^{j-1}_h(x_n,y_m) \\ \mathbf{D}'^{j-1}_v(x_n,y_m) & \mathbf{D}'^{j-1}_d(x_n,y_m) \end{bmatrix} \tag{4.96}$$

$$= \sum\sum \begin{bmatrix} +1 & -1 \\ -1 & +1 \end{bmatrix} \otimes \begin{bmatrix} 0 & \mathbf{D}'^{j-1}_h(x_n,y_m) \\ \mathbf{D}'^{j-1}_v(x_n,y_m) & \mathbf{D}'^{j-1}_d(x_n,y_m) \end{bmatrix}. \tag{4.97}$$

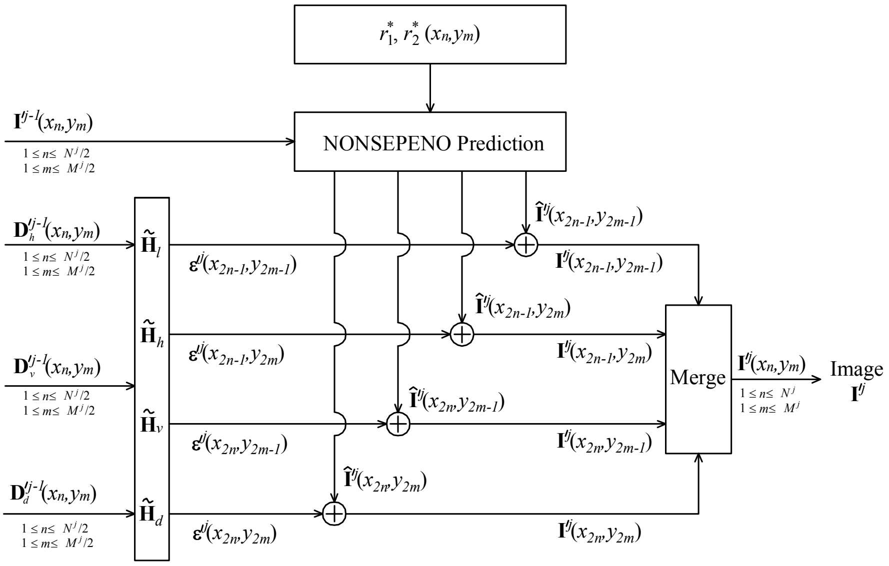

Figure 4.16: *Non-separable ENO reconstruction.*

5.3.2 Modified predicted values in 2D cell-average scheme

Since the best stencils $\mathbf{S}^{j-1}(x_n, y_m, r_1^*, r_2^*)$ are stored, the modified predicted values are interpolated on the modified approximation resolution level $\mathbf{I}'^{j-1}(x_n, y_m)$, and defined in one-fourths (i.e. $[n, n+1/2] \times [m, m+1/2]$, $[n, n+1/2] \times [m+1/2, m+1]$, $[n+1/2, n+1] \times [m, m+1/2]$ and $[n+1/2, n+1] \times [m+1/2, m+1]$) of the 2D cell as follows:

$$\begin{bmatrix} \hat{\mathbf{I}}'^{j}(x_{2n-1}, y_{2m-1}) & \hat{\mathbf{I}}'^{j}(x_{2n-1}, y_{2m}) \\ \hat{\mathbf{I}}'^{j}(x_{2n}, y_{2m-1}) & \hat{\mathbf{I}}'^{j}(x_{2n}, y_{2m}) \end{bmatrix} =$$

$$4 \begin{bmatrix} \int_n^{n+1/2} \int_m^{m+1/2} p_{(r_1^*, r_2^*)}(x,y)\,dx\,dy & \int_n^{n+1/2} \int_{m+1/2}^{m+1} p_{(r_1^*, r_2^*)}(x,y)\,dx\,dy \\ \int_{n+1/2}^{n+1} \int_m^{m+1/2} p_{(r_1^*, r_2^*)}(x,y)\,dx\,dy & \int_{n+1/2}^{n+1} \int_m^{m+1} p_{(r_1^*, r_2^*)}(x,y)\,dx\,dy \end{bmatrix}. \tag{4.98}$$

The four predicted values are one of nine possibilities as shown in Appendix B. For example, if the pair of $(r_1^*, r_2^*) = (0, 0)$ as the center-center case, the four predicted values are deduced as follows:

$$\begin{bmatrix} \hat{\mathbf{I}}'^{j}(x_{2n-1}, y_{2m-1}) & \hat{\mathbf{I}}'^{j}(x_{2n-1}, y_{2m}) \\ \hat{\mathbf{I}}'^{j}(x_{2n}, y_{2m-1}) & \hat{\mathbf{I}}'^{j}(x_{2n}, y_{2m}) \end{bmatrix} =$$

$$= 4 \begin{bmatrix} \sum\sum \begin{bmatrix} +\frac{1}{256} & +\frac{1}{32} & -\frac{1}{256} \\ +\frac{1}{32} & +\frac{1}{4} & -\frac{1}{32} \\ -\frac{1}{256} & -\frac{1}{32} & +\frac{1}{256} \end{bmatrix} \otimes \mathbf{I}'^{j-1}_{CC} & \sum\sum \begin{bmatrix} -\frac{1}{256} & +\frac{1}{32} & +\frac{1}{256} \\ -\frac{1}{32} & +\frac{1}{4} & +\frac{1}{32} \\ +\frac{1}{256} & -\frac{1}{32} & -\frac{1}{256} \end{bmatrix} \otimes \mathbf{I}'^{j-1}_{CC} \\ \\ \sum\sum \begin{bmatrix} -\frac{1}{256} & -\frac{1}{32} & +\frac{1}{256} \\ +\frac{1}{32} & +\frac{1}{4} & -\frac{1}{32} \\ +\frac{1}{256} & +\frac{1}{32} & -\frac{1}{256} \end{bmatrix} \otimes \mathbf{I}'^{j-1}_{CC} & \sum\sum \begin{bmatrix} +\frac{1}{256} & -\frac{1}{32} & -\frac{1}{256} \\ -\frac{1}{32} & +\frac{1}{4} & +\frac{1}{32} \\ -\frac{1}{256} & +\frac{1}{32} & +\frac{1}{256} \end{bmatrix} \otimes \mathbf{I}'^{j-1}_{CC} \end{bmatrix} \tag{4.99}$$

where

$$\mathbf{I}'^{j-1}_{CC} = \begin{bmatrix} \mathbf{I}'^{j-1}(x_{n-1}, y_{m-1}) & \mathbf{I}'^{j-1}(x_{n-1}, y_m) & \mathbf{I}'^{j-1}(x_{n-1}, y_{m+1}) \\ \mathbf{I}'^{j-1}(x_n, y_{m-1}) & \mathbf{I}'^{j-1}(x_n, y_m) & \mathbf{I}'^{j-1}(x_n, y_{m+1}) \\ \mathbf{I}'^{j-1}(x_{n+1}, y_{m-1}) & \mathbf{I}'^{j-1}(x_{n+1}, y_m) & \mathbf{I}'^{j-1}(x_{n+1}, y_{m+1}) \end{bmatrix}. \tag{4.100}$$

5.3.3 Merge four indexes into 2D-signal

See Figure 4.16. Therefore, all pixels of finer multiresolution level are deduced

$$\begin{bmatrix} \mathbf{I}'^{j}(x_{2n-1}, y_{2m-1}) & \mathbf{I}'^{j}(x_{2n-1}, y_{2m}) \\ \mathbf{I}'^{j}(x_{2n}, y_{2m-1}) & \mathbf{I}'^{j}(x_{2n}, y_{2m}) \end{bmatrix} =$$

$$= \begin{bmatrix} \varepsilon'^{j}(x_{2n-1}, y_{2m-1}) & \varepsilon'^{j}(x_{2n-1}, y_{2m}) \\ \varepsilon'^{j}(x_{2n}, y_{2m-1}) & \varepsilon'^{j}(x_{2n}, y_{2m}) \end{bmatrix} + \begin{bmatrix} \hat{\mathbf{I}}'^{j}(x_{2n-1}, y_{2m-1}) & \hat{\mathbf{I}}'^{j}(x_{2n-1}, y_{2m}) \\ \hat{\mathbf{I}}'^{j}(x_{2n}, y_{2m-1}) & \hat{\mathbf{I}}'^{j}(x_{2n}, y_{2m}) \end{bmatrix} \tag{4.101}$$

, or

$$\begin{cases} \mathbf{I}'^{j}(x_{2n-1},y_{2m-1}) = \varepsilon'^{j}(x_{2n-1},y_{2m-1}) + \hat{\mathbf{I}}'^{j}(x_{2n-1},y_{2m-1}) \\ \mathbf{I}'^{j}(x_{2n-1},y_{2m}) = \varepsilon'^{j}(x_{2n-1},y_{2m}) + \hat{\mathbf{I}}'^{j}(x_{2n-1},y_{2m}) \\ \mathbf{I}'^{j}(x_{2n},y_{2m-1}) = \varepsilon'^{j}(x_{2n},y_{2m-1}) + \hat{\mathbf{I}}'^{j}(x_{2n},y_{2m-1}) \\ \mathbf{I}'^{j}(x_{2n},y_{2m}) = \varepsilon'^{j}(x_{2n},y_{2m}) + \hat{\mathbf{I}}'^{j}(x_{2n},y_{2m}). \end{cases} \tag{4.102}$$

Finally four kinds of predicted values are merged into the image $\mathbf{I}'^{j}$. The image $\mathbf{I}'^{j}$ can be written as follows:

$$\mathbf{I}'^{j} \quad := \quad \mathcal{M}^{-1}\left(\mathbf{I}^{j-1}, \mathbf{D}_h^{j-1}, \mathbf{D}_v^{j-1}, \mathbf{D}_d^{j-1}\right). \tag{4.103}$$

This iterates till $j = J$ in order to reconstruct the finest image $\mathbf{I}'^{J}$:

$$\mathbf{I}'^{J} \quad := \quad \mathcal{M}^{-1}\left(\mathbf{I}'^{0}, \mathbf{D}_h'^{0}, \mathbf{D}_v'^{0}, \mathbf{D}_d'^{0}, \ldots, \mathbf{D}_h'^{j-1}, \mathbf{D}_v'^{j-1}, \mathbf{D}_d'^{j-1}, \ldots, \mathbf{D}_h'^{J-1}, \mathbf{D}_v'^{J-1}, \mathbf{D}_d'^{J-1}\right). \tag{4.104}$$

Simulation results will be discussed in section 6.2.

6 Simulation results and discussions

The simulation results are organized in two parts: the first part concerns the separable mutiresolution (ENO PV, ENO CA) approaches (see section 3 and section 4, respectively) and the second part is related to the non-separable mutiresolution (ENO CA) approach (see section 5) described in the following sections.

6.1 For separable mutiresolution approaches

This section compares the quality of the tone mapped images using the mutiresolution families described in section 3 and section 4. Two TMO operators, namely:

i. "Proposed_SEPENOPV_LJ" for ENO Point-Value,

ii. "Proposed_SEPENOCA_LJ" for ENO Cell-Average,

are used with the following parameters: $\alpha_a = 0.3$, $\alpha_d = 0.7$ and $J = 1,2$. The parameters α_a, α_d are set less than 1, and the condition $\alpha_a < \alpha_d$ is set in an empirical way in order to get the best tone mapped images in term of details visibility.

Figure 4.17 and Figure 4.18 show the "Light" and "BottlesSmall" HDR test tone mapped images. One can conclude that the tone mapped images show good details preservations as well as details visibility due to the decomposition level. However, considering on the level, the more level J the more artifacts appear (see in Figure 4.17b and Figure 4.17d), therefore we limit the number of level to 2, although the highest metrics are mostly belonged to the method "Proposed_SEPENOCA_L2" in Table 4.1. The range of values is clamped by 255, that is why the normalized histograms are abruptly increased in the last bin.

(a) SEPENOPV_L1 (TMQI1=0.968) **(b)** SEPENOPV_L2 (TMQI1=0.960)

(c) SEPENOCA_L1 (TMQI1=0.972) **(d)** SEPENOCA_L2 (TMQI1=0.970)

Figure 4.17: *"Light" HDR test image (17.46 f-stops) - Proposed_SEPENO (PV and CA) with* $J = 1, 2$.

(a) SEPENOPV_L1 (TMQI1=0.903) **(b)** SEPENOPV_L2 (TMQI1=0.931)

(c) SEPENOCA_L1 (TMQI1=0.901) **(d)** SEPENOCA_L2 (TMQI1=0.934)

Figure 4.18: *"BottlesSmall" HDR test image (16.03 f-stops) - Proposed_SEPENO (PV and CA) with* $J = 1,2$.

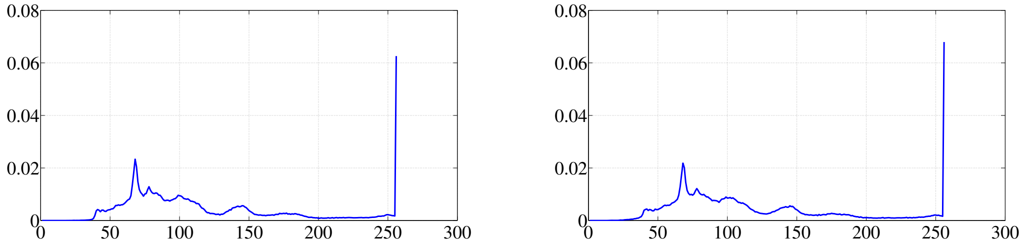

(a) SEPENOPV_L1 (TMQI1=0.968) **(b)** SEPENOPV_L2 (TMQI1=0.960)

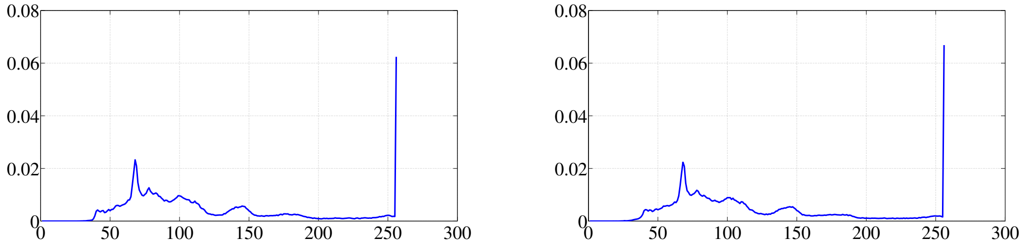

(c) SEPENOCA_L1 (TMQI1=0.972) **(d)** SEPENOCA_L2 (TMQI1=0.970)

Figure 4.19: *Normalized histograms of "Light" tone mapped images - Proposed_SEPENO (PV and CA) with* $J = 1,2$.

Table 4.1: *Tone Mapped Image Quality Index 1 (TMQI1) - Separable (PV and CA) approach for levels* $J = 1, 2$.

Images	DR f-stops	SEPCA_L1	SEPCA_L2	SEPPV_L1	SEPPV_L2
Lausanne1	7.71	0.817	**0.835**	0.817	0.830
CraterLake1	8.13	0.833	**0.863**	0.838	0.862
Shasta2	8.48	0.770	0.788	0.779	**0.790**
Synagogue	8.57	**0.755**	0.755	0.754	0.747
Anturium	8.73	0.882	**0.896**	0.880	0.888
BowRiver	9.53	0.835	**0.868**	0.834	0.862
Bridges	11.17	0.855	**0.863**	0.855	0.861
Stairway1	13.37	0.762	0.773	0.767	**0.775**
ArchRock	13.60	0.921	**0.957**	0.919	0.950
DollDoll	13.89	0.730	**0.732**	0.728	0.728
ClockBuilding	14.19	0.751	**0.753**	0.752	0.750
OxfordChurch	15.43	0.876	**0.895**	0.873	0.885
BottlesSmall	16.03	0.901	**0.934**	0.903	0.931
Montreal	16.06	0.606	0.613	0.608	**0.618**
SmallOffice	16.29	**0.943**	0.934	0.942	0.928
Light	17.46	**0.972**	0.970	0.968	0.960
BridgeStudios2	18.13	0.733	0.747	0.742	**0.757**
Memorial	18.38	**0.932**	0.918	0.927	0.903
ClaridgeHotel	23.44	0.840	**0.857**	0.842	0.855
Mistaya1	23.77	0.840	**0.863**	0.837	0.853
BrookHouse	23.98	0.970	**0.981**	0.967	0.973
PeaceRocks	24.13	**0.841**	0.830	0.840	0.822
GGpark2	24.41	0.843	**0.851**	0.840	0.841
AtriumNight	28.68	**0.973**	0.970	0.966	0.950

6.2 For non-separable mutiresolution approach

This section concerns the non-separable mutiresolution approach described in section 5. TMO operator namely "Proposed_NONSEPENO_LJ" is used with the following parameters: $J = 1,2$, $\gamma = 0.6$ and $\xi = 0.1$.

(a) NONSEPENO_L1 (TMQI1=0.962) **(b)** NONSEPENO_L2 (TMQI1=0.951)

Figure 4.20: *"Light" HDR test image (17.46 f-stops) - Proposed_NONSEPENO with* $J = 1,2$.

(a) NONSEPENO_L1 (TMQI1=0.900) **(b)** NONSEPENO_L2 (TMQI1=0.903)

Figure 4.21: *"BottlesSmall" HDR test image (16.03 f-stops) - Proposed_NONSEPENO with* $J = 1,2$.

Figure 4.20 and Figure 4.21 show "Light" and "Bottle" HDR test tone mapped images. The tone mapped images are good in terms of details visibility. The more details are extracted due to the non-separable approach as well as the adaptive weighting technique. This confirms the behaviors of the normalized histograms in Figures 4.22 with existing many peaks or edges. We limit the number of level to 2. The highest metrics are mostly belonged in the method "Proposed_NONSEPENOCA_L1" in Table 4.2.

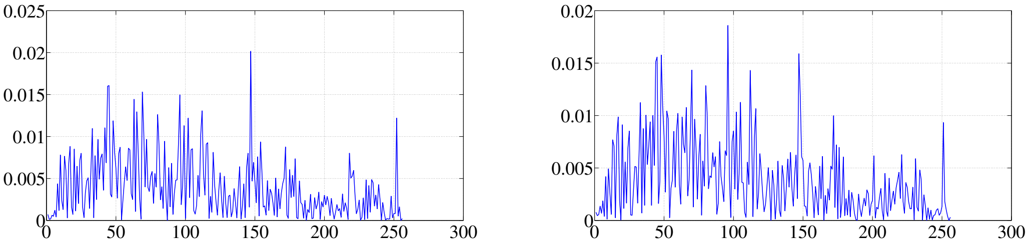

(a) NONSEPENO_L1 (TMQI1=0.962) **(b)** NONSEPENO_L2 (TMQI1=0.951)

Figure 4.22: *Normalized histograms of "Light" tone mapped images - Proposed_NONSEPENO with* $J = 1, 2$.

Table 4.2: *Tone Mapped Image Quality Index 1 (TMQI1) - Non-separable approach for levels* $J = 1, 2$.

Images	DR f-stops	NONSEP_L1	NONSEP_L2
Lausanne1	7.71	0.916	**0.933**
CraterLake1	8.13	**0.943**	0.940
Shasta2	8.48	**0.918**	0.863
Synagogue	8.57	**0.972**	0.968
Anturium	8.73	0.969	**0.978**
BowRiver	9.53	**0.953**	0.952
Bridges	11.17	**0.968**	0.956
Stairway1	13.37	**0.896**	0.892
ArchRock	13.60	**0.952**	0.943
DollDoll	13.89	0.888	**0.905**
ClockBuilding	14.19	**0.939**	0.935
OxfordChurch	15.43	**0.934**	0.916
BottlesSmall	16.03	0.900	**0.903**
Montreal	16.06	**0.820**	0.816
SmallOffice	16.29	0.945	**0.954**
Light	17.46	**0.962**	0.951
BridgeStudios2	18.13	0.913	**0.917**
Memorial	18.38	**0.913**	0.885
ClaridgeHotel	23.44	0.925	**0.936**
Mistaya1	23.77	0.974	**0.980**
BrookHouse	23.98	**0.983**	0.970
PeaceRocks	24.13	**0.943**	0.925
GGpark2	24.41	**0.980**	0.974
AtriumNight	28.68	**0.934**	0.916

6.3 Comparison and discussion

Figure 4.23a shows "Light" HDR tone mapped image with Proposed_NONSEPENO_L1 method. It can be seen that the reconstruction of details with natural ways is better than "Li" approach (Figure 4.23b). Indeed, Li added the post-processing methods in visual results such as cutting off the brightest and darkest parts as well as adding 15% of a histogram equalized layer to the result.

(a) NONSEPENO_L1 (TMQI1=0.962) **(b)** "Li" (TMQI1=0.888)

Figure 4.23: *"Light" HDR test image (17.46 f-stops) - Proposed_NONSEPENO_L1 versus "Li".*

The "Anturium" HDR tone mapped image with Proposed_SEPENOCA_L1 in Figure 4.24a shows better details than "Duan" method in Figure 4.24b particularly around leaves.

(a) SEPENOCA_L1 (TMQI1=0.882) **(b)** "Duan" (TMQI1=0.964)

Figure 4.24: *"Anturium" HDR test image (8.73 f-stops) - Proposed_SEPENOCA_L1 versus "Duan".*

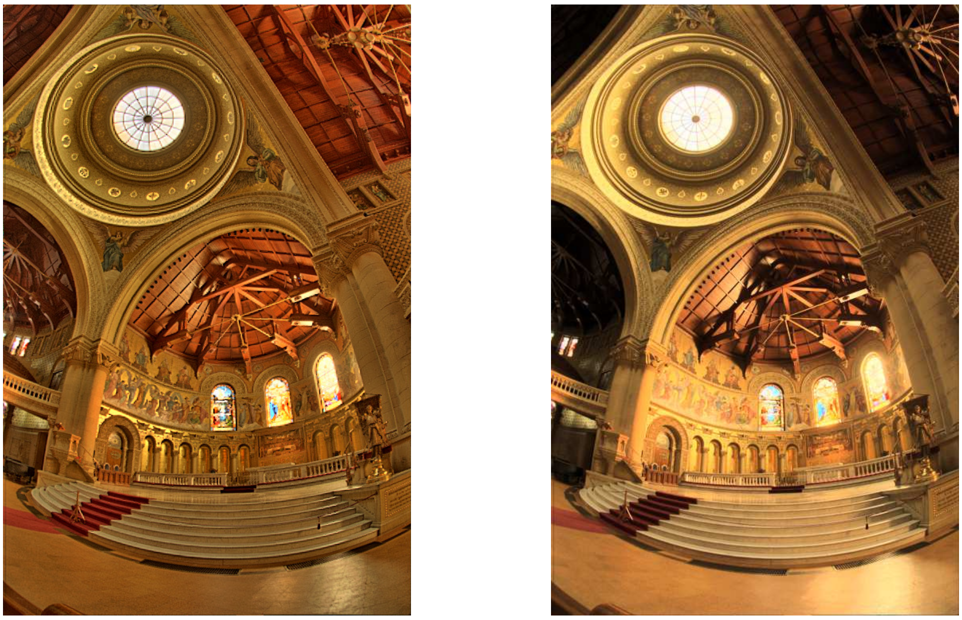

(a) NONSEPENO_L1 (TMQI1=0.913) **(b)** "Duan" (TMQI1=0.935)

(c) "Fattal" WRB (TMQI1=0.927) **(d)** "Li" (TMQI1=0.834)

Figure 4.25: *"Memorial" HDR test image (18.38 f-stops) - Proposed_NONSEPENO_L1 versus "Duan", "Fattal" and "Li".*

Figure 4.25a, Figure 4.25b, Figure 4.25c and Figure 4.25d provide the visual quality of the "Memorial" HDR tone mapped images. One can observe that the details are well rendered in favor of our method (e.g. tiles, rosette). In Figure 4.25a, the tiles on the top right on the tone mapped image are better rendered in the method Proposed_NONSEPENO_L1. Figure 4.26 compare the visual quality between separable and non-separable method; one can see that the non-separable is better than the separable.

(a) SEPENOCA_L1 (TMQI1=0.932) **(b)** NONSEPENO_L1 (TMQI1=0.913)

Figure 4.26: *"Memorial" HDR test image (18.38 f-stops) - Proposed_SEPENOCA_L1 versus Proposed_NONSEPENO_L1.*

Our TMOs using ENO approaches have the ability to solve isolated singularities. The luminance of "AtriumNight" HDR tone mapped image is represented on Figure 4.27a where the red rectangle frames a specific area. This area is shown in Figure 4.27b, Figure 4.27c, Figure 4.27d, Figure 4.27e, as close-ups of the four tone mapped images using "Fattal" WRB [25], "Fattal" WCDF [25], Proposed_SEPENOCA_L1 and Proposed_SEPENOPV_L1. It can be seen that the horizontal edge of the staircase step is better rendered with non-linear multiresolution families using dependent data interpolation. We can observe that horizontal and vertical edges of all tone mapped images are well rendered. This is related to advantages of the ENO approaches.

(a) AtriumNight (LDR luminance)

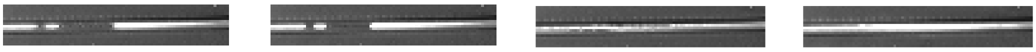

(b) "Fattal" WRB **(c)** "Fattal" WCDF **(d)** SEPENOCA_L1 **(e)** SEPENOPV_L1

Figure 4.27: *Close-up of the tone mapped image luminance using "Fattal" RWB [25], "Fattal" WCDF [25], Proposed_SEPENOCA_L1 and Proposed_SEPENOPV_L1.*

7 Conclusion

This chapter proposed image tone mapping operators based on Essential Non-oscillatory multiresolutions such as separable approaches (Point-Value, Cell-Average) and non-separable approach (Cell-Average). These TMO methods, which are global and local, have the ability to reduce the dynamic range while preserving details in the tone mapped image.

The aim of the following chapter is to preserve the details and enhance the contrast of the tone mapped images.

CHAPTER 5

Proposed TMO based on the contrast enhancement and details preservation

Abstract

This chapter concerns High Dynamic Range (HDR) image Tone Mapping (TM) issue to convert HDR images into Low Dynamic Range (LDR) images while preserving as much as possible the HDR image visual quality. The developed approach proceeds in three main stages. The first one decomposes the HDR image using a separable near optimal lifting scheme. This latter relies on an adaptive powerful prediction step formulated by a linear weighted combination of the neighboring pixels at each resolution level. These weights are deduced in such a way to extract as much as possible the relevant finest details in the complex HDR image. The second stage, before reconstructing the decomposed image, judiciously modifies the approximation and detail coefficients according to their entropy. Finally, the third stage acts as a perceptual quantizer. It adjusts the distribution of the logarithm intermediate LDR luminance with respect to the HVS using a piecewise linear function. Simulation results show that the proposed TM approach provides good results compared to existing competitive TM operators. The results of our work have been published at the 22nd IEEE Signal Processing: Algorithms, Architectures, Arrangements, and Applications (SPA) [1], and the Journal of Visual Communication and Image Representation (JVCI) [2].

---

[1] [57] B. C. Thai, A. Mokraoui, and B. Matei. "HDR Image Tone Mapping Approach based on Near Optimal Separable Adaptive Lifting Scheme". In: 22nd IEEE Signal Processing: Algorithms, Architectures, Arrangements, and Applications (SPA) (Sept. 2018).

[2] [58] B. C. Thai, A. Mokraoui, and B. Matei. "Contrast Enhancement and Details Preservation of Tone Mapped High Dynamic Range Images". Journal of Visual Communication and Image Representation (JVCI), Elsevier, 2018.

Chapter content

1 Introduction

The great difficulty in setting up an HDR image tone mapping algorithm lies in the way in which the relevant information is chosen, responding both to a good visual quality rendering confirmed by an observer (or measured by a quality metric) on low-dynamic display devices and to a faithfulness fairly close to the HDR image. In this objective, the TM algorithm described in this section first proposes to decompose the HDR image into several levels of resolution, approximations and details, then to analyze and refine each level of resolution to retain only the relevant information in the sense of a visual rendering evaluated by a quality metric.

The developed HDR image TM algorithm is composed of four main stages described in the following sections and summarized by the block diagram in Figure 5.1. The first stage, described in section 3, concerns the separable adaptive lifting scheme. After having appropriately weighted the coefficients of each resolution levels (in section 4), the third stage presented in section 5 reconstructs the intermediate LDR image. Finally the last stage, given in section 6, adjusts the logarithm luminance of the intermediate LDR image according to a perceptual linear quantizer with respect to the HVS properties. Before describing the proposed HDR image TM algorithm, the following section introduces some notations.

2 Notations

The original HDR image, considered at the finest resolution level denoted J, is assumed to be of size $N^J \times M^J$. Denote $\mathbf{L}_{HDR}$ and $\mathbf{L}_{LDR}$ respectively the HDR and LDR image luminance. The index j refers to the resolution level (with $j = 1, ..., J$); B is the total number of bins; and the index i represents the given bin ($i = 1, ..., B$).

In the rest of this chapter, the HDR image luminance is considered in the logarithm domain since it is well adapted to the HVS. It is denoted $\mathbf{I}^J$ and defined as follows:

$$\mathbf{I}^J = \left\{ \mathbf{I}^J(x_n, y_m) = \log_{10}(\mathbf{L}_{HDR}(x_n, y_m)) \text{ for } 1 \leq n \leq N^J \text{ and } 1 \leq m \leq M^J \right\}, \quad (5.1)$$

where $\mathbf{I}^J(x_n, y_m)$ is the HDR logarithm luminance value of the pixel located at position (x_n, y_m).

3 The adaptive lifting scheme forward algorithm

This section concerns the first stage of the HDR image TM algorithm. It decomposes the logarithm luminance of the original HDR image into approximations and details resolution levels. This decomposition is achieved according to the forward process of a separable (i.e. 1D-signal in horizontal and vertical directions) near optimal Cell-Average lifting scheme. This choice, among the various developed decomposition strategies in

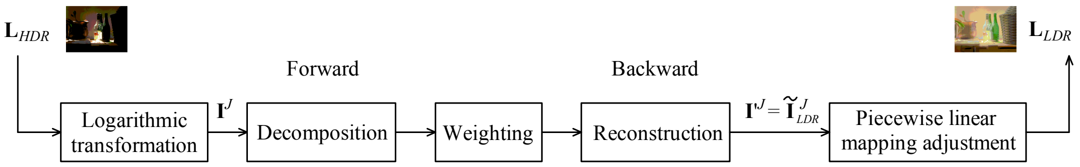

Figure 5.1: *Diagram block of the proposed HDR image TM algorithm based on contrast and details combination scheme.*

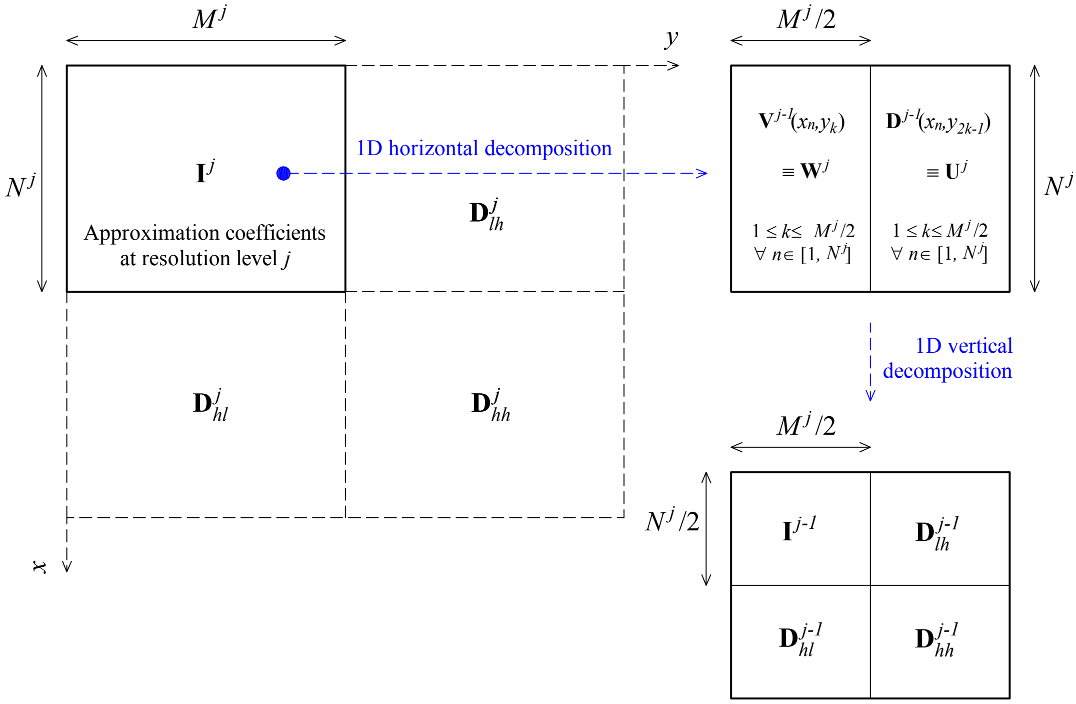

Figure 5.2: *Separable lifting scheme decomposition principle (this scheme is given in Chapter 4).*

the literature, is motivated by the fact that the relevant details are accurately predicted since the coefficients of the filters are adapted locally to the data to be processed.

The decomposition process consists to go from the finest resolution level J to the coarse resolution level 0. At a given resolution level j (with $1 \leq j \leq J$), the algorithm deals with the approximation coefficients obtained at resolution level j i.e. $\mathbf{I}^j(x_n, y_k)$ (with $1 \leq n \leq N^j$ and $1 \leq k \leq M^j$) as shown in Figure 5.2. The forward process steps of the separable decomposition algorithm are described below.

1. **Split 1D-signal into odd and even indexes**

At a given resolution level j and a given n belonging to $[1, N^j]$ (i.e. x_n), the algorithm starts with splitting the horizontal 1D-signal, i.e. $\mathbf{I}^j(x_n, y_k)$ for $1 \leq k \leq M^j$, into a set of odd $\mathbf{I}^j(x_n, y_{2k-1})$ and even $\mathbf{I}^j(x_n, y_{2k})$ indexes as follows:

$$\begin{aligned} &\{\mathbf{I}^j(x_n, y_k) \text{ with } 1 \le k \le M^j\} \\ := &\{\mathbf{I}^j(x_n, y_{2k-1}),\ \mathbf{I}^j(x_n, y_{2k}) \ \text{ with } \ 1 \le k \le M^j/2\ \}. \end{aligned} \tag{5.2}$$

The process is then repeated until $n = N^j$.

2. Approximation resolution level in a cell-average scheme

Based on this split, the approximation coefficient located at position (x_n, y_k), denoted $\mathbf{V}^{j-1}(x_n, y_k)$ for a given n, is computed on a Cell-Average (CA) scheme as follows:

$$\mathbf{V}^{j-1}(x_n, y_k) = \frac{1}{2}\Big(\mathbf{I}^j(x_n, y_{2k-1}) + \mathbf{I}^j(x_n, y_{2k})\Big) \ \text{ for } 1 \le k \le M^j/2. \tag{5.3}$$

The process is then repeated until $n = N^j$.

3. Detail resolution level based on an adaptive prediction

The detail coefficient, denoted $\mathbf{D}^{j-1}(x_n, y_{2k-1})$ for a given n, is then computed at odd indexes (x_n, y_{2k-1}) as follows:

$$\mathbf{D}^{j-1}(x_n, y_{2k-1}) = \mathbf{I}^j(x_n, y_{2k-1}) - \hat{\mathbf{I}}^j(x_n, y_{2k-1}) \text{ for } 1 \le k \le M^j/2, \tag{5.4}$$

where $\hat{\mathbf{I}}^j(x_n, y_{2k-1})$ is the predicted logarithm luminance value at odd position (x_n, y_{2k-1}) and resolution level j.

This predicted value is expressed as a linear weighted combination of the neighboring approximation coefficients:

$$\hat{\mathbf{I}}^j(x_n, y_{2k-1}) = \sum_{i=0}^{2} u_i^{j-1}(x_n) \cdot \mathbf{V}^{j-1}(x_n, y_{k+i-1}) \text{ for } 1 \le k \le M^j/2, \tag{5.5}$$

where the weights $u_i^{j-1}(x_n)$ (with $i = 0, 1, 2$) have to preserve the average of the initial 1D-signal satisfying then the following condition:

$$\sum_{i=0}^{2} u_i^{j-1}(x_n) = 1. \tag{5.6}$$

These weights $u_i^{j-1}(x_n)$ are deduced so that the Mean Squared Error (MSE) between $\hat{\mathbf{I}}^j(x_n, y_{2k-1})$ and $\mathbf{I}^j(x_n, y_{2k-1})$ (for $1 \le k \le M^j/2$) is minimized:

$$E = \arg\min_{u_i^{j-1}} \|\hat{\mathbf{I}}^j(x_n, y_{2k-1}) - \mathbf{I}^j(x_n, y_{2k-1})\|_2^2 \text{ for } 1 \le k \le M^j/2. \tag{5.7}$$

Therefore these weights are computed so that the partial derivatives of the MSE, given by equation (5.7), with respect to $u_i^{j-1}(x_n)$ (i.e. $i = 0, 1, 2$) are equal to zero. See more in Appendix C. Denote $\mathbf{u}^{j-1}(x_n) = [u_0^{j-1}(x_n),\ u_1^{j-1}(x_n),\ u_2^{j-1}(x_n)]^{\mathbf{T}}$ the weight vector at resolution level $j-1$ related to the row (x_n) according to the coefficient to be approximated. Calculations lead to solve this system of equations provided in a matrix form:

$$\mathbf{\Gamma}^{j-1} \cdot \mathbf{u}^{j-1} = \mathbf{r}^{j-1}, \tag{5.8}$$

where $\mathbf{\Gamma}^{j-1}$ is the autocorrelation matrix defined as follows:

$$\mathbf{\Gamma}^{j-1} = \begin{bmatrix} R^{j-1}(0) & R^{j-1}(1) & R^{j-1}(2) \\ R^{j-1}(-1) & R^{j-1}(0) & R^{j-1}(1) \\ R^{j-1}(-2) & R^{j-1}(-1) & R^{j-1}(0) \end{bmatrix}, \tag{5.9}$$

with $R^{j-1}(i)$ the autocorrelation of $\mathbf{V}^{j-1}(x_n, y_k)$ given by:

$$R^{j-1}(i) = \mathbf{V}^{j-1}(x_n, y_{k+i-1}) \cdot \mathbf{V}^{j-1}(x_n, y_{k-1}), \tag{5.10}$$

and $\mathbf{r}^{j-1}$ is the cross-correlation vector defined as:

$$\mathbf{r}^{j-1} = \begin{bmatrix} r^{j-1}(0) \\ r^{j-1}(1) \\ r^{j-1}(2) \end{bmatrix}, \tag{5.11}$$

where $\mathbf{r}^{j-1}(i)$ represents the cross-correlation function between $\mathbf{V}^{j-1}(x_n, y_k)$ and $\mathbf{I}^j(x_n, y_{2k-1})$ for $1 \leq k \leq M^j/2$ provided by:

$$\mathbf{r}^{j-1}(i) = \mathbf{V}^{j-1}(x_n, y_{k+i-1}) \cdot \mathbf{I}^j(x_n, y_{2k-1}). \tag{5.12}$$

Therefore the weights, associated to the row x_n, are deduced as follows:

$$\mathbf{u}^{j-1}(x_n) = (\mathbf{\Gamma}^{j-1})^{-1} \cdot \mathbf{r}^{j-1}. \tag{5.13}$$

All the weight vectors are stored to be used in the adaptive lifting scheme backward process to reconstruct the decomposed 1D-signal. The horizontal decomposition steps (i.e. 1, 2 and 3) are summarized in Figure 5.3.

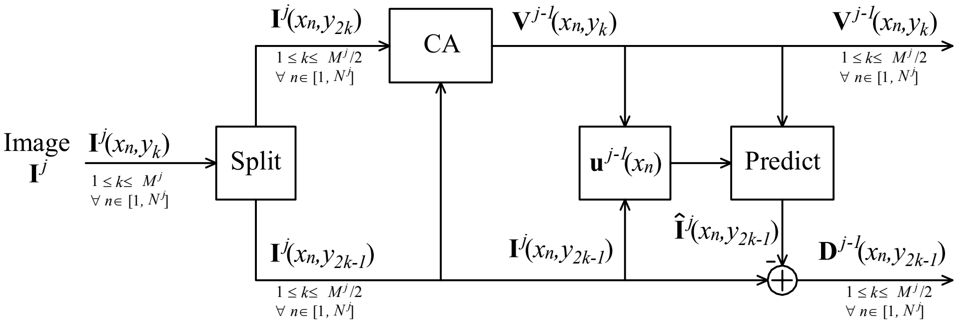

Figure 5.3: *1D-signal decomposition in a horizontal direction.*

4. Arrangement of approximation and detail coefficients

To process the 1D-signal in the vertical direction and for sake of convenience, the approximation and details coefficients are organized as shown in Figure 5.2 and renamed as follows:

$$\begin{aligned}&\{\mathbf{V}^{j-1}(x_n,y_k) \text{ for } 1\le k\le M^j/2 \text{ and } \forall n\in[1,N^j]\}\\ :=&\{\mathbf{W}^j(x_k,y_m) \text{ for } 1\le k\le N^j \text{ and } \forall m\in[1,M^j/2]\}.\end{aligned} \tag{5.14}$$

$$\begin{aligned}&\{\mathbf{D}^{j-1}(x_n,y_{2k-1}) \text{ for } 1\le k\le M^j/2 \text{ and } \forall n\in[1,N^j]\}\\ :=&\{\mathbf{U}^j(x_k,y_m) \text{ for } 1\le k\le N^j \text{ and } \forall m\in[1,M^j/2]\}.\end{aligned} \tag{5.15}$$

5. Repeat steps 1, 2 and 3

Steps 1, 2 and 3 are now being applied on $\mathbf{W}^j(x_k,y_m)$ and $\mathbf{U}^j(x_k,y_m)$ for a given $m\in[1,M^j/2]$. Figure 5.4 summarizes the vertical 1D-signal forward decomposition. Note that the approximation step requires the prediction of $\hat{\mathbf{W}}^j(x_{2k-1},y_m)$ (respectively $\hat{\mathbf{U}}^j(x_{2k-1},y_m)$) based on a set of weights v_i^{j-1} (respectively w_i^{j-1}). These weights need to be stored for the backward process lifting scheme to reconstruct the decomposed logarithm luminance image.

Finally, the approximation resolution level $\mathbf{I}^j(x_n,y_m)$ is divided into 4 blocks: ll, lh, hl and hh. The block ll concerns the approximation resolution denoted $\mathbf{I}^{j-1}$; and the other three blocks lh, hl and hh contain the detail resolutions, named $\mathbf{D}_{lh}^{j-1}, \mathbf{D}_{hl}^{j-1}, \mathbf{D}_{hh}^{j-1}$, respectively (see Figure 5.2). Note that the size of each block is deduced as the half size of $\mathbf{I}^j$ in each direction:

$$\mathcal{M}\,\mathbf{I}^j \quad := \quad \left(\mathbf{I}^{j-1},\ \mathbf{D}_{lh}^{j-1},\ \mathbf{D}_{hl}^{j-1},\ \mathbf{D}_{hh}^{j-1}\right). \tag{5.16}$$

The decomposition process can be iterated on $\mathbf{I}^{j-1}$ until $\mathbf{I}^0$. The finest HDR logarithm luminance $\mathbf{I}^J$ is then represented by $3J+1$ resolution levels as follows:

$$\mathcal{M}\,\mathbf{I}^J \quad := \quad \left(\mathbf{I}^0,\mathbf{D}_{lh}^0,\mathbf{D}_{hl}^0,\mathbf{D}_{hh}^0,\ldots,\mathbf{D}_{lh}^{j-1},\mathbf{D}_{hl}^{j-1},\mathbf{D}_{hh}^{j-1},\ldots,\mathbf{D}_{lh}^{J-1},\mathbf{D}_{hl}^{J-1},\mathbf{D}_{hh}^{J-1}\right). \tag{5.17}$$

4 Weighting step according to the entropy of each subband

Before performing the adaptive lifting scheme backward process, the HDR image TM approach proposes to modify the approximation and detail coefficients in an appropriate way taking into account the information available in each subband measured by the entropy as explained below.

Denote E_a the entropy of the approximation coefficients at the coarsest resolution level 0; and E_d^{j-1} the entropy at resolution level $j-1$ of the detail coefficients set $\{\mathbf{D}_{lh}^{j-1}, \mathbf{D}_{hl}^{j-1}, \mathbf{D}_{hh}^{j-1}\}$. The weighting algorithm initializes the number of resolution levels, denoted N_l, to J (i.e. $N_l = J$). The weighting algorithm processes as follows.

1. Computation of the entropies

The weighting algorithm computes the N_l+1 entropies namely E_a, E_d^0, E_d^1, ..., E_d^{j-1},..., $E_d^{N_l-1}$.

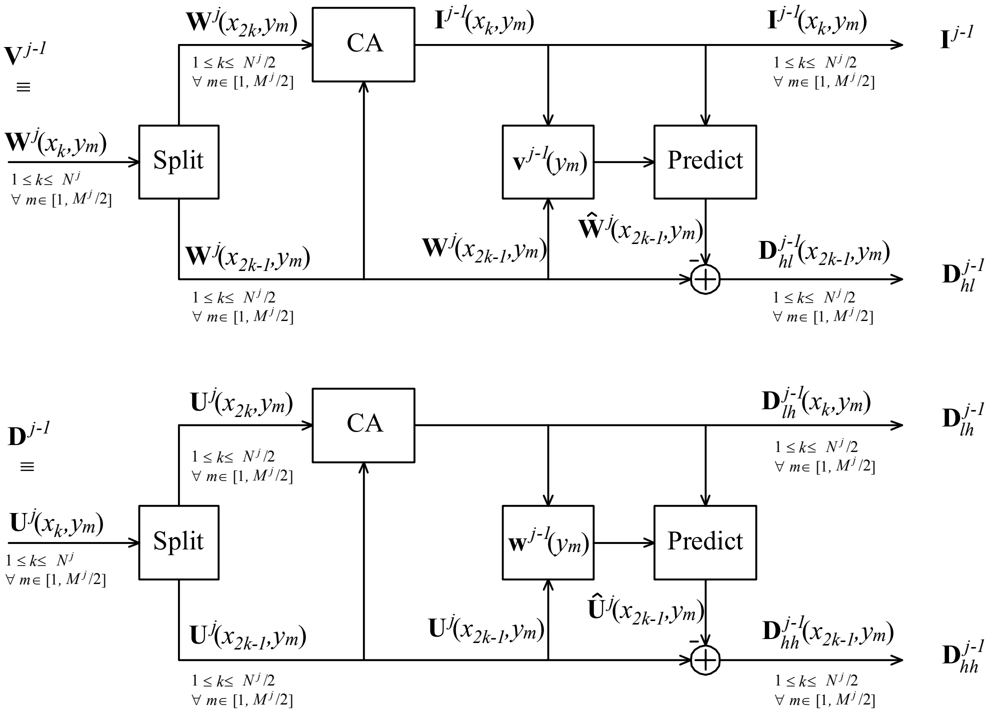

Figure 5.4: *1D-signal decomposition in a vertical direction.*

2. Computation of the weights

Based on the $N_l + 1$ calculated entropies, positive weights smaller than one are deduced as follows:

$$\begin{cases} \alpha_a = \frac{\sum_{i=1}^{N_l} E_d^{i-1}}{E_a + \sum_{i=1}^{N_l} E_d^{i-1}} \\ \alpha_d^{j-1} = \frac{E_a + \sum_{i=1,\neq(j-1)}^{N_l} E_d^{i-1}}{E_a + \sum_{i=1}^{N_l} E_d^{i-1}} \quad \text{for } j = 1, ..., N_l \end{cases} \tag{5.18}$$

where α_a is the weight associated to the approximation coefficients at coarsest resolution level 0; and α_d^{j-1} is the weight related to detail coefficients at resolution level $j-1$.

3. Modification of the detail and approximation coefficients

The coefficients of the four coarsest resolution levels are modified according to:

$$\mathbf{I}'^0 = \alpha_a \times \mathbf{I}^0,$$
$$\mathbf{D}'^0_{lh} = \alpha_d^0 \times \mathbf{D}^0_{lh}, \quad \mathbf{D}'^0_{hl} = \alpha_d^0 \times \mathbf{D}^0_{hl}, \quad \mathbf{D}'^0_{hh} = \alpha_d^0 \times \mathbf{D}^0_{hh}. \tag{5.19}$$

4. Reconstruction of the coarsest subband

The modified coefficients in step 2 are used to reconstruct the coarsest subband, denoted $\mathbf{I}'^1$, according to the adaptive lifting scheme backward process (see section 5). The number of resolution levels $N_l = J$ is then reduced to $N_l - 1$ (i.e. $N_l = N_l - 1$) to deal with step 4.

5. Repeat steps 1, 2, 3 and 4

The N_l entropies (associated to $3N_l - 2$ subbands) are computed again to update the

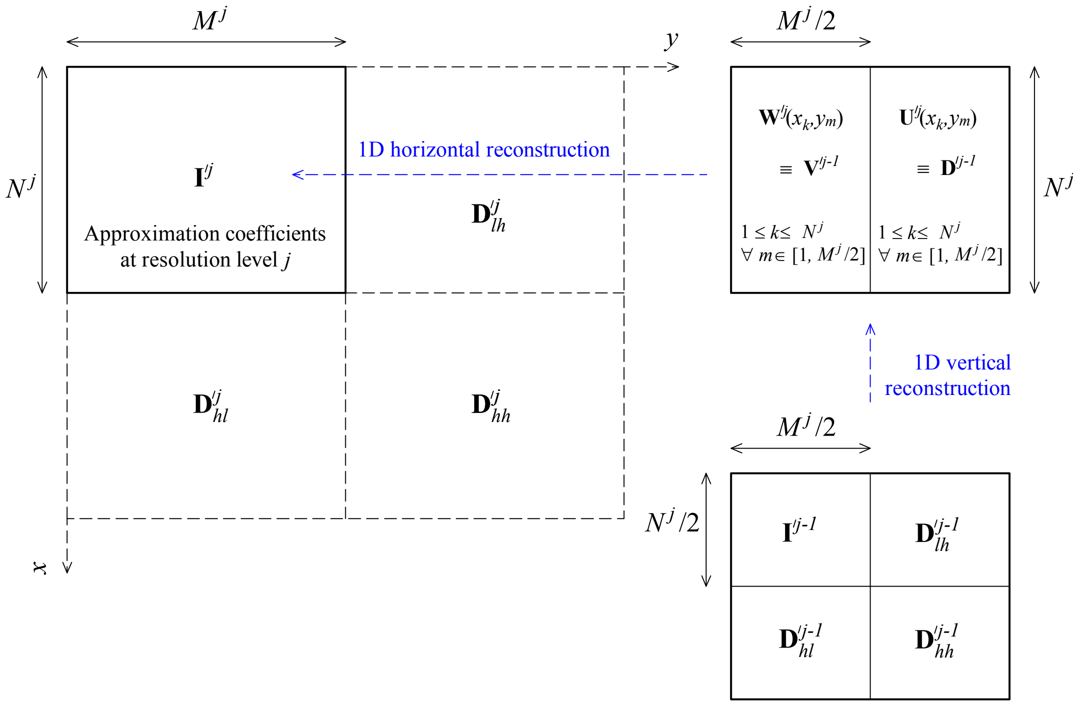

Figure 5.5: *Separable lifting scheme reconstruction principle (this scheme is given in Chapter 4).*

weights α_a and $\{\alpha_d^{j-1}$ with $j = 1, ..., N_l\}$ according to steps 1 and 2 (see equation (5.18)). After that, these weights are applied on the coefficients $\mathbf{I}'^1$, $\mathbf{D}'^1_{lh}$, $\mathbf{D}'^1_{hl}$, $\mathbf{D}'^1_{hh}$ to build $\mathbf{I}'^2$ as explained in step 3. These steps are repeated until $N_l = 0$ thus reconstructing the coarse tone mapped HDR image denoted $\widetilde{\mathbf{I}}^J_{LDR}$, called coarse LDR image.

5 The adaptive lifting scheme backward algorithm

The adaptive lifting scheme backward process starts with the 4 coarsest resolution levels, i.e ($\mathbf{I}'^0$, $\mathbf{D}'^0_{lh}$, $\mathbf{D}'^0_{hl}$, $\mathbf{D}'^0_{hh}$), to generate the approximation coefficients $\mathbf{I}'^1$. The same process is then iterated until reaching the finest resolution i.e. $j = J$ corresponding to the intermediate HDR image, denoted $\mathbf{I}'^J$, of size $N^J \times M^J$.

Assume first that the algorithm processed all resolution levels until $j-1$. Therefore the next step consists to recover the approximation image $\mathbf{I}'^j$ of size $N^j \times M^j$ using the following blocks: $\mathbf{I}'^{j-1}$, $\mathbf{D}'^{j-1}_{lh}$, $\mathbf{D}'^{j-1}_{hl}$ and $\mathbf{D}'^{j-1}_{hh}$. The reconstruction processes are carried out inversely to the decomposition stage, first in a vertical direction (see Figure 5.6) and then in a horizontal direction (see Figure 5.7). The mathematical equations describing this process are derived in what follows.

First the algorithm deals with the coefficients in a vertical direction using $\mathbf{I}'^{j-1}$ and $\mathbf{D}'^{j-1}_{hl}$. At a given m, the approximation coefficients at odd positions $\mathbf{W}'^j(x_{2k-1}, y_m)$

with $1 \leq k \leq N^j/2$ are deduced as follows:

$$\mathbf{W}'^{j}(x_{2k-1}, y_m) = \hat{\mathbf{W}}'^{j}(x_{2k-1}, y_m) + \mathbf{D}'^{j-1}_{hl}(x_k, y_m) \text{ for } 1 \leq k \leq N^j/2, \tag{5.20}$$

where $\hat{\mathbf{W}}'^{j}(x_{2k-1}, y_m)$ is the predicted coefficient, at odd position, deduced from the weighted combination $v_i^{j-1}(y_m)$ (with $i = 0, 1, 2$) of the neighboring approximation coefficients $\mathbf{I}'^{j-1}(x_{2k-1}, y_m)$ as follows:

$$\hat{\mathbf{W}}'^{j}(x_{2k-1}, y_m) = \sum_{i=0}^{2} v_i^{j-1}(y_m) \cdot \mathbf{I}'^{j-1}(x_{k+i-1}, y_m) \text{ for } 1 \leq k \leq N^j/2. \tag{5.21}$$

The weights $v_i^{j-1}(y_m)$ are those computed and stored in the decomposition process. While the approximation coefficients $\mathbf{W}'^{j}(x_{2k}, y_m)$, at even positions, are deduced in a CA scheme:

$$\mathbf{W}'^{j}(x_{2k}, y_m) = 2\mathbf{I}'^{j-1}(x_k, y_m) - \mathbf{W}'^{j}(x_{2k-1}, y_m) \text{ for } 1 \leq k \leq N^j/2. \tag{5.22}$$

The odd and even approximation coefficients are then merged to constitute the 1D-signal as follows:

$$\begin{aligned} &\{\mathbf{W}'^{j}(x_k, y_m) \text{ for } 1 \leq k \leq N^j\} \\ := &\{\mathbf{W}'^{j-1}(x_{2k-1}, y_m),\ \mathbf{W}'^{j-1}(x_{2k}, y_m) \text{ for } 1 \leq k \leq N^j/2\}. \end{aligned} \tag{5.23}$$

This process is repeated for all m to build $\mathbf{W}'^{j}$ of size $N^j \times M^j/2$.

In the other hand, these same steps are applied to $\mathbf{D}'^{j-1}_{lh}$ and $\mathbf{D}'^{j-1}_{hh}$ to generate the new block $\mathbf{U}'^{j}$ of size $N^j \times M^j/2$ (see Figure 5.6). As in the decomposition strategy, $\mathbf{W}'^{j}$ and $\mathbf{U}'^{j}$ are respectively renamed $\mathbf{V}'^{j-1}$ and $\mathbf{D}'^{j-1}$ and the same steps are performed but according to a horizontal direction (see Figure 5.6). Finally, we get the approximation coefficients $\mathbf{I}'^{j}$ at resolution level j. The process is then iterated until $j = J$:

$$\mathbf{I}'^{J} \quad := \quad \mathcal{M}^{-1}\left(\mathbf{I}'^{0}, \mathbf{D}'^{0}_{lh}, \mathbf{D}'^{0}_{hl}, \mathbf{D}'^{0}_{hh}, \ldots, \mathbf{D}'^{j-1}_{lh}, \mathbf{D}'^{j-1}_{hl}, \mathbf{D}'^{j-1}_{hh}, \ldots, \mathbf{D}'^{J-1}_{lh}, \mathbf{D}'^{J-1}_{hl}, \mathbf{D}'^{J-1}_{hh}\right). \tag{5.24}$$

Denote $\widetilde{\mathbf{I}}^J_{LDR} \equiv \mathbf{I}'^{J}$ the coarse LDR image logarithm luminance image.

6 Perceptual quantizer with respect to the human visual system using a piecewise linear function

This stage proposes to adjust locally the distribution of the coarse LDR image logarithm luminance $\widetilde{\mathbf{I}}^J_{LDR}$ according to the HVS to enhance the contrast using a piecewise linear function. This strategy is inherited from Chapter 3 with the same procedures in section 3. The horizontal axis "HDR logarithm luminance values" $\widetilde{l}^i_{HDR}(k)$ is replaced by "Coarse LDR luminance values" $\widetilde{l}^i_{LDR}(k)$ in Figure 3.3.

The lower bound (cutting point) of each bin is then adjusted as follows:

$$\widetilde{l}^i_{LDR}(1) = c^i_{uLDR} + \beta_i (c^i_{nuLDR} - c^i_{uLDR}), \tag{5.25}$$

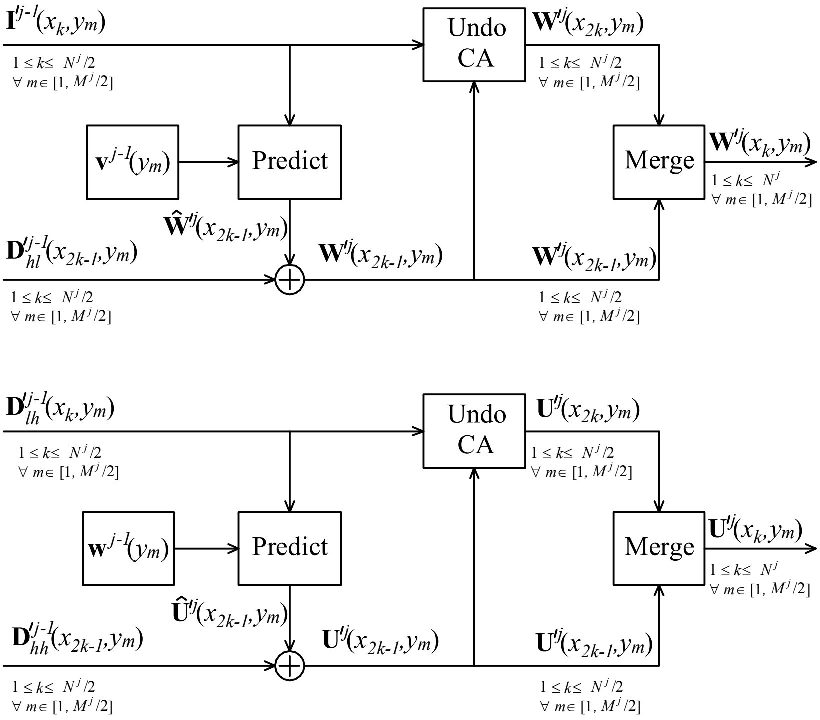

Figure 5.6: *1D-signal reconstruction in a vertical direction.*

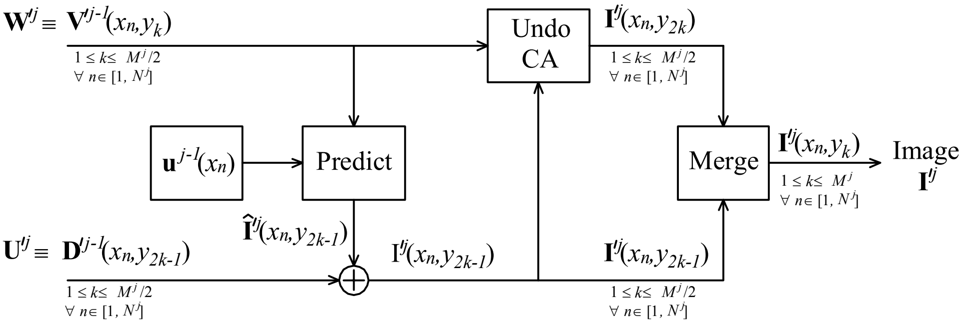

Figure 5.7: *1D-signal reconstruction in a horizontal direction.*

where β_i is a positive parameter smaller than 1 depending on the sub-interval $[c^i_{uLDR},\, c^i_{nuLDR}]$. Since the lower cutting point $\widetilde{l}^i_{LDR}(1)$ is deduced as the average of the logarithm luminance values on each sub-interval $[c^i_{uLDR},\, c^i_{nuLDR}]$ as in [30], the parameter β_i is then given by:

$$\beta_i = \frac{\text{mean}(\widetilde{\mathbf{I}}_{LDR}[c^i_{uLDR},\, c^i_{nuLDR}]) - c^i_{uLDR}}{c^i_{nuLDR} - c^i_{uLDR}}. \tag{5.26}$$

The parameter β_i can be set constant.

The parameter a_i is expressed as follows:

$$a_i = \frac{\hat{l}^i_{LDR}(K_i) - \hat{l}^i_{LDR}(1)}{\widetilde{l}^i_{LDR}(K_i) - \widetilde{l}^i_{LDR}(1)}, \tag{5.27}$$

where $\hat{l}^i_{LDR}(K_i)$ and $\hat{l}^i_{LDR}(1)$ are unknown values. See section 3 in Chapter 3. p_i is the probability of the $\tilde{l}^i_{LDR}(k)$ value in the i-th bin given by:

$$p_i = \frac{K_i}{\sum_{i=1}^{B} K_i}. \tag{5.28}$$

Introduce δ_i as the difference between coarse LDR luminance in two consecutive bins:

$$\delta_i = \tilde{l}^{i+1}_{LDR}(1) - \tilde{l}^i_{LDR}(1). \tag{5.29}$$

The constraint related to the limit sum of the projected heights equal to the entire LDR range:

$$\sum_{i=1}^{B} a_i \cdot \delta_i = l_{LDRmax} - l_{LDRmin}. \tag{5.30}$$

The final equation involves the following result:

$$a_i = \frac{l_{LDRmax} - l_{LDRmin}}{\sum_{i=1}^{B} (\delta_i)^{M/(M+1)} \cdot (p_i)^{1/(M+1)}} \cdot (\frac{p_i}{\delta_i})^{1/(M+1)}. \tag{5.31}$$

See section 3 in Chapter 3. In the specific cases: (i) if the parameter $M \to \infty$, the limitation of slope a_i is constant:

$$a_i = \frac{l_{LDRmax} - l_{LDRmin}}{\tilde{l}^B_{LDR}(K_B) - \tilde{l}^1_{LDR}(1)} = const, \tag{5.32}$$

(ii) if the parameter $M \to 0$, the limitation of slope a_i is:

$$a_i = \frac{l_{LDRmax} - l_{LDRmin}}{\delta_i} \cdot p_i. \tag{5.33}$$

The unknown parameter b_i is calculated by the equation: $b_i = \hat{l}^i_{LDR}(1) - a_i \times \tilde{l}^i_{LDR}(1)$. LDR mapped values are computed as follows:

$$\hat{l}^i_{LDR}(k) = a_i \tilde{l}^i_{LDR}(k) + b_i \quad \text{with } k \in [1, K_i]. \tag{5.34}$$

The global piecewise linear curve is continuous and strictly monotonic increasing according to the positive slopes (i.e $a_i > 0$, or angles $0° < \text{atan}(a_i) < 90°$).

7 Simulation results

This section evaluates the quality of the proposed HDR tone mapped images. Simulations have been conducted under Matlab environment using the HDR Toolbox using a large set of test HDR images with low, medium and high f-stops ([1]). The tone-mapped image quality is measured with the Tone-Mapped image Quality Index 1 (TMQI1) metric developed in [34]. This metric, upper-bounded by 1, evaluates the quality of the LDR image using the original HDR image.

The proposed TM approaches, namely:

i. "Proposed_CEDP_Opt_LJ_NM" for adaptive β_i deduced from equation (5.26) with $M = 1,2,3,4,6,10$ ($\ell_1, \ell_2, \ell_3, \ell_4, \ell_6, \ell_{10}$),

ii. "Proposed_CEDP_Lin_LJ_NM" for constant $\beta_i = 0.25$ with $M = 1,2,3,4,6,10$,

iii. "Proposed_CEDP_LJ_NIn" for the case ℓ_∞ with a_i given by equation (5.32),

iv. "Proposed_CEDP_LJ_NZe" for a_i given by equation (5.33),

are deployed with $B = 256$, $l_{LDRmax} = 255$, $l_{LDRmin} = 0$, $J = 1, ..., 5$.

TMQI1 metrics of those algorithms are provided in Table 5.1 for different levels ($J = 1, ..., 5$) and in Table 5.2 for different norms ($M = 1,2,3,4,6,10$). Almost the TMQI1 metrics of "Proposed_CEDP_Lin" method are higher than those of "Proposed_CEDP_Opt". The visual quality for two approaches is good and almost the same as shown in Figure 5.8 although the intermediate mapping curves are fairly different (see Figure 5.9).

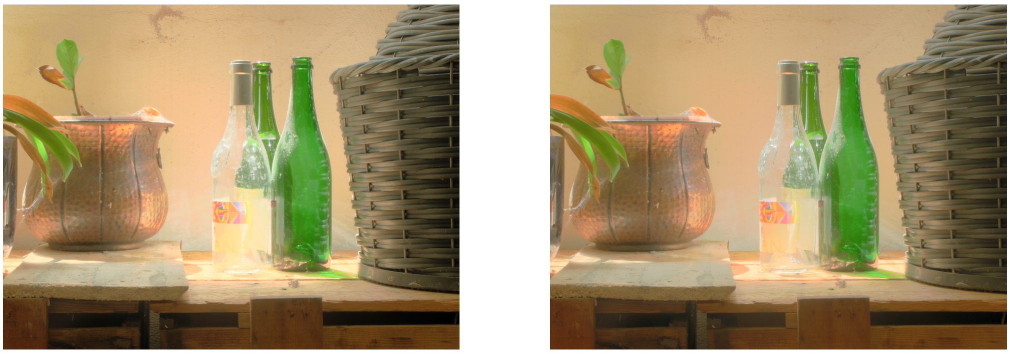

Figure 5.8: *"BottlesSmall" HDR test image (16.03 f-stops) - Left image: Pro_CEDP_Lin_L1_N1 (TMQI1=0.878); Right image: Pro_CEDP_Opt_L1_N1 (TMQI1=0.854).*

In most cases, one can observe that (i) less norm space concerns, more the performance increases; (ii) more number of decomposition level concerns, more the metric performance is. Figure 5.10 compares the visual quality of the "BottlesSmall" tone mapped image using 1 and 5 decomposition levels. One can notice that the details are well rendered when 5 decompositions are used. This is shown in Figure 5.11 by zooming in on the table board of the luminance tone mapped images. This is found the intermediate mapping curves in Figure 5.12 with impacts of increasing the number of resolution levels from $J = 1$ until $J = 5$. The intermediate mapping curves in Figure 5.13 and Figure 5.14 show impacts of increasing the number of norm spaces ($M = 1,2,3,4,6,10$) for the "Light" and "BottlesSmall" HDR test images. The curves' behaviors are very different.

Table 5.3 shows TMQI1 of both methods "Pro_CEDP_Lin" and "Pro_CEDP_Opt" for the "Light" HDR test image at several norms ($M = 1,2,3,4,5$) and levels ($J =$

Table 5.1: *Tone Mapped Image Quality Index 1 (TMQI1) for several levels $J = 1,2,3,4,5$ (absolute norm $M = 1$).*

Images	DR f-stops	Pro_CEDP_Lin_L1_N1	Pro_CEDP_Lin_L2_N1	Pro_CEDP_Lin_L3_N1	Pro_CEDP_Lin_L4_N1	Pro_CEDP_Lin_L5_N1	Pro_CEDP_Opt_L1_N1	Pro_CEDP_Opt_L2_N1	Pro_CEDP_Opt_L3_N1	Pro_CEDP_Opt_L4_N1	Pro_CEDP_Opt_L5_N1
Lausanne1	7.71	0.903	0.920	0.946	0.965	**0.970**	0.875	0.886	0.906	0.924	**0.930**
CraterLake1	8.13	0.899	0.913	0.934	0.947	**0.949**	0.866	0.876	0.888	0.905	**0.914**
Shasta2	8.48	0.885	0.904	0.929	0.955	**0.968**	0.830	0.841	0.856	0.866	**0.875**
Synagogue	8.57	0.877	0.890	0.905	**0.908**	0.902	0.813	0.823	0.838	0.847	**0.861**
Anturium	8.73	0.957	0.975	**0.984**	0.980	0.969	0.931	0.928	0.931	0.935	**0.936**
BowRiver	9.53	0.951	0.966	**0.969**	0.956	0.937	**0.838**	0.823	0.821	0.816	0.812
Bridges	11.17	0.955	0.965	**0.974**	0.971	0.959	0.935	0.933	0.936	0.944	**0.949**
Stairway1	13.37	0.882	0.898	0.920	0.939	**0.952**	**0.842**	0.829	0.827	0.827	0.828
ArchRock	13.60	0.986	**0.987**	0.976	0.950	0.925	**0.907**	0.885	0.873	0.871	0.873
DollDoll	13.89	0.873	0.896	0.920	0.935	**0.944**	0.842	0.839	0.840	**0.843**	0.841
ClockBuilding	14.19	0.940	0.949	**0.951**	0.940	0.925	0.901	0.903	0.905	0.907	**0.910**
OxfordChurch	15.43	0.980	**0.989**	0.982	0.963	0.942	**0.878**	0.864	0.861	0.860	0.859
BottlesSmall	16.03	0.878	0.897	0.919	0.933	**0.939**	0.854	0.868	0.882	0.893	**0.901**
Montreal	16.06	0.900	0.921	0.935	**0.937**	0.930	0.751	0.747	0.749	0.752	**0.757**
SmallOffice	16.29	0.943	**0.946**	0.945	0.935	0.921	**0.918**	0.903	0.891	0.887	0.885
Light	17.46	0.971	**0.973**	0.968	0.957	0.945	0.920	0.923	0.931	0.937	**0.942**
BridgeStudios2	18.13	0.912	0.941	0.962	**0.963**	0.953	0.847	0.853	0.852	0.855	**0.861**
Memorial	18.38	**0.960**	0.945	0.917	0.889	0.867	**0.923**	0.918	0.917	0.915	0.912
ClaridgeHotel	23.44	0.920	0.934	0.952	0.963	**0.967**	**0.743**	0.717	0.700	0.705	0.702
Mistaya1	23.77	0.935	0.959	0.972	**0.974**	0.966	**0.810**	0.785	0.770	0.763	0.761
BrookHouse	23.98	0.979	**0.985**	0.980	0.961	0.938	**0.850**	0.841	0.839	0.838	0.840
PeaceRocks	24.13	**0.950**	0.937	0.914	0.881	0.855	**0.772**	0.761	0.755	0.748	0.745
GGpark2	24.41	0.979	**0.985**	0.982	0.964	0.942	**0.779**	0.766	0.762	0.760	0.760
AtriumNight	28.68	**0.970**	0.945	0.917	0.894	0.878	**0.806**	0.790	0.778	0.771	0.768

Table 5.2: *Tone Mapped Image Quality Index 1 (TMQI1) for several norms* $M = 1,2,3,6$, *NIn and NZe (one level* $J = 1$*).*

Images	DR f-stops	Pro_CEDP_L1_NZe	Pro_CEDP_L1_NIn	Pro_CEDP_Lin_L1_N1	Pro_CEDP_Lin_L1_N2	Pro_CEDP_Lin_L1_N3	Pro_CEDP_Opt_L1_N6	Pro_CEDP_Opt_L1_N1	Pro_CEDP_Opt_L1_N2	Pro_CEDP_Opt_L1_N3	Pro_CEDP_Opt_L1_N6
Lausanne1	7.71	**0.924**	0.846	0.903	0.889	0.881	0.868	0.875	0.866	0.861	0.854
CraterLake1	8.13	**0.953**	0.821	0.899	0.877	0.864	0.847	0.866	0.851	0.843	0.833
Shasta2	8.48	**0.942**	0.779	0.885	0.854	0.836	0.811	0.830	0.810	0.801	0.791
Synagogue	8.57	**0.971**	0.761	0.877	0.835	0.814	0.789	0.813	0.792	0.783	0.773
Anturium	8.73	**0.963**	0.896	0.957	0.946	0.938	0.924	0.931	0.921	0.915	0.907
BowRiver	9.53	**0.958**	0.782	0.951	0.928	0.911	0.876	0.838	0.815	0.805	0.794
Bridges	11.17	**0.959**	0.905	0.955	0.946	0.939	0.927	0.935	0.926	0.921	0.915
Stairway1	13.37	**0.915**	0.793	0.882	0.865	0.854	0.834	0.842	0.828	0.820	0.809
ArchRock	13.60	0.938	0.836	**0.986**	0.967	0.948	0.908	0.907	0.880	0.868	0.853
DollDoll	13.89	**0.896**	0.800	0.873	0.855	0.843	0.826	0.842	0.828	0.820	0.812
ClockBuilding	14.19	**0.962**	0.848	0.940	0.925	0.912	0.889	0.901	0.884	0.875	0.863
OxfordChurch	15.43	0.969	0.816	**0.980**	0.954	0.935	0.902	0.878	0.855	0.845	0.833
BottlesSmall	16.03	**0.922**	0.823	0.878	0.863	0.854	0.841	0.854	0.844	0.838	0.831
Montreal	16.06	**0.947**	0.687	0.900	0.833	0.790	0.742	0.751	0.728	0.718	0.704
SmallOffice	16.29	**0.963**	0.863	0.943	0.938	0.934	0.924	0.918	0.902	0.893	0.881
Light	17.46	0.955	0.831	**0.971**	0.954	0.933	0.895	0.920	0.891	0.876	0.856
BridgeStudios2	18.13	**0.965**	0.780	0.912	0.875	0.857	0.829	0.847	0.825	0.814	0.800
Memorial	18.38	0.896	0.833	**0.960**	0.951	0.929	0.888	0.923	0.891	0.875	0.855
ClaridgeHotel	23.44	**0.939**	0.702	0.920	0.900	0.881	0.836	0.743	0.729	0.722	0.713
Mistaya1	23.77	**0.967**	0.744	0.935	0.896	0.868	0.829	0.810	0.786	0.777	0.764
BrookHouse	23.98	0.971	0.772	**0.979**	0.951	0.910	0.833	0.850	0.809	0.796	0.784
PeaceRocks	24.13	0.889	0.735	**0.950**	0.965	0.960	0.907	0.772	0.760	0.755	0.747
GGpark2	24.41	0.970	0.737	**0.979**	0.956	0.925	0.859	0.779	0.765	0.760	0.753
AtriumNight	28.68	0.905	0.744	**0.970**	0.958	0.929	0.867	0.806	0.784	0.774	0.762

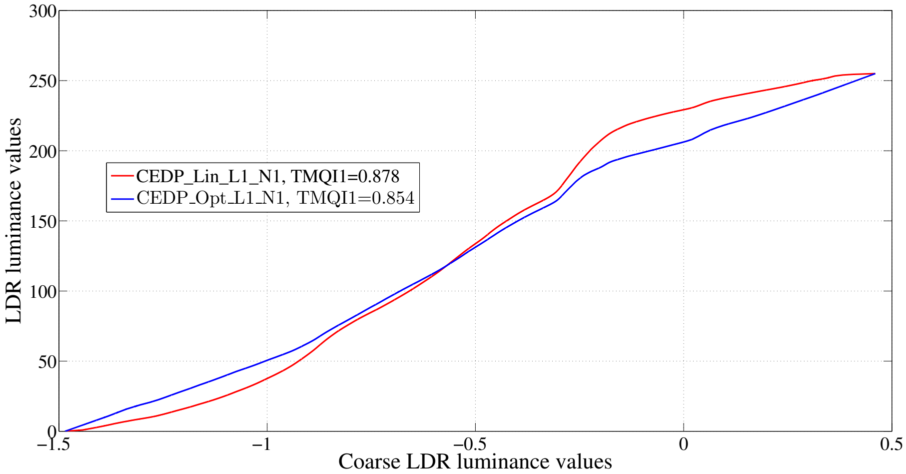

Figure 5.9: *Intermediate mapping curves for "BottlesSmall" HDR test image: Pro_CEDP_Lin_L1_N1 versus Pro_CEDP_Opt_L1_N1.*

Figure 5.10: *"BottlesSmall" HDR test image (16.03 f-stops) - Left image: Pro_CEDP_Lin_L5_N1 (TMQI1=0.939); Right image: Pro_CEDP_Lin_L1_N1 (TMQI1=0.878).*

1, 2, 3, 4, 5). There are two directional ways: the norm is represented for enhancing contrast while the level is for extracting details visibility. There are 50 (= 5 × 10) metric results. One can see that the highest value (0.973) is belonged to method "Pro_CEDP_Lin" at norm 1 and level 1.

Figure 5.15 compares the visual quality of the "SmallOffice" tone mapped image using "Duan", "Fattal" WRB, "Li" and our approach. Compared to other tone mapped images, "Li" tone mapped image doesn't seem to be natural. Indeed its normalized histogram given in Figure 5.16 shows that the pixel grey levels are limited to 60. Some of the details from outside the office (via the window) are lost on "Fattal" tone mapped image (brightness) contrary to our approach and "Duan" method. Indeed the brightness on "Fattal" tone mapped image is confirmed by the pic corresponding to a grey level equal to 255 on its normalized histogram (see Figure 5.16). However "Duan" tone

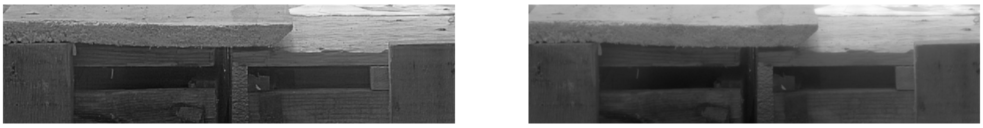

Figure 5.11: *"BottlesSmall" LDR image luminance cropped and zoomed - Left image: Pro_CEDP_Lin_L5_N1 (TMQI1=0.939); Right image: Pro_CEDP_Lin_L1_N1 (TMQI1=0.878).*

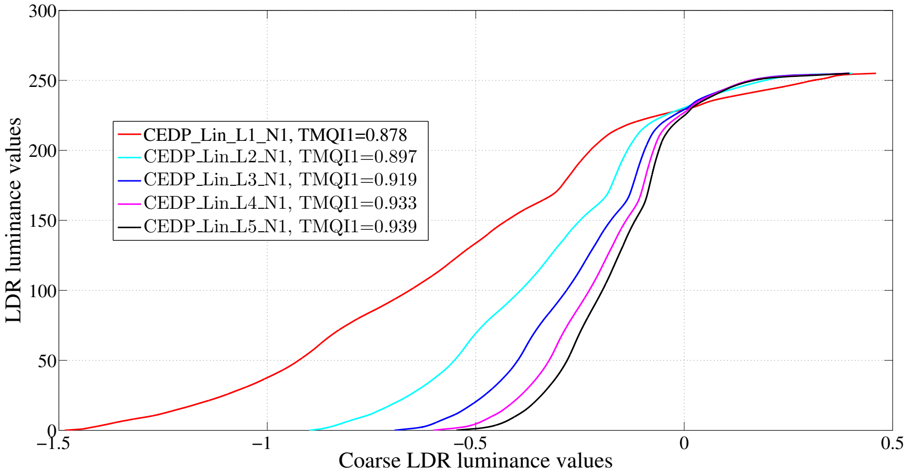

Figure 5.12: *Intermediate mapping curves for "BottlesSmall" HDR test image for Pro_CEDP_Lin_LJ_N1: impact of increasing the number of resolution levels from $J = 1$ until $J = 5$.*

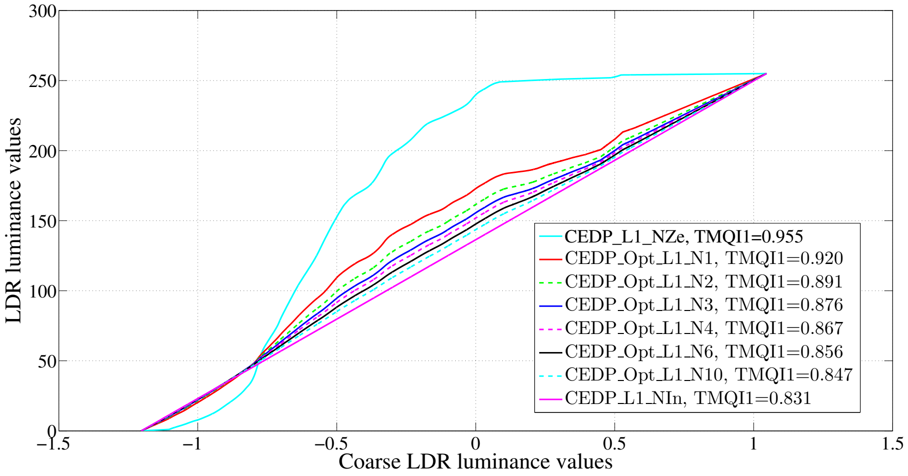

Figure 5.13: *"Light" HDR test image (17.46 f-stops) - Intermediate mapping curves for Pro_CEDP_Opt_L1_NM: impact of increasing the number of norm spaces $M = 1, 2, 3, 4, 6, 10$, NIn and NZe.*

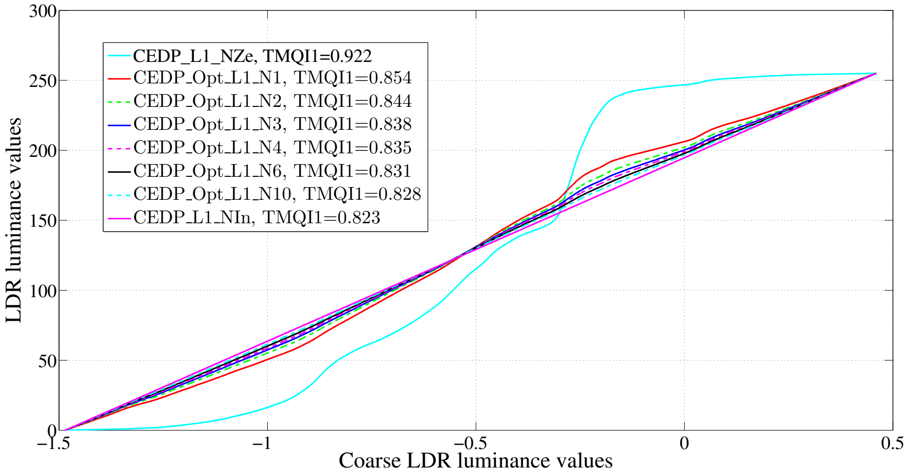

Figure 5.14: *"BottlesSmall" HDR test image (16.03 f-stops) - Intermediate mapping curves for Pro_CEDP_Opt_L1_NM: impact of increasing the number of norm spaces* $M = 1, 2, 3, 4, 6, 10$, *NIn and NZe.*

Table 5.3: *"Light" HDR test image (17.46 f-stops) - Tone Mapped Image Quality Index 1 (TMQI1) for several norms* ($M = 1, 2, 3, 6$, *NIn and NZe) and levels* ($J = 1, 2, 3, 4, 5$).

Levels \Ns	Pro_CEDP_LJ_NZe	Pro_CEDP_LJ_NIn	Pro_CEDP_Lin_LJ_N1	Pro_CEDP_Lin_LJ_N2	Pro_CEDP_Lin_LJ_N3	Pro_CEDP_Lin_LJ_N6	Pro_CEDP_Opt_LJ_N1	Pro_CEDP_Opt_LJ_N2	Pro_CEDP_Opt_LJ_N3	Pro_CEDP_Opt_LJ_N6
Level $J = 1$	0.955	0.831	0.971	0.954	0.933	0.895	0.920	0.891	0.876	0.856
Level $J = 2$	0.942	0.841	**0.973**	0.963	0.947	0.911	0.923	0.897	0.883	0.864
Level $J = 3$	0.920	0.853	0.968	0.969	0.959	0.929	0.931	0.907	0.894	0.876
Level $J = 4$	0.894	0.864	0.957	0.969	0.964	0.941	0.937	0.915	0.903	0.887
Level $J = 5$	0.872	0.873	0.945	0.966	0.966	0.947	0.942	0.922	0.911	0.895

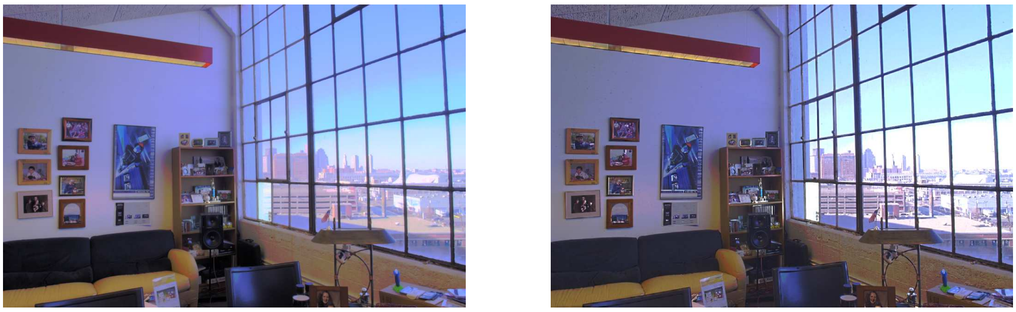

(a) Pro_CEDP_Lin_L1_N1 (TMQI1=0.943) **(b)** "Fattal" WRB (TMQI1=0.943)

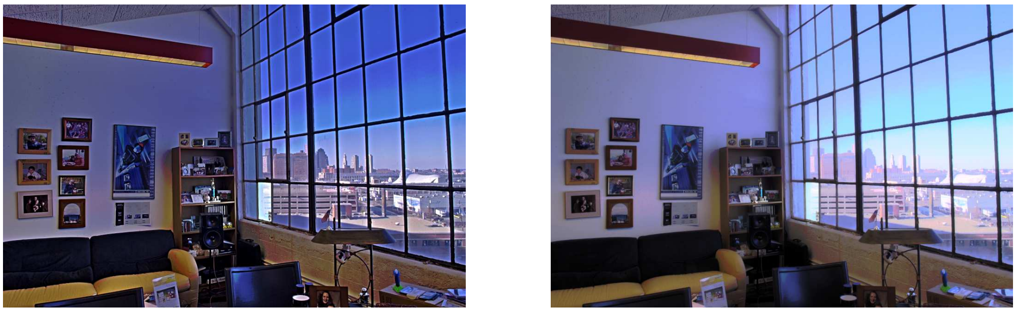

(c) "Li" (TMQI1=0.854) **(d)** "Duan" (TMQI1=0.955)

Figure 5.15: *"SmallOffice" HDR test image (16.29 f-stops) for some tone mapping operators.*

mapped image is a little darker (armchair, office wall) than our tone mapped image. This analysis is well supported by the normalized histograms of our approach and "Duan" method. The comparison of the histograms proves that our strategy stretches the too-dark areas and suppresses the too-bright areas.

Figure 5.17 compares the visual quality of the "Memorial" tone mapped image using "Duan" and "Fattal" methods and our approach. One can observe that the details are well rendered in favor of our method (e.g. tiles, rosette). Indeed the details on tills (see Figure 5.17) and rosette (see Figure 5.18) are better rendered by our approach. This is indeed confirmed by the metric values.

Figure 5.19 presents "AttriumNight" tone mapped image considered as high f-stops HDR image. Even if the TMQI related to the TM "Pro_SEPENOCA_L1" approach (0.973) is higher than our approach "Pro_CEDP_Opt_L1_N1" (0.806), the visual rendering is of better quality for the image mapped with our method (see details e.g. stairs). A similar result is provided by Figure 5.20 where the HDR "BrookHouse" image (high f-stops) has been mapped using "Fattal" method (0.982) and our approach (0.979). However the contrast of our tone mapped image is better. This also can be observed on Figure 5.21 using "Montreal" HDR test image where some details are indeed preserved (e.g. the tower roof). This can be explained by the fact that the choice of TMQI1

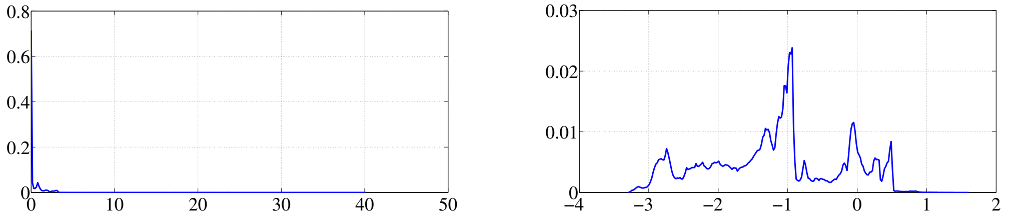

(a) Original HDR luminance **(b)** Logarithm of original HDR luminance

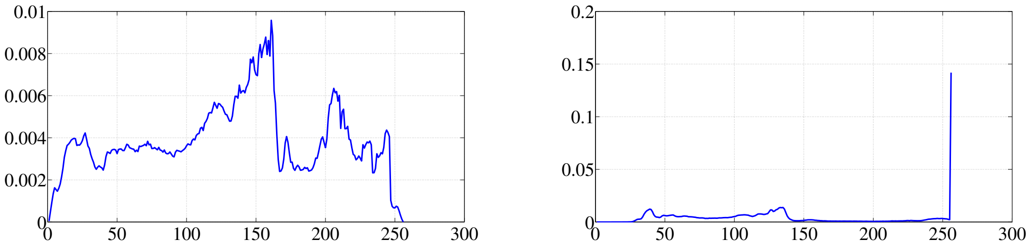

(c) Pro_CEDP_Lin_L1_N1 **(d)** "Fattal" WRB

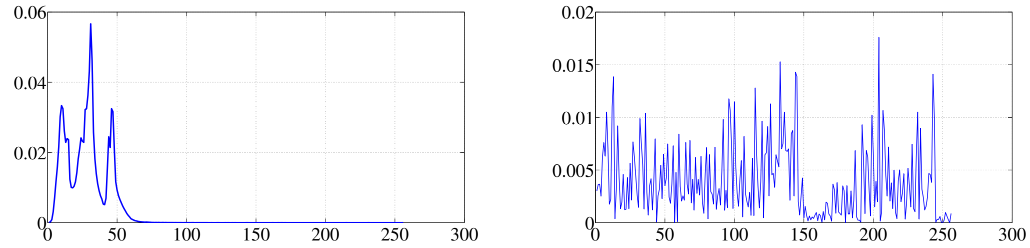

(e) "Li" **(f)** "Duan"

Figure 5.16: *Normalized histograms of original "SmallOffice" HDR luminance and its tone mapped images.*

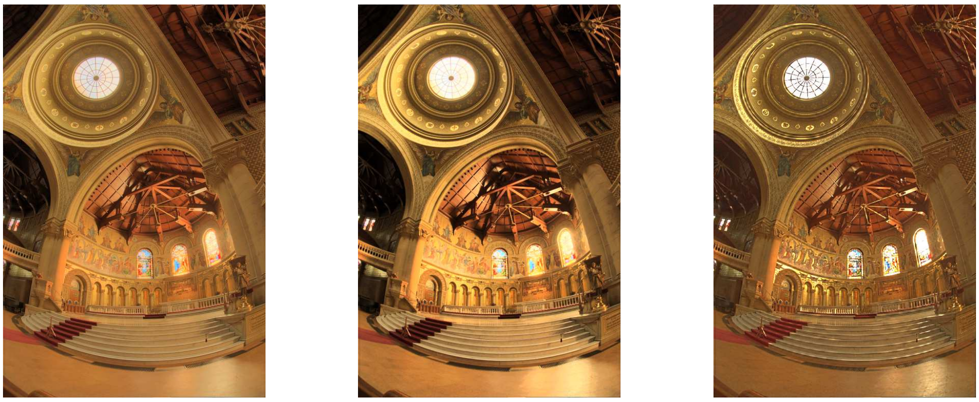

Figure 5.17: *"Memorial" HDR test image (18.38 f-stops) - Left image: Pro_CEDP_Lin_L1_N1 (TMQI1=0.960); Middle image: "Duan" (TMQI1=0.935); Right image: "Fattal" WRB (TMQI1=0.927).*

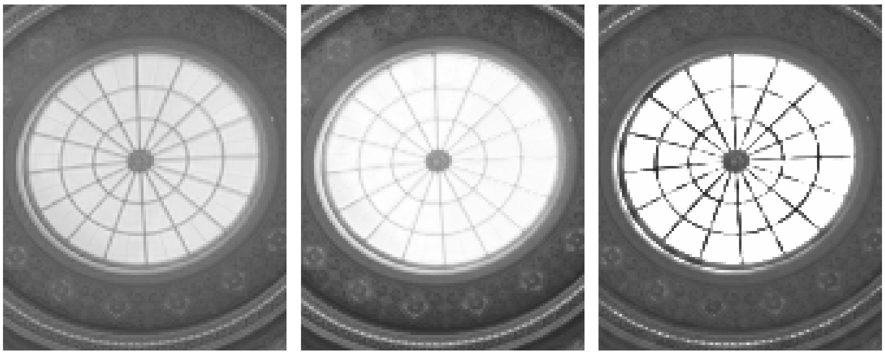

Figure 5.18: *"Memorial" LDR image luminance "Rosette" zoomed - Left image: Pro_CEDP_Lin_L1_N1 (TMQI1=0.960); Middle image: "Duan" (TMQI1=0.935); Right image: "Fattal" WRB (TMQI1=0.927).*

parameters were learned on 8 TM algorithms and therefore may not correspond to a relevant choice of its parameters in our favor (see [34]).

Figure 5.22 represents "OxfordChurch" tone mapped image, considered as medium f-stops HDR image, using "Duan" method and our approach. Although the metrics are slightly different (0.986 versus 0.980, respectively), the visual rendering is of better quality in favour of our method, especially in the stained glass window at the back of the church.

Figure 5.23 compares the visual quality of the "WardFlowers" tone mapped image using "Fattal" and our approach. Some details, on flowers and rocks, are lost on "Fattal" tone mapped image compared to our approach. Moreover, our tone mapped image if of better contrast. A similar result is provided by Figure 5.24 where the HDR "StreetLamp" image has been mapped using "Pro_SEPENOCA_L1" method and our method. The brightness of our tone mapped is better.

This approach increases the number of the multiresolution level up to 5, compared to the TMOs using ENO multiresoltion (to 2). The performance of our approach is confirmed on more than 274 test HDR images where the details and contrast are better represented than other competitive methods.

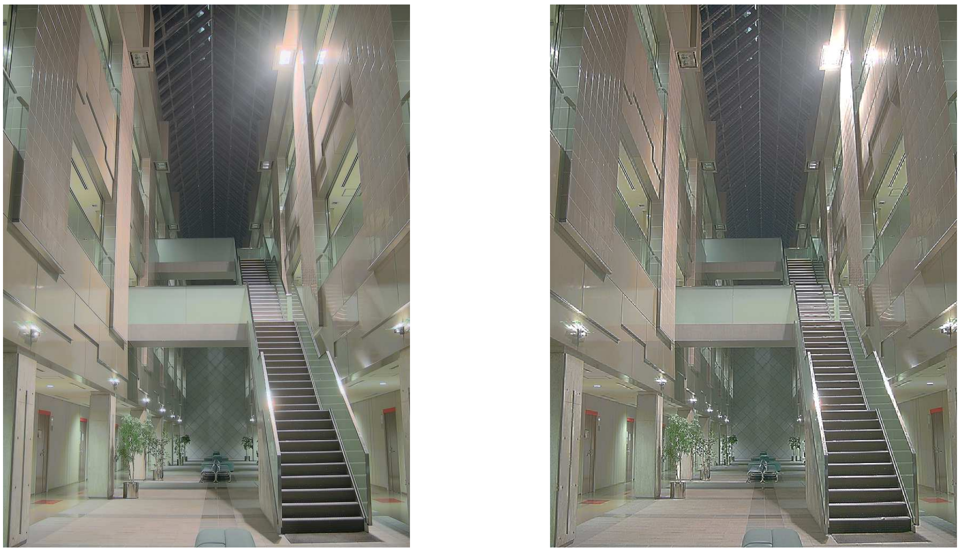

Figure 5.19: *"AtriumNight" HDR test image (28.68 f-stops) - Left image: Pro_CEDP_Opt_L1_N1 (TMQI1=0.806); Right image: Pro_SEPENOCA_L1 (TMQI1=0.973).*

Figure 5.20: *"BrookHouse" HDR test image (23.98 f-stops) - Left image: Pro_CEDP_Lin_L1_N1 (TMQI1=0.979); Right image: "Fattal" WRB (TMQI1=0.982).*

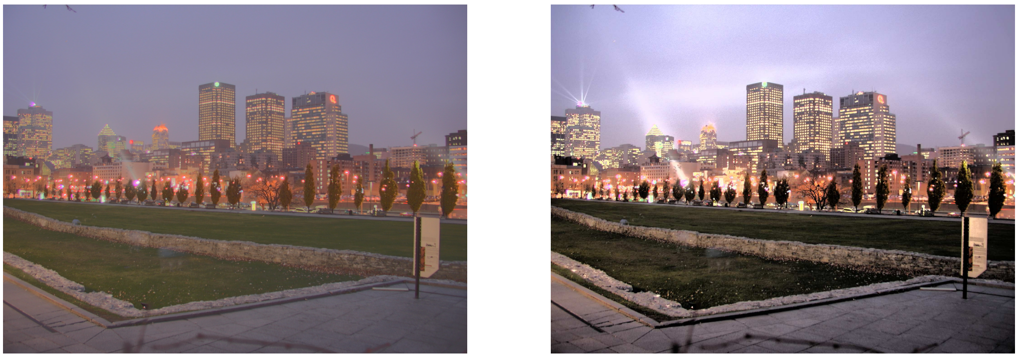

Figure 5.21: *"Montreal" HDR test image (16.06 f-stops) - Left image: Pro_CEDP_Opt_L1_N1 (TMQI1=0.751); Right image: "Husseis" (TMQI1=0.945).*

Figure 5.22: *"OxfordChurch" HDR test image (15.43 f-stops) - Left image: Pro_CEDP_Lin_L1_N1 (TMQI1=0.980); Right image: "Duan" (TMQI1=0.986).*

Figure 5.23: *"WardFlowers" HDR test image (14.01 f-stops) - Left image: Pro_CEDP_Lin_L1_N1 (TMQI1=0.930); Right image: "Fattal" WRB (TMQI1=0.875).*

Figure 5.24: *"StreetLamp" HDR test image (13.83 f-stops) - Left image: Pro_CEDP_Lin_L1_N1 (TMQI1=0.911); Right image: "Pro_SEPENOCA_L1" (TMQI1=0.855).*

8 Conclusion

A new HDR image TM approach which is able not only to preserve the relevant details but also to enhance the contrast of LDR images has been proposed. This is essentially related to: (i) the forward process of the near optimal local adaptive Cell- Average lifting scheme where the filter coefficients are locally adapted to the content; (ii) the weighting operation depending on the entropy of each resolution level; (iii) the adjustment of the coarse LDR image luminance distribution according to the perceptual piecewise linear function. Simulation results performed on a large set of HDR test images (low, medium and high f-stops) confirm the relevance of the proposed approach both in terms of the TMQI metric and the visual quality of the displayed image.

The next chapter presents a study of HDR image tone mapping assessment based on the improvement of the tone mapped quality index (TMQI) according to our training dataset.

CHAPTER 6

Impact of the TMQI parameters on the visual quality of the tone mapped images

Abstract

This chapter discusses the choice of the parameters of the TMQI metric. A discussion around these parameters shows their inadequacy since the experimental context has been modified. The proposed parameters show a strong correlation between the modified metric and the MOS.

Chapter content

1 Introduction

The authors in [34] proposed the TMQI1 and used a small dataset of 8 TMOs named "Reinhard" [12], "Drago" [10], "Durand" [16], "Mantiuk [59], "Pattanaik" [9] and three remained TMOs in Adobe Photoshop namely "Exposure and Gamma", "Equalize Histogram" and "Local Adaptation" respectively, and 15 HDR test images whose dynamic range from 8 f-stops to 18 f-stops. These images are available at the web-page site [1]. The mean opinion scores were given with corresponding HDR displays ranging from 1 until 8: 1 for the best, 8 for the worst, upon 20 observers. The training process was based on the Pearson's Linear Correlation Coefficient. The parameters of the TMQI1 were obtained: $a = 0.8012$, $\alpha = 0.3046$ and $\beta = 0.7088$ with the following equation (see section 3.2.2 in Chapter 2).

$$TMQI1(\mathbf{I}_{HDR}, \mathbf{I}_{LDR}) = a \times SF1^{\alpha}(\mathbf{I}_{HDR}, \mathbf{I}_{LDR}) + (1-a) \times SN1^{\beta}(\mathbf{I}_{LDR}). \quad (6.1)$$

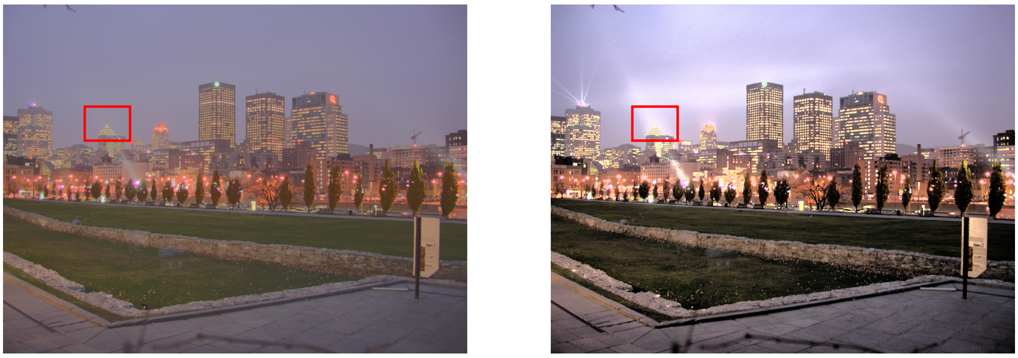

Figure 6.1: *"Montreal" HDR test image (16.06 f-stops) - Left image: Pro_CEDP_Opt_L1_N1 (TMQI1=0.751); Right image: "Husseis" (TMQI1=0.945).*

Figure 6.2: *"Montreal" LDR image luminance of "tower roof" zoomed - Left image: Pro_CEDP_Opt_L1_N1 (TMQI1=0.751); Right image: "Husseis" (TMQI1=0.945).*

For the TMQI1, there is no relation between the visual quality and the metric for the "Montreal" HDR tone mapped image where some details are indeed preserved (e.g.

---

[1] `http://qtpfsgui.sourceforge.net/`

the tower roof) as Figure 6.1 where the red rectangles frame the specific areas shown in Figure 6.2. This can be explained by the fact that the choice of TMQI1 parameters were learned on the small dataset (8 TM algorithms and 15 HDR test images) and therefore may not correspond to a relevant choice of its parameters in our favor.

2 Tone mapping quality index for machine learning

The Mean Opinion Score (MOS), as subjective quality measure requiring the services of a huge number of human observers, has been long regarded as the best method of image quality measurement. However, the MOS method is expensive, and it is usually too slow to be useful in real-world applications. The goal of objective image quality assessment research is to design computational model that can predict perceived image quality accurately and automatically. The modified metric is described as follows.

2.1 Build the training dataset

The training dataset uses 24 HDR test images with different dynamic range (or contrast ratio) from 7 f-stops to 29 f-stops namely "Lausanne1", "CraterLake1", "Shasta2", "Synagogue", "Anturium", "BowRiver", "Bridges", "Stairway1", "ArchRock", "DollDoll", "ClockBuilding", "OxfordChurch", "BottlesSmall", "Montreal", "SmallOffice", "Light", "BridgeStudios2", "Memorial", "ClaridgeHotel", "Mistaya1", "BrookHouse", "PeaceRocks", "GGpark2" and "AtriumNight", see Figure D.1a to Figure D.1x in Appendix D.

15 TM methods are used to test such as "Drago" [10], "Reinhard" [44], "Ward" [7], "Durand" [16], "Tumblin" [31], "Schlick" [3], "Duan" [8], "Fattal" WRB [25], "Li" [26], "Husseis" [30], "Proposed_NUHA", "Proposed_SEPENO", "Proposed_NONSEPENO", "Proposed_CEDP_Lin" and "Proposed_CEDP_Opt".

2.2 Mean opinion score

The TM images are shown on the ColorEdge CG242W Color LCD monitor with a good calibration in a random order (with no-reference of HDR displays) during the testing period. An observer notes each tone mapped image with the corresponding mark ranging from 0 until 5: 5 for *excellent*, 4 *very good*, 3 *good*, 2 *accepted*, 1 *unsatisfactory* and 0 *failed*. The chosen criteria is based on ability to recover details with natural ways. In order to have a confidential calculation, a Matlab User Graphic Interface has been proposed in Appendix D. The outcome of the experiments with 26 observers is shown in the MOS table (see Table 6.1).

2.3 Training, learning parameters

Our modified parameters are based on TMQI1 [34] with the bigger training dataset.

Table 6.1: *MOS with no-reference of HDR displays (ranging from 0 until 5: 5 for excellent, 4 very good, 3 good, 2 accepted, 1 unsatisfactory and 0 failed; All values are rounded by two-decimals precision).*

Images	Drago [10]	Reinhard [44]	Ward [7]	Durand [16]	Tumblin [31]	Schlick [3]	Duan [8]	Fattal [25]	Li [26]	Husseis [30]	Pro_NUHA	Pro_SEPENO	NONSEPENO	Pro_CEDP_Lin	Pro_CEDP_Opt
Lausanne1	1.56	1.63	1.06	0.63	1.00	1.13	3.06	3.00	2.31	2.94	3.44	3.13	3.00	3.63	3.75
CraterLake1	1.75	1.88	1.25	1.06	1.13	2.19	2.50	2.50	2.19	2.38	2.75	2.56	2.31	2.88	3.00
Shasta2	1.25	1.19	0.81	0.69	1.13	1.25	2.44	2.56	2.00	2.31	2.75	2.63	2.38	2.81	2.94
Synagogue	2.19	2.00	0.38	0.31	0.63	1.13	2.63	2.88	2.19	2.69	3.13	3.00	2.81	3.75	4.06
Anturium	2.00	1.81	0.69	0.63	0.94	0.75	2.94	3.31	1.88	3.00	3.75	3.44	3.13	4.06	4.38
BowRiver	1.63	1.75	1.00	1.06	1.25	1.81	2.44	2.56	2.00	2.50	2.50	2.63	2.38	2.75	3.13
Bridges	2.38	2.31	0.81	0.25	1.69	1.44	3.19	3.38	2.31	3.00	3.94	3.44	3.25	4.06	4.19
Stairway1	2.06	2.13	1.25	0.44	1.75	1.63	2.88	2.94	2.00	2.94	3.00	3.00	2.94	3.06	3.13
ArchRock	2.19	2.31	1.69	0.44	0.94	0.75	2.94	3.06	2.38	2.94	3.19	3.13	3.00	3.13	3.00
DollDoll	1.75	1.13	0.63	0.50	0.38	1.19	3.38	2.88	2.63	3.25	3.63	3.00	3.44	3.75	4.06
ClockBuilding	2.00	2.06	0.75	0.44	0.56	2.00	3.19	2.63	2.69	3.19	3.50	2.88	3.25	3.63	3.94
OxfordChurch	2.13	2.19	2.00	0.13	1.13	1.19	2.81	2.94	2.06	2.94	3.38	3.06	3.00	3.50	3.69
BottlesSmall	2.19	2.00	0.38	0.31	0.63	1.13	2.63	2.88	2.19	2.69	3.13	3.00	2.81	3.75	4.06
Montreal	1.75	1.88	1.25	1.06	1.13	2.19	2.50	2.50	2.19	2.38	2.75	2.56	2.31	2.88	3.00
SmallOffice	1.63	1.75	1.00	1.06	1.25	1.81	2.44	2.56	2.00	2.50	2.50	2.63	2.38	2.75	3.13
Light	1.56	1.63	1.06	0.63	1.00	1.13	3.06	3.00	2.31	2.94	3.44	3.13	3.00	3.63	3.75
BridgeStudios2	2.00	1.81	0.69	0.63	0.94	0.75	2.94	3.31	1.88	3.00	3.75	3.44	3.13	4.06	4.38
Memorial	1.25	1.19	0.81	0.69	1.13	1.25	2.44	2.56	2.00	2.31	2.75	2.63	2.38	2.81	2.94
ClaridgeHotel	2.06	2.13	1.25	0.44	1.75	1.63	2.88	2.94	2.00	2.94	3.00	3.00	2.94	3.06	2.13
Mistaya1	2.00	2.06	0.75	0.44	0.56	2.00	3.19	2.63	2.69	3.19	3.50	2.88	3.25	3.63	2.94
BrookHouse	2.19	2.31	1.69	0.44	0.94	0.75	2.94	3.06	2.38	2.94	3.19	3.13	3.00	3.13	2.00
PeaceRocks	2.13	2.19	2.00	0.13	1.13	1.19	2.81	2.94	2.06	2.94	3.38	3.06	3.00	3.50	2.69
GGpark2	2.38	2.31	0.81	0.25	1.69	1.44	3.19	3.38	2.31	3.00	3.94	3.44	3.25	4.06	2.19
AtriumNight	1.75	1.13	0.63	0.50	0.38	1.19	3.38	2.88	2.63	3.25	3.63	3.00	3.44	3.75	2.06
Average	1.91	1.86	1.03	0.55	1.04	1.37	2.86	2.89	2.22	2.84	**3.24**	**2.99**	**2.91**	**3.42**	**3.27**

2.3.1 Pearson's linear correlation coefficient

Denote

i. normalized matrix **MOS** for all figures in Table 6.1 with 24 HDR test images and 15 TMOs ($N = 24$ rows, $M = 15$ columns),

ii. matrix **TMQI** for the respective values that have been predicted by an objective quality metric (same size of **MOS**).

The predicted scores have been mapped to the same scale between 0 and 1. The Pearson's Linear Correlation Coefficient ($PLCC$) is a measure of the linear correlation between two matrices **MOS** and **TMQI**. This can be measured by $PLCC$ as

$$PLCC = \frac{\sum_{n=1}^{N}\sum_{m=1}^{M}(\mathbf{MOS}(n,m) - \overline{\mathbf{MOS}}) \cdot (\mathbf{TMQI}(n,m) - \overline{\mathbf{TMQI}})}{\sqrt{\sum_{n=1}^{N}\sum_{m=1}^{M}(\mathbf{MOS}(n,m) - \overline{\mathbf{MOS}})^2 \cdot \sum_{n=1}^{N}\sum_{m=1}^{M}(\mathbf{TMQI}(n,m) - \overline{\mathbf{TMQI}})^2}}, \tag{6.2}$$

where $\overline{\mathbf{MOS}}$ and $\overline{\mathbf{TMQI}}$ are mean values of two matrices **MOS** and **TMQI**, respectively. $PLCC$ has a value between -1 and $+1$, where $+1$ is total positive linear correlation, 0 is no linear correlation, and -1 is total negative linear correlation.

2.3.2 Approach 1

Approach 1 namely "TMQI_A1": Compute the best parameters by an iteration method for 24 HDR test images. See Algorithm 6.1.

2.3.3 Approach 2

Approach 2 namely "TMQI_A2": Compute the best parameters by an iteration method for each image and then compute final average results. See Algorithm 6.2.

Algorithm 6.1: Approach 1. Compute the best parameters in terms of the Pearson's linear correlation coefficient.

```
Input: MOS (24 images $\times$ 15 TMOs);
24 reference HDR images $\mathbf{I}_{HDR}(n)$, $n = 1..24$;
360 LDR images $\mathbf{I}_{LDR}(n,m)$, $n = 1..24$ and $m = 1..15$;
Output: Best set of parameters $a$, $\alpha$, $\beta$;

$Pmax = -1$;
for $a \leftarrow 0.1$ to 1 by 0.1 do
    for $\alpha \leftarrow 0.1$ to 1 by 0.1 do
        for $\beta \leftarrow 0.1$ to 1 by 0.1 do
            // Compute TMQI table (24 images x 15 TMOs) named $myTable$
               with current parameters
            for $n \leftarrow 1$ to 24 do
                for $m \leftarrow 1$ to 15 do
                    $myTable(n,m)$=theTMQI($\mathbf{I}_{HDR}(n)$, $\mathbf{I}_{LDR}(n,m)$, $a$, $\alpha$, $\beta$);
            // Compute Pearson's Linear Correlation Coefficient
            $P = PLCC(MOS,\ myTable)$;
            // Save max values
            if $P > Pmax$ then
                $best\_a = a$;
                $best\_alpha = \alpha$;
                $best\_beta = \beta$;
                $Pmax = P$;
```

```
Function theTMQI($\mathbf{I}_{HDR}$, $\mathbf{I}_{LDR}$, $a$, $\alpha$, $\beta$):
    Compute $SF1(\mathbf{I}_{HDR},\mathbf{I}_{LDR})$;
    Compute $SN1(\mathbf{I}_{LDR})$;
    $TMQI1 = a \times SF1^{\alpha} + (1-a) \times SN1^{\beta}$;
    return $TMQI1$;
```

Algorithm 6.2: Approach 2. Compute the best parameters in terms of the Pearson's linear correlation coefficient for each image and then compute final average results.

```
Input: MOS (24 images $\times$ 15 TMOs);
24 reference HDR images $\mathbf{I}_{HDR}(n)$, $n = 1..24$;
360 LDR images $\mathbf{I}_{LDR}(n,m)$, $n = 1..24$ and $m = 1..15$;
Output: Best final set of parameters $a$, $\alpha$, $\beta$;

for $n \leftarrow 1$ to 24 do
    $Pmax(n) = -1$;
    for $a \leftarrow 0.1$ to 1 by 0.1 do
        for $\alpha \leftarrow 0.1$ to 1 by 0.1 do
            for $\beta \leftarrow 0.1$ to 1 by 0.1 do
                // Compute TMQI vector (15 TMOs) named $myLine$ with
                   current parameters
                for $m \leftarrow 1$ to 15 do
                    $myLine(m)$=theTMQI($\mathbf{I}_{HDR}(n)$, $\mathbf{I}_{LDR}(n,m)$, $a$, $\alpha$, $\beta$);
                // Compute Pearson's Linear Correlation Coefficient
                $P = PLCC(MOS(n,:), myLine)$;
                // Save max values
                if $P > Pmax(n)$ then
                    $best\_a(n) = a$;
                    $best\_alpha(n) = \alpha$;
                    $best\_beta(n) = \beta$;
                    $Pmax(n) = P$;

// Save final results
$best\_final\_a = \text{mean}(best\_a)$;
$best\_final\_alpha = \text{mean}(best\_alpha)$;
$best\_final\_beta = \text{mean}(best\_beta)$;
```

3 Experimental results

After the training processes, the best parameters in terms of the PLCC for two approaches are described as follows:

i. Approach 1. TMQI_A1 with $a = 0.1$, $\alpha = 0.1$, $\beta = 0.2$ and $PLCC = 0.7120$,

ii. Approach 2. TMQI_A2 with $a = 0.192$, $\alpha = 0.213$, $\beta = 0.254$ and $PLCC = 0.7102$. Table 6.2 describes the best parameters for every HDR test image.

Table 6.3, Table 6.4 and Table 6.5 show tone mapped quality indexes for TMQI1, TMQI_A1 and TMQI_A2, respectively.

The experimental results based on four criteria are described as follows.

Table 6.2: *Approach 2 namely TMQI_A2. Compute the best parameters by an iteration method for each image and then compute final average results.*

Images	a	α	β	$Pmax$
Lausanne1	0.100	0.100	0.200	0.729
CraterLake1	0.100	0.100	0.200	0.708
Shasta2	0.100	0.100	0.100	0.824
Synagogue	0.100	0.100	0.100	0.340
Anturium	0.300	1.000	0.300	0.816
BowRiver	0.100	0.100	0.100	0.636
Bridges	0.100	0.100	0.100	0.838
Stairway1	0.100	0.100	0.100	0.640
ArchRock	0.100	0.100	0.800	0.776
DollDoll	0.100	0.100	0.200	0.858
ClockBuilding	0.100	0.100	0.100	0.837
OxfordChurch	0.100	0.100	0.400	0.694
BottlesSmall	0.600	1.000	0.300	0.774
Montreal	0.100	0.100	0.100	0.640
SmallOffice	0.600	0.100	0.200	0.917
Light	0.100	0.100	0.400	0.933
BridgeStudios2	0.100	0.100	0.100	0.713
Memorial	0.300	0.100	0.500	0.964
ClaridgeHotel	0.100	1.000	0.100	0.420
Mistaya1	0.100	0.100	0.200	0.597
BrookHouse	0.400	0.100	0.300	0.786
PeaceRocks	0.600	0.100	1.000	0.502
GGpark2	0.100	0.100	0.100	0.499
AtriumNight	0.100	0.100	0.100	0.835
Average	0.192	0.213	0.254	____

Table 6.3: *Default Tone Mapped Image Quality Index 1 (TMQI1) with* $a = 0.8012$*,* $\alpha = 0.3046$ *and* $\beta = 0.7088$ *(*$PLCC = 0.5880$*; All values are rounded by two-decimals precision).*

Images	Drago [10]	Reinhard [44]	Ward [7]	Durand [16]	Tumblin [31]	Schlick [3]	Duan [8]	Fattal [25]	Li [26]	Husseis [30]	Pro_NUHA	Pro_SEPENO	NONSEPENO	Pro_CEDP_Lin	Pro_CEDP_Opt
Lausanne1	0.82	0.79	0.70	0.84	0.78	0.75	0.91	0.83	0.98	0.92	0.92	0.83	0.93	0.97	0.93
CraterLake1	0.84	0.79	0.72	0.79	0.76	0.78	0.95	0.86	0.97	0.95	0.95	0.86	0.94	0.95	0.91
Shasta2	0.76	0.73	0.57	0.74	0.71	0.65	0.91	0.79	0.95	0.93	0.93	0.79	0.92	0.97	0.87
Synagogue	0.92	0.91	0.83	0.87	0.88	0.91	0.96	0.75	0.95	0.97	0.96	0.76	0.97	0.91	0.86
Anturium	0.86	0.79	0.72	0.81	0.77	0.76	0.96	0.89	0.96	0.96	0.96	0.90	0.98	0.98	0.94
BowRiver	0.82	0.78	0.73	0.88	0.79	0.78	0.96	0.86	0.96	0.96	0.96	0.87	0.95	0.97	0.84
Bridges	0.79	0.76	0.65	0.78	0.72	0.71	0.97	0.86	0.91	0.95	0.96	0.86	0.97	0.97	0.95
Stairway1	0.76	0.74	0.55	0.78	0.72	0.79	0.91	0.78	0.89	0.91	0.91	0.78	0.90	0.95	0.84
ArchRock	0.80	0.78	0.61	0.80	0.78	0.84	0.98	0.95	0.91	0.96	0.94	0.96	0.95	0.99	0.91
DollDoll	0.73	0.72	0.57	0.72	0.72	0.71	0.88	0.73	0.86	0.89	0.89	0.73	0.91	0.94	0.84
ClockBuilding	0.76	0.75	0.49	0.76	0.74	0.75	0.95	0.76	0.92	0.97	0.97	0.75	0.94	0.95	0.91
OxfordChurch	0.79	0.77	0.46	0.79	0.70	0.84	0.99	0.89	0.88	0.98	0.97	0.89	0.93	0.99	0.88
BottlesSmall	0.77	0.77	0.55	0.76	0.69	0.77	0.92	0.93	0.95	0.92	0.92	0.93	0.90	0.94	0.90
Montreal	0.62	0.34	0.34	0.67	0.59	0.59	0.86	0.62	0.90	0.94	0.94	0.62	0.82	0.94	0.76
SmallOffice	0.74	0.73	0.52	0.74	0.67	0.73	0.96	0.94	0.85	0.97	0.96	0.94	0.95	0.95	0.92
Light	0.79	0.78	0.36	0.76	0.55	0.76	0.97	0.97	0.89	0.97	0.96	0.97	0.96	0.97	0.94
BridgeStudios2	0.70	0.66	0.46	0.74	0.65	0.77	0.96	0.76	0.89	0.96	0.96	0.76	0.92	0.96	0.86
Memorial	0.78	0.77	0.36	0.77	0.54	0.76	0.94	0.93	0.83	0.92	0.92	0.93	0.91	0.96	0.92
ClaridgeHotel	0.81	0.77	0.69	0.83	0.75	0.24	0.93	0.86	0.96	0.93	0.93	0.86	0.94	0.97	0.70
Mistaya1	0.81	0.79	0.63	0.84	0.78	0.16	0.96	0.86	0.96	0.96	0.96	0.86	0.98	0.97	0.76
BrookHouse	0.81	0.77	0.66	0.82	0.76	0.09	0.98	0.98	0.93	0.98	0.97	0.98	0.98	0.98	0.84
PeaceRocks	0.84	0.79	0.74	0.82	0.78	0.11	0.92	0.83	0.85	0.91	0.89	0.84	0.94	0.95	0.75
GGpark2	0.82	0.78	0.70	0.84	0.77	0.11	0.97	0.84	0.93	0.97	0.97	0.85	0.98	0.99	0.76
AtriumNight	0.78	0.74	0.40	0.78	0.62	0.15	0.96	0.97	0.89	0.94	0.92	0.97	0.93	0.97	0.77

Table 6.4: *Approach 1. New Tone Mapped Image Quality Index 1 (TMQI_A1) with* $a = 0.1$, $\alpha = 0.1$ *and* $\beta = 0.2$ *(*$PLCC = 0.7120$*; All values are rounded by two-decimals precision).*

Images	Drago [10]	Reinhard [44]	Ward [7]	Durand [16]	Tumblin [31]	Schlick [3]	Duan [8]	Fattal [25]	Li [26]	Husseis [30]	Pro_NUHA	Pro_SEPENO	NONSEPENO	Pro_CEDP_Lin	Pro_CEDP_Opt
Lausanne1	0.64	0.49	0.28	0.69	0.43	0.47	0.90	0.73	0.99	0.90	0.91	0.75	0.94	0.98	0.94
CraterLake1	0.80	0.65	0.32	0.63	0.56	0.61	0.96	0.84	1.00	0.96	0.95	0.85	0.95	0.97	0.94
Shasta2	0.58	0.41	0.22	0.39	0.36	0.39	0.89	0.65	0.98	0.92	0.93	0.66	0.92	0.99	0.90
Synagogue	0.92	0.89	0.71	0.86	0.84	0.94	0.96	0.51	0.98	0.96	0.96	0.50	0.97	0.89	0.86
Anturium	0.79	0.60	0.31	0.61	0.49	0.55	0.97	0.86	0.97	0.97	0.96	0.87	0.99	1.00	0.95
BowRiver	0.70	0.47	0.32	0.84	0.51	0.64	0.99	0.82	0.97	0.99	0.98	0.84	0.97	1.00	0.77
Bridges	0.53	0.43	0.24	0.44	0.32	0.38	0.99	0.82	0.89	1.00	0.97	0.83	0.99	0.99	0.97
Stairway1	0.43	0.34	0.17	0.45	0.32	0.61	0.88	0.57	0.85	0.89	0.89	0.57	0.86	0.96	0.74
ArchRock	0.48	0.34	0.19	0.48	0.31	0.73	0.99	0.96	0.89	0.97	0.95	0.97	0.95	1.00	0.88
DollDoll	0.48	0.41	0.16	0.35	0.36	0.41	0.89	0.48	0.85	0.89	0.88	0.48	0.93	0.98	0.83
ClockBuilding	0.40	0.37	0.12	0.39	0.30	0.38	0.99	0.45	0.94	0.99	1.00	0.46	0.98	0.99	0.95
OxfordChurch	0.41	0.29	0.14	0.42	0.23	0.70	0.99	0.85	0.82	1.00	0.98	0.86	0.92	1.00	0.81
BottlesSmall	0.47	0.49	0.15	0.48	0.21	0.73	0.91	0.93	0.98	0.92	0.92	0.95	0.90	0.97	0.93
Montreal	0.20	0.09	0.09	0.26	0.20	0.18	0.91	0.26	0.94	0.97	0.97	0.26	0.85	1.00	0.78
SmallOffice	0.34	0.32	0.12	0.32	0.19	0.35	0.99	0.98	0.85	1.00	0.99	0.99	0.99	0.98	0.95
Light	0.48	0.46	0.09	0.42	0.13	0.42	1.00	1.00	0.87	1.00	0.98	0.99	0.98	1.00	0.97
BridgeStudios2	0.29	0.24	0.14	0.30	0.23	0.59	0.97	0.59	0.89	0.98	0.99	0.60	0.93	1.00	0.88
Memorial	0.40	0.32	0.09	0.40	0.14	0.30	0.95	0.94	0.73	0.94	0.94	0.93	0.91	0.99	0.94
ClaridgeHotel	0.65	0.50	0.25	0.74	0.40	0.18	0.92	0.79	0.98	0.92	0.93	0.80	0.94	0.99	0.50
Mistaya1	0.58	0.45	0.19	0.73	0.40	0.18	0.97	0.78	0.96	0.97	0.97	0.79	1.00	0.99	0.55
BrookHouse	0.56	0.45	0.22	0.61	0.37	0.14	0.99	1.00	0.92	0.99	0.99	1.00	1.00	1.00	0.81
PeaceRocks	0.75	0.51	0.27	0.70	0.45	0.20	0.94	0.76	0.75	0.93	0.90	0.79	0.97	0.98	0.51
GGpark2	0.65	0.46	0.31	0.70	0.44	0.14	0.99	0.76	0.91	0.99	0.98	0.79	1.00	1.00	0.62
AtriumNight	0.42	0.25	0.12	0.58	0.16	0.21	0.98	0.99	0.87	0.96	0.93	0.99	0.94	0.99	0.59

Table 6.5: *Approach 2. New Tone Mapped Image Quality Index 1 (TMQI_A2) with* $a = 0.192$, $\alpha = 0.213$ *and* $\beta = 0.254$ *(*$PLCC = 0.7102$*; All values are rounded by two-decimals precision).*

Images	Drago [10]	Reinhard [44]	Ward [7]	Durand [16]	Tumblin [31]	Schlick [3]	Duan [8]	Fattal [25]	Li [26]	Husseis [30]	Pro_NUHA	Pro_SEPENO	NONSEPENO	Pro_CEDP_Lin	Pro_CEDP_Opt
Lausanne1	0.62	0.47	0.28	0.66	0.42	0.45	0.88	0.71	0.99	0.89	0.89	0.73	0.92	0.98	0.93
CraterLake1	0.78	0.62	0.32	0.60	0.53	0.58	0.95	0.82	0.99	0.95	0.95	0.83	0.94	0.96	0.93
Shasta2	0.55	0.39	0.22	0.37	0.34	0.36	0.87	0.62	0.97	0.91	0.92	0.63	0.90	0.99	0.88
Synagogue	0.90	0.87	0.68	0.84	0.82	0.93	0.95	0.48	0.97	0.96	0.95	0.47	0.97	0.87	0.84
Anturium	0.76	0.58	0.31	0.58	0.47	0.52	0.96	0.84	0.96	0.96	0.95	0.86	0.99	0.99	0.94
BowRiver	0.67	0.45	0.32	0.82	0.49	0.61	0.98	0.80	0.97	0.98	0.98	0.82	0.96	0.99	0.75
Bridges	0.50	0.41	0.25	0.42	0.32	0.36	0.98	0.79	0.88	0.99	0.97	0.81	0.98	0.99	0.96
Stairway1	0.41	0.34	0.19	0.43	0.31	0.58	0.86	0.54	0.83	0.88	0.88	0.54	0.84	0.96	0.71
ArchRock	0.46	0.34	0.21	0.46	0.32	0.70	0.99	0.95	0.88	0.97	0.94	0.96	0.94	1.00	0.86
DollDoll	0.45	0.39	0.18	0.34	0.35	0.39	0.87	0.45	0.83	0.87	0.86	0.46	0.91	0.97	0.81
ClockBuilding	0.39	0.36	0.15	0.38	0.30	0.37	0.98	0.43	0.93	0.99	0.99	0.44	0.97	0.98	0.94
OxfordChurch	0.40	0.30	0.16	0.41	0.25	0.67	0.99	0.83	0.80	0.99	0.98	0.84	0.91	1.00	0.79
BottlesSmall	0.45	0.47	0.17	0.45	0.23	0.70	0.90	0.92	0.98	0.91	0.91	0.94	0.89	0.96	0.91
Montreal	0.21	0.11	0.11	0.26	0.21	0.20	0.89	0.25	0.92	0.96	0.96	0.26	0.82	0.99	0.75
SmallOffice	0.34	0.32	0.15	0.32	0.22	0.34	0.99	0.98	0.83	0.99	0.99	0.98	0.99	0.98	0.94
Light	0.46	0.44	0.11	0.40	0.16	0.40	0.99	0.99	0.85	0.99	0.98	0.99	0.98	1.00	0.96
BridgeStudios2	0.29	0.25	0.16	0.30	0.24	0.56	0.97	0.56	0.87	0.98	0.98	0.57	0.92	0.99	0.86
Memorial	0.39	0.32	0.12	0.39	0.17	0.31	0.94	0.92	0.70	0.92	0.92	0.92	0.90	0.98	0.93
ClaridgeHotel	0.62	0.48	0.26	0.71	0.38	0.14	0.91	0.77	0.98	0.91	0.92	0.78	0.93	0.98	0.47
Mistaya1	0.55	0.43	0.21	0.71	0.39	0.12	0.96	0.76	0.96	0.96	0.96	0.77	1.00	0.98	0.52
BrookHouse	0.54	0.43	0.23	0.58	0.36	0.09	0.99	1.00	0.91	0.99	0.98	1.00	1.00	1.00	0.79
PeaceRocks	0.73	0.49	0.28	0.67	0.43	0.13	0.92	0.73	0.73	0.91	0.88	0.76	0.96	0.97	0.48
GGpark2	0.62	0.44	0.30	0.67	0.42	0.09	0.98	0.74	0.90	0.98	0.98	0.76	1.00	1.00	0.59
AtriumNight	0.40	0.26	0.13	0.55	0.19	0.14	0.98	0.99	0.85	0.95	0.92	0.99	0.93	0.99	0.56

3.1 Higher Pearson's linear correlation coefficient

Reapplying the equation (6.2), the Pearson's Linear Correlation Coefficient with the corresponding MOS increases from 0.588 (TMQI1) to 0.7102 (TMQI_A2) and to 0.7120 (TMQI_A1).

3.2 Lower absolute mean error

The Absolute Mean Error (AME) between the metric and normalized MOS (using the same training dataset) has been reduced: 0.3758 for TMQI1, 0.2722 for TMQI_A2 and 0.2626 for TMQI_A1.

$$AME = \frac{1}{N \times M} \sum_{n=1}^{N} \sum_{m=1}^{M} |\mathbf{TMQI}(n,m) - \mathbf{MOS}(n,m)| \tag{6.3}$$

As it can be seen in Table 6.6, the default TMQI1 is not well-designed for the dataset, particularly for the images: "CraterLake1", "Shasta2", "Synagogue", "BowRiver", "ArchRock", "SmallOffice" and "Memorial" with high absolute errors in last column with red marks (0.44, 0.43, 0.45, 0.46, 0.41, 0.42, 0.43 respectively). In addition, it is not good for most of TM operators such as "Drago", "Durand", "Tumblin", "Schlick", "Li" with high errors in last row (0.41, 0.68, 0.51, 0.40, 0.47 respectively).

The number of red marks in Table 6.7 is reduced such as for only the image "Synagogue" (0.42), and for two methods: "Durand" and "Li" (0.42 and 0.46 respectively). The blue marks, which are shown well-designed, appear with images: "DollDoll" (0.18) and "ClockBuilding" (0.19), and with TMOs: "Drago" (0.18), "Reinhard" (0.13), "Ward" (0.11), "Tumblin" (0.16) and "Proposed_CEDP_Opt" (0.17).

In coincidence with Table 6.7, the number of red marks in Table 6.8 is reduced (0.41 for the image "Synagogue", 0.40 and 0.45 for methods "Durand" and "Li" respectively). More blue marks appears for images: "Bridges" (0.19), "Stairway1" (0.19), "DollDoll" (0.17), "ClockBuilding" (0.19), and for methods: "Drago", "Reinhard", "Ward", "Tumblin" and "Proposed_CEDP_Opt" (0.16, 0.12, 0.11, 0.15, 0.15 respectively).

Figure 6.3 and Figure 6.4 show one of the best designed on our training dataset. The absolute mean errors are reduced for the image "DollDoll" and method "Ward". However, the method "Ward" in Figure 6.4 is still limited for the image "Synagogue" and remained at the high errors (0.6) for two approaches (TMQI_A1 and TMQI_A2).

Table 6.6: *Absolute errors between the normalized MOS scores and the default TMQI1 metrics (Ordering of images is shown as previous tables; All errors are rounded by two-decimals precision; The AME is 0.3758; Last row and column show averages: the red marks are related to high errors (≥ 0.4); the blue marks are related to low errors (< 0.2)).*

Drago [10]	Reinhard [44]	Ward [7]	Durand [16]	Tumblin [31]	Schlick [3]	Duan [8]	Fattal [25]	Li [26]	Husseis [30]	Pro_NUHA	Pro_SEPENO	NONSEPENO	Pro_CEDP_Lin	Pro_CEDP_Opt	Average
0.51	0.47	0.49	0.71	0.58	0.52	0.30	0.23	0.52	0.33	0.23	0.21	0.33	0.25	0.18	0.39
0.49	0.41	0.47	0.58	0.54	0.34	0.45	0.36	0.54	0.48	0.40	0.35	0.48	0.37	0.31	**0.44**
0.51	0.49	0.41	0.61	0.48	0.40	0.42	0.28	0.55	0.46	0.38	0.26	0.44	0.41	0.29	**0.43**
0.48	0.51	0.75	0.81	0.76	0.69	0.44	0.18	0.51	0.43	0.34	0.16	0.41	0.16	0.05	**0.45**
0.46	0.43	0.59	0.68	0.58	0.61	0.38	0.23	0.59	0.36	0.21	0.21	0.35	0.17	0.06	0.39
0.49	0.43	0.53	0.67	0.54	0.42	0.47	0.35	0.56	0.46	0.46	0.34	0.48	0.42	0.21	**0.46**
0.31	0.29	0.48	0.73	0.38	0.43	0.33	0.18	0.45	0.35	0.17	0.18	0.32	0.16	0.11	0.33
0.35	0.32	0.30	0.69	0.37	0.47	0.33	0.19	0.49	0.32	0.31	0.18	0.31	0.34	0.22	0.35
0.36	0.32	0.28	0.71	0.59	0.69	0.39	0.34	0.44	0.37	0.31	0.33	0.35	0.36	0.31	**0.41**
0.38	0.50	0.44	0.62	0.65	0.47	0.21	0.16	0.34	0.24	0.16	0.13	0.22	0.19	0.03	0.32
0.36	0.34	0.34	0.67	0.62	0.35	0.31	0.23	0.38	0.33	0.27	0.18	0.29	0.23	0.12	0.33
0.37	0.33	0.06	0.77	0.48	0.60	0.42	0.30	0.46	0.40	0.30	0.28	0.33	0.29	0.14	0.37
0.33	0.37	0.47	0.70	0.57	0.55	0.39	0.35	0.52	0.38	0.29	0.33	0.34	0.19	0.09	0.39
0.27	0.04	0.09	0.46	0.36	0.15	0.36	0.12	0.46	0.47	0.39	0.11	0.36	0.36	0.16	0.28
0.41	0.38	0.32	0.52	0.42	0.37	0.47	0.43	0.45	0.47	0.46	0.42	0.48	0.40	0.29	**0.42**
0.47	0.45	0.14	0.64	0.35	0.53	0.36	0.37	0.43	0.38	0.27	0.35	0.36	0.25	0.19	0.37
0.30	0.30	0.32	0.61	0.46	0.62	0.37	0.10	0.52	0.36	0.21	0.07	0.29	0.15	0.01	0.31
0.53	0.53	0.20	0.64	0.31	0.51	0.45	0.41	0.43	0.46	0.37	0.41	0.44	0.40	0.34	**0.43**
0.39	0.35	0.44	0.75	0.40	0.09	0.35	0.27	0.56	0.34	0.33	0.26	0.35	0.35	0.28	0.37
0.41	0.37	0.48	0.76	0.67	0.24	0.32	0.34	0.42	0.33	0.26	0.29	0.33	0.25	0.17	0.38
0.37	0.31	0.33	0.73	0.57	0.06	0.39	0.37	0.46	0.39	0.33	0.36	0.38	0.36	0.44	0.39
0.42	0.36	0.34	0.79	0.56	0.13	0.36	0.24	0.44	0.32	0.22	0.23	0.34	0.25	0.21	0.35
0.35	0.31	0.54	0.79	0.43	0.18	0.34	0.17	0.47	0.37	0.18	0.16	0.33	0.17	0.32	0.34
0.43	0.52	0.28	0.68	0.55	0.09	0.29	0.39	0.36	0.29	0.20	0.37	0.25	0.22	0.36	0.35
0.41	0.38	0.38	**0.68**	**0.51**	**0.40**	0.37	0.28	**0.47**	0.38	0.29	0.26	0.36	0.28	0.20	

Table 6.7: *Approach 1. Absolute errors between the normalized MOS scores and the new TMQI_A1 metrics (Ordering of images is shown as previous tables; All errors are rounded by two-decimals precision; The AME is 0.2626; Last row and column show averages: the red marks are related to high errors* (≥ 0.4)*; the blue marks are related to low errors* (< 0.2)*).*

Drago [10]	Reinhard [44]	Ward [7]	Durand [16]	Tumblin [31]	Schlick [3]	Duan [8]	Fattal [25]	Li [26]	Husseis [30]	Pro_NUHA	Pro_SEPENO	NONSEPENO	Pro_CEDP_Lin	Pro_CEDP_Opt	Average
0.33	0.17	0.06	0.56	0.23	0.25	0.28	0.13	0.53	0.32	0.22	0.13	0.34	0.26	0.19	0.27
0.45	0.28	0.07	0.42	0.34	0.17	0.46	0.34	0.56	0.49	0.40	0.34	0.49	0.40	0.34	0.37
0.33	0.17	0.06	0.25	0.13	0.14	0.40	0.14	0.58	0.46	0.38	0.14	0.44	0.43	0.31	0.29
0.48	0.49	0.63	0.80	0.71	0.72	0.43	0.07	0.54	0.42	0.33	0.10	0.41	0.14	0.05	**0.42**
0.39	0.24	0.17	0.49	0.31	0.40	0.38	0.20	0.60	0.37	0.21	0.19	0.37	0.18	0.07	0.30
0.37	0.12	0.12	0.62	0.26	0.28	0.50	0.31	0.57	0.49	0.48	0.32	0.50	0.45	0.15	0.37
0.05	0.03	0.08	0.39	0.02	0.09	0.35	0.14	0.43	0.40	0.19	0.14	0.34	0.18	0.13	0.20
0.02	0.08	0.08	0.36	0.03	0.29	0.30	0.02	0.45	0.30	0.29	0.03	0.27	0.35	0.11	0.20
0.04	0.12	0.15	0.39	0.13	0.58	0.40	0.34	0.42	0.39	0.31	0.35	0.35	0.37	0.28	0.31
0.13	0.19	0.03	0.25	0.29	0.17	0.21	0.10	0.33	0.24	0.15	0.12	0.24	0.23	0.02	**0.18**
0.00	0.04	0.03	0.30	0.18	0.02	0.35	0.07	0.40	0.36	0.30	0.11	0.33	0.26	0.17	**0.19**
0.01	0.15	0.26	0.40	0.00	0.46	0.43	0.26	0.41	0.41	0.31	0.25	0.32	0.30	0.07	0.27
0.03	0.09	0.07	0.42	0.09	0.51	0.39	0.36	0.55	0.39	0.29	0.35	0.34	0.22	0.11	0.28
0.15	0.28	0.16	0.05	0.03	0.26	0.41	0.24	0.50	0.50	0.42	0.25	0.38	0.42	0.18	0.28
0.02	0.03	0.08	0.11	0.06	0.01	0.51	0.47	0.45	0.50	0.49	0.46	0.52	0.43	0.33	0.30
0.17	0.13	0.12	0.30	0.07	0.19	0.38	0.40	0.41	0.41	0.30	0.37	0.38	0.27	0.22	0.27
0.11	0.12	0.00	0.17	0.05	0.44	0.39	0.07	0.51	0.38	0.24	0.08	0.30	0.19	0.00	0.20
0.15	0.08	0.07	0.26	0.09	0.05	0.47	0.42	0.33	0.47	0.39	0.41	0.44	0.43	0.35	0.29
0.24	0.08	0.00	0.65	0.05	0.15	0.34	0.21	0.58	0.33	0.33	0.20	0.35	0.37	0.08	0.26
0.18	0.04	0.04	0.64	0.29	0.22	0.33	0.26	0.42	0.33	0.27	0.22	0.35	0.26	0.03	0.26
0.13	0.02	0.12	0.52	0.18	0.01	0.40	0.39	0.45	0.40	0.35	0.37	0.40	0.37	0.41	0.30
0.33	0.07	0.13	0.67	0.22	0.03	0.37	0.17	0.34	0.34	0.22	0.18	0.37	0.28	0.03	0.25
0.17	0.00	0.15	0.65	0.10	0.15	0.35	0.09	0.45	0.39	0.20	0.10	0.35	0.19	0.19	0.23
0.07	0.02	0.01	0.48	0.09	0.03	0.31	0.42	0.35	0.31	0.21	0.39	0.25	0.24	0.18	0.22
0.18	**0.13**	**0.11**	**0.42**	**0.16**	0.23	0.38	0.23	**0.46**	0.39	0.30	0.23	0.37	0.30	**0.17**	

Table 6.8: *Approach 2. Absolute errors between the normalized MOS scores and the new TMQI_A2 metrics (Ordering of images is shown as previous tables; All errors are rounded by two-decimals precision; The AME is 0.2722; Last row and column show averages: the red marks are related to high errors* (≥ 0.4)*; the blue marks are related to low errors* (< 0.2)*).*

Drago [10]	Reinhard [44]	Ward [7]	Durand [16]	Tumblin [31]	Schlick [3]	Duan [8]	Fattal [25]	Li [26]	Husseis [30]	Pro_NUHA	Pro_SEPENO	NONSEPENO	Pro_CEDP_Lin	Pro_CEDP_Opt	Average
0.30	0.14	0.07	0.54	0.22	0.22	0.27	0.11	0.53	0.30	0.21	0.10	0.32	0.26	0.18	0.25
0.43	0.25	0.07	0.39	0.30	0.14	0.45	0.32	0.56	0.48	0.40	0.32	0.48	0.39	0.33	0.35
0.30	0.15	0.06	0.23	0.12	0.11	0.39	0.11	0.57	0.45	0.37	0.11	0.43	0.43	0.29	0.27
0.47	0.47	0.60	0.78	0.69	0.70	0.43	0.09	0.54	0.42	0.33	0.13	0.41	0.12	0.03	**0.41**
0.36	0.21	0.17	0.46	0.28	0.37	0.37	0.18	0.59	0.36	0.20	0.17	0.37	0.18	0.06	0.29
0.34	0.10	0.12	0.60	0.24	0.24	0.49	0.29	0.57	0.48	0.48	0.30	0.49	0.44	0.12	0.35
0.03	0.05	0.08	0.37	0.02	0.07	0.34	0.12	0.41	0.39	0.18	0.12	0.33	0.18	0.13	**0.19**
0.00	0.09	0.06	0.34	0.04	0.26	0.29	0.05	0.43	0.29	0.28	0.06	0.25	0.34	0.09	**0.19**
0.02	0.12	0.13	0.37	0.13	0.55	0.40	0.34	0.40	0.38	0.31	0.34	0.34	0.37	0.26	0.30
0.10	0.17	0.06	0.24	0.27	0.15	0.19	0.12	0.31	0.22	0.14	0.14	0.22	0.22	0.00	**0.17**
0.01	0.05	0.00	0.29	0.19	0.03	0.34	0.09	0.39	0.35	0.29	0.14	0.32	0.25	0.15	**0.19**
0.02	0.14	0.24	0.39	0.02	0.43	0.43	0.24	0.38	0.41	0.30	0.23	0.31	0.30	0.05	0.26
0.01	0.07	0.10	0.39	0.11	0.47	0.37	0.35	0.54	0.37	0.28	0.34	0.33	0.21	0.10	0.27
0.14	0.26	0.14	0.05	0.01	0.24	0.39	0.25	0.49	0.49	0.41	0.26	0.36	0.41	0.15	0.27
0.01	0.03	0.05	0.11	0.03	0.02	0.50	0.46	0.43	0.49	0.49	0.45	0.51	0.43	0.32	0.29
0.15	0.11	0.10	0.28	0.04	0.17	0.38	0.39	0.39	0.41	0.29	0.37	0.38	0.27	0.21	0.26
0.11	0.11	0.02	0.18	0.05	0.41	0.38	0.10	0.50	0.38	0.23	0.12	0.29	0.18	0.02	0.20
0.14	0.08	0.05	0.25	0.06	0.06	0.46	0.41	0.30	0.46	0.37	0.40	0.43	0.42	0.34	0.28
0.21	0.05	0.01	0.62	0.03	0.19	0.33	0.18	0.58	0.32	0.32	0.18	0.34	0.37	0.04	0.25
0.15	0.02	0.06	0.62	0.28	0.28	0.32	0.24	0.42	0.33	0.26	0.19	0.35	0.26	0.06	0.26
0.10	0.04	0.10	0.50	0.17	0.06	0.40	0.38	0.44	0.40	0.34	0.37	0.40	0.37	0.39	0.30
0.30	0.05	0.12	0.64	0.20	0.10	0.36	0.15	0.32	0.33	0.21	0.15	0.36	0.27	0.06	0.24
0.14	0.02	0.14	0.62	0.08	0.20	0.34	0.06	0.44	0.38	0.19	0.07	0.35	0.18	0.15	0.23
0.05	0.04	0.01	0.45	0.12	0.09	0.30	0.41	0.33	0.30	0.19	0.39	0.24	0.24	0.15	0.22
0.16	**0.12**	**0.11**	**0.40**	**0.15**	0.23	0.37	0.23	**0.45**	0.38	0.29	0.23	0.36	0.30	**0.15**	

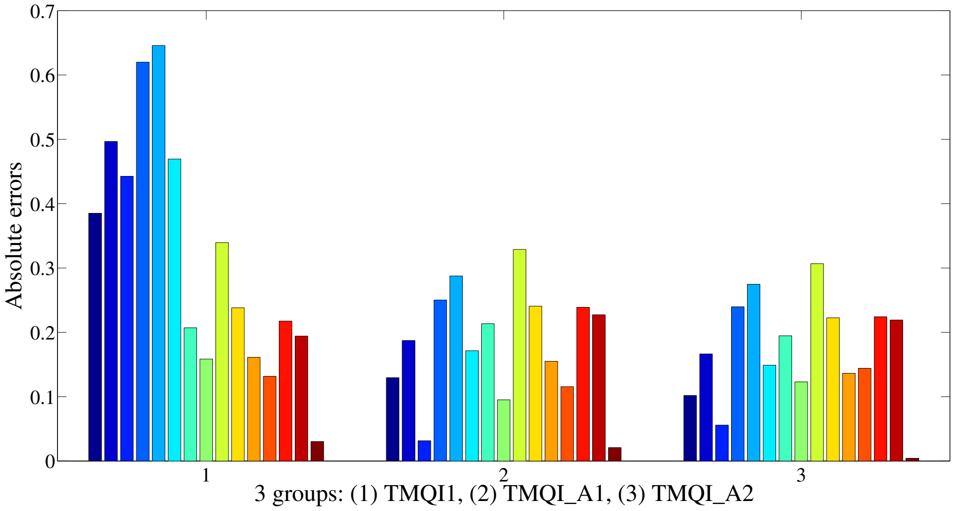

Figure 6.3: *Compare between TMQI1, TMQI_A1 and TMQI_A2 for "DollDoll" HDR test image (each group has 15 corresponding methods).*

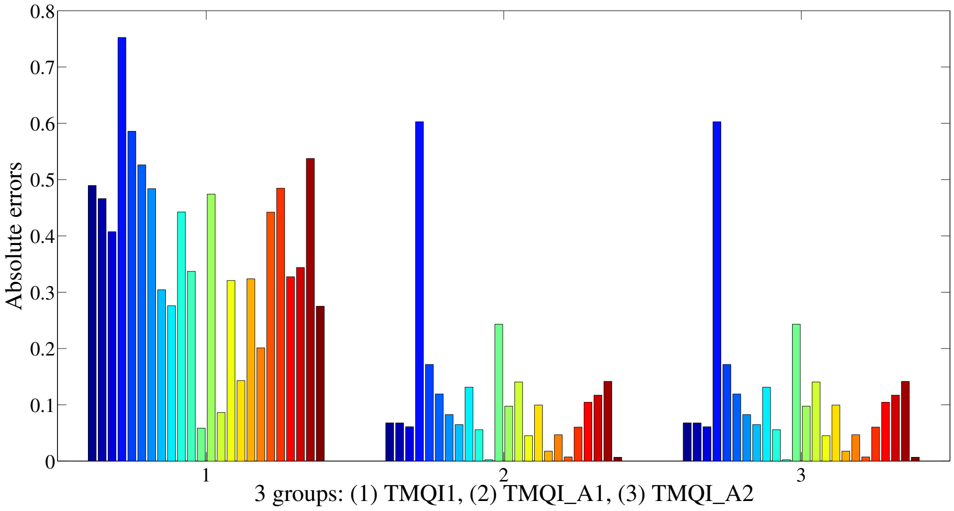

Figure 6.4: *Compare between TMQI1, TMQI_A1 and TMQI_A2 for "Ward" method (each group has 24 corresponding images).*

3.3 More relevant region

Define 2D Cartesian coordinate system with two axises: the (upward) vertical axis *tmqi* and the (rightward) horizontal axis *mos* which correspond to values of **TMQI** and normalized matrix **MOS**, respectively. One node is generated from a pair of their values between 0 and 1. An objective quality metric will be ideal if all values are same ($\mathbf{TMQI} \equiv \mathbf{MOS}$) as well as all nodes are marked on the "black" line 45° (or $tmqi = mos$) shown in Figure 6.5, Figure 6.6, Figure 6.7 and Figure 6.8. The more population of points near the line the better metric.

It is possible to rescale the corresponding marks ranging from 0 until 5: 5 for *excellent*, 4 *very good*, 3 *good*, 2 *accepted*, 1 *unsatisfactory* and 0 *failed* into the normalized levels: 1 for *excellent*, 0.8 *very good*, 0.6 *good*, 0.4 *accepted*, 0.2 *unsatisfactory* and 0 *failed*. Therefore, the interval 0.2 is a minimal difference between two consecutive levels so that the metric gives a mark either a upper level or a lower level from the best level ($tmqi = mos$).

Based on the minimal difference between two consecutive levels, it is defined 3 regions as follows:

i. Define **relevant region:** (make sure nodes around the best level; the metric gives a mark either a upper level or a lower level from the best level)

$$\begin{cases} 0 \le mos \le 1 \\ 0 \le tmqi \le 1 \\ |tmqi - mos| < 0.2 \end{cases} \Leftrightarrow \begin{cases} 0 \le mos \le 1 \\ 0 \le tmqi \le 1 \\ tmqi < mos + 0.2 \\ tmqi > mos - 0.2 \end{cases} \tag{6.4}$$

ii. Define **near-relevant region:** (skip one level, up or down)

$$\begin{cases} 0 \le mos \le 1 \\ 0 \le tmqi \le 1 \\ 0.2 \le |tmqi - mos| < 0.4 \end{cases} \tag{6.5}$$

It can be divided into two sides:

$$\text{Up side} \quad \begin{cases} 0 \le mos \le 1 \\ 0 \le tmqi \le 1 \\ tmqi \ge mos + 0.2 \\ tmqi < mos + 0.4 \end{cases} \tag{6.6}$$

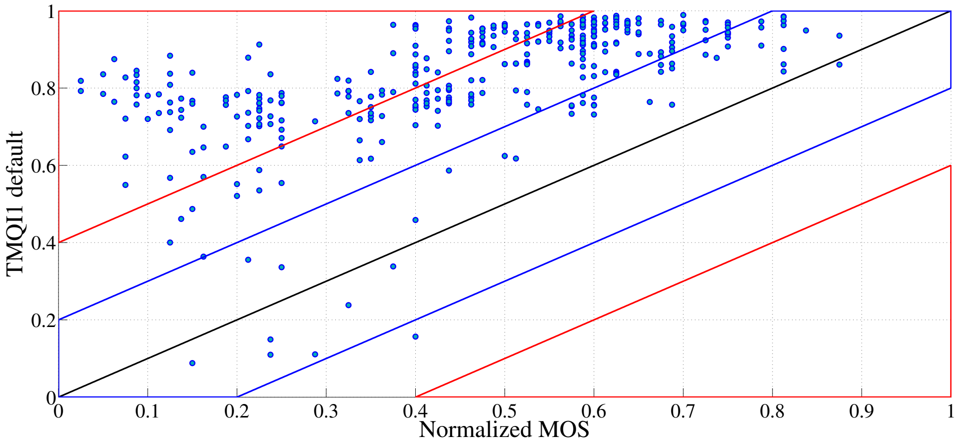

Figure 6.5: *Relevant, near-relevant and irrelevant regions on the default TMQI1 metrics versus the normalized MOS scores.*

$$\text{Down side} \quad \begin{cases} 0 \leq mos \leq 1 \\ 0 \leq tmqi \leq 1 \\ tmqi > mos - 0.4 \\ tmqi \leq mos - 0.2 \end{cases} \tag{6.7}$$

iii. Define **irrelevant regions:** (skip two levels, up or down)

$$\begin{cases} 0 \leq mos \leq 1 \\ 0 \leq tmqi \leq 1 \\ |tmqi - mos| \geq 0.4 \end{cases} \tag{6.8}$$

It can be divided into two sides:

$$\text{Up side} \quad \begin{cases} 0 \leq mos \leq 1 \\ 0 \leq tmqi \leq 1 \\ tmqi \geq mos + 0.4 \end{cases} \tag{6.9}$$

$$\text{Down side} \quad \begin{cases} 0 \leq mos \leq 1 \\ 0 \leq tmqi \leq 1 \\ tmqi \leq mos - 0.4. \end{cases} \tag{6.10}$$

For the TMQI1, the number of points falling into the relevant region is 48 (13.33%), near-relevant 172 (47.77%) and irrelevant 140 (38.88%). In TMQI_A1, the number of points falling into the relevant region is 138 (38.33%), near-relevant 138 (38.33%) and irrelevant 84 (23.33%). In TMQI_A2, the number of points falling into the relevant region is 143 (39.72%), near-relevant 147 (40.83%) and irrelevant 70 (19.44%). In term

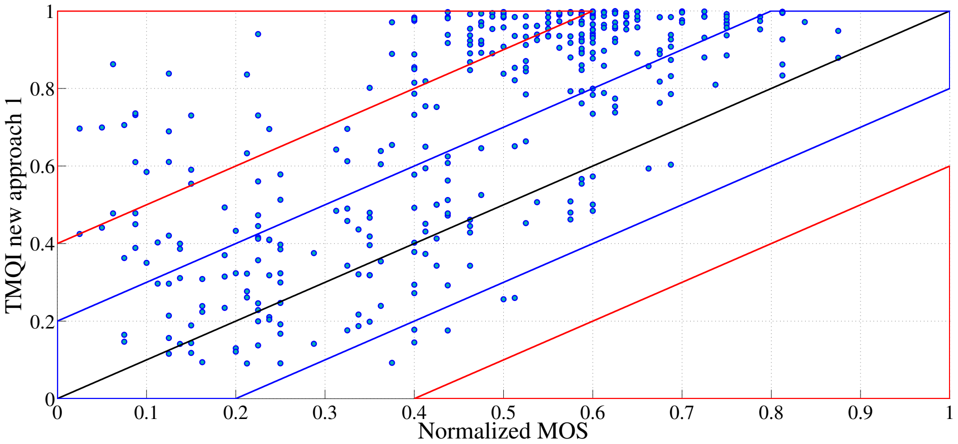

Figure 6.6: *Relevant, near-relevant and irrelevant regions on the new TMQI_A1 metrics versus the normalized MOS scores.*

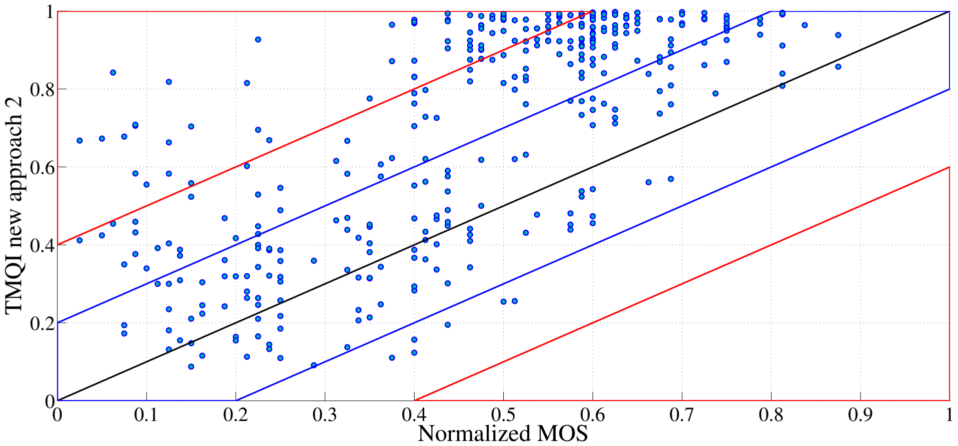

Figure 6.7: *Relevant, near-relevant and irrelevant regions on the new TMQI_A2 metrics versus the normalized MOS scores.*

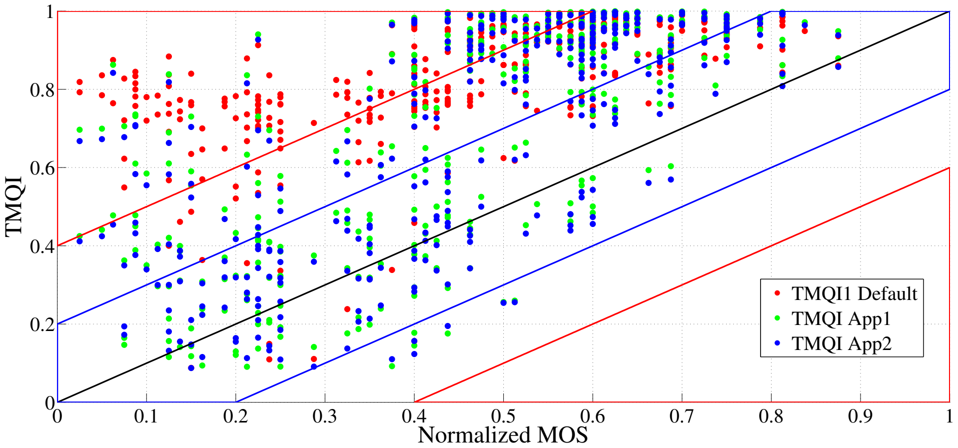

Figure 6.8: *Relevant, near-relevant and irrelevant regions on the TMQI1, new TMQI_A1 and TMQI_A2 metrics versus normalized MOS scores.*

of the relevant region, one can conclude that the TMQI_A2 metric is the best because of the highest number of points (143 with 39.72%).

3.4 More visual correlation

This section discusses the visual quality versus the TMQI.

3.4.1 Low quality tone mapped images

Figure 6.9: *"Stairway1" HDR test image (13.37 f-stops) - "Drago" with MOS=0.412, TMQI1=0.760 and TMQI_A1=0.431 (too bright at window, too dark around walls).*

Figure 6.10: *"ClaridgeHotel" HDR test image (23.44 f-stops) - "Tumblin" with MOS=0.350, TMQI1=0.751 and TMQI_A1=0.396 (too dark).*

Figure 6.11: *"BrookHouse" HDR test image (23.98 f-stops) - "Reinhard" with MOS=0.463, TMQI1=0.768 and TMQI_A1=0.445 (too dark).*

Figure 6.12: *"SmallOffice" HDR test image (16.29 f-stops) - "Schlick" with MOS=0.363, TMQI1=0.728 and TMQI_A2=0.344 (too dark).*

Figure 6.13: *"Stairway1" HDR test image (13.37 f-stops) - "Fattal" WRB with MOS=0.588, TMQI1=0.782 and TMQI_A2=0.538 (too bright at window).*

3.4.2 High quality tone mapped images

Figure 6.14: *"DollDoll" HDR test image (13.89 f-stops) - Proposed_CEDP_Opt_L1_N1 with MOS=0.813, TMQI1=0.843 and TMQI_A2=0.808 (close to the MOS).*

Figure 6.15: *"BottlesSmall" HDR test image (16.03 f-stops) - Proposed_NONSEP_L2 with MOS=0.563, TMQI1=0.903 and TMQI_A2=0.889 (close to the MOS).*

Figure 6.16: *"ClaridgeHotel" HDR test image (23.44 f-stops) - Proposed_SEPENOCA_L2 with MOS=0.600, TMQI1=0.857 and TMQI_A1=0.799 (close to the MOS).*

Figure 6.17: *"Lausanne1" HDR test image (7.71 f-stops) - Proposed_SEPENOCA_L2 with MOS=0.625, TMQI1=0.835 and TMQI_A1=0.754 (close to the MOS).*

Figure 6.18: *"PeaceRocks" HDR test image (24.13 f-stops) - Proposed_SEPENOCA_L1 with MOS=0.613, TMQI1=0.841 and TMQI_A1=0.788 (close to the MOS).*

Figure 6.19: *"Synagogue" HDR test image (8.57 f-stops) - Proposed_CEDP_Lin_L4_N1 with MOS=0.750, TMQI1=0.908 and TMQI_A2=0.869 (close to the MOS).*

Figure 6.20: *"OxfordChurch" HDR test image (15.43 f-stops) - Proposed_CEDP_Opt_L1_N1 with MOS=0.738, TMQI1=0.878 and TMQI_A2=0.788 (close to the MOS).*

Figure 6.21: *"AtriumNight" HDR test image (28.68 f-stops) - Proposed_CEDP_Opt_L5_N1 with MOS=0.412, TMQI1=0.768 and TMQI_A2=0.562 (close to the MOS).*

Figure 6.22: *"BowRiver" HDR test image (9.53 f-stops) - Proposed_CEDP_Opt_L1_N1 with MOS=0.625, TMQI1=0.838 and TMQI_A2=0.747 (close to the MOS).*

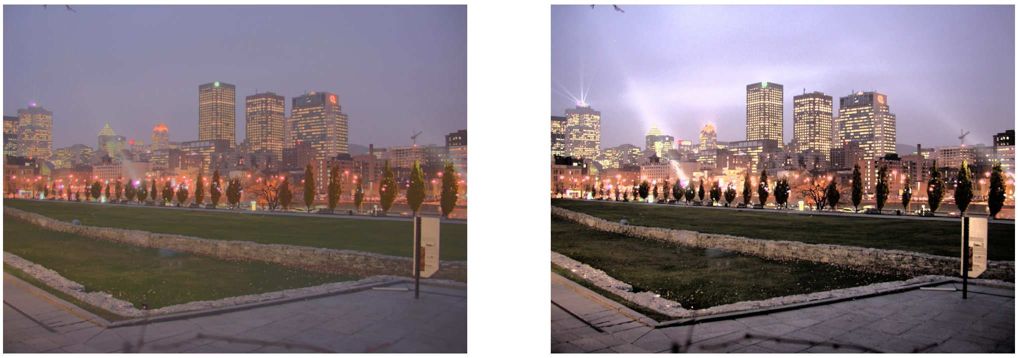

Figure 6.23: *"Montreal" HDR test image (16.06 f-stops) - Left image: Pro_CEDP_Opt_L1_N1 with TMQI_A1=0.987 (TMQI1=0.751); Right image: "Husseis" with TMQI_A1=0.963 (TMQI1=0.945) (improved metric).*

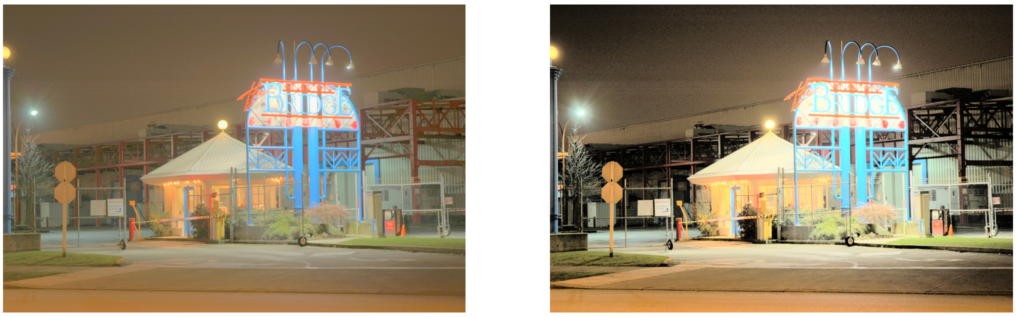

Figure 6.24: *"BridgeStudio2" HDR test image (18.13 f-stops) - Left image: Pro_CEDP_Opt_L1_N1 with TMQI_A1=0.987 (TMQI1=0.847); Right image: "Husseis" with TMQI_A1=0.978 (TMQI1=0.964) (improved metric).*

4 Conclusion

Two modified metrics (TMQI_A1 and TMQI_A2) have been proposed to evaluate the visual quality of HDR tone mapped images. These metrics have the closer relation with the visual quality compared to the default metric TMQI1: (i) the PLCC with the corresponding MOS increases from 0.588 (TMQI1) to 0.7102 (TMQI_A2) and to 0.7120 (TMQI_A1); (ii) the AME between metrics and normalized MOS has been improved such as 0.3758 for TMQI1, 0.2722 for TMQI_A2 and 0.2626 for TMQI_A1; (iii) the population of points in relevant region is higher; and (iv) the visual correlation has been improved according to the MOS.

The visual quality of our TMOs is confirmed and competitive to the image tone mapping operators available in the state of the art. One can see in Table 6.1 the average MOS for our methods, i.e. "Pro_NUHA", "Pro_SEPENO", "Pro_NONSEPENO", "Pro_CEDP_Lin" and "Pro_CEDP_Opt", remain at higher levels (3.24, 2.99, 2.91, 3.42 and 3.27 respectively).

Chapter 7

Conclusion

The objective of this thesis is to propose tone mapping operator to convert high dynamic range image into low dynamic range image so that the latter is of good visual quality in accordance to the TMQI. Four TMOs have been developed: (i) Non-uniform histogram adjustment, (ii) Separable ENO multiresolution families (Point-Value, Cell-Average), (iii) Non-separable ENO multiresolution (Cell-Average), and (iv) TMO based on combination between contrast enhancement and details preservation.

The first global tone mapping operator using non-uniform histogram adjustment solves the contrast problem based on piecewise linear equation modeling the "s-shaped" curve in adequation to the well-adapted perception of the HVS. It takes for all account pixels divided by B-bin non-uniform histogram distributions. The purpose of this strategy is to enhance the contrast by acting on the M-norm space.

The second and third local tone mapping operators using ENO multiresolution families according to separable (Point-Value, Cell-Average) or non-separable (Cell-Average) multiresolution approaches improve detail visibility because the purpose of decomposition is used to extract the details of the complex HDR image preserving as much as possible the HDR image quality. These families have the ability to introduce in their mathematical model the isolated singularities such as edge points in the image thus avoiding the Gibbs phenomenon particularly harmful in tone mapped images.

The fourth (global, local) tone mapping operator based on a separable near optimal lifting scheme combined to the perceptual quantizer with respect to the HVS solving both advantages of contrast enhancement as well as detail visibility.

The study related to the HDR tone mapped metric (TMQI) shows that the parameters that have been tuned in the original paper [34] are not relevant since they have been trained on a small dataset of TMOs (only 8) and HDR test images (only 15). New parameters, more adapted, have been proposed in the accordance to the MOS. Two proposed metrics have been improved the performance with visual quality in four aspects: (i) the PLCC with the corresponding MOS increases; (ii) the overall absolute mean error between metrics and normalized MOS has been improved; (iii) the population of points in relevant region is higher; and (iv) the visual correlation has been improved according to the MOS.

For future work, several investigations are possible. The first direction consists to extend the HDR tone mapped image with ENO multiresolution families to HDR video. Indeed, the temporal direction of the HDR video will be processed. The second direction concerns the non-uniform histogram adjustment approach which will be exploited for compression of the HDR content. The latter can be stored, processed and transmitted with the LDR information and its residual information using JPEG frameworks, for example. The third direction concerns the development of TMQI metric with an HDR reference.

APPENDIX

A

Computation of separable multiresolution ENO coefficients

This appendix concerns the computation of separable ENO coefficients in PV and CA cases. **Requirements**: These coefficients are constant, independent to an index k and applied for all pixels in the vector of image. An index k will shift through the length of vectorial approximation (i.e. $\mathbf{V}^{j-1}(x_n, y_k)$) with the same performance of one polynomial as the case $k = 0$.

1 ENO point-value

Denote $p_{-1}(x)$, $p_0(x)$ and $p_1(x)$ the three polynomials which corresponding to the following points on the coarse scale:

$$\begin{cases} p_{-1}(x) \longrightarrow \mathbf{P}u^{j-1}(x_n, y_k, -1) \longrightarrow [k-2,\ k-1,\ k,\ k+1] \\ p_0(x) \quad \longrightarrow \mathbf{P}u^{j-1}(x_n, y_k, 0) \quad \longrightarrow [k-1,\ k,\ k+1,\ k+2] \\ p_1(x) \quad \longrightarrow \mathbf{P}u^{j-1}(x_n, y_k, 1) \quad \longrightarrow [k,\ k+1,\ k+2,\ k+3]. \end{cases} \tag{A.1}$$

These are attached to the corresponding stencils $\mathbf{P}u^{j-1}(x_n, y_k, u)$ with $u = -1, 0, 1$. The pixel value $\mathbf{V}^{j-1}(x_n, y_k)$ is defined by the Point-Value of the underlying cubic Lagrange function $p_u(x)$ modeling the vector, as follows:

$$\mathbf{V}^{j-1}(x_n, y_k) = p_u(k). \tag{A.2}$$

Since the approximation $\mathbf{V}^{j-1}(x_n, y_k)$ is from $\mathbf{I}^j(x_n, y_k)$ at even index by down-sampling operator, the predicted value $\hat{\mathbf{I}}^j(x_n, y_{2k-1})$ at odd index is the value of function at the

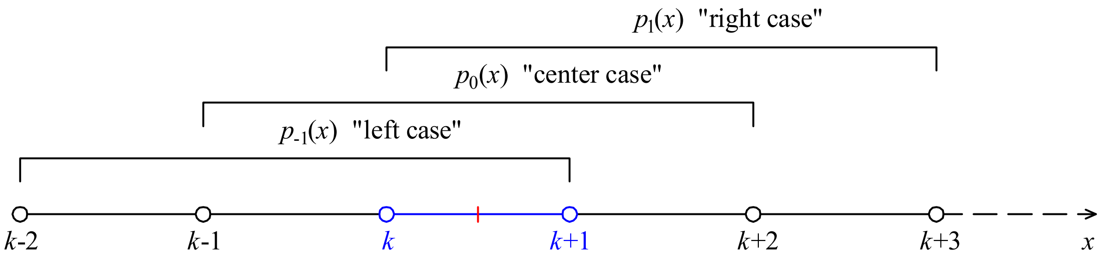

Figure A.1: *Three of corresponding polynomials are attached on the coarse scale.*

mid point on the cell $[k,\ k+1]$:

$$\hat{\mathbf{I}}^j(x_n, y_{2k-1}, u) = p_u(k+1/2). \tag{A.3}$$

1.1 At the center case

See Figure A.1. The cubic polynomial $p_0(x) = ax^3 + bx^2 + cx + d$ interpolates on $\{\mathbf{V}^{j-1}(x_n, y_{k-1}),\ \mathbf{V}^{j-1}(x_n, y_k),\ \mathbf{V}^{j-1}(x_n, y_{k+1}),\ \mathbf{V}^{j-1}(x_n, y_{k+2})\}$. Four values have the following relationships:

$$\begin{cases} \mathbf{V}^{j-1}(x_n, y_{k-1}) = p_0(k-1) = d + c(k-1) + a(k-1)^3 + b(k-1)^2 \\ \mathbf{V}^{j-1}(x_n, y_k) = p_0(k) = d + ck + ak^3 + bk^2 \\ \mathbf{V}^{j-1}(x_n, y_{k+1}) = p_0(k+1) = d + c(k+1) + a(k+1)^3 + b(k+1)^2 \\ \mathbf{V}^{j-1}(x_n, y_{k+2}) = p_0(k+2) = d + c(k+2) + a(k+2)^3 + b(k+2)^2. \end{cases} \tag{A.4}$$

On the other hand, as mentioned the requirements above, the index k will shift through the length of $\mathbf{V}^{j-1}$ with the same performance of one polynomial as the case $k = 0$. Therefore,

$$\begin{cases} \mathbf{V}^{j-1}(x_n, y_{-1}) = b - a - c + d \\ \mathbf{V}^{j-1}(x_n, y_0) = d \\ \mathbf{V}^{j-1}(x_n, y_1) = a + b + c + d \\ \mathbf{V}^{j-1}(x_n, y_2) = 8a + 4b + 2c + d. \end{cases} \tag{A.5}$$

Solve the system (A.5) to find the polynomial coefficients a, b, c, d:

$$\begin{cases} a = -\frac{1}{6}\mathbf{V}^{j-1}(x_n, y_{-1}) + \frac{1}{2}\mathbf{V}^{j-1}(x_n, y_0) - \frac{1}{2}\mathbf{V}^{j-1}(x_n, y_1) + \frac{1}{6}\mathbf{V}^{j-1}(x_n, y_2) \\ b = \frac{1}{2}\mathbf{V}^{j-1}(x_n, y_{-1}) - \mathbf{V}^{j-1}(x_n, y_0) + \frac{1}{2}\mathbf{V}^{j-1}(x_n, y_1) \\ c = -\frac{1}{3}\mathbf{V}^{j-1}(x_n, y_{-1}) - \frac{1}{2}\mathbf{V}^{j-1}(x_n, y_0) + \mathbf{V}^{j-1}(x_n, y_1) - \frac{1}{6}\mathbf{V}^{j-1}(x_n, y_2) \\ d = \mathbf{V}^{j-1}(x_n, y_0). \end{cases} \tag{A.6}$$

Replacing these results in equation (A.3), the predicted value is applied for the case

$k = 0$:

$$\hat{\mathbf{I}}^j(x_n, y_{2k-1}, 0) = p_0(k+1/2) = \tag{A.7}$$
$$= -\frac{1}{16}\mathbf{V}^{j-1}(x_n, y_{k-1}) + \frac{9}{16}\mathbf{V}^{j-1}(x_n, y_k) + \frac{9}{16}\mathbf{V}^{j-1}(x_n, y_{k+1}) - \frac{1}{16}\mathbf{V}^{j-1}(x_n, y_{k+2}).$$

1.2 At the left case

See Figure A.1. The cubic polynomial $p_{-1}(x) = ax^3 + bx^2 + cx + d$ interpolates on $\{\mathbf{V}^{j-1}(x_n, y_{k-2}),\ \mathbf{V}^{j-1}(x_n, y_{k-1}),\ \mathbf{V}^{j-1}(x_n, y_k),\ \mathbf{V}^{j-1}(x_n, y_{k+1})\}$. Four values have the following relationships:

$$\begin{cases} \mathbf{V}^{j-1}(x_n, y_{k-2}) = p_{-1}(k-2) = d + c(k-2) + a(k-2)^3 + b(k-2)^2 \\ \mathbf{V}^{j-1}(x_n, y_{k-1}) = p_{-1}(k-1) = d + c(k-1) + a(k-1)^3 + b(k-1)^2 \\ \mathbf{V}^{j-1}(x_n, y_k) = p_{-1}(k) = d + ck + ak^3 + bk^2 \\ \mathbf{V}^{j-1}(x_n, y_{k+1}) = p_{-1}(k+1) = d + c(k+1) + a(k+1)^3 + b(k+1)^2. \end{cases} \tag{A.8}$$

On the coarse scale, k will shift through the length of $\mathbf{V}^{j-1}(x_n, y_k)$ with the same performance of one polynomial as the case $k = 0$. Therefore,

$$\begin{cases} \mathbf{V}^{j-1}(x_n, y_{-2}) = 4b - 8a - 2c + d \\ \mathbf{V}^{j-1}(x_n, y_{-1}) = b - a - c + d \\ \mathbf{V}^{j-1}(x_n, y_0) \ = d \\ \mathbf{V}^{j-1}(x_n, y_1) \ = a + b + c + d. \end{cases} \tag{A.9}$$

Solve the system (A.9) to find the polynomial coefficients a, b, c, d:

$$\begin{cases} a = -\frac{1}{6}\mathbf{V}^{j-1}(x_n, y_{-2}) + \frac{1}{2}\mathbf{V}^{j-1}(x_n, y_{-1}) - \frac{1}{2}\mathbf{V}^{j-1}(x_n, y_0) + \frac{1}{6}\mathbf{V}^{j-1}(x_n, y_1) \\ b = \frac{1}{2}\mathbf{V}^{j-1}(x_n, y_{-1}) - \mathbf{V}^{j-1}(x_n, y_0) + \frac{1}{2}\mathbf{V}^{j-1}(x_n, y_1) \\ c = \frac{1}{6}\mathbf{V}^{j-1}(x_n, y_{-2}) - \mathbf{V}^{j-1}(x_n, y_{-1}) + \frac{1}{2}\mathbf{V}^{j-1}(x_n, y_0) + \frac{1}{3}\mathbf{V}^{j-1}(x_n, y_1) \\ d = \mathbf{V}^{j-1}(x_n, y_0). \end{cases} \tag{A.10}$$

Replacing these results in equation (A.3), the predicted value is applied for the case $k = 0$:

$$\hat{\mathbf{I}}^j(x_n, y_{2k-1}, -1) = p_{-1}(k+1/2) = \tag{A.11}$$
$$= \frac{1}{16}\mathbf{V}^{j-1}(x_n, y_{k-2}) - \frac{5}{16}\mathbf{V}^{j-1}(x_n, y_{k-1}) + \frac{15}{16}\mathbf{V}^{j-1}(x_n, y_k) + \frac{5}{16}\mathbf{V}^{j-1}(x_n, y_{k+1}).$$

1.3 At the right case

See Figure A.1. The cubic polynomial $p_1(x) = ax^3 + bx^2 + cx + d$ interpolates on $\{\mathbf{V}^{j-1}(x_n, y_k),\ \mathbf{V}^{j-1}(x_n, y_{k+1}),\ \mathbf{V}^{j-1}(x_n, y_{k+2}),\ \mathbf{V}^{j-1}(x_n, y_{k+3})\}$. Four values have the following relationships:

$$\begin{cases}\mathbf{V}^{j-1}(x_n, y_k) = p_1(k) = d + ck + ak^3 + bk^2 \\ \mathbf{V}^{j-1}(x_n, y_{k+1}) = p_1(k+1) = d + c(k+1) + a(k+1)^3 + b(k+1)^2 \\ \mathbf{V}^{j-1}(x_n, y_{k+2}) = p_1(k+2) = d + c(k+2) + a(k+2)^3 + b(k+2)^2 \\ \mathbf{V}^{j-1}(x_n, y_{k+3}) = p_1(k+3) = d + c(k+3) + a(k+3)^3 + b(k+3)^2. \end{cases} \tag{A.12}$$

On the coarse scale, k will shift through the length of $\mathbf{V}^{j-1}(x_n, y_k)$ with the same performance of one polynomial as the case $k = 0$. Therefore,

$$\begin{cases}\mathbf{V}^{j-1}(x_n, y_0) = d \\ \mathbf{V}^{j-1}(x_n, y_1) = a + b + c + d \\ \mathbf{V}^{j-1}(x_n, y_2) = 8a + 4b + 2c + d \\ \mathbf{V}^{j-1}(x_n, y_3) = 27a + 9b + 3c + d. \end{cases} \tag{A.13}$$

Solve the system (A.13) to find the polynomial coefficients a, b, c:

$$\begin{cases} a = -\frac{1}{6}\mathbf{V}^{j-1}(x_n, y_0) + \frac{1}{2}\mathbf{V}^{j-1}(x_n, y_1) - \frac{1}{2}\mathbf{V}^{j-1}(x_n, y_2) + \frac{1}{6}\mathbf{V}^{j-1}(x_n, y_3) \\ b = \mathbf{V}^{j-1}(x_n, y_0) - \frac{5}{2}\mathbf{V}^{j-1}(x_n, y_1) + 2\mathbf{V}^{j-1}(x_n, y_2) - \frac{1}{2}\mathbf{V}^{j-1}(x_n, y_3) \\ c = -\frac{11}{6}\mathbf{V}^{j-1}(x_n, y_0) + 3\mathbf{V}^{j-1}(x_n, y_1) - \frac{3}{2}\mathbf{V}^{j-1}(x_n, y_2) + \frac{1}{3}\mathbf{V}^{j-1}(x_n, y_3) \\ d = \mathbf{V}^{j-1}(x_n, y_0). \end{cases} \tag{A.14}$$

Replacing these results in the equation (A.3), the predicted value is applied for the case $k = 0$:

$$\begin{aligned} &\hat{\mathbf{I}}^j(x_n, y_{2k-1}, +1) = p_1(k + 1/2) = \\ &= \frac{5}{16}\mathbf{V}^{j-1}(x_n, y_k) + \frac{15}{16}\mathbf{V}^{j-1}(x_n, y_{k+1}) - \frac{5}{16}\mathbf{V}^{j-1}(x_n, y_{k+2}) + \frac{1}{16}\mathbf{V}^{j-1}(x_n, y_{k+3}). \end{aligned} \tag{A.15}$$

The results are rewritten by the equation (A.7), equation (A.11) and equation (A.15) as follows:

$$\hat{\mathbf{I}}^j(x_n, y_{2k-1}) = \begin{cases} \hat{\mathbf{I}}^j(x_n, y_{2k-1}, -1) & \text{for the left case} \\ \hat{\mathbf{I}}^j(x_n, y_{2k-1}, 0) & \text{for the center case} \\ \hat{\mathbf{I}}^j(x_n, y_{2k-1}, +1) & \text{for the right case} \end{cases} \tag{A.16}$$

$$= \begin{cases} +\frac{1}{16}\mathbf{V}^{j-1}(x_n, y_{k-2}) - \frac{5}{16}\mathbf{V}^{j-1}(x_n, y_{k-1}) + \frac{15}{16}\mathbf{V}^{j-1}(x_n, y_k) + \frac{5}{16}\mathbf{V}^{j-1}(x_n, y_{k+1}) \\ -\frac{1}{16}\mathbf{V}^{j-1}(x_n, y_{k-1}) + \frac{9}{16}\mathbf{V}^{j-1}(x_n, y_k) + \frac{9}{16}\mathbf{V}^{j-1}(x_n, y_{k+1}) - \frac{1}{16}\mathbf{V}^{j-1}(x_n, y_{k+2}) \\ +\frac{5}{16}\mathbf{V}^{j-1}(x_n, y_k) + \frac{15}{16}\mathbf{V}^{j-1}(x_n, y_{k+1}) - \frac{5}{16}\mathbf{V}^{j-1}(x_n, y_{k+2}) + \frac{1}{16}\mathbf{V}^{j-1}(x_n, y_{k+3}) \end{cases} \tag{A.17}$$

$$= \begin{cases} \sum\left[+\frac{1}{16} \quad -\frac{5}{16} \quad +\frac{15}{16} \quad +\frac{5}{16}\right] \otimes \left[\mathbf{V}^{j-1}(x_n,y_{k-2}) \quad \mathbf{V}^{j-1}(x_n,y_{k-1}) \quad \mathbf{V}^{j-1}(x_n,y_k) \quad \mathbf{V}^{j-1}(x_n,y_{k+1})\right] \\ \sum\left[-\frac{1}{16} \quad +\frac{9}{16} \quad +\frac{9}{16} \quad -\frac{1}{16}\right] \otimes \left[\mathbf{V}^{j-1}(x_n,y_{k-1}) \quad \mathbf{V}^{j-1}(x_n,y_k) \quad \mathbf{V}^{j-1}(x_n,y_{k+1}) \quad \mathbf{V}^{j-1}(x_n,y_{k+2})\right] \\ \sum\left[+\frac{5}{16} \quad +\frac{15}{16} \quad -\frac{5}{16} \quad +\frac{1}{16}\right] \otimes \left[\mathbf{V}^{j-1}(x_n,y_k) \quad \mathbf{V}^{j-1}(x_n,y_{k+1}) \quad \mathbf{V}^{j-1}(x_n,y_{k+2}) \quad \mathbf{V}^{j-1}(x_n,y_{k+3})\right] \end{cases} \tag{A.18}$$

in compact forms where $\otimes$ is the product term by term.

2 ENO cell-average

Denote $p_{-1}(x)$, $p_0(x)$ and $p_1(x)$ the three polynomials which corresponding to the following intervals on the coarse scale:

$$\begin{cases} p_{-1}(x) \longrightarrow \mathbf{C}u^{j-1}(x_n,y_k,-1) \longrightarrow \{[k-2,k-1],\ [k-1,k],\ [k,k+1]\} \\ p_0(x) \quad \longrightarrow \mathbf{C}u^{j-1}(x_n,y_k,0) \quad \longrightarrow \{[k-1,k],\ [k,k+1],\ [k+1,k+2]\} \\ p_1(x) \quad \longrightarrow \mathbf{C}u^{j-1}(x_n,y_k,1) \quad \longrightarrow \{[k,k+1],\ [k+1,k+2],\ [k+2,k+3]\}. \end{cases} \tag{A.19}$$

These are attached to the corresponding stencils $\mathbf{C}u^{j-1}(x_n,y_k,u)$ with $u=-1,0,1$.

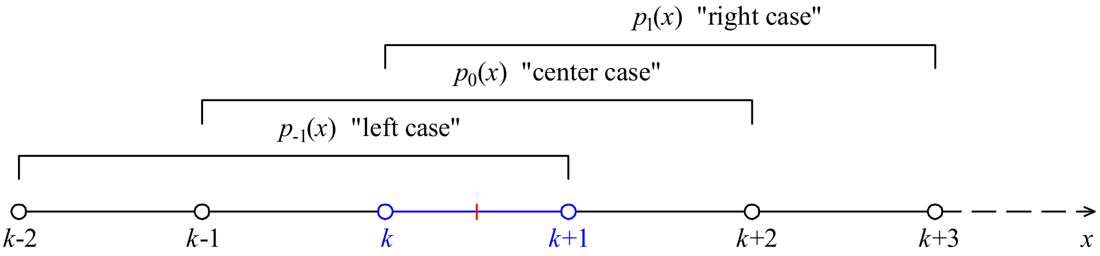

Figure A.2: *Three of corresponding polynomials are attached on the coarse scale.*

The pixel value $\mathbf{I}^{j-1}(x_n,y_k)$ is defined by the Cell-Average of the underlying quadratic function $p_u(x)$ modeling the vector, as follows:

$$\mathbf{V}^{j-1}(x_n,y_k) = \int\limits_{C_k^{j-1}} p_u(x)dx = \int_k^{k+1} p_u(x)dx, \tag{A.20}$$

where the 1D cell C_k^{j-1} is defined as $[k,\ k+1]$. Two predicted values are deduced as follows: at the odd index:

$$\hat{\mathbf{I}}^j(x_n,y_{2k-1},u) = 2\int_k^{k+1/2} p_u(x)dx, \tag{A.21}$$

at the even index:

$$\hat{\mathbf{I}}^j(x_n,y_{2k},u) = 2\int_{k+1/2}^{k+1} p_u(x)dx \tag{A.22}$$

Note that $\hat{\mathbf{I}}^j(x_n,y_{2k-1},u) + \hat{\mathbf{I}}^j(x_n,y_{2k},u) = 2\mathbf{V}^{j-1}(x_n,y_k)$.

2.1 At the center case

See Figure A.2. The quadratic polynomial $p_0(x) = ax^2 + bx + c$ interpolates on $\{\mathbf{V}^{j-1}(x_n, y_{k-1}),\ \mathbf{V}^{j-1}(x_n, y_k),\ \mathbf{V}^{j-1}(x_n, y_{k+1})\}$. Three values have the following relationships:

$$\begin{cases} \mathbf{V}^{j-1}(x_n, y_{k-1}) = \int_{k-1}^{k} p_0(x)dx = \frac{1}{3}a - \frac{1}{2}b + c - ak + bk + ak^2 \\ \mathbf{V}^{j-1}(x_n, y_k) \quad = \int_{k}^{k+1} p_0(x)dx = \frac{1}{3}a + \frac{1}{2}b + c + ak + bk + ak^2 \\ \mathbf{V}^{j-1}(x_n, y_{k+1}) = \int_{k+1}^{k+2} p_0(x)dx = \frac{7}{3}a + \frac{3}{2}b + c + 3ak + bk + ak^2. \end{cases} \tag{A.23}$$

On the coarse scale, k will shift through the length of $\mathbf{V}^{j-1}(x_n, y_k)$ with the same performance of one polynomial as the case $k = 0$. Therefore,

$$\begin{cases} \mathbf{V}^{j-1}(x_n, y_{-1}) = \frac{1}{3}a - \frac{1}{2}b + c \\ \mathbf{V}^{j-1}(x_n, y_0) \quad = \frac{1}{3}a + \frac{1}{2}b + c \\ \mathbf{V}^{j-1}(x_n, y_1) \quad = \frac{7}{3}a + \frac{3}{2}b + c. \end{cases} \tag{A.24}$$

Solve the system (A.24) to find the polynomial coefficients a, b, c:

$$\begin{cases} a = \frac{1}{2}\mathbf{V}^{j-1}(x_n, y_{-1}) - \mathbf{V}^{j-1}(x_n, y_0) + \frac{1}{2}\mathbf{V}^{j-1}(x_n, y_1) \\ b = -\mathbf{V}^{j-1}(x_n, y_{-1}) + \mathbf{V}^{j-1}(x_n, y_0) \\ c = +\frac{1}{3}\mathbf{V}^{j-1}(x_n, y_{-1}) + \frac{5}{6}\mathbf{V}^{j-1}(x_n, y_0) - \frac{1}{6}\mathbf{V}^{j-1}(x_n, y_1). \end{cases} \tag{A.25}$$

Replacing these results (a, b, c) in the equation (A.21), the predicted value at the odd index is applied for the case $k = 0$:

$$\hat{\mathbf{I}}^j(x_n, y_{2k-1}, 0) = 2\int_{k}^{k+1/2} p_0(x)dx = \frac{1}{8}\mathbf{V}^{j-1}(x_n, y_{k-1}) + \mathbf{V}^{j-1}(x_n, y_k) - \frac{1}{8}\mathbf{V}^{j-1}(x_n, y_{k+1}) \tag{A.26}$$

Replacing the results (a, b, c) in the equation (A.22), the predicted value at the even index is applied for the case $k = 0$:

$$\hat{\mathbf{I}}^j(x_n, y_{2k}, 0) = 2\int_{k+1/2}^{k+1} p_0(x)dx = -\frac{1}{8}\mathbf{V}^{j-1}(x_n, y_{k-1}) + \mathbf{V}^{j-1}(x_n, y_k) + \frac{1}{8}\mathbf{V}^{j-1}(x_n, y_{k+1}) \tag{A.27}$$

2.2 At the left case

See Figure A.2. The quadratic polynomial $p_{-1}(x) = ax^2 + bx + c$ interpolates on $\{\mathbf{V}^{j-1}(x_n, y_{k-2}),\ \mathbf{V}^{j-1}(x_n, y_{k-1}),\ \mathbf{V}^{j-1}(x_n, y_k)\}$. Three values have the following relationships:

$$\begin{cases} \mathbf{V}^{j-1}(x_n, y_{k-2}) = \int_{k-2}^{k-1} p_{-1}(x)dx = \frac{7}{3}a - \frac{3}{2}b + c - 3ak + bk + ak^2 \\ \mathbf{V}^{j-1}(x_n, y_{k-1}) \ = \int_{k-1}^{k} p_{-1}(x)dx = \frac{1}{3}a - \frac{1}{2}b + c - ak + bk + ak^2 \\ \mathbf{V}^{j-1}(x_n, y_k) = \int_{k}^{k+1} p_{-1}(x)dx = \frac{1}{3}a + \frac{1}{2}b + c + ak + bk + ak^2. \end{cases} \tag{A.28}$$

On the coarse scale, k will shift through the length of $\mathbf{V}^{j-1}(x_n, y_k)$ with the same performance of one polynomial as the case $k = 0$. Therefore,

$$\begin{cases} \mathbf{V}^{j-1}(x_n, y_{-2}) = \frac{7}{3}a - \frac{3}{2}b + c \\ \mathbf{V}^{j-1}(x_n, y_{-1}) = \frac{1}{3}a - \frac{1}{2}b + c \\ \mathbf{V}^{j-1}(x_n, y_0) = \frac{1}{3}a + \frac{1}{2}b + c. \end{cases} \tag{A.29}$$

Solve the system (A.29) to find the polynomial coefficients a, b, c:

$$\begin{cases} a = \frac{1}{2}\mathbf{V}^{j-1}(x_n, y_{-2}) - \mathbf{V}^{j-1}(x_n, y_{-1}) + \frac{1}{2}\mathbf{V}^{j-1}(x_n, y_0) \\ b = -\mathbf{V}^{j-1}(x_n, y_{-1}) + \mathbf{V}^{j-1}(x_n, y_0) \\ c = -\frac{1}{6}\mathbf{V}^{j-1}(x_n, y_{-2}) + \frac{5}{6}\mathbf{V}^{j-1}(x_n, y_{-1}) + \frac{1}{3}\mathbf{V}^{j-1}(x_n, y_0). \end{cases} \tag{A.30}$$

Replacing these results (a, b, c) in the equation (A.21), the predicted value at the odd index is applied for the case $k = 0$:

$$\hat{\mathbf{I}}^j(x_n, y_{2k-1}, -1) = 2\int_k^{k+1/2} p_{-1}(x)dx = -\frac{1}{8}\mathbf{V}^{j-1}(x_n, y_{k-2}) + \frac{1}{2}\mathbf{V}^{j-1}(x_n, y_{k-1}) + \frac{5}{8}\mathbf{V}^{j-1}(x_n, y_k) \tag{A.31}$$

Replacing the results (a, b, c) in the equation (A.22), the predicted value at the even index is applied for the case $k = 0$:

$$\hat{\mathbf{I}}^j(x_n, y_{2k}, -1) = 2\int_{k+1/2}^{k+1} p_{-1}(x)dx = \frac{1}{8}\mathbf{V}^{j-1}(x_n, y_{k-2}) - \frac{1}{2}\mathbf{V}^{j-1}(x_n, y_{k-1}) + \frac{11}{8}\mathbf{V}^{j-1}(x_n, y_k) \tag{A.32}$$

2.3 At the right case

See Figure A.2. The quadratic polynomial $p_1(x) = ax^2 + bx + c$ interpolates on $\{\mathbf{V}^{j-1}(x_n, y_k),\ \mathbf{V}^{j-1}(x_n, y_{k+1}),\ \mathbf{V}^{j-1}(x_n, y_{k+2})\}$. Three values have the following relationships:

$$\begin{cases} \mathbf{V}^{j-1}(x_n, y_k) = \int_k^{k+1} p_1(x)dx = \frac{1}{3}a + \frac{1}{2}b + c + ak + bk + ak^2 \\ \mathbf{V}^{j-1}(x_n, y_{k+1}) = \int_{k+1}^{k+2} p_1(x)dx = \frac{7}{3}a + \frac{3}{2}b + c + 3ak + bk + ak^2 \\ \mathbf{V}^{j-1}(x_n, y_{k+2}) = \int_{k+2}^{k+3} p_1(x)dx = \frac{19}{3}a + \frac{5}{2}b + c + 5ak + bk + ak^2. \end{cases} \tag{A.33}$$

On the coarse scale, k will shift through the length of $\mathbf{V}^{j-1}(x_n, y_k)$ with the same performance of one polynomial as the case $k = 0$. Therefore,

$$\begin{cases} \mathbf{V}^{j-1}(x_n, y_0) = \frac{1}{3}a + \frac{1}{2}b + c \\ \mathbf{V}^{j-1}(x_n, y_1) = \frac{7}{3}a + \frac{3}{2}b + c \\ \mathbf{V}^{j-1}(x_n, y_2) = \frac{19}{3}a + \frac{5}{2}b + c. \end{cases} \tag{A.34}$$

Solve the system (A.34) to find the polynomial coefficients a, b, c:

$$\begin{cases} a = \frac{1}{2}\mathbf{V}^{j-1}(x_n, y_0) - \mathbf{V}^{j-1}(x_n, y_1) + \frac{1}{2}\mathbf{V}^{j-1}(x_n, y_2) \\ b = -2\mathbf{V}^{j-1}(x_n, y_0) + 3\mathbf{V}^{j-1}(x_n, y_1) - \mathbf{V}^{j-1}(x_n, y_2) \\ c = \frac{11}{6}\mathbf{V}^{j-1}(x_n, y_0) - \frac{7}{6}\mathbf{V}^{j-1}(x_n, y_1) + \frac{1}{3}\mathbf{V}^{j-1}(x_n, y_2). \end{cases} \tag{A.35}$$

Replacing these results (a, b, c) in the equation (A.21), the predicted value at the odd index is applied for the case $k=0$:

$$\hat{\mathbf{I}}^j(x_n,y_{2k-1},+1)=2\int_k^{k+1/2}p_1(x)dx=\frac{11}{8}\mathbf{V}^{j-1}(x_n,y_k)-\frac{1}{2}\mathbf{V}^{j-1}(x_n,y_{k+1})+\frac{1}{8}\mathbf{V}^{j-1}(x_n,y_{k+2}) \tag{A.36}$$

Replacing the results (a, b, c) in the equation (A.22), the predicted value at the even index is applied for the case $k=0$:

$$\hat{\mathbf{I}}^j(x_n,y_{2k},+1)=2\int_{k+1/2}^{k+1}p_1(x)dx=\frac{5}{8}\mathbf{V}^{j-1}(x_n,y_k)+\frac{1}{2}\mathbf{V}^{j-1}(x_n,y_{k+1})-\frac{1}{8}\mathbf{V}^{j-1}(x_n,y_{k+2}) \tag{A.37}$$

The following predicted values at odd indexes are rewritten from the equation (A.26), equation (A.31) and equation (A.36):

$$\begin{cases}\hat{\mathbf{I}}^j(x_n,y_{2k-1},-1)=-\frac{1}{8}\mathbf{V}^{j-1}(x_n,y_{k-2})+\frac{1}{2}\mathbf{V}^{j-1}(x_n,y_{k-1})+\frac{5}{8}\mathbf{V}^{j-1}(x_n,y_k)\\ \hat{\mathbf{I}}^j(x_n,y_{2k-1},0)=\frac{1}{8}\mathbf{V}^{j-1}(x_n,y_{k-1})+\mathbf{V}^{j-1}(x_n,y_k)-\frac{1}{8}\mathbf{V}^{j-1}(x_n,y_{k+1})\\ \hat{\mathbf{I}}^j(x_n,y_{2k-1},+1)=\frac{11}{8}\mathbf{V}^{j-1}(x_n,y_k)-\frac{1}{2}\mathbf{V}^{j-1}(x_n,y_{k+1})+\frac{1}{8}\mathbf{V}^{j-1}(x_n,y_{k+2}).\end{cases} \tag{A.38}$$

The following predicted values at even indexes are rewritten from the equation (A.27), equation (A.32) and equation (A.37):

$$\begin{cases}\hat{\mathbf{I}}^j(x_n,y_{2k},-1)=\frac{1}{8}\mathbf{V}^{j-1}(x_n,y_{k-2})-\frac{1}{2}\mathbf{V}^{j-1}(x_n,y_{k-1})+\frac{11}{8}\mathbf{V}^{j-1}(x_n,y_k)\\ \hat{\mathbf{I}}^j(x_n,y_{2k},0)\quad=-\frac{1}{8}\mathbf{V}^{j-1}(x_n,y_{k-1})+\mathbf{V}^{j-1}(x_n,y_k)+\frac{1}{8}\mathbf{V}^{j-1}(x_n,y_{k+1})\\ \hat{\mathbf{I}}^j(x_n,y_{2k},+1)=\frac{5}{8}\mathbf{V}^{j-1}(x_n,y_k)+\frac{1}{2}\mathbf{V}^{j-1}(x_n,y_{k+1})-\frac{1}{8}\mathbf{V}^{j-1}(x_n,y_{k+2}).\end{cases} \tag{A.39}$$

In the thesis, only predicted values at odd indexes are used:

$$\hat{\mathbf{I}}^j(x_n,y_{2k-1})=\begin{cases}\hat{\mathbf{I}}^j(x_n,y_{2k-1},-1) & \text{for the left case}\\ \hat{\mathbf{I}}^j(x_n,y_{2k-1},0) & \text{for the center case}\\ \hat{\mathbf{I}}^j(x_n,y_{2k-1},+1) & \text{for the right case}\end{cases} \tag{A.40}$$

$$=\begin{cases}-\frac{1}{8}\mathbf{V}^{j-1}(x_n,y_{k-2})+\frac{1}{2}\mathbf{V}^{j-1}(x_n,y_{k-1})+\frac{5}{8}\mathbf{V}^{j-1}(x_n,y_k)\\ +\frac{1}{8}\mathbf{V}^{j-1}(x_n,y_{k-1})+\mathbf{V}^{j-1}(x_n,y_k)-\frac{1}{8}\mathbf{V}^{j-1}(x_n,y_{k+1})\\ +\frac{11}{8}\mathbf{V}^{j-1}(x_n,y_k)-\frac{1}{2}\mathbf{V}^{j-1}(x_n,y_{k+1})+\frac{1}{8}\mathbf{V}^{j-1}(x_n,y_{k+2})\end{cases} \tag{A.41}$$

$$=\begin{cases}\sum\left[-\frac{1}{8}\quad+\frac{1}{2}\quad+\frac{5}{8}\right]\otimes\left[\mathbf{V}^{j-1}(x_n,y_{k-2})\quad\mathbf{V}^{j-1}(x_n,y_{k-1})\quad\mathbf{V}^{j-1}(x_n,y_k)\right]\\ \sum\left[+\frac{1}{8}\quad+1\quad-\frac{1}{8}\right]\otimes\left[\mathbf{V}^{j-1}(x_n,y_{k-1})\quad\mathbf{V}^{j-1}(x_n,y_k)\quad\mathbf{V}^{j-1}(x_n,y_{k+1})\right]\\ \sum\left[+\frac{11}{8}\quad-\frac{1}{2}\quad+\frac{1}{8}\right]\otimes\left[\mathbf{V}^{j-1}(x_n,y_k)\quad\mathbf{V}^{j-1}(x_n,y_{k+1})\quad\mathbf{V}^{j-1}(x_n,y_{k+2})\right]\end{cases} \tag{A.42}$$

in compact forms where $\otimes$ is the product term by term.

APPENDIX B

Computation of non-separable multiresolution ENO coefficients

This appendix concerns the computation of non-separable ENO Cell-Average coefficients. **Requirements**: These coefficients are constant, independent to parameters (n,m) and applied for all pixels of the image. A pair of (n,m) will shift through the area of 2D approximation (i.e. $\mathbf{I}^{j-1}(x_n,y_m)$) with the same performance of one polynomial as the case $(n,m)=(0,0)$.

Denote $p_{(-1,-1)}(x,y)$, $p_{(-1,0)}(x,y)$, $p_{(-1,1)}(x,y)$, $p_{(0,-1)}(x,y)$, $p_{(0,0)}(x,y)$, $p_{(0,1)}(x,y)$, $p_{(1,-1)}(x,y)$, $p_{(1,0)}(x,y)$, $p_{(1,1)}(x,y)$ the nine polynomials which corresponding to the coarse scale. These are attached to the 2D stencils $\mathbf{S}^{j-1}(x_n,y_m,r_1,r_2)$ with r_1,r_2 in $[-1,0,1]$ corresponding to the position of the stencil with respect to (n,m) as follows:

$$\mathbf{S}^{j-1}(x_n,y_m,r_1,r_2)=\begin{bmatrix}\mathbf{C}^{j-1}_{(n+r_1-1,m+r_2-1)} & \mathbf{C}^{j-1}_{(n+r_1-1,m+r_2)} & \mathbf{C}^{j-1}_{(n+r_1-1,m+r_2+1)}\\ \mathbf{C}^{j-1}_{(n+r_1,m+r_2-1)} & \mathbf{C}^{j-1}_{(n+r_1,m+r_2)} & \mathbf{C}^{j-1}_{(n+r_1,m+r_2+1)}\\ \mathbf{C}^{j-1}_{(n+r_1+1,m+r_2-1)} & \mathbf{C}^{j-1}_{(n+r_1+1,m+r_2)} & \mathbf{C}^{j-1}_{(n+r_1+1,m+r_2+1)}\end{bmatrix}. \tag{B.1}$$

There are then nine kinds of stencil positions: down-left (DL) with $(r_1,r_2)=(-1,-1)$, down-center (DC) with $(r_1,r_2)=(-1,0)$, down-right (DR) with $(r_1,r_2)=(-1,1)$, center-left (CL) with $(r_1,r_2)=(0,-1)$, center-center (CC) with $(r_1,r_2)=(0,0)$, center-right (CR) with $(r_1,r_2)=(0,1)$, upper-left (UL) with $(r_1,r_2)=(1,-1)$, upper-center (UC) with $(r_1,r_2)=(1,0)$ and upper-right (UR) with $(r_1,r_2)=(1,1)$. See Figure B.1.

The general bi-quadractic polynomial is $p_{(r_1,r_2)}(x,y)=ax^2y^2+bx^2y+cxy^2+dxy+ex^2+fy^2+gx+hy+k$. Through the Cartesian coordinate system, there are nine bi-quadractic polynomials $p_{(r_1,r_2)}$ corresponding to each stencil $\mathbf{S}^{j-1}(x_n,y_m,r_1,r_2)$ with

$(r_1,r_2) \in \{(-1,-1),\ (-1,0),\ (-1,1),\ (0,-1),\ (0,0),\ (0,1),\ (1,-1),\ (1,0),\ (1,1)\}$. It is attached to the nine cells in 3×3 square.

The pixel value $\mathbf{I}^{j-1}(x_n,y_m)$ is defined by the Cell-Average of the underlying bidimensional polynomial $p_{(r_1,r_2)}(x,y)$ modeling the image, as follows:

$$\mathbf{I}^{j-1}(x_n,y_m) = \int\limits_{\mathbf{C}^{j-1}_{(n,m)}} p_{(r_1,r_2)}(x,y)dxdy = \int_n^{n+1}\int_m^{m+1} p_{(r_1,r_2)}(x,y)dxdy, \tag{B.2}$$

where the 2D cell $\mathbf{C}^{j-1}_{(n,m)}$ is defined as $[n,n+1] \times [m,m+1]$.

Four predicted values, $\hat{\mathbf{I}}^j(x_{2n-1},y_{2m-1})$, $\hat{\mathbf{I}}^j(x_{2n-1},y_{2m})$, $\hat{\mathbf{I}}^j(x_{2n},y_{2m-1})$ and $\hat{\mathbf{I}}^j(x_{2n},y_{2m})$, are interpolated from $\mathbf{I}^{j-1}$ at the interest position (x_n,y_m), and defined in one-fourths (i.e. $[n,n+1/2]\times[m,m+1/2]$, $[n,n+1/2]\times[m+1/2,m+1]$, $[n+1/2,n+1]\times[m,m+1/2]$ and $[n+1/2,n+1]\times[m+1/2,m+1]$) of the 2D cell as follows:

$$\begin{bmatrix} \hat{\mathbf{I}}^j(x_{2n-1},y_{2m-1}) & \hat{\mathbf{I}}^j(x_{2n-1},y_{2m}) \\ \hat{\mathbf{I}}^j(x_{2n},y_{2m-1}) & \hat{\mathbf{I}}^j(x_{2n},y_{2m}) \end{bmatrix} =$$

$$4\begin{bmatrix} \int_n^{n+1/2}\int_m^{m+1/2} p_{(r_1,r_2)}(x,y)dxdy & \int_n^{n+1/2}\int_{m+1/2}^{m+1} p_{(r_1,r_2)}(x,y)dxdy \\ \int_{n+1/2}^{n+1}\int_m^{m+1/2} p_{(r_1,r_2)}(x,y)dxdy & \int_{n+1/2}^{n+1}\int_m^{m+1} p_{(r_1,r_2)}(x,y)dxdy \end{bmatrix}. \tag{B.3}$$

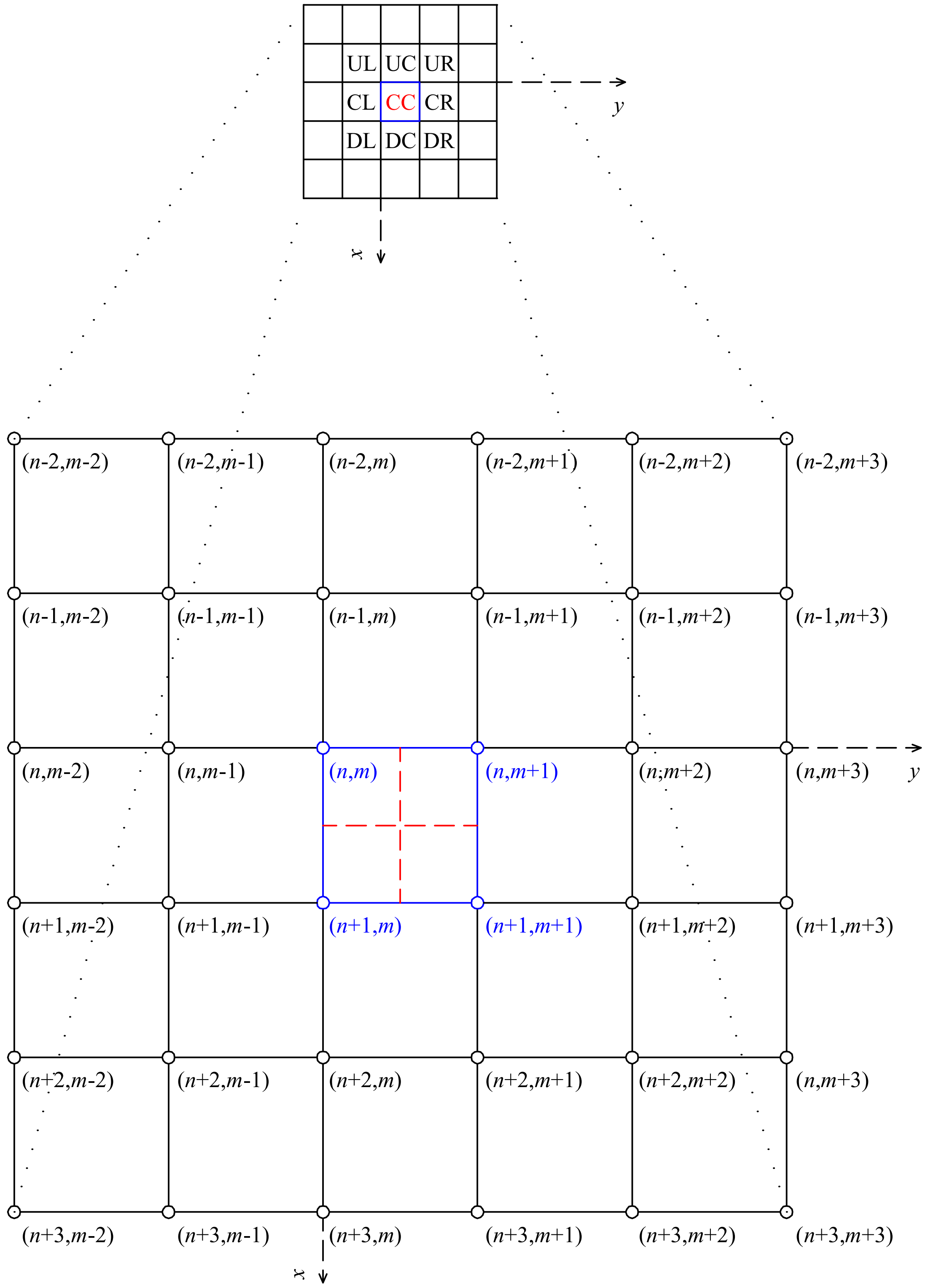

Figure B.1: *There are nine bi-quadratic polynomials attached to the 2D cartezian coordinates system of the coarse scale: (Up) Each has size of* 3×3 *cells with the centered cell marked by the label: upper-left (UL) with* $(r_1,r_2)=(-1,-1)$*, upper-center (UC) with* $(r_1,r_2)=(-1,0)$*, upper-right (UR) with* $(r_1,r_2)=(-1,1)$*, center-left (CL) with* $(r_1,r_2)=(0,-1)$*, center-center (CC) with* $(r_1,r_2)=(0,0)$*, center-right (CR) with* $(r_1,r_2)=(0,1)$*, down-left (DL) with* $(r_1,r_2)=(1,-1)$*, down-center (DC) with* $(r_1,r_2)=(1,0)$ *and down-right (DR) with* $(r_1,r_2)=(1,1)$*; (Down) Zooming part.*

1 At the center-center case

See Figure B.1. On the coarse scale, a pair of (n,m) will shift through the area of $\mathbf{I}^{j-1}(x_n,y_m)$ with the same performance of one polynomial as the case $(n,m)=(0,0)$. Therefore, the bi-quadratic polynomial $p_{(0,0)}(x,y)=ax^2y^2+bx^2y+cxy^2+dxy+ex^2+fy^2+gx+hy+k$ interpolates on:

$$\begin{bmatrix} \mathbf{I}^{j-1}(x_{-1},y_{-1}) & \mathbf{I}^{j-1}(x_{-1},y_0) & \mathbf{I}^{j-1}(x_{-1},y_1) \\ \mathbf{I}^{j-1}(x_0,y_{-1}) & \mathbf{I}^{j-1}(x_0,y_0) & \mathbf{I}^{j-1}(x_0,y_1) \\ \mathbf{I}^{j-1}(x_1,y_{-1}) & \mathbf{I}^{j-1}(x_1,y_0) & \mathbf{I}^{j-1}(x_1,y_1) \end{bmatrix} = \begin{bmatrix} m1 & m2 & m3 \\ m4 & m0 & m5 \\ m6 & m7 & m8 \end{bmatrix} \tag{B.4}$$

Nine values have the following relationships:

$$\begin{cases} \mathbf{I}^{j-1}(x_{-1},y_1) = \int_{-1}^{0}\int_{1}^{2} p(x,y)dxdy = \frac{7}{9}a+\frac{1}{2}b-\frac{7}{6}c-\frac{3}{4}d+\frac{1}{3}e+\frac{7}{3}f-\frac{1}{2}g+\frac{3}{2}h+k \\ \mathbf{I}^{j-1}(x_0,y_1) = \int_{0}^{1}\int_{1}^{2} p(x,y)dxdy = \frac{7}{9}a+\frac{1}{2}b+\frac{7}{6}c+\frac{3}{4}d+\frac{1}{3}e+\frac{7}{3}f+\frac{1}{2}g+\frac{3}{2}h+k \\ \mathbf{I}^{j-1}(x_1,y_1) = \int_{1}^{2}\int_{1}^{2} p(x,y)dxdy = \frac{49}{9}a+\frac{7}{2}b+\frac{7}{2}c+\frac{9}{4}d+\frac{7}{3}e+\frac{7}{3}f+\frac{3}{2}g+\frac{3}{2}h+k \\ \mathbf{I}^{j-1}(x_{-1},y_0) = \int_{-1}^{0}\int_{0}^{1} p(x,y)dxdy = \frac{1}{9}a+\frac{1}{6}b-\frac{1}{6}c-\frac{1}{4}d+\frac{1}{3}e+\frac{1}{3}f-\frac{1}{2}g+\frac{1}{2}h+k \\ \mathbf{I}^{j-1}(x_0,y_0) = \int_{0}^{1}\int_{0}^{1} p(x,y)dxdy = \frac{1}{9}a+\frac{1}{6}b+\frac{1}{6}c+\frac{1}{4}d+\frac{1}{3}e+\frac{1}{3}f+\frac{1}{2}g+\frac{1}{2}h+k \\ \mathbf{I}^{j-1}(x_1,y_0) = \int_{1}^{2}\int_{0}^{1} p(x,y)dxdy = \frac{7}{9}a+\frac{7}{6}b+\frac{1}{2}c+\frac{3}{4}d+\frac{7}{3}e+\frac{1}{3}f+\frac{3}{2}g+\frac{1}{2}h+k \\ \mathbf{I}^{j-1}(x_{-1},y_{-1}) = \int_{-1}^{0}\int_{-1}^{0} p(x,y)dxdy = \frac{1}{9}a-\frac{1}{6}b-\frac{1}{6}c+\frac{1}{4}d+\frac{1}{3}e+\frac{1}{3}f-\frac{1}{2}g-\frac{1}{2}h+k \\ \mathbf{I}^{j-1}(x_0,y_{-1}) = \int_{0}^{1}\int_{-1}^{0} p(x,y)dxdy = \frac{1}{9}a-\frac{1}{6}b+\frac{1}{6}c-\frac{1}{4}d+\frac{1}{3}e+\frac{1}{3}f+\frac{1}{2}g-\frac{1}{2}h+k \\ \mathbf{I}^{j-1}(x_1,y_{-1}) = \int_{1}^{2}\int_{-1}^{0} p(x,y)dxdy = \frac{7}{9}a-\frac{7}{6}b+\frac{1}{2}c-\frac{3}{4}d+\frac{7}{3}e+\frac{1}{3}f+\frac{3}{2}g-\frac{1}{2}h+k. \end{cases} \tag{B.5}$$

Solve the system (B.5) to find the polynomial coefficients a, b, c, d, e, f, g, h, k:

$$\Longrightarrow \begin{cases} a = m0+\frac{1}{4}m1-\frac{1}{2}m2+\frac{1}{4}m3-\frac{1}{2}m4-\frac{1}{2}m5+\frac{1}{4}m6-\frac{1}{2}m7+\frac{1}{4}m8 \\ b = \frac{1}{2}m4-m0+\frac{1}{2}m5-\frac{1}{2}m6+m7-\frac{1}{2}m8 \\ c = \frac{1}{2}m2-\frac{1}{2}m1-m0+m4-\frac{1}{2}m6+\frac{1}{2}m7 \\ d = m0-m4+m6-m7 \\ e = \frac{1}{6}m2-\frac{1}{12}m1-\frac{5}{6}m0-\frac{1}{12}m3+\frac{5}{12}m4+\frac{5}{12}m5+\frac{1}{6}m6-\frac{1}{3}m7+\frac{1}{6}m8 \\ f = \frac{1}{6}m1-\frac{5}{6}m0+\frac{5}{12}m2-\frac{1}{12}m3-\frac{1}{3}m4+\frac{1}{6}m5+\frac{1}{6}m6+\frac{5}{12}m7-\frac{1}{12}m8 \\ g = \frac{5}{6}m0+\frac{1}{6}m1-\frac{1}{6}m2-\frac{5}{6}m4-\frac{1}{3}m6+\frac{1}{3}m7 \\ h = \frac{5}{6}m0+\frac{1}{3}m4-\frac{1}{6}m5-\frac{1}{3}m6-\frac{5}{6}m7+\frac{1}{6}m8 \\ k = \frac{25}{36}m0-\frac{1}{18}m1-\frac{5}{36}m2+\frac{1}{36}m3+\frac{5}{18}m4-\frac{5}{36}m5+\frac{1}{9}m6+\frac{5}{18}m7-\frac{1}{18}m8. \end{cases} \tag{B.6}$$

Replacing these results in the equation (B.3), four predicted values are applied for the case $(n,m) = (0,0)$ as follows:

$$\begin{cases} \hat{\mathbf{I}}^j(x_{2n-1}, y_{2m-1}) = 4[+\frac{1}{256}m1 + \frac{1}{32}m2 - \frac{1}{256}m3 + \frac{1}{32}m4 + \frac{1}{4}m0 - \frac{1}{32}m5 - \frac{1}{256}m6 - \frac{1}{32}m7 + \frac{1}{256}m8] \\ \hat{\mathbf{I}}^j(x_{2n-1}, y_{2m}) \quad = 4[-\frac{1}{256}m1 + \frac{1}{32}m2 + \frac{1}{256}m3 - \frac{1}{32}m4 + \frac{1}{4}m0 + \frac{1}{32}m5 + \frac{1}{256}m6 - \frac{1}{32}m7 - \frac{1}{256}m8] \\ \hat{\mathbf{I}}^j(x_{2n}, y_{2m-1}) \quad = 4[-\frac{1}{256}m1 - \frac{1}{32}m2 + \frac{1}{256}m3 + \frac{1}{32}m4 + \frac{1}{4}m0 - \frac{1}{32}m5 + \frac{1}{256}m6 + \frac{1}{32}m7 - \frac{1}{256}m8] \\ \hat{\mathbf{I}}^j(x_{2n}, y_{2m}) \quad = 4[+\frac{1}{256}m1 - \frac{1}{32}m2 - \frac{1}{256}m3 - \frac{1}{32}m4 + \frac{1}{4}m0 + \frac{1}{32}m5 - \frac{1}{256}m6 + \frac{1}{32}m7 + \frac{1}{256}m8] \end{cases} \tag{B.7}$$

Denote

$$\mathbf{I}_{CC}^{j-1} = \begin{bmatrix} \mathbf{I}^{j-1}(x_{n-1}, y_{m-1}) & \mathbf{I}^{j-1}(x_{n-1}, y_m) & \mathbf{I}^{j-1}(x_{n-1}, y_{m+1}) \\ \mathbf{I}^{j-1}(x_n, y_{m-1}) & \mathbf{I}^{j-1}(x_n, y_m) & \mathbf{I}^{j-1}(x_n, y_{m+1}) \\ \mathbf{I}^{j-1}(x_{n+1}, y_{m-1}) & \mathbf{I}^{j-1}(x_{n+1}, y_m) & \mathbf{I}^{j-1}(x_{n+1}, y_{m+1}) \end{bmatrix} = \begin{bmatrix} m1 & m2 & m3 \\ m4 & m0 & m5 \\ m6 & m7 & m8 \end{bmatrix} \tag{B.8}$$

In compact forms, four predicted values are rewritten as follows:

$$\begin{bmatrix} \hat{\mathbf{I}}^j(x_{2n-1}, y_{2m-1}) & \hat{\mathbf{I}}^j(x_{2n-1}, y_{2m}) \\ \hat{\mathbf{I}}^j(x_{2n}, y_{2m-1}) & \hat{\mathbf{I}}^j(x_{2n}, y_{2m}) \end{bmatrix} = \tag{B.9}$$

$$= 4 \begin{bmatrix} \sum\sum \begin{bmatrix} +\frac{1}{256} & +\frac{1}{32} & -\frac{1}{256} \\ +\frac{1}{32} & +\frac{1}{4} & -\frac{1}{32} \\ -\frac{1}{256} & -\frac{1}{32} & +\frac{1}{256} \end{bmatrix} \otimes \mathbf{I}_{CC}^{j-1} & \sum\sum \begin{bmatrix} -\frac{1}{256} & +\frac{1}{32} & +\frac{1}{256} \\ -\frac{1}{32} & +\frac{1}{4} & +\frac{1}{32} \\ +\frac{1}{256} & -\frac{1}{32} & -\frac{1}{256} \end{bmatrix} \otimes \mathbf{I}_{CC}^{j-1} \\ \\ \sum\sum \begin{bmatrix} -\frac{1}{256} & -\frac{1}{32} & +\frac{1}{256} \\ +\frac{1}{32} & +\frac{1}{4} & -\frac{1}{32} \\ +\frac{1}{256} & +\frac{1}{32} & -\frac{1}{256} \end{bmatrix} \otimes \mathbf{I}_{CC}^{j-1} & \sum\sum \begin{bmatrix} +\frac{1}{256} & -\frac{1}{32} & -\frac{1}{256} \\ -\frac{1}{32} & +\frac{1}{4} & +\frac{1}{32} \\ -\frac{1}{256} & +\frac{1}{32} & +\frac{1}{256} \end{bmatrix} \otimes \mathbf{I}_{CC}^{j-1} \end{bmatrix} \tag{B.10}$$

where $\otimes$ is the product term by term.

2 At the center-left case

See Figure B.1. The bi-quadratic polynomial $p_{(-1,0)}(x,y) = ax^2y^2 + bx^2y + cxy^2 + dxy + ex^2 + fy^2 + gx + hy + k$ interpolates on:

$$\begin{bmatrix} \mathbf{I}^{j-1}(x_{-1}, y_{-2}) & \mathbf{I}^{j-1}(x_{-1}, y_{-1}) & \mathbf{I}^{j-1}(x_{-1}, y_0) \\ \mathbf{I}^{j-1}(x_0, y_{-2}) & \mathbf{I}^{j-1}(x_0, y_{-1}) & \mathbf{I}^{j-1}(x_0, y_0) \\ \mathbf{I}^{j-1}(x_1, y_{-2}) & \mathbf{I}^{j-1}(x_1, y_{-1}) & \mathbf{I}^{j-1}(x_1, y_0) \end{bmatrix} = \begin{bmatrix} m1 & m2 & m3 \\ m4 & m0 & m5 \\ m6 & m7 & m8 \end{bmatrix} \tag{B.11}$$

With the same procedures as the center-center case, it derives nine relationships and then solves the system to find nine polynomial coefficients (a, b, c, d, e, f, g, h, k). Finally replacing these coefficients in the equation (B.3), four predicted values are applied for the case $(n,m) = (0,0)$ as follows:

$$\begin{cases} \hat{\mathbf{I}}^j(x_{2n-1}, y_{2m-1}) = 4[-\frac{1}{256}m1 + \frac{1}{64}m2 + \frac{5}{256}m3 - \frac{1}{32}m4 + \frac{1}{8}m0 + \frac{5}{32}m5 + \frac{1}{256}m6 - \frac{1}{64}m7 - \frac{5}{256}m8] \\ \hat{\mathbf{I}}^j(x_{2n-1}, y_{2m}) \quad = 4[+\frac{1}{256}m1 - \frac{1}{64}m2 + \frac{11}{256}m3 + \frac{1}{32}m4 - \frac{1}{8}m0 + \frac{11}{32}m5 - \frac{1}{256}m6 + \frac{1}{64}m7 - \frac{11}{256}m8] \\ \hat{\mathbf{I}}^j(x_{2n}, y_{2m-1}) \quad = 4[+\frac{1}{256}m1 - \frac{1}{64}m2 - \frac{5}{256}m3 - \frac{1}{32}m4 + \frac{1}{8}m0 + \frac{5}{32}m5 - \frac{1}{256}m6 + \frac{1}{64}m7 + \frac{5}{256}m8] \\ \hat{\mathbf{I}}^j(x_{2n}, y_{2m}) \quad = 4[-\frac{1}{256}m1 + \frac{1}{64}m2 - \frac{11}{256}m3 + \frac{1}{32}m4 - \frac{1}{8}m0 + \frac{11}{32}m5 + \frac{1}{256}m6 - \frac{1}{64}m7 + \frac{11}{256}m8] \end{cases} \tag{B.12}$$

Denote

$$\mathbf{I}_{CL}^{j-1} = \begin{bmatrix} \mathbf{I}^{j-1}(x_{n-1}, y_{m-2}) & \mathbf{I}^{j-1}(x_{n-1}, y_{m-1}) & \mathbf{I}^{j-1}(x_{n-1}, y_m) \\ \mathbf{I}^{j-1}(x_n, y_{m-2}) & \mathbf{I}^{j-1}(x_n, y_{m-1}) & \mathbf{I}^{j-1}(x_n, y_m) \\ \mathbf{I}^{j-1}(x_{n+1}, y_{m-2}) & \mathbf{I}^{j-1}(x_{n+1}, y_{m-1}) & \mathbf{I}^{j-1}(x_{n+1}, y_m) \end{bmatrix} = \begin{bmatrix} m1 & m2 & m3 \\ m4 & m0 & m5 \\ m6 & m7 & m8 \end{bmatrix} \tag{B.13}$$

In compact forms, four predicted values are rewritten as follows:

$$\begin{bmatrix} \hat{\mathbf{I}}^j(x_{2n-1}, y_{2m-1}) & \hat{\mathbf{I}}^j(x_{2n-1}, y_{2m}) \\ \hat{\mathbf{I}}^j(x_{2n}, y_{2m-1}) & \hat{\mathbf{I}}^j(x_{2n}, y_{2m}) \end{bmatrix} = \tag{B.14}$$

$$= 4 \begin{bmatrix} \sum\sum \begin{bmatrix} -\frac{1}{256} & +\frac{1}{64} & +\frac{5}{256} \\ -\frac{1}{32} & +\frac{1}{8} & +\frac{5}{32} \\ +\frac{1}{256} & -\frac{1}{64} & -\frac{5}{256} \end{bmatrix} \otimes \mathbf{I}_{CL}^{j-1} & \sum\sum \begin{bmatrix} +\frac{1}{256} & -\frac{1}{64} & +\frac{11}{256} \\ +\frac{1}{32} & -\frac{1}{8} & +\frac{11}{32} \\ -\frac{1}{256} & +\frac{1}{64} & -\frac{11}{256} \end{bmatrix} \otimes \mathbf{I}_{CL}^{j-1} \\ \sum\sum \begin{bmatrix} +\frac{1}{256} & -\frac{1}{64} & -\frac{5}{256} \\ -\frac{1}{32} & +\frac{1}{8} & +\frac{5}{32} \\ -\frac{1}{256} & +\frac{1}{64} & +\frac{5}{256} \end{bmatrix} \otimes \mathbf{I}_{CL}^{j-1} & \sum\sum \begin{bmatrix} -\frac{1}{256} & +\frac{1}{64} & -\frac{11}{256} \\ +\frac{1}{32} & -\frac{1}{8} & +\frac{11}{32} \\ +\frac{1}{256} & -\frac{1}{64} & +\frac{11}{256} \end{bmatrix} \otimes \mathbf{I}_{CL}^{j-1} \end{bmatrix} \tag{B.15}$$

3 At the center-right case

See Figure B.1.

$$\begin{cases} \hat{\mathbf{I}}^j(x_{2n-1}, y_{2m-1}) = 4[+\frac{11}{256}m1 - \frac{1}{64}m2 + \frac{1}{256}m3 + \frac{11}{32}m4 - \frac{1}{8}m0 + \frac{1}{32}m5 - \frac{11}{256}m6 + \frac{1}{64}m7 - \frac{1}{256}m8] \\ \hat{\mathbf{I}}^j(x_{2n-1}, y_{2m}) \quad = 4[+\frac{5}{256}m1 + \frac{1}{64}m2 - \frac{1}{256}m3 + \frac{5}{32}m4 + \frac{1}{8}m0 - \frac{1}{32}m5 - \frac{5}{256}m6 - \frac{1}{64}m7 + \frac{1}{256}m8] \\ \hat{\mathbf{I}}^j(x_{2n}, y_{2m-1}) \quad = 4[-\frac{11}{256}m1 + \frac{1}{64}m2 - \frac{1}{256}m3 + \frac{11}{32}m4 - \frac{1}{8}m0 + \frac{1}{32}m5 + \frac{11}{256}m6 - \frac{1}{64}m7 + \frac{1}{256}m8] \\ \hat{\mathbf{I}}^j(x_{2n}, y_{2m}) \quad = 4[-\frac{5}{256}m1 - \frac{1}{64}m2 + \frac{1}{256}m3 + \frac{5}{32}m4 + \frac{1}{8}m0 - \frac{1}{32}m5 + \frac{5}{256}m6 + \frac{1}{64}m7 - \frac{1}{256}m8] \end{cases} \tag{B.16}$$

Denote

$$\mathbf{I}_{CR}^{j-1} = \begin{bmatrix} \mathbf{I}^{j-1}(x_{n-1}, y_m) & \mathbf{I}^{j-1}(x_{n-1}, y_{m+1}) & \mathbf{I}^{j-1}(x_{n-1}, y_{m+2}) \\ \mathbf{I}^{j-1}(x_n, y_m) & \mathbf{I}^{j-1}(x_n, y_{m+1}) & \mathbf{I}^{j-1}(x_n, y_{m+2}) \\ \mathbf{I}^{j-1}(x_{n+1}, y_m) & \mathbf{I}^{j-1}(x_{n+1}, y_{m+1}) & \mathbf{I}^{j-1}(x_{n+1}, y_{m+2}) \end{bmatrix} = \begin{bmatrix} m1 & m2 & m3 \\ m4 & m0 & m5 \\ m6 & m7 & m8 \end{bmatrix} \tag{B.17}$$

In compact forms, four predicted values are rewritten as follows:

$$\begin{bmatrix} \hat{\mathbf{I}}^j(x_{2n-1}, y_{2m-1}) & \hat{\mathbf{I}}^j(x_{2n-1}, y_{2m}) \\ \hat{\mathbf{I}}^j(x_{2n}, y_{2m-1}) & \hat{\mathbf{I}}^j(x_{2n}, y_{2m}) \end{bmatrix} = \tag{B.18}$$

$$= 4 \begin{bmatrix} \sum\sum \begin{bmatrix} +\frac{11}{256} & -\frac{1}{64} & +\frac{1}{256} \\ +\frac{11}{32} & -\frac{1}{8} & +\frac{1}{32} \\ -\frac{11}{256} & +\frac{1}{64} & -\frac{1}{256} \end{bmatrix} \otimes \mathbf{I}_{CR}^{j-1} & \sum\sum \begin{bmatrix} +\frac{5}{256} & +\frac{1}{64} & -\frac{1}{256} \\ +\frac{5}{32} & +\frac{1}{8} & -\frac{1}{32} \\ -\frac{5}{256} & -\frac{1}{64} & +\frac{1}{256} \end{bmatrix} \otimes \mathbf{I}_{CR}^{j-1} \\ \\ \sum\sum \begin{bmatrix} -\frac{11}{256} & +\frac{1}{64} & -\frac{1}{256} \\ +\frac{11}{32} & -\frac{1}{8} & +\frac{1}{32} \\ +\frac{11}{256} & -\frac{1}{64} & +\frac{1}{256} \end{bmatrix} \otimes \mathbf{I}_{CR}^{j-1} & \sum\sum \begin{bmatrix} -\frac{5}{256} & -\frac{1}{64} & +\frac{1}{256} \\ +\frac{5}{32} & +\frac{1}{8} & -\frac{1}{32} \\ +\frac{5}{256} & +\frac{1}{64} & -\frac{1}{256} \end{bmatrix} \otimes \mathbf{I}_{CR}^{j-1} \end{bmatrix} \tag{B.19}$$

4 At the upper-left case

See Figure B.1.

$$\begin{cases} \hat{\mathbf{I}}^j(x_{2n-1}, y_{2m-1}) = 4[+\frac{1}{256}m1 - \frac{1}{64}m2 - \frac{5}{256}m3 - \frac{1}{64}m4 + \frac{1}{16}m0 + \frac{5}{64}m5 - \frac{5}{256}m6 + \frac{5}{64}m7 + \frac{25}{256}m8] \\ \hat{\mathbf{I}}^j(x_{2n-1}, y_{2m}) \quad = 4[-\frac{1}{256}m1 + \frac{1}{64}m2 - \frac{11}{256}m3 + \frac{1}{64}m4 - \frac{1}{16}m0 + \frac{11}{64}m5 + \frac{5}{256}m6 - \frac{5}{64}m7 + \frac{55}{256}m8] \\ \hat{\mathbf{I}}^j(x_{2n}, y_{2m-1}) \quad = 4[-\frac{1}{256}m1 + \frac{1}{64}m2 + \frac{5}{256}m3 + \frac{1}{64}m4 - \frac{1}{16}m0 - \frac{5}{64}m5 - \frac{11}{256}m6 + \frac{11}{64}m7 + \frac{55}{256}m8] \\ \hat{\mathbf{I}}^j(x_{2n}, y_{2m}) \quad = 4[+\frac{1}{256}m1 - \frac{1}{64}m2 + \frac{11}{256}m3 - \frac{1}{64}m4 + \frac{1}{16}m0 - \frac{11}{64}m5 + \frac{11}{256}m6 - \frac{11}{64}m7 + \frac{121}{256}m8] \end{cases} \tag{B.20}$$

Denote

$$\mathbf{I}_{UL}^{j-1} = \begin{bmatrix} \mathbf{I}^{j-1}(x_{n-2}, y_{m-2}) & \mathbf{I}^{j-1}(x_{n-2}, y_{m-1}) & \mathbf{I}^{j-1}(x_{n-2}, y_m) \\ \mathbf{I}^{j-1}(x_{n-1}, y_{m-2}) & \mathbf{I}^{j-1}(x_{n-1}, y_{m-1}) & \mathbf{I}^{j-1}(x_{n-1}, y_m) \\ \mathbf{I}^{j-1}(x_n, y_{m-2}) & \mathbf{I}^{j-1}(x_n, y_{m-1}) & \mathbf{I}^{j-1}(x_n, y_m) \end{bmatrix} = \begin{bmatrix} m1 & m2 & m3 \\ m4 & m0 & m5 \\ m6 & m7 & m8 \end{bmatrix} \tag{B.21}$$

In compact forms, four predicted values are rewritten as follows:

$$\begin{bmatrix} \hat{\mathbf{I}}^j(x_{2n-1}, y_{2m-1}) & \hat{\mathbf{I}}^j(x_{2n-1}, y_{2m}) \\ \hat{\mathbf{I}}^j(x_{2n}, y_{2m-1}) & \hat{\mathbf{I}}^j(x_{2n}, y_{2m}) \end{bmatrix} = \tag{B.22}$$

$$= 4 \begin{bmatrix} \sum\sum \begin{bmatrix} +\frac{1}{256} & -\frac{1}{64} & -\frac{5}{256} \\ -\frac{1}{64} & +\frac{1}{16} & +\frac{5}{64} \\ -\frac{5}{256} & +\frac{5}{64} & +\frac{25}{256} \end{bmatrix} \otimes \mathbf{I}_{UL}^{j-1} & \sum\sum \begin{bmatrix} -\frac{1}{256} & +\frac{1}{64} & -\frac{11}{256} \\ +\frac{1}{64} & -\frac{1}{16} & +\frac{11}{64} \\ +\frac{5}{256} & -\frac{5}{64} & +\frac{55}{256} \end{bmatrix} \otimes \mathbf{I}_{UL}^{j-1} \\ \\ \sum\sum \begin{bmatrix} -\frac{1}{256} & +\frac{1}{64} & +\frac{5}{256} \\ +\frac{1}{64} & -\frac{1}{16} & -\frac{5}{64} \\ -\frac{11}{256} & +\frac{11}{64} & +\frac{55}{256} \end{bmatrix} \otimes \mathbf{I}_{UL}^{j-1} & \sum\sum \begin{bmatrix} +\frac{1}{256} & -\frac{1}{64} & +\frac{11}{256} \\ -\frac{1}{64} & +\frac{1}{16} & -\frac{11}{64} \\ +\frac{11}{256} & -\frac{11}{64} & +\frac{121}{256} \end{bmatrix} \otimes \mathbf{I}_{UL}^{j-1} \end{bmatrix} \tag{B.23}$$

5 At the upper-center case

See Figure B.1.

$$\begin{cases} \hat{\mathbf{I}}^j(x_{2n-1},y_{2m-1}) = 4[-\frac{1}{256}m1 - \frac{1}{32}m2 + \frac{1}{256}m3 + \frac{1}{64}m4 + \frac{1}{8}m0 - \frac{1}{64}m5 + \frac{5}{256}m6 + \frac{5}{32}m7 - \frac{5}{256}m8] \\ \hat{\mathbf{I}}^j(x_{2n-1},y_{2m}) \quad = 4[+\frac{1}{256}m1 - \frac{1}{32}m2 - \frac{1}{256}m3 - \frac{1}{64}m4 + \frac{1}{8}m0 + \frac{1}{64}m5 - \frac{5}{256}m6 + \frac{5}{32}m7 + \frac{5}{256}m8] \\ \hat{\mathbf{I}}^j(x_{2n},y_{2m-1}) \quad = 4[+\frac{1}{256}m1 + \frac{1}{32}m2 - \frac{1}{256}m3 - \dfrac{1}{64}m4 - \frac{1}{8}m0 + \frac{1}{64}m5 + \frac{11}{256}m6 + \frac{11}{32}m7 - \frac{11}{256}m8] \\ \hat{\mathbf{I}}^j(x_{2n},y_{2m}) \quad = 4[-\frac{1}{256}m1 + \frac{1}{32}m2 + \frac{1}{256}m3 + \frac{1}{64}m4 - \frac{1}{8}m0 - \frac{1}{64}m5 - \frac{11}{256}m6 + \frac{11}{32}m7 + \frac{11}{256}m8] \end{cases} \tag{B.24}$$

Denote

$$\mathbf{I}^{j-1}_{UC} = \begin{bmatrix} \mathbf{I}^{j-1}(x_{n-2},y_{m-1}) & \mathbf{I}^{j-1}(x_{n-2},y_{m}) & \mathbf{I}^{j-1}(x_{n-2},y_{m+1}) \\ \mathbf{I}^{j-1}(x_{n-1},y_{m-1}) & \mathbf{I}^{j-1}(x_{n-1},y_{m}) & \mathbf{I}^{j-1}(x_{n-1},y_{m+1}) \\ \mathbf{I}^{j-1}(x_{n},y_{m-1}) & \mathbf{I}^{j-1}(x_{n},y_{m}) & \mathbf{I}^{j-1}(x_{n},y_{m+1}) \end{bmatrix} = \begin{bmatrix} m1 & m2 & m3 \\ m4 & m0 & m5 \\ m6 & m7 & m8 \end{bmatrix} \tag{B.25}$$

In compact forms, four predicted values are rewritten as follows:

$$\begin{bmatrix} \hat{\mathbf{I}}^j(x_{2n-1},y_{2m-1}) & \hat{\mathbf{I}}^j(x_{2n-1},y_{2m}) \\ \hat{\mathbf{I}}^j(x_{2n},y_{2m-1}) & \hat{\mathbf{I}}^j(x_{2n},y_{2m}) \end{bmatrix} = \tag{B.26}$$

$$= 4 \begin{bmatrix} \sum\sum \begin{bmatrix} -\frac{1}{256} & -\frac{1}{32} & +\frac{1}{256} \\ +\frac{1}{64} & +\frac{1}{8} & -\frac{1}{64} \\ +\frac{5}{256} & +\frac{5}{32} & -\frac{5}{256} \end{bmatrix} \otimes \mathbf{I}^{j-1}_{UC} & \sum\sum \begin{bmatrix} +\frac{1}{256} & -\frac{1}{32} & -\frac{1}{256} \\ -\frac{1}{64} & +\frac{1}{8} & +\frac{1}{64} \\ -\frac{5}{256} & +\frac{5}{32} & +\frac{5}{256} \end{bmatrix} \otimes \mathbf{I}^{j-1}_{UC} \\ \\ \sum\sum \begin{bmatrix} +\frac{1}{256} & +\frac{1}{32} & -\frac{1}{256} \\ -\frac{1}{64} & -\frac{1}{8} & +\frac{1}{64} \\ +\frac{11}{256} & +\frac{11}{32} & -\frac{11}{256} \end{bmatrix} \otimes \mathbf{I}^{j-1}_{UC} & \sum\sum \begin{bmatrix} -\frac{1}{256} & +\frac{1}{32} & +\frac{1}{256} \\ +\frac{1}{64} & -\frac{1}{8} & -\frac{1}{64} \\ -\frac{11}{256} & +\frac{11}{32} & +\frac{11}{256} \end{bmatrix} \otimes \mathbf{I}^{j-1}_{UC} \end{bmatrix} \tag{B.27}$$

6 At the upper-right case

See Figure B.1.

$$\begin{cases} \hat{\mathbf{I}}^j(x_{2n-1},y_{2m-1}) = 4[-\frac{11}{256}m1 + \frac{1}{64}m2 - \frac{1}{256}m3 + \frac{11}{64}m4 - \frac{1}{16}m0 + \frac{1}{64}m5 + \frac{55}{256}m6 - \frac{5}{64}m7 + \frac{5}{256}m8] \\ \hat{\mathbf{I}}^j(x_{2n-1},y_{2m}) \quad = 4[-\frac{5}{256}m1 - \frac{1}{64}m2 + \frac{1}{256}m3 + \frac{5}{64}m4 + \frac{1}{16}m0 - \frac{1}{64}m5 + \frac{25}{256}m6 + \frac{5}{64}m7 - \frac{5}{256}m8] \\ \hat{\mathbf{I}}^j(x_{2n},y_{2m-1}) \quad = 4[+\frac{11}{256}m1 - \frac{1}{64}m2 + \frac{1}{256}m3 - \frac{11}{64}m4 + \frac{1}{16}m0 - \frac{1}{64}m5 + \frac{121}{256}m6 - \frac{11}{64}m7 + \frac{11}{256}m8] \\ \hat{\mathbf{I}}^j(x_{2n},y_{2m}) \quad = 4[+\frac{5}{256}m1 + \frac{1}{64}m2 - \frac{1}{256}m3 - \frac{5}{64}m4 - \frac{1}{16}m0 + \frac{1}{64}m5 + \frac{55}{256}m6 + \frac{11}{64}m7 - \frac{11}{256}m8] \end{cases} \tag{B.28}$$

Denote

$$\mathbf{I}_{UR}^{j-1} = \begin{bmatrix} \mathbf{I}^{j-1}(x_{n-2}, y_m) & \mathbf{I}^{j-1}(x_{n-2}, y_{m+1}) & \mathbf{I}^{j-1}(x_{n-2}, y_{m+2}) \\ \mathbf{I}^{j-1}(x_{n-1}, y_m) & \mathbf{I}^{j-1}(x_{n-1}, y_{m+1}) & \mathbf{I}^{j-1}(x_{n-1}, y_{m+2}) \\ \mathbf{I}^{j-1}(x_n, y_m) & \mathbf{I}^{j-1}(x_n, y_{m+1}) & \mathbf{I}^{j-1}(x_n, y_{m+2}) \end{bmatrix} = \begin{bmatrix} m1 & m2 & m3 \\ m4 & m0 & m5 \\ m6 & m7 & m8 \end{bmatrix} \tag{B.29}$$

In compact forms, four predicted values are rewritten as follows:

$$\begin{bmatrix} \hat{\mathbf{I}}^j(x_{2n-1}, y_{2m-1}) & \hat{\mathbf{I}}^j(x_{2n-1}, y_{2m}) \\ \hat{\mathbf{I}}^j(x_{2n}, y_{2m-1}) & \hat{\mathbf{I}}^j(x_{2n}, y_{2m}) \end{bmatrix} = \tag{B.30}$$

$$= 4 \begin{bmatrix} \sum\sum \begin{bmatrix} -\frac{11}{256} & +\frac{1}{64} & -\frac{1}{256} \\ +\frac{11}{64} & -\frac{1}{16} & +\frac{1}{64} \\ +\frac{55}{256} & -\frac{5}{64} & +\frac{5}{256} \end{bmatrix} \otimes \mathbf{I}_{UR}^{j-1} & \sum\sum \begin{bmatrix} -\frac{5}{256} & -\frac{1}{64} & +\frac{1}{256} \\ +\frac{5}{64} & +\frac{1}{16} & -\frac{1}{64} \\ +\frac{25}{256} & +\frac{5}{64} & -\frac{5}{256} \end{bmatrix} \otimes \mathbf{I}_{UR}^{j-1} \\ \\ \sum\sum \begin{bmatrix} +\frac{11}{256} & -\frac{1}{64} & +\frac{1}{256} \\ -\frac{11}{64} & +\frac{1}{16} & -\frac{1}{64} \\ +\frac{121}{256} & -\frac{11}{64} & +\frac{11}{256} \end{bmatrix} \otimes \mathbf{I}_{UR}^{j-1} & \sum\sum \begin{bmatrix} +\frac{5}{256} & +\frac{1}{64} & -\frac{1}{256} \\ -\frac{5}{64} & -\frac{1}{16} & +\frac{1}{64} \\ +\frac{55}{256} & +\frac{11}{64} & -\frac{11}{256} \end{bmatrix} \otimes \mathbf{I}_{UR}^{j-1} \end{bmatrix} \tag{B.31}$$

7 At the down-left case

See Figure B.1.

$$\begin{cases} \hat{\mathbf{I}}^j(x_{2n-1}, y_{2m-1}) = 4[-\frac{11}{256}m1 + \frac{11}{64}m2 + \frac{55}{256}m3 + \frac{1}{64}m4 - \frac{1}{16}m0 - \frac{5}{64}m5 - \frac{1}{256}m6 + \frac{1}{64}m7 + \frac{5}{256}m8] \\ \hat{\mathbf{I}}^j(x_{2n-1}, y_{2m}) \quad = 4[+\frac{11}{256}m1 - \frac{11}{64}m2 + \frac{121}{256}m3 - \frac{1}{64}m4 + \frac{1}{16}m0 - \frac{11}{64}m5 + \frac{1}{256}m6 - \frac{1}{64}m7 + \frac{11}{256}m8] \\ \hat{\mathbf{I}}^j(x_{2n}, y_{2m-1}) \quad = 4[-\frac{5}{256}m1 + \frac{5}{64}m2 + \frac{25}{256}m3 - \frac{1}{64}m4 + \frac{1}{16}m0 + \frac{5}{64}m5 + \frac{1}{256}m6 - \frac{1}{64}m7 - \frac{5}{256}m8] \\ \hat{\mathbf{I}}^j(x_{2n}, y_{2m}) \quad = 4[+\frac{5}{256}m1 - \frac{5}{64}m2 + \frac{55}{256}m3 + \frac{1}{64}m4 - \frac{1}{16}m0 + \frac{11}{64}m5 - \frac{1}{256}m6 + \frac{1}{64}m7 - \frac{11}{256}m8] \end{cases} \tag{B.32}$$

Denote

$$\mathbf{I}_{DL}^{j-1} = \begin{bmatrix} \mathbf{I}^{j-1}(x_n, y_{m-2}) & \mathbf{I}^{j-1}(x_n, y_{m-1}) & \mathbf{I}^{j-1}(x_n, y_m) \\ \mathbf{I}^{j-1}(x_{n+1}, y_{m-2}) & \mathbf{I}^{j-1}(x_{n+1}, y_{m-1}) & \mathbf{I}^{j-1}(x_{n+1}, y_m) \\ \mathbf{I}^{j-1}(x_{n+2}, y_{m-2}) & \mathbf{I}^{j-1}(x_{n+2}, y_{m-1}) & \mathbf{I}^{j-1}(x_{n+2}, y_m) \end{bmatrix} = \begin{bmatrix} m1 & m2 & m3 \\ m4 & m0 & m5 \\ m6 & m7 & m8 \end{bmatrix} \tag{B.33}$$

In compact forms, four predicted values are rewritten as follows:

$$\begin{bmatrix} \hat{\mathbf{I}}^j(x_{2n-1}, y_{2m-1}) & \hat{\mathbf{I}}^j(x_{2n-1}, y_{2m}) \\ \hat{\mathbf{I}}^j(x_{2n}, y_{2m-1}) & \hat{\mathbf{I}}^j(x_{2n}, y_{2m}) \end{bmatrix} = \tag{B.34}$$

$$= 4 \begin{bmatrix} \sum\sum \begin{bmatrix} -\frac{11}{256} & +\frac{11}{64} & +\frac{55}{256} \\ +\frac{1}{64} & -\frac{1}{16} & -\frac{5}{64} \\ -\frac{1}{256} & +\frac{1}{64} & +\frac{5}{256} \end{bmatrix} \otimes \mathbf{I}_{DL}^{j-1} & \sum\sum \begin{bmatrix} +\frac{11}{256} & -\frac{11}{64} & +\frac{121}{256} \\ -\frac{1}{64} & +\frac{1}{16} & -\frac{11}{64} \\ +\frac{1}{256} & -\frac{1}{64} & +\frac{11}{256} \end{bmatrix} \otimes \mathbf{I}_{DL}^{j-1} \\ \\ \sum\sum \begin{bmatrix} -\frac{5}{256} & +\frac{5}{64} & +\frac{25}{256} \\ -\frac{1}{64} & +\frac{1}{16} & +\frac{5}{64} \\ +\frac{1}{256} & -\frac{1}{64} & -\frac{5}{256} \end{bmatrix} \otimes \mathbf{I}_{DL}^{j-1} & \sum\sum \begin{bmatrix} +\frac{5}{256} & -\frac{5}{64} & +\frac{55}{256} \\ +\frac{1}{64} & -\frac{1}{16} & +\frac{11}{64} \\ -\frac{1}{256} & +\frac{1}{64} & -\frac{11}{256} \end{bmatrix} \otimes \mathbf{I}_{DL}^{j-1} \end{bmatrix} \tag{B.35}$$

8 At the down-center case

See Figure B.1.

$$\begin{cases} \hat{\mathbf{I}}^j(x_{2n-1}, y_{2m-1}) = 4[+\frac{11}{256}m1 + \frac{11}{32}m2 - \frac{11}{256}m3 - \frac{1}{64}m4 - \frac{1}{8}m0 + \frac{1}{64}m5 + \frac{1}{256}m6 + \frac{1}{32}m7 - \frac{1}{256}m8] \\ \hat{\mathbf{I}}^j(x_{2n-1}, y_{2m}) \quad = 4[-\frac{11}{256}m1 + \frac{11}{32}m2 + \frac{11}{256}m3 + \frac{1}{64}m4 - \frac{1}{8}m0 - \frac{1}{64}m5 - \frac{1}{256}m6 + \frac{1}{32}m7 + \frac{1}{256}m8] \\ \hat{\mathbf{I}}^j(x_{2n}, y_{2m-1}) \quad = 4[+\frac{5}{256}m1 + \frac{5}{32}m2 - \frac{5}{256}m3 + \frac{1}{64}m4 + \frac{1}{8}m0 - \frac{1}{64}m5 - \frac{1}{256}m6 - \frac{1}{32}m7 + \frac{1}{256}m8] \\ \hat{\mathbf{I}}^j(x_{2n}, y_{2m}) \quad = 4[-\frac{5}{256}m1 + \frac{5}{32}m2 + \frac{5}{256}m3 - \frac{1}{64}m4 + \frac{1}{8}m0 + \frac{1}{64}m5 + \frac{1}{256}m6 - \frac{1}{32}m7 - \frac{1}{256}m8] \end{cases} \tag{B.36}$$

Denote

$$\mathbf{I}_{DC}^{j-1} = \begin{bmatrix} \mathbf{I}^{j-1}(x_n, y_{m-1}) & \mathbf{I}^{j-1}(x_n, y_m) & \mathbf{I}^{j-1}(x_n, y_{m+1}) \\ \mathbf{I}^{j-1}(x_{n+1}, y_{m-1}) & \mathbf{I}^{j-1}(x_{n+1}, y_m) & \mathbf{I}^{j-1}(x_{n+1}, y_{m+1}) \\ \mathbf{I}^{j-1}(x_{n+2}, y_{m-1}) & \mathbf{I}^{j-1}(x_{n+2}, y_m) & \mathbf{I}^{j-1}(x_{n+2}, y_{m+1}) \end{bmatrix} = \begin{bmatrix} m1 & m2 & m3 \\ m4 & m0 & m5 \\ m6 & m7 & m8 \end{bmatrix} \tag{B.37}$$

In compact forms, four predicted values are rewritten as follows:

$$\begin{bmatrix} \hat{\mathbf{I}}^j(x_{2n-1}, y_{2m-1}) & \hat{\mathbf{I}}^j(x_{2n-1}, y_{2m}) \\ \hat{\mathbf{I}}^j(x_{2n}, y_{2m-1}) & \hat{\mathbf{I}}^j(x_{2n}, y_{2m}) \end{bmatrix} = \tag{B.38}$$

$$= 4 \begin{bmatrix} \sum\sum \begin{bmatrix} +\frac{11}{256} & +\frac{11}{32} & -\frac{11}{256} \\ -\frac{1}{64} & -\frac{1}{8} & +\frac{1}{64} \\ +\frac{1}{256} & +\frac{1}{32} & -\frac{1}{256} \end{bmatrix} \otimes \mathbf{I}_{DC}^{j-1} & \sum\sum \begin{bmatrix} -\frac{11}{256} & +\frac{11}{32} & +\frac{11}{256} \\ +\frac{1}{64} & -\frac{1}{8} & -\frac{1}{64} \\ -\frac{1}{256} & +\frac{1}{32} & +\frac{1}{256} \end{bmatrix} \otimes \mathbf{I}_{DC}^{j-1} \\ \\ \sum\sum \begin{bmatrix} +\frac{5}{256} & +\frac{5}{32} & -\frac{5}{256} \\ +\frac{1}{64} & +\frac{1}{8} & -\frac{1}{64} \\ -\frac{1}{256} & -\frac{1}{32} & +\frac{1}{256} \end{bmatrix} \otimes \mathbf{I}_{DC}^{j-1} & \sum\sum \begin{bmatrix} -\frac{5}{256} & +\frac{5}{32} & +\frac{5}{256} \\ -\frac{1}{64} & +\frac{1}{8} & +\frac{1}{64} \\ +\frac{1}{256} & -\frac{1}{32} & -\frac{1}{256} \end{bmatrix} \otimes \mathbf{I}_{DC}^{j-1} \end{bmatrix} \tag{B.39}$$

9 At the down-right case

See Figure B.1.

$$\begin{cases}\hat{\mathbf{I}}^j(x_{2n-1},y_{2m-1}) = 4[+\frac{121}{256}m1-\frac{11}{64}m2+\frac{11}{256}m3-\frac{11}{64}m4+\frac{1}{16}m0-\frac{1}{64}m5+\frac{11}{256}m6-\frac{1}{64}m7+\frac{1}{256}m8]\\ \hat{\mathbf{I}}^j(x_{2n-1},y_{2m}) = 4[+\frac{55}{256}m1+\frac{11}{64}m2-\frac{11}{256}m3-\frac{5}{64}m4-\frac{1}{16}m0+\frac{1}{64}m5+\frac{5}{256}m6+\frac{1}{64}m7-\frac{1}{256}m8]\\ \hat{\mathbf{I}}^j(x_{2n},y_{2m-1}) = 4[+\frac{55}{256}m1-\frac{5}{64}m2+\frac{5}{256}m3+\frac{11}{64}m4-\frac{1}{16}m0+\frac{1}{64}m5-\frac{11}{256}m6+\frac{1}{64}m7-\frac{1}{256}m8]\\ \hat{\mathbf{I}}^j(x_{2n},y_{2m}) = 4[+\frac{25}{256}m1+\frac{5}{64}m2-\frac{5}{256}m3+\frac{5}{64}m4+\frac{1}{16}m0-\frac{1}{64}m5-\frac{5}{256}m6-\frac{1}{64}m7+\frac{1}{256}m8]\end{cases} \tag{B.40}$$

Denote

$$\mathbf{I}_{DR}^{j-1} = \begin{bmatrix}\mathbf{I}^{j-1}(x_n,y_m) & \mathbf{I}^{j-1}(x_n,y_{m+1}) & \mathbf{I}^{j-1}(x_n,y_{m+2})\\ \mathbf{I}^{j-1}(x_{n+1},y_m) & \mathbf{I}^{j-1}(x_{n+1},y_{m+1}) & \mathbf{I}^{j-1}(x_{n+1},y_{m+2})\\ \mathbf{I}^{j-1}(x_{n+2},y_m) & \mathbf{I}^{j-1}(x_{n+2},y_{m+1}) & \mathbf{I}^{j-1}(x_{n+2},y_{m+2})\end{bmatrix} = \begin{bmatrix}m1 & m2 & m3\\ m4 & m0 & m5\\ m6 & m7 & m8\end{bmatrix} \tag{B.41}$$

In compact forms, four predicted values are rewritten as follows:

$$\begin{bmatrix}\hat{\mathbf{I}}^j(x_{2n-1},y_{2m-1}) & \hat{\mathbf{I}}^j(x_{2n-1},y_{2m})\\ \hat{\mathbf{I}}^j(x_{2n},y_{2m-1}) & \hat{\mathbf{I}}^j(x_{2n},y_{2m})\end{bmatrix} = \tag{B.42}$$

$$= 4\begin{bmatrix}\sum\sum\begin{bmatrix}+\frac{121}{256} & -\frac{11}{64} & +\frac{11}{256}\\ -\frac{11}{64} & +\frac{1}{16} & -\frac{1}{64}\\ +\frac{11}{256} & -\frac{1}{64} & +\frac{1}{256}\end{bmatrix}\otimes\mathbf{I}_{DR}^{j-1} & \sum\sum\begin{bmatrix}+\frac{55}{256} & +\frac{11}{64} & -\frac{11}{256}\\ -\frac{5}{64} & -\frac{1}{16} & +\frac{1}{64}\\ +\frac{5}{256} & +\frac{1}{64} & -\frac{1}{256}\end{bmatrix}\otimes\mathbf{I}_{DR}^{j-1}\\ \\ \sum\sum\begin{bmatrix}+\frac{55}{256} & -\frac{5}{64} & +\frac{5}{256}\\ +\frac{11}{64} & -\frac{1}{16} & +\frac{1}{64}\\ -\frac{11}{256} & +\frac{1}{64} & -\frac{1}{256}\end{bmatrix}\otimes\mathbf{I}_{DR}^{j-1} & \sum\sum\begin{bmatrix}+\frac{25}{256} & +\frac{5}{64} & -\frac{5}{256}\\ +\frac{5}{64} & +\frac{1}{16} & -\frac{1}{64}\\ -\frac{5}{256} & -\frac{1}{64} & +\frac{1}{256}\end{bmatrix}\otimes\mathbf{I}_{DR}^{j-1}\end{bmatrix} \tag{B.43}$$

APPENDIX C

Computation of near optimal filter coefficients

This appendix concerns the computation of near optimal filter coefficients later called weights. These weights are computed based on the vector of approximation at the coarse level (i.e. $\mathbf{V}^{j-1}(x_n, y_k)$ for a given row n) and the odd-index vector of approximation at the finer level (i.e. $\mathbf{I}^j(x_n, y_{2k-1})$ for a given row n). While the separable ENO multiresolution approach uses three kinds of polynomials (left, center and right) whose coefficients are constant and applied for all rows or columns, in the separable near optimal multiresolution approach, however, these coefficients are different and depending on each row or column. This approach is used to find the minimization of Mean Squared Error (MSE) between the odd-index values of approximation at the finer level (i.e. $\mathbf{I}^j(x_n, y_{2k-1})$ for a given row n) and the corresponding predicted values (i.e. $\hat{\mathbf{I}}^j(x_n, y_{2k-1})$).

The approximation coefficient located at position (x_n, y_k), denoted $\mathbf{V}^{j-1}(x_n, y_k)$ for a given n for $1 \leq k \leq M^j/2$.

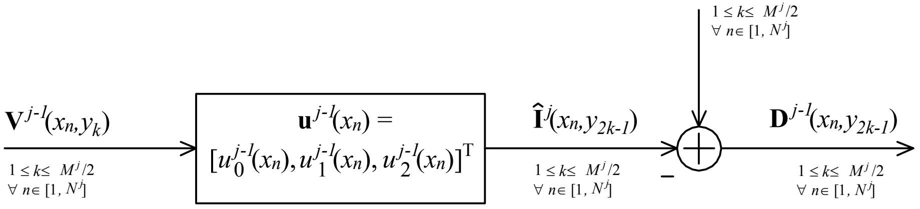

Figure C.1: *Near optimal filter for estimating a designed signal* $\mathbf{I}^j(x_n, y_{2k-1})$ *based on an excitation* $\mathbf{V}^{j-1}(x_n, y_k)$ *(with* $1 \leq k \leq M^j/2$ *and for a given* n*).*

The prediction of pixel at the position (x_n, y_{2k-1}), denote $\hat{\mathbf{I}}^j(x_n, y_{2k-1})$ for $1 \le k \le M^j/2$, of the 1-D signal $\mathbf{I}^j(x_n, y_k)$ for $1 \le k \le M^j$ is based on weighted combination $u_i^{j-1}(x_n)$, $(i = 0,1,2)$ of the neighborhood pixels of the approximation coefficients $\mathbf{V}^{j-1}(x_n, y_k)$ for $1 \le k \le M^j/2$:

$$\hat{\mathbf{I}}^j(x_n, y_{2k-1}) = \sum_{i=0}^{2} u_i^{j-1}(x_n) \cdot \mathbf{V}^{j-1}(x_n, y_{k+i-1}), \tag{C.1}$$

corresponding to the weighting of a filter preserving the average of the initial signal and therefore satisfying the following relationships:

$$\sum_{i=0}^{2} u_i^{j-1}(x_n) = 1. \tag{C.2}$$

The weights u_i^{j-1}, $(i = 0,1,2)$ are deduced so that the MSE between $\hat{\mathbf{I}}^j(x_n, y_{2k-1})$ and $\mathbf{I}^j(x_n, y_{2k-1})$ for $1 \le k \le M^j/2$ is minimized:

$$\arg\min_{w_i^{j-1}} \|\hat{\mathbf{I}}^j(x_n, y_{2k-1}) - \mathbf{I}^j(x_n, y_{2k-1})\|_2^2 \quad \text{for } 1 \le k \le M^j/2. \tag{C.3}$$

Denote

$$E = \|\hat{\mathbf{I}}^j(x_n, y_{2k-1}) - \mathbf{I}^j(x_n, y_{2k-1})\|_2^2 \quad \text{for } 1 \le k \le M^j/2. \tag{C.4}$$

It can be written by

$$E = \Big[\sum_{i=0}^{2} u_i^{j-1}(x_n) \cdot \mathbf{V}^{j-1}(x_n, y_{k+i-1}) - \mathbf{I}^j(x_n, y_{2k-1})\Big]^2 \quad \text{for } 1 \le k \le M^j/2. \tag{C.5}$$

To find $u_i^{j-1}(x_n)$, the partial derivatives of the error E with respect to the parameters u_i^{j-1} must be equal to zero:

$$\begin{cases} \dfrac{\partial E}{\partial u_0^{j-1}} = 0 \\ \dfrac{\partial E}{\partial u_1^{j-1}} = 0 \\ \dfrac{\partial E}{\partial u_2^{j-1}} = 0. \end{cases} \tag{C.6}$$

For the parameter u_0^{j-1}:

$$\begin{aligned} \frac{\partial E}{\partial u_0^{j-1}} &= 2\Big[\sum_{i=0}^{2} u_i^{j-1} \cdot \mathbf{V}^{j-1}(x_n, y_{k+i-1}) - \mathbf{I}^j(x_n, y_{2k-1})\Big] \cdot \mathbf{V}^{j-1}(x_n, y_{k-1}) \quad \text{for } 1 \le k \le M^j/2 \\ &= 2\sum_{i=0}^{2} u_i^{j-1} \cdot \mathbf{V}^{j-1}(x_n, y_{k+i-1}) \cdot \mathbf{V}^{j-1}(x_n, y_{k-1}) - 2\mathbf{I}^j(x_n, y_{2k-1}) \cdot \mathbf{V}^{j-1}(x_n, y_{k-1}). \end{aligned} \tag{C.7}$$

Denote

$$R^{j-1}(i) = \mathbf{V}^{j-1}(x_n, y_{k+i-1}) \cdot \mathbf{V}^{j-1}(x_n, y_{k-1}), \tag{C.8}$$

$$r^{j-1}(i) = \mathbf{V}^{j-1}(x_n, y_{k+i-1}) \cdot \mathbf{I}^j(x_n, y_{2k-1}), \tag{C.9}$$

where $R^{j-1}(i)$ is autocorrelation function of $\mathbf{V}^{j-1}(x_n, y_k)$ for $1 \le k \le M^j/2$; and $r^{j-1}(i)$ is cross-correlation function between $\mathbf{V}^{j-1}(x_n, y_k)$ and $\mathbf{I}^j(x_n, y_{2k-1})$ for $1 \le k \le M^j/2$. Then it gives

$$\frac{\partial E}{\partial u_0^{j-1}} = 2\sum_{i=0}^{2} w_i^{j-1} \cdot R^{j-1}(i) - 2r^{j-1}(0). \tag{C.10}$$

For the parameter u_1^{j-1}:

$$\begin{aligned}
\frac{\partial E}{\partial u_1^{j-1}} &= 2\Big[\sum_{i=0}^{2} u_i^{j-1} \cdot \mathbf{I}^{j-1}(x_n, y_{k+i-1}) - \mathbf{I}^j(x_n, y_{2k-1})\Big] \cdot \mathbf{I}^{j-1}(x_n, y_k) \quad \text{for } 1 \le k \le M^j/2 \\
&= 2\sum_{i=0}^{2} u_i^{j-1} \cdot \mathbf{I}^{j-1}(x_n, y_{k+i-1}) \cdot \mathbf{I}^{j-1}(x_n, y_k) - 2\mathbf{I}^j(x_n, y_{2k-1}) \cdot \mathbf{I}^{j-1}(x_n, y_k) \\
&= 2\sum_{i=0}^{2} u_i^{j-1} \cdot R^{j-1}(i-1) - 2r^{j-1}(1).
\end{aligned} \tag{C.11}$$

For the parameter u_2^{j-1}:

$$\begin{aligned}
\frac{\partial E}{\partial u_2^{j-1}} &= 2\Big[\sum_{i=0}^{2} u_i^{j-1} \cdot \mathbf{I}^{j-1}(x_n, y_{k+i-1}) - \mathbf{I}^j(x_n, y_{2k-1})\Big] \cdot \mathbf{I}^{j-1}(x_n, y_{k+1}) \quad \text{for } 1 \le k \le M^j/2 \\
&= 2\sum_{i=0}^{2} u_i^{j-1} \cdot \mathbf{I}^{j-1}(x_n, y_{k+i-1}) \cdot \mathbf{I}^{j-1}(x_n, y_{k+1}) - 2\mathbf{I}^j(x_n, y_{2k-1}) \cdot \mathbf{I}^{j-1}(x_n, y_{k+1}) \\
&= 2\sum_{i=0}^{2} u_i^{j-1} \cdot R^{j-1}(i-2) - 2r^{j-1}(2).
\end{aligned} \tag{C.12}$$

From the results given by the equation (C.10), equation (C.11) and equation (C.12) the system (C.6) is rewritten as follows:

$$\begin{cases}
\sum_{i=0}^{2} u_i^{j-1}(x_n) \cdot R^{j-1}(i) & = r^{j-1}(0) \\
\sum_{i=0}^{2} u_i^{j-1}(x_n) \cdot R^{j-1}(i-1) & = r^{j-1}(1) \\
\sum_{i=0}^{2} u_i^{j-1}(x_n) \cdot R^{j-1}(i-2) & = r^{j-1}(2).
\end{cases} \tag{C.13}$$

In matrix form, the weights $\mathbf{u}_i^{j-1}(x_n)$ are the solution of the linear system:

$$\mathbf{\Gamma}^{j-1} \cdot \mathbf{u}^{j-1}(x_n) = \mathbf{r}^{j-1} \tag{C.14}$$

where

$$\mathbf{\Gamma}^{j-1} = \begin{bmatrix} R^{j-1}(0) & R^{j-1}(1) & R^{j-1}(2) \\ R^{j-1}(-1) & R^{j-1}(0) & R^{j-1}(1) \\ R^{j-1}(-2) & R^{j-1}(-1) & R^{j-1}(0) \end{bmatrix} \tag{C.15}$$

and

$$\mathbf{r}^{j-1} = \begin{bmatrix} r^{j-1}(0) \\ r^{j-1}(1) \\ r^{j-1}(2) \end{bmatrix} \tag{C.16}$$

It solves

$$\mathbf{u}^{j-1}(x_n) = (\mathbf{\Gamma}^{j-1})^{-1} \cdot \mathbf{r}^{j-1}.$$

The weights $\mathbf{u}^{j-1}$ are stored for the row n so as later to reconstruct the signal in the backward process.

APPENDIX D

Matlab graphic user interface for the assessment of the visual quality of the tone mapped images

This appendix concerns the protocols of the graphic user interface for the assessment of the visual quality of the tone mapped images under Matlab environment. An observer is invited to the testing room in the laboratory L2TI. All HDR tone mapped images are shown on the ColorEdge CG242W Color LCD monitor with a good calibration. A Matlab graphic user interface has been developed. It saves the time and stores the elapsed time of each observer during the test and can statistically analyze the results. It helps the computation more confidential.

The training dataset uses 24 HDR test images with different dynamic range (or contrast ratio) from 7 f-stops to 29 f-stops namely "Lausanne1", "CraterLake1", "Shasta2", "Synagogue", "Anturium", "BowRiver", "Bridges", "Stairway1", "ArchRock", "DollDoll", "ClockBuilding", "OxfordChurch", "BottlesSmall", "Montreal", "SmallOffice", "Light", "BridgeStudios2", "Memorial", "ClaridgeHotel", "Mistaya1", "BrookHouse", "PeaceRocks", "GGpark2" and "AtriumNight", see Figure D.1a to Figure D.1x.

15 TM methods are used to test such as "Drago" [10], "Reinhard" [44], "Ward" [7], "Durand" [16], "Tumblin" [31], "Schlick" [3], "Duan" [8], "Fattal" WRB [25], "Li" [26], "Husseis" [30], "Proposed_NUHA", "Proposed_SEPENO", "Proposed_NONSEPENO", "Proposed_CEDP_Lin" and "Proposed_CEDP_Opt".

Each tone mapped image is marked (with no-reference of HDR displays) ranging from 0 until 5: 5 for *excellent*, 4 *very good*, 3 *good*, 2 *accepted*, 1 *unsatisfactory* and 0 *failed*.

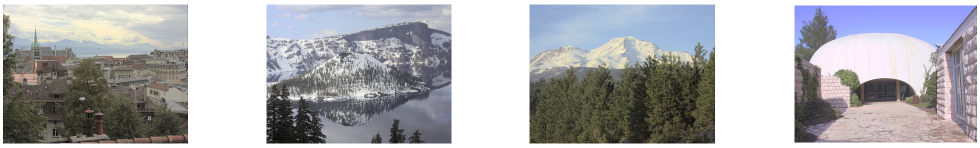

(a) Lausanne1 **(b)** CraterLake1 **(c)** Shasta2 **(d)** Synagogue

(e) Anturium **(f)** BowRiver **(g)** Bridges **(h)** Stairway1

(i) ArchRock **(j)** DollDoll **(k)** ClockBuilding **(l)** OxfordChurch

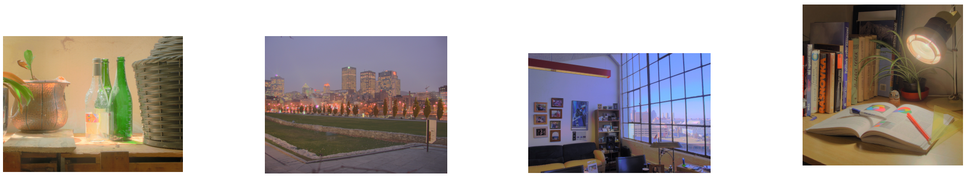

(m) BottlesSmall **(n)** Montreal **(o)** SmallOffice **(p)** Light

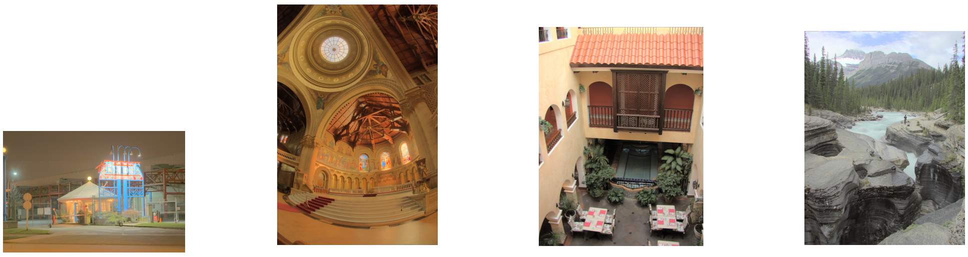

(q) BridgeStudios2 **(r)** Memorial **(s)** ClaridgeHotel **(t)** Mistaya1

(u) BrookHouse **(v)** PeaceRocks **(w)** GGpark2 **(x)** AtriumNight

Figure D.1: *Training dataset of 24 HDR test images.*

There are some instructions shown on the screen:

i. The number of test images is 24,

ii. There are fifteen methods with random orders displayed on the screen,

iii. Fifteen methods are divided in five sessions, namely A, B, C, D and E,

iv. The mark for each image is between 0 and 5: 5=Excellent, 4=Very Good, 3=Good, 2=Accepted, 1=Unsatisfactory and 0=Failed,

v. The chosen criteria is based on ability to recover details with natural ways.

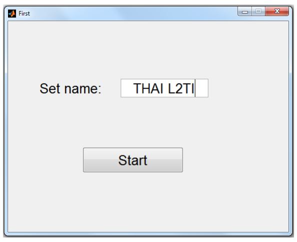

Set name: THAI L2TI

Figure D.2: *Starting form*

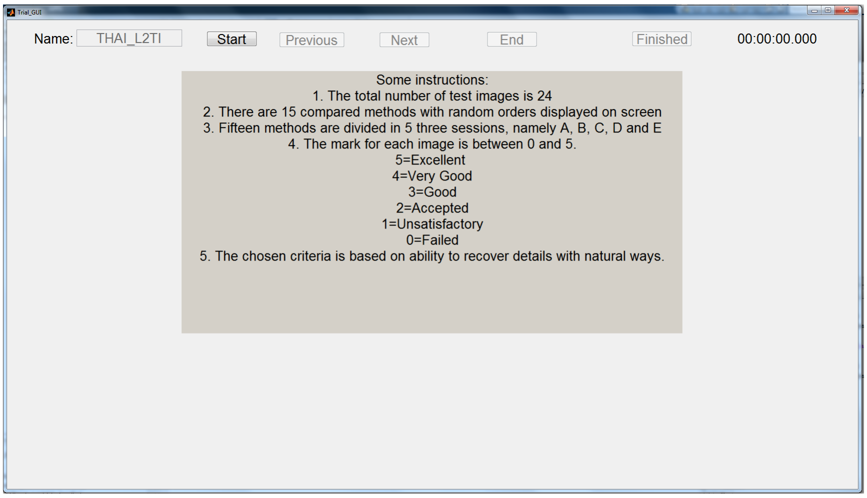

Name: THAI_L2TI

00:00:00.000

Some instructions:
1. The total number of test images is 24
2. There are 15 compared methods with random orders displayed on screen
3. Fifteen methods are divided in 5 three sessions, namely A, B, C, D and E
4. The mark for each image is between 0 and 5.
5=Excellent
4=Very Good
3=Good
2=Accepted
1=Unsatisfactory
0=Failed
5. The chosen criteria is based on ability to recover details with natural ways.

Figure D.3: *Instruction form*

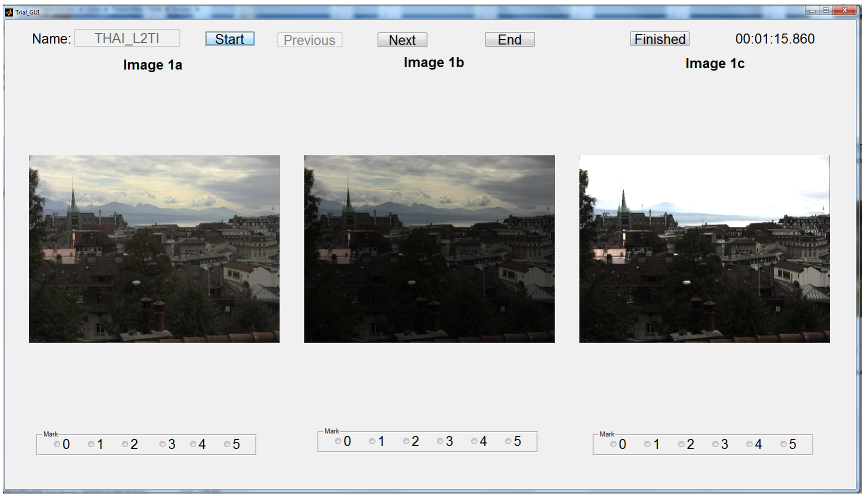

Name: THAI_L2TI

00:01:15.860

Figure D.4: *First session form - Session A*

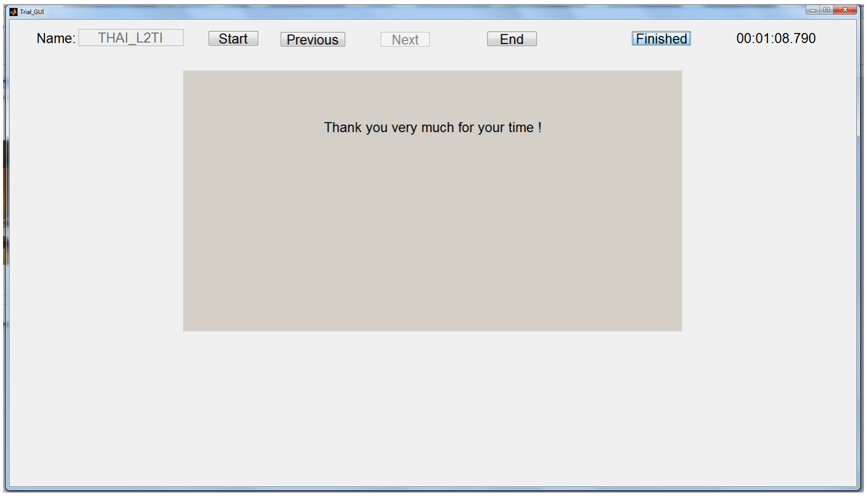

Name: THAI_L2TI

00:01:08.790

Thank you very much for your time !

Figure D.5: *Closing form*

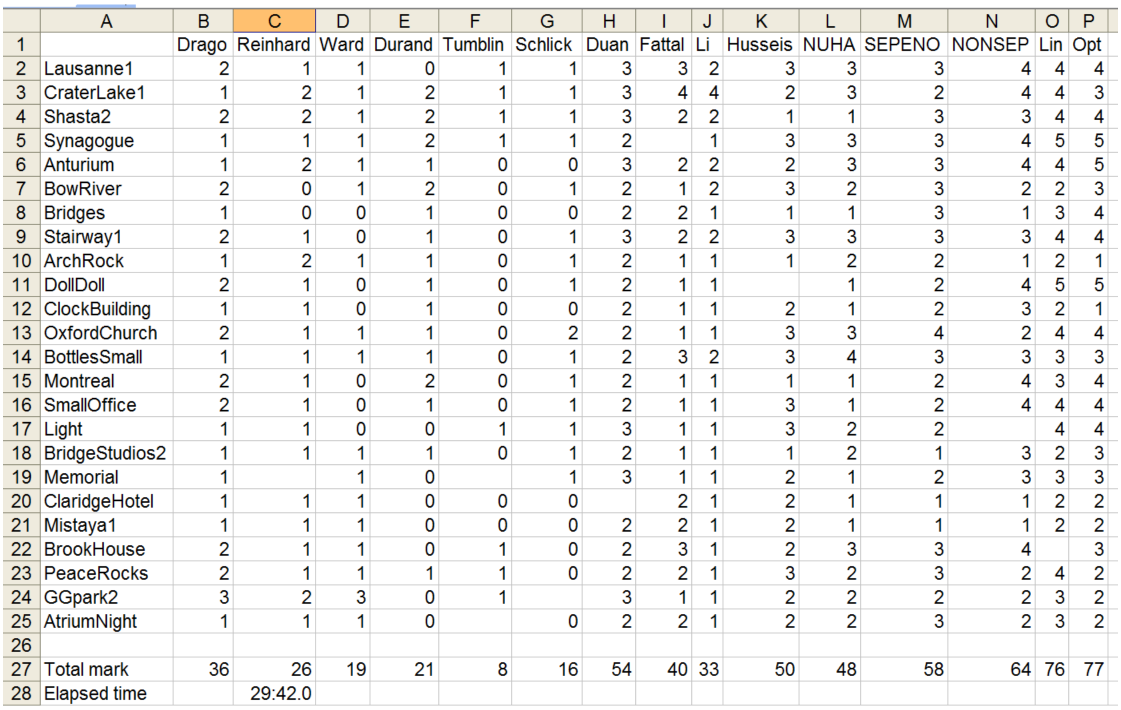

	A	B	C	D	E	F	G	H	I	J	K	L	M	N	O	P
1		Drago	Reinhard	Ward	Durand	Tumblin	Schlick	Duan	Fattal	Li	Husseis	NUHA	SEPENO	NONSEP	Lin	Opt
2	Lausanne1	2	1	1	0	1	1	3	3	2	3	3	3	4	4	4
3	CraterLake1	1	2	1	2	1	1	3	4	4	2	3	2	4	4	3
4	Shasta2	2	2	1	2	1	1	3	2	2	1	1	3	3	4	4
5	Synagogue	1	1	1	2	1	1	2		1	3	3	3	4	5	5
6	Anturium	1	2	1	1	0	0	3	2	2	2	3	3	4	4	5
7	BowRiver	2	0	1	2	0	1	2	1	2	3	2	3	2	2	3
8	Bridges	1	0	0	1	0	0	2	2	1	1	1	3	1	3	4
9	Stairway1	2	1	0	1	0	1	3	2	2	3	3	3	3	4	4
10	ArchRock	1	2	1	1	0	1	2	1	1	1	2	2	1	2	1
11	DollDoll	2	1	0	1	0	1	2	1	1		1	2	4	5	5
12	ClockBuilding	1	1	0	1	0	0	2	1	1	2	1	2	3	2	1
13	OxfordChurch	2	1	1	1	0	2	2	1	1	3	3	4	2	4	4
14	BottlesSmall	1	1	1	1	0	1	2	3	2	3	4	3	3	3	3
15	Montreal	2	1	0	2	0	1	2	1	1	1	1	2	4	3	4
16	SmallOffice	2	1	0	1	0	1	2	1	1	3	1	2	4	4	4
17	Light	1	1	0	0	1	1	3	1	1	3	2	2		4	4
18	BridgeStudios2	1	1	1	1	0	1	2	1	1	1	2	1	3	2	3
19	Memorial	1		1	0		1	3	1	1	2	1	2	3	3	3
20	ClaridgeHotel	1	1	1	0	0	0		2	1	2	1	1	1	2	2
21	Mistaya1	1	1	1	0	0	0	2	2	1	2	1	1	1	2	2
22	BrookHouse	2	1	1	0	1	0	2	3	1	2	3	3	4		3
23	PeaceRocks	2	1	1	1	1	0	2	2	1	3	2	3	2	4	2
24	GGpark2	3	2	3	0	1		3	1	1	2	2	2	2	3	2
25	AtriumNight	1	1	1	0		0	2	2	1	2	2	3	2	3	2
26																
27	Total mark	36	26	19	21	8	16	54	40	33	50	48	58	64	76	77
28	Elapsed time		29:42.0													

Figure D.6: *"THAI_L2TI.xls" data-sheet result*

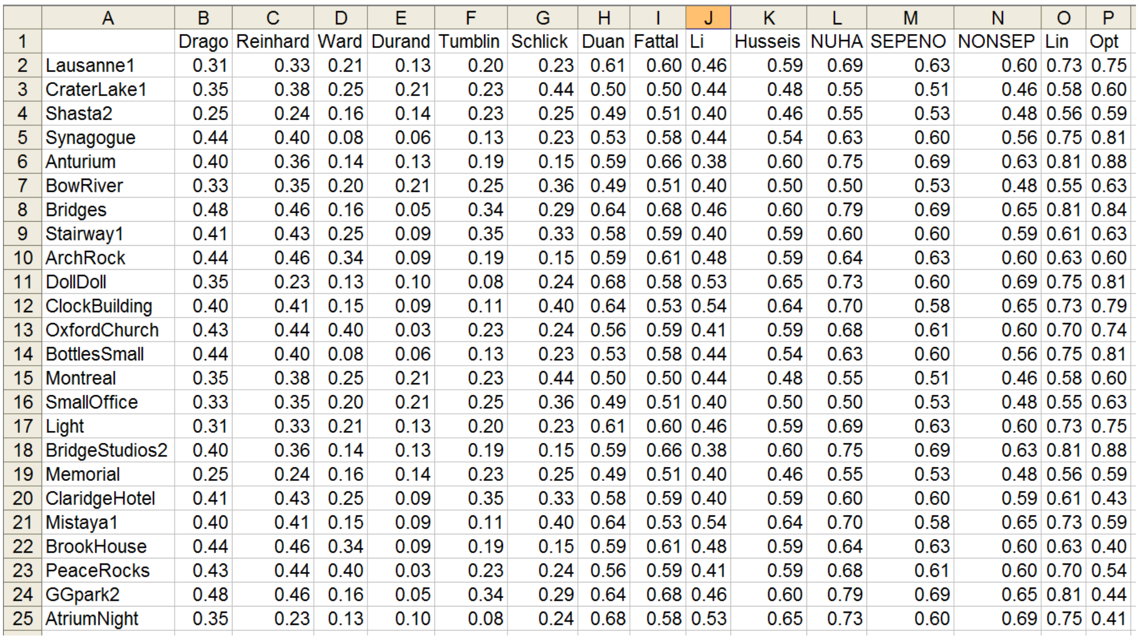

	A	B	C	D	E	F	G	H	I	J	K	L	M	N	O	P
1		Drago	Reinhard	Ward	Durand	Tumblin	Schlick	Duan	Fattal	Li	Husseis	NUHA	SEPENO	NONSEP	Lin	Opt
2	Lausanne1	0.31	0.33	0.21	0.13	0.20	0.23	0.61	0.60	0.46	0.59	0.69	0.63	0.60	0.73	0.75
3	CraterLake1	0.35	0.38	0.25	0.21	0.23	0.44	0.50	0.50	0.44	0.48	0.55	0.51	0.46	0.58	0.60
4	Shasta2	0.25	0.24	0.16	0.14	0.23	0.25	0.49	0.51	0.40	0.46	0.55	0.53	0.48	0.56	0.59
5	Synagogue	0.44	0.40	0.08	0.06	0.13	0.23	0.53	0.58	0.44	0.54	0.63	0.60	0.56	0.75	0.81
6	Anturium	0.40	0.36	0.14	0.13	0.19	0.15	0.59	0.66	0.38	0.60	0.75	0.69	0.63	0.81	0.88
7	BowRiver	0.33	0.35	0.20	0.21	0.25	0.36	0.49	0.51	0.40	0.50	0.50	0.53	0.48	0.55	0.63
8	Bridges	0.48	0.46	0.16	0.05	0.34	0.29	0.64	0.68	0.46	0.60	0.79	0.69	0.65	0.81	0.84
9	Stairway1	0.41	0.43	0.25	0.09	0.35	0.33	0.58	0.59	0.40	0.59	0.60	0.60	0.59	0.61	0.63
10	ArchRock	0.44	0.46	0.34	0.09	0.19	0.15	0.59	0.61	0.48	0.59	0.64	0.63	0.60	0.63	0.60
11	DollDoll	0.35	0.23	0.13	0.10	0.08	0.24	0.68	0.58	0.53	0.65	0.73	0.60	0.69	0.75	0.81
12	ClockBuilding	0.40	0.41	0.15	0.09	0.11	0.40	0.64	0.53	0.54	0.64	0.70	0.58	0.65	0.73	0.79
13	OxfordChurch	0.43	0.44	0.40	0.03	0.23	0.24	0.56	0.59	0.41	0.59	0.68	0.61	0.60	0.70	0.74
14	BottlesSmall	0.44	0.40	0.08	0.06	0.13	0.23	0.53	0.58	0.44	0.54	0.63	0.60	0.56	0.75	0.81
15	Montreal	0.35	0.38	0.25	0.21	0.23	0.44	0.50	0.50	0.44	0.48	0.55	0.51	0.46	0.58	0.60
16	SmallOffice	0.33	0.35	0.20	0.21	0.25	0.36	0.49	0.51	0.40	0.50	0.50	0.53	0.48	0.55	0.63
17	Light	0.31	0.33	0.21	0.13	0.20	0.23	0.61	0.60	0.46	0.59	0.69	0.63	0.60	0.73	0.75
18	BridgeStudios2	0.40	0.36	0.14	0.13	0.19	0.15	0.59	0.66	0.38	0.60	0.75	0.69	0.63	0.81	0.88
19	Memorial	0.25	0.24	0.16	0.14	0.23	0.25	0.49	0.51	0.40	0.46	0.55	0.53	0.48	0.56	0.59
20	ClaridgeHotel	0.41	0.43	0.25	0.09	0.35	0.33	0.58	0.59	0.40	0.59	0.60	0.60	0.59	0.61	0.43
21	Mistaya1	0.40	0.41	0.15	0.09	0.11	0.40	0.64	0.53	0.54	0.64	0.70	0.58	0.65	0.73	0.59
22	BrookHouse	0.44	0.46	0.34	0.09	0.19	0.15	0.59	0.61	0.48	0.59	0.64	0.63	0.60	0.63	0.40
23	PeaceRocks	0.43	0.44	0.40	0.03	0.23	0.24	0.56	0.59	0.41	0.59	0.68	0.61	0.60	0.70	0.54
24	GGpark2	0.48	0.46	0.16	0.05	0.34	0.29	0.64	0.68	0.46	0.60	0.79	0.69	0.65	0.81	0.44
25	AtriumNight	0.35	0.23	0.13	0.10	0.08	0.24	0.68	0.58	0.53	0.65	0.73	0.60	0.69	0.75	0.41

Figure D.7: *Mean opinion scores calculation*

Bibliography

[1] Francesco Banterle et al. *Advanced High Dynamic Range Imaging: Theory and Practice*. 1st. Natick, MA, USA: A. K. Peters, Ltd., 2011 *Cited on pages 3, 27, 31, 41, 100.*

[2] Erik Reinhard et al. *High Dynamic Range Imaging: Acquisition, Display, and Image-Based Lighting*. Morgan Kaufmann Publishers Inc., 2005 *Cited on page 3.*

[3] Christophe Schlick. "Quantization Techniques for Visualization of High Dynamic Range Pictures". In: *Photorealistic Rendering Techniques*. Ed. by Georgios Sakas, Stefan Müller, and Peter Shirley. Berlin, Heidelberg: Springer Berlin Heidelberg, 1995, pp. 7–20 *Cited on pages 11–13, 15, 27, 28, 30, 31, 118, 119, 125–127, 129–131, 171.*

[4] Jack Tumblin, Jessica K. Hodgins, and Brian K. Guenter. "Two Methods for Display of High Contrast Images". In: *ACM Trans. Graph.* 18.1 (Jan. 1999), pp. 56–94 *Cited on pages 11–13.*

[5] Greg Ward. "A Contrast-based Scale factor for Luminance Display". In: ed. by Paul S. Heckbert. San Diego, CA, USA: Academic Press Professional, Inc., 1994. Chap. A Contrast-based Scalefactor for Luminance Display, pp. 415–421 *Cited on pages 11–15.*

[6] James A. Ferwerda et al. "A Model of Visual Adaptation for Realistic Image Synthesis". In: *Proceedings of the 23rd Annual Conference on Computer Graphics and Interactive Techniques*. SIGGRAPH '96. New York, NY, USA: ACM, 1996, pp. 249–258 *Cited on pages 11–13, 15.*

[7] G. W. Larson, H. Rushmeier, and C. Piatko. "A Visibility Matching Tone Reproduction Operator for High Dynamic Range Scenes". In: *IEEE Transactions on Visualization and Computer Graphics* 3.4 (Oct. 1997), pp. 291–306 *Cited on pages 11–13, 27, 28, 30, 31, 118, 119, 125–127, 129–131, 171.*

[8] Jiang Duan et al. "Tone-mapping High Dynamic Range Images by Novel Histogram Adjustment". In: *Pattern Recogn.* 43.5 (May 2010), pp. 1847–1862 *Cited on pages 11–13, 16, 27, 28, 30, 31, 118, 119, 125–127, 129–131, 171.*

[9] Sumanta N. Pattanaik et al. “Time-dependent Visual Adaptation for Fast Realistic Image Display”. In: *Proceedings of the 27th Annual Conference on Computer Graphics and Interactive Techniques*. SIGGRAPH ’00. New York, NY, USA: ACM Press/Addison-Wesley Publishing Co., 2000, pp. 47–54 *Cited on pages 11–13, 19, 117.*

[10] F. Drago et al. “Adaptive Logarithmic Mapping For Displaying High Contrast Scenes”. In: *Computer Graphics Forum* 22 (2003), pp. 419–426 *Cited on pages 11–13, 15, 27, 28, 30, 31, 117–119, 125–127, 129–131, 171.*

[11] K Chiu et al. “Spatially Nonuniform Scaling Functions for High Contrast Images”. In: *Proceedings of Graphics Interface ’93*. 1993, pp. 245–253 *Cited on pages 12, 13, 17.*

[12] Erik Reinhard et al. “Photographic Tone Reproduction for Digital Images”. In: *ACM Trans. Graph.* 21.3 (July 2002), pp. 267–276 *Cited on pages 12, 13, 18, 117.*

[13] Sumanta N. Pattanaik et al. “A Multiscale Model of Adaptation and Spatial Vision for Realistic Image Display”. In: *Proceedings of the 25th Annual Conference on Computer Graphics and Interactive Techniques*. SIGGRAPH ’98. New York, NY, USA: ACM, 1998, pp. 287–298 *Cited on pages 12, 13.*

[14] Michael Ashikhmin. “A Tone Mapping Algorithm for High Contrast Images”. In: *Proceedings of the 13th Eurographics Workshop on Rendering*. EGRW ’02. Pisa, Italy: Eurographics Association, 2002, pp. 145–156 *Cited on pages 12, 13, 18.*

[15] Patrick Ledda, Luis Paulo Santos, and Alan Chalmers. “A Local Model of Eye Adaptation for High Dynamic Range Images”. In: *Proceedings of the 3rd International Conference on Computer Graphics, Virtual Reality, Visualisation and Interaction in Africa*. AFRIGRAPH ’04. Stellenbosch, South Africa: ACM, 2004, pp. 151–160 *Cited on pages 12, 13.*

[16] Frédo Durand and Julie Dorsey. “Fast Bilateral Filtering for the Display of High-dynamic-range Images”. In: *Proceedings of the 29th Annual Conference on Computer Graphics and Interactive Techniques*. SIGGRAPH ’02. San Antonio, Texas: ACM, 2002, pp. 257–266 *Cited on pages 12, 13, 19, 27, 28, 30, 31, 117–119, 125–127, 129–131, 171.*

[17] Raanan Fattal, Dani Lischinski, and Michael Werman. “Gradient Domain High Dynamic Range Compression”. In: *ACM Trans. Graph.* 21.3 (July 2002), pp. 249–256 *Cited on pages 12, 13, 19.*

[18] Prasun Choudhury and Tumblin. “The Trilateral Filter for High Contrast Images and Meshes”. In: *Proceedings of the 14th Eurographics Workshop on Rendering*. EGRW ’03. Leuven, Belgium: Eurographics Association, 2003, pp. 186–196 *Cited on pages 12, 13.*

[19] Jiangtao Kuang, Garrett M. Johnson, and Mark D. Fairchild. "iCAM06: A Refined Image Appearance Model for HDR Image Rendering". In: *J. Vis. Comun. Image Represent.* 18.5 (Oct. 2007), pp. 406–414 *Cited on pages 12, 13.*

[20] Rahman Zia-ur, Jobson Daniel J., and Woodell Glenn A. *A Multiscale Retinex for Color Rendition and Dynamic Range Compression.* Tech. rep. 1996 *Cited on pages 12, 13, 17.*

[21] Dani Lischinski et al. "Interactive Local Adjustment of Tonal Values". In: *ACM Trans. Graph.* 25.3 (July 2006), pp. 646–653 *Cited on pages 12, 13, 21.*

[22] Tom Mertens, Jan Kautz, and Frank Van Reeth. "Exposure Fusion". In: *Proceedings of the 15th Pacific Conference on Computer Graphics and Applications.* PG '07. Washington, DC, USA: IEEE Computer Society, 2007, pp. 382–390 *Cited on pages 12, 13.*

[23] Yangli Hector Yee and Pattanaik. "Segmentation and Adaptive Assimilation for Detail-preserving Display of High-dynamic Range Images". In: *The Visual Computer* 19.7 (2003), pp. 457–466 *Cited on pages 12, 13, 21.*

[24] Grzegorz Krawczyk, Karol Myszkowski, and Hans-Peter Seidel. "Lightness Perception in Tone Reproduction for High Dynamic Range Images". In: *The European Association for Computer Graphics 26th Annual Conference EUROGRAPHICS.* Vol. 24. Blackwell, 2005 *Cited on pages 12, 13.*

[25] Raanan Fattal. "Edge-avoiding Wavelets and their Applications". In: *ACM Trans. Graph.* 28.3 (July 2009), 22:1–22:10 *Cited on pages 11–13, 20, 27, 28, 30, 31, 87, 88, 118, 119, 125–127, 129–131, 171.*

[26] Yuanzhen Li, Lavanya Sharan, and Edward H. Adelson. "Compressing and Companding High Dynamic Range Images with Subband Architectures". In: *ACM SIGGRAPH Papers.* ACM, 2005, pp. 836–844 *Cited on pages 11–13, 20, 27, 28, 30, 31, 74, 118, 119, 125–127, 129–131, 171.*

[27] Z. Mai et al. "On-the-fly Tone Mapping for Backward-Compatible High Dynamic Range Image/Video Compression". In: *Proceedings of 2010 IEEE International Symposium on Circuits and Systems.* May 2010, pp. 1831–1834 *Cited on pages 11–13.*

[28] Z. Mai et al. "Optimizing a Tone Curve for Backward-Compatible High Dynamic Range Image and Video Compression". In: *IEEE Transactions on Image Processing* 20.6 (June 2011), pp. 1558–1571 *Cited on pages 11–13.*

[29] P. Lauga et al. "Improved Tone Mapping Operator for HDR Coding Optimizing the Distortion/Spatial Complexity Trade-off". In: *2014 22nd European Signal Processing Conference (EUSIPCO).* Sept. 2014, pp. 1607–1611 *Cited on pages 11–13.*

[30] Anas Husseis, Anissa Mokraoui, and Basarab Matei. “Revisited Histogram Equalization as HDR Images Tone Mapping Operators”. In: *2017 IEEE International Symposium on Signal Processing and Information Technology (ISSPIT)*. Bilbao – Spain, Dec. 2017 *Cited on pages 11, 12, 16, 27, 28, 30, 31, 36, 99, 118, 119, 125–127, 129–131, 171.*

[31] J. Tumblin and H. Rushmeier. “Tone Reproduction for Realistic Images”. In: *IEEE Computer Graphics and Applications* 13.6 (Nov. 1993), pp. 42–48 *Cited on pages 14, 27, 28, 30, 31, 118, 119, 125–127, 129–131, 171.*

[32] Rahman Zia-ur, Woodell Glenn A., and Jobson Daniel J. *A Comparison of the Multiscale Retinex With Other Image Enhancement Techniques.* Tech. rep. 1997 *Cited on page 17.*

[33] Tunç Ozan Aydin, Karol Mantiuk Rafałand Myszkowski, and Hans-Peter Seidel. “Dynamic Range Independent Image Quality Assessment”. In: *ACM Trans. Graph.* 27.3 (Aug. 2008), 69:1–69:10 *Cited on pages 22, 23.*

[34] Hojatollah Yeganeh and Zhou Wang. “Objective Quality Assessment of Tone-Mapped Images”. In: *Trans. Img. Proc.* 22.2 (Feb. 2013), pp. 657–667 *Cited on pages 22, 23, 31, 41, 100, 109, 117, 118, 146.*

[35] K. Ma et al. “High Dynamic Range Image Compression by Optimizing Tone Mapped Image Quality Index”. In: *IEEE Transactions on Image Processing* 24.10 (Oct. 2015), pp. 3086–3097 *Cited on pages 22, 26, 31.*

[36] H. Ziaei Nafchi et al. “FSITM: A Feature Similarity Index For Tone-Mapped Images”. In: *IEEE Signal Processing Letters* 22.8 (Aug. 2015), pp. 1026–1029 *Cited on pages 22, 26, 31.*

[37] H.R. Sheikh et al. *Live Image Quality Assessment Database Release 2.* Ed. by H.R. Sheikh et al. *Cited on page 22.*

[38] Rafal Mantiuk et al. “Predicting Visible Differences in High Dynamic Range Images - Model and its Calibration”. In: 5666 (Mar. 2005) *Cited on page 23.*

[39] Andrew B. Watson. “Visual Detection of Spatial Contrast Patterns: Evaluation of Five Simple Models.” In: *Opt. Express* 6.1 (Jan. 2000), pp. 12–33 *Cited on page 23.*

[40] Z. Wang, E. P. Simoncelli, and A. C. Bovik. “Multiscale structural similarity for image quality assessment”. In: *37th Asilomar Conference on Signals, Systems Computers.* Vol. 2. Nov. 2003, 1398–1402 Vol.2 *Cited on page 24.*

[41] W. J. Crozier, ed. *On the Variability of Critical Illumination for Flicker Fusion and Intensity Discrimination.* 1935 *Cited on page 25.*

[42] J. Mannos and D. Sakrison. “The Effects of a Visual Fidelity Criterion of the Encoding of Images”. In: *IEEE Trans. Inf. Theor.* 20.4 (Sept. 2006), pp. 525–536 *Cited on page 25.*

[43] D. H. Kelly. “Effects of Sharp Edges on the Visibility of Sinusoidal Gratings”. In: *Journal of the Optical Society of America (1917-1983)* 60 (Jan. 1970), p. 98 *Cited on page 25.*

[44] E. Reinhard and K. Devlin. “Dynamic Range Reduction Inspired by Photoreceptor Physiology”. In: *IEEE Transactions on Visualization and Computer Graphics* 11.1 (2005), pp. 13–24 *Cited on pages 27, 28, 30, 31, 118, 119, 125–127, 129–131, 171.*

[45] B. C. Thai, A. Mokraoui, and B. Mateï. “Piecewise Linear Perceptual Quantizer as a Non-Uniform Histogram Equalization Adjustment for Contrast Enhancement of Tone Mapped HDR Images”. In: *9th IEEE International Symposium on Signal, Image, Video and Communications (ISIVC)* (Nov. 2018) *Cited on page 33.*

[46] Eric A. Newman. “The Retina: An Approachable Part of the Brain by John E. Dowling”. In: 87 (Dec. 2012) *Cited on page 35.*

[47] Qasim Zaidi, Arthur Shapiro, and Donald Hood. “The Effect of Adaptation on the Differential Sensitivity of the s-cone Color System”. In: *Vision Research* 32.7 (1992), pp. 1297–1318 *Cited on page 35.*

[48] Zicong Mai et al. *Visually-Favorable Tone-mapping With High Compression Performance.* Sept. 2010 *Cited on page 36.*

[49] B. C. Thai, A. Mokraoui, and B. Mateï. “Performance Evaluation of High Dynamic Range Image Tone Mapping Operators Based on Separable Nonlinear Multiresolution Families”. In: *24th IEEE European Signal Processing Conference (EUSIPCO)* (Aug. 2016), pp. 1891–1895 *Cited on page 49.*

[50] B. C. Thai et al. “Image Tone Mapping Approach Using Essentially Non-Oscillatory Bi-quadratic Interpolations Combined with a Weighting Coefficients Strategy”. In: *IEEE International Symposium on Signal Processing and Information Technology (ISSPIT)* (Dec. 2017), pp. 089–094 *Cited on page 49.*

[51] Ami Harten et al. “Uniformly High Order Accurate Essentially Non-oscillatory Schemes, III”. In: *J. Comput. Phys.* 71.2 (Aug. 1987), pp. 231–303 *Cited on page 53.*

[52] Ami Harten. “Multiresolution Representation of Data: A General Framework”. In: *SIAM Journal on Numerical Analysis* 33.3 (1996), pp. 1205–1256 *Cited on page 53.*

[53] Francesc Aràndiga and Rosa Donat. “Nonlinear Multiscale Decompositions: the Approach of A. Harten”. In: *Numerical Algorithms* 23.2 (2000), pp. 175–216 *Cited on page 53.*

[54] Sergio Amat et al. “Data Compression with ENO Schemes: A Case Study”. In: *Applied and Computational Harmonic Analysis* 11.2 (2001), pp. 273–288 *Cited on page 53.*

[55] B. Mateï and S. Meignen. “Nonlinear and Nonseparable Bidimensional Multiscale Representation Based on Cell-Average Representation”. In: *IEEE Transactions on Image Processing* 24.11 (Nov. 2015), pp. 4570–4580 *Cited on page 68.*

[56] Basarab Mateï and Sylvain Meignen. “Nonlinear Cell-average Multiscale Signal Representations: Application to Signal Denoising”. In: *Signal Process.* 92.11 (Nov. 2012), pp. 2738–2746 *Cited on pages 68, 74.*

[57] B. C. Thai, A. Mokraoui, and B. Mateï. “HDR Image Tone Mapping Approach based on Near Optimal Separable Adaptive Lifting Scheme”. In: *22nd IEEE Signal Processing: Algorithms, Architectures, Arrangements, and Applications (SPA)* (Sept. 2018) *Cited on page 89.*

[58] B. C. Thai, A. Mokraoui, and B. Mateï. “Contrast Enhancement and Details Preservation of Tone Mapped High Dynamic Range Images”. In: *Journal of Visual Communication and Image Representation (JVCI)*. Elsevier, 2018 *Cited on page 89.*

[59] Rafal Mantiuk, Karol Myszkowski, and Hans-Peter Seidel. “A Perceptual Framework for Contrast Processing of High Dynamic Range Images”. In: *ACM Trans. Appl. Percept.* (June 2006), pp. 286–308 *Cited on page 117.*

Titre : Opérateurs de mise en correspondance tonale d'images à grande gamme dynamique.

Mots-clefs : Image à grande gamme dynamique, Image à faible gamme dynamique, Mise en correspondance tonale d'image à grande gamme dynamique, Système visuel humain, Note moyenne d'opinion, Egalisation d'histogramme, Multiresolution séparable, Multiresolution non-séparable, Schéma de lifting, Interpolation non-oscillatoire, Prédiction.

Résumé : La conversion d'une image à grande gamme dynamique (HDR) en une image à faible gamme dynamique est étudiée de façon à garantir un rendu visuel de cette dernière de bonne qualité. La première contribution concerne le rehaussement de contraste de l'image mappée en utilisant une fonction linéaire par morceaux pour que l'égalisation d'histogramme soit ajustée à la "s-courbe" d'adaptation du système visuel humain. La deuxième et troisième contributions portent sur la préservation des détails de l'image HDR. Des approches multirésolution séparables et non séparables, basées sur des stratégies non oscillatoires, prenant en compte les singularités de l'image HDR dans la dérivation du modèle mathématique, sont proposées. La quatrième contribution non seulement préserve les détails mais également améliore le contraste de l'image HDR mappée. Un schéma de lifting séparable "presque optimal" est proposé. Il s'appuie sur une étape de prédiction adaptative des coefficients. Cette dernière repose sur une combinaison linéaire pondérée des coefficients voisins pour extraire les détails pertinents sur l'image HDR à chaque niveau de résolution. Un mappage linéaire par morceaux est ensuite appliqué à la reconstruction grossière. Les résultats de simulation fournissent de bonnes performances en termes de qualité visuelle et de métrique TMQI (Tone Mapped Quality Index) par rapport aux approches de mise en correspondance tonale classiques. L'impact des paramètres TMQI sur la qualité visuelle des images mappées est discuté. Les paramètres proposés montrent une forte corrélation entre la métrique modifiée et la note moyenne d'opinion.

Title : Tone Mapping Operators for High Dynamic Range Images.

Keywords : High Dynamic Range (HDR) image, Low Dynamic Range (LDR) image, Image tone Mapping Operators, Human Visual System, Mean Opinion Score, Histogram equalization, Tone Mapped Quality Index, Separable multiresolution, Non-separable multiresolution, Lifting scheme, Essentially Non-Oscillatory interpolation, Prediction.

Abstract : The conversion of High Dynamic Range (HDR) image into Low Dynamic Range (LDR) image is investigated so that the visual rendering of the latter is of good quality. The first contribution focused on the contrast enhancement of the tone mapped image using a piecewise linear function as a non-uniform histogram equalization adjustment to model the "s-shaped" curve of the human visual adaptation. The second and third contributions are concerned with the details preservation of the HDR image on the tone mapped image. Separable and non-separable multiresolution approaches based on essential non-oscillatory strategies, taking into account the HDR image singularities in the mathematical model derivation, are proposed. The fourth contribution not only preserves details but also enhances the contrast of the HDR tone mapped image. A separable "near optimal" lifting scheme using an adaptive powerful prediction step is proposed. The latter relies on a linear weighted combination depending on the neighbouring coefficients to extract the relevant finest details on the HDR image at each resolution level. A piecewise linear mapping is then applied on the coarse reconstruction. Simulation results provide good performance, both in terms of visual quality and Tone Mapped Quality Index (TMQI) metric, compared to existing competitive tone mapping approaches. The impact of the TMQI parameters on the visual quality of the tone mapped images is discussed. The proposed parameters show a strong correlation between the modified metric and the Mean Opinion Score (MOS).

Université Paris 13 - Institut Galilée
Laboratoire de Traitement et Transport de l'Information (L2TI)